Development of Green Synthetic Approaches for the Potential Application of Carbon and Semiconductor Nanomaterials for Emerging Applications

by

Paola Russo

A thesis
presented to the University of Waterloo
in fulfillment of the
thesis requirement for the degree of
Doctor of Philosophy
in
Mechanical and Mechatronics Engineering (Nanotechnology)

Waterloo, Ontario, Canada, 2017

Author's declaration

I hereby declare that I am the sole author of this thesis. This is a true copy of the thesis, including any required final revisions, as accepted by my examiners.

I understand that my thesis may be made electronically available to the public.

Examining Committee Membership

The following served on the Examining Committee for this thesis. The decision of the Examining Committee is by majority vote.

External Examiner	Professor Martin Kuball, School of Physics, University of Bristol, UK
Supervisor	Professor Norman Y. Zhou, Mechanical & Mechatronics Engineering, University of Waterloo, Canada
Internal Member	Professor Ehsan Toyserkani, Mechanical & Mechatronics Engineering, University of Waterloo, Canada
Internal Member	Professor Mustafa Yavuz, Mechanical & Mechatronics Engineering, University of Waterloo, Canada
Internal-external Member	Professor Walter W. Duley, Physics & Astronomy, University of Waterloo, Canada

Abstract

The increasing interest towards the synthesis and modification of different nanomaterials is attributed to their outstanding mechanical, physical and electrical properties that allow their use in different fields. In the last decades, novel nanomaterials have been successfully synthesized in order to provide materials with improved performances to be employed for water treatment, photocatalysis, to replace silicon–based devices in electronics and so on. For example, carbon-based materials are promising candidates for the fabrication of conductive inks and future non-volatile memory devices. However, the absence of an eco-sustainable, straightforward and time effective process for their production has hindered their large-scale application in electronics.

The aim of this thesis is to explore alternative synthetic approaches for the synthesis of different materials and their structural modification in order to gain a better understanding how the processes could be controlled to have desired structure and hence materials with improved performances. In particular, laser ablation in liquids (PLA) and electrochemical processes will be the focus of this study.

It has been shown that pulsed laser ablation of carbon materials and TiO_2 nanoparticles can be used for the synthesis of new materials and/or modification of their structure. The laser ablation compared to other common synthetic approaches has many advantages. One of which is the eco-sustainability of the process, since the synthesis is performed in water without the use or production of products harmful for the environment. The second advantage is the versatility of the technique that allows the synthesis and modification of different nanomaterials depending on the target material employed. In this thesis it will be demonstrated that laser ablation of a dispersion of graphene oxide can be employed as a straightforward technique to induce structural modifications of the material, i.e. reduction of the graphene oxide sheets and synthesis of graphene quantum dots varying laser ablation time and ablation power. The nanomaterials obtained can be mixed with silver nanoparticles for the fabrication of hybrid conductive inks, which have a resistivity lower than inks made with only silver nanoparticles. The versatility of the laser ablation is demonstrated by extending the study to titanium dioxide powders. It will be discussed that the laser ablation of TiO_2 nanoparticles leads to nanoparticles with different crystalline structures. Indeed, with a proper control over the laser ablation parameters, such as

ablation time and laser power, it is possible to induce a phase transformation of TiO_2 nanoparticles whether they are dispersed in water or deposited onto a substrate.

Similar to the laser ablation, the electrochemical processes such as the electrophoretic deposition (EPD) allows the synthesis and deposition of different type of materials. In particular, in this thesis this technique will be employed for the straightforward synthesis of carbon nanowalls (CNWs). These carbon-based materials are usually synthesized by chemical vapor deposition, which requires the use of precursor gases and high temperatures and pressures. Whereas, the method developed during my research allows a time-effective synthesis of these nanomaterials; moreover, the deposition of the CNWs directly onto conductive substrate permits for the first time the fabrication of carbon-based resistive switching memory devices. This technique could be used for the development on a large scale of this type of devices, whose broad fabrication has been hindered due to the complex production mechanisms. Another advantage of the electrochemical processes is the possibility of modifying the chemical composition of the materials. In this thesis, the anodic oxidation has been used for the first time to oxidize the carbon structures obtained by EPD in order to engineer their electrical performances. In literature, the anodic oxidation has been used to study the redox processes in electronic devices or to increase the electrochemical capacitance of carbon materials, but never as a specific technique to tailor the materials properties. As aforementioned EPD, like PLA, is a versatile technique and in this study it has been used for the growth of ZnO rods. ZnO rods are usually grown by hydrothermal processes, which can be time consuming. In this thesis, the growth of the rods has been conducted directly on conductive substrates, which were then patterned for the fabrication of electronic devices.

Acknowledgements

I would like to thank my supervisor, Professor Norman Zhou for his guidance and support he gave to me throughout my doctoral studies.

I would like to express my sincere gratitude to Professor Giuseppe Compagnini, from University of Catania, for giving me suggestions and advices. I would like to thank all my colleagues, who I consider my friends and who supported me in research and life: Gitanjali Shanbhag, Stephen Peterkin, Foss Jiao, Robert Liang, Emanuel Santos, Rafael Ribeiro, Peng Peng, Ayah Taji, Jenny Ye, Jennifer Lou, Ali Akbar Shokati, Emad Shahnam, Daozhi Shen, Joyce Koo, Elahe Jabari, Ehsan Marzbanrad, Dulal Saha, Neil Huang, Tirdad Niknejad, Luchan Lin.

A special thanks to my friend and colleague Ming Xiao, with whom I had thoughtful discussion and suggestions of research throughout my doctoral studies.

I would like to thank all my colleagues in CAMJ with whom I had the pleasure spending my studies.

I would like to thank Dr. Carmen Andrei for the TEM/HRTEM analysis performed at the Canadian Centre for Electron Microscopy (CCEM) at McMaster University. I would like to thank the Waterloo Institute of Nanotechnology (WIN), which helped supporting my work.

I would like to thank my friend Chiara Privitera, although we are more than 7000 km apart, she is always there for me, no matter where I am or where I will be.

My warmest thank to my partner Andrew Townshend, who supported, encouraged me and gave me strength day after day.

I have no words to express my infinite gratitude to my parents, Sebastiano Russo and Maria Luisa Indelicato and to my sisters Brunella and Valeria for their endless love, support and encouragement.

Thank you for everything

Dedication

To my Beloved Family

and

Andrew

Table of Contents

Author's declaration ii

Examining Committee Membership iii

Abstract iv

Acknowledgements vi

Dedication vii

List of Figures xiii

List of Tables xxi

List of Abbreviations xxii

Chapter 1. Introduction 1

1.1. Background 1

1.2. Objectives 2

1.3. Organization of the thesis 3

Chapter 2. Literature Review 5

2.1. Graphene and Graphene-Based Nanomaterials 5

2.1.1. Graphene 6

2.1.2. Graphene Oxide 7

2.1.3. Graphene Quantum Dots 7

2.1.4. Graphene Nanowalls 8

2.1.5. Carbynes 9

2.2. Properties of Graphene and its Derivatives 9

2.3. Synthesis of Graphene and Graphene-based nanomaterials 10

2.3.1. Synthesis of Graphene 11

2.3.1.1. Mechanical Exfoliation 11

2.3.1.2. Chemical Exfoliation 11

2.3.1.3. Synthesis and Reduction of Graphene Oxide 12

2.3.2. Synthesis of Graphene Quantum Dots 12

2.3.2.1. Hydrothermal and Solvothermal Methods 12

2.3.2.2. Cage-opening of fullerene C_{60} 13

2.3.3. Synthesis of Graphene Nanowalls 13
2.4. Alternative Method for the Synthesis of Graphene-based Nanomaterials 14
2.4.1. Pulsed Laser Ablation 14
2.4.1.1. Graphene from laser exfoliation of graphite……..15
2.4.1.2. Graphene from laser reduction of graphene oxid……...17
2.4.2. GNWs by Electric Field-Assisted Laser ablation of Carbon in Water 18
2.5. Semiconductor nanomaterials: Titanium Dioxide and Zinc Oxide.....18
2.5.1. TiO_2.....18
2.5.2. ZnO 19
2.6. Synthesis of TiO_2 19
2.6.1. Hydrothermal Synthesis.....19
2.6.2. Sol-gel Method.....20
2.6.3. Laser Ablation of Titanium Target 20
2.7. Synthesis of ZnO 20
2.7.1. Hydrothermal Synthesis.....21
2.7.2. Electrochemical Method 21
2.8. Summary 22
Chapter 3. Characterization Methodologies 24
3.1. Optical Microscope.....24
3.2. Raman Spectroscopy.....25
3.2.1. Graphene-based materials.....25
3.2.2. TiO_2.....27
3.2.3. ZnO 27
3.3. Atomic Force Microscopy (AFM) 27
3.4. Scanning Electron Microscopy (SEM) 28
3.5. Transmission Electron Microscopy (TEM) 28
3.5.1. Graphene-based nanomaterials 28
3.5.2. TiO_2.....29
3.5.3. ZnO 29

PART 1 30

Chapter 4. Single-step synthesis of graphene quantum dots by femtosecond laser ablation of graphene oxide dispersions[250] 31

4.1. Introduction 31

4.2. Experimental 33

4.2.1. GQDs synthesis 33

4.2.2. Separation of the GQDs 34

4.2.3. Preparation of the hybrid ink and of the hybrid ink printed patterns 35

4.2.4. Temperature profile simulation method 35

4.2.5. Instrumentation 36

4.2.6. Size Distribution Analysis 37

4.2.7. Quantum Yield Measurements 38

4.2.8. Calculation of the resistivity of the printed patterns 38

4.3. Results and Discussion 39

4.3.1. Morphology of fs laser processed GO dispersions at low power 39

4.3.2. Mechanism of GQDs formation on femtosecond laser ablated GO 49

4.3.3. GO dispersion defect density as a function of laser ablation time 54

4.3.4. GQDs nanostructure dependence on laser type and frequency 55

4.3.5. Effect of high laser power (2.4 W) on the morphology of GO dispersions 55

4.3.6. Photoluminescence of femtosecond laser processed GO dispersions 59

4.3.7. Application: Conductive ink using GQDs in GO dispersion 62

4.4. Summary 64

Chapter 5. Phase Transformation of TiO_2 Nanoparticles by Femtosecond Laser Ablation in Aqueous Solutions and Deposition on Conductive Substrates[139] 66

5.1. Introduction 66

5.2. Experimental 68

5.2.1. Laser ablation of TiO_2 in water 68

5.2.2. Deposition of TiO_2 onto FTO substrates (P25/FTO) 69

5.2.3. Laser patterning of TiO_2 on FTO substrate 69

5.3. Results and discussion 70
5.3.1. TiO_2 phase transformation upon laser ablation in water 70
5.3.2. Laser ablation of P25/FTO substrates 84
5.4. Summary 87
PART 2 89
Chapter 6. Carbon Materials for Next Generation Resistive Switching Memory Devices[15] 90
6.1. Introduction 90
6.2. Experimental 93
6.2.1. Instrumentation 95
6.3. Results and Discussion 95
6.4. Synthesis of the Cs 106
6.5. Electrochemical oxidation of the Cs 106
6.6. Results and discussion 106
6.7. Summary 120
Chapter 7. UV-induced multilevel current amplification memory effect in zinc oxide rods resistive switching devices. 121
7.1. Introduction 121
7.2. Experimental 123
7.2.1. Deposition of the ZnO seed layer 123
7.2.2. Growth of the ZnO rods 123
7.2.3. Device fabrication 124
7.2.4. Instrumentation 124
7.3. Results and Discussion 124
7.4. Summary 135
Chapter 8. Conclusions and Outlook 136
8.1. Conclusions 137
8.1.1. Single-step synthesis of graphene quantum dots by femtosecond laser ablation of graphene oxide dispersions 137

8.1.2. Phase Transformation of TiO_2 Nanoparticles by Femtosecond Laser Ablation in Aqueous Solutions and Deposition on Conductive Substrates 137

8.1.3. Carbon Materials for Next Generation Resistive Switching Memory Devices.....138

8.1.4. UV-induced multilevel current amplification memory effect in zinc oxide rods resistive switching devices.....138

8.2. Outlook 139

Chapter 9. Research Contributions 140

9.1. Articles Published in Refereed Journals 140

9.2. Submitted/To be submitted 141

9.3. Conference Presentations/Attendance: 141

9.4. Posters 142

9.5. Awards received.....142

Copyright Permissions 143

References.....185

List of Figures

Figure 1: Block Diagram illustrating the research carried out during the doctoral studies.....3

Figure 2: (a) Graphite structure; (b) diamond structure; (c) fullerene structure; (d) carbon nanotube structure and (e) graphene structure. From Ref. [31] © IOP Publishing. Reproduced with permission. All rights reserved.....5

Figure 3: Graphene can be employed as building block for the synthesis of carbon nanostructures with different dimensionality . Reproduced from ref. [40] open access article distributed under the Creative Commons Attribution License.....6

Figure 4: (a) Schematic view (top) of graphene nanowalls structure obtained from the stacking of many graphene (b) layers.....8

Figure 5: (a) Graphene structure; (b) graphite structure as a result of the stacking of graphene layers (c) schematic of the in-plane σ bonds and the π orbitals perpendicular to the plane of the graphene sheets. Reproduced from ref. [82] with permission of The Royal Society of Chemistry.....9

Figure 6: On the left the electronic dispersion in graphene in shown, while on the right a zoom in of the energy bands close to one of the Dirac points is displayed. Reprinted with permission from ref. [83] by the American Physical Society.....10

Figure 7: Optical image of graphene sample obtained from mechanical exfoliation of graphite. From ref. [103] reprinted with permission from AAAS.....11

Figure 8: Schematic of the setup employed by Cotton for the synthesis of metal nanoparticles by PLAL. Adapted from ref. [120].....15

Figure 9: (a) high and (b) low fluence ablation thresholds in graphite. Reprinted with permission from ref. [125] by the American Physical Society.....16

Figure 10: (a) low and (b) high magnification SEM images of r-GO layers obtained upon nanosecond laser exfolitiaon of HOPG in water; (c) AFM of the detached layer showing a heigth step of 1.56 nm. From ref. [129] © IOP Publishing. Reproduced with permission. All rights reserved.....17

Figure 11: (a) Graphene layers deposited on 300 nm SiO_2 imaged with white light, (b) green light and (c) graphene sample on 200 nm SiO2 imaged with white light. The top and bottom panels represents the flakes shown in (a) and (c) illuminated with different bandpass filters. Reprinted from ref. [161], with the permission of AIP Publishing.....24

Figure 12: (a) Raman spectra of graphite and graphene; (b) evolution of the 2D increasing the number of graphene layers. Adapted from ref. [167]. 26

Figure 13: Raman spectrum of graphene oxide (GO). Adapted from ref. [169] open access article distributed under the Creative Commons CC-BY License http://creativecommons.org/ 26

Figure 14: High-resolution TEM showing single-, three- , and four-layer graphene sheets. Adapted with permission from ref. [180] Copyright 2017 American Chemical Society. 28

Figure 15: Defects detected in graphene by TEM. Adapted with permission from ref.[183] Copyright 2017 American Chemical Society.....29

Figure 16: Picture of the laser ablation setup. Reproduced from ref. [202] by permission of The Royal Society of Chemistry.....34

Figure 17: : a) AFM image of GO sheets deposited onto the Si/SiO2 substrate; b) magnification of the area highlighted with a dash rectangular in panel a); c) section profile along the white line in panel b); d) SEM image of GO sheets. Reproduced from ref. [202] by permission of The Royal Society of Chemistry 40

Figure 18: SEM images of GO dispersion after (a) 5, (b-b1) 15, (c-c1) 30 and (d-d1) 60 minutes of laser ablation. Reproduced from ref. [202] by permission of The Royal Society of Chemistry 41

Figure 19: AFM images of the GO dispersions after (a) 5 minutes. (b) 15 minutes, (c) 30 minutes and (d) 60 minutes of laser ablation; (e) and (f) height profiles of image (c) and (d) respectively. Reproduced from ref. [202] by permission of The Royal Society of Chemistry 42

Figure 20: TEM images of a) non-treated GO solution and GO solution after (c) 5 minutes and (e) 15 minutes of laser ablation. In panel (b) HRTEM image of the non-modified GO sheets shows an interlayer d-spacing of 0.375 nm, which is larger than that of the graphite due to the presence of oxygen/containing groups. HR images (d) and (f), show the presence of few graphene quantum dots within the graphene oxide sheets after 5 and 15 minutes of laser treatment, respectively. Reproduced from ref. [202] by permission of The Royal Society of Chemistry 43

Figure 21: Raw and (2) binned size distribution of GQDs after (a) 5 minutes, (b) 15 minutes, (c) 30 minutes and (d) 60 minutes of laser ablation at 1.3W. Reproduced from ref. [202] by permission of The Royal Society of Chemistry 45

Figure 22: a) TEM image of GO sheets after 30 minutes of laser ablation, in the inset GQDs can be seen embedded in the residual GO sheets; b) HRTEM image of a GQDs and its relative FFT image showing a d-spacing of 0.21nm. Reproduced from ref. [202] by permission of The Royal Society of Chemistry ..46

Figure 23: a) TEM overview of the GO sheets after 60 minutes of laser treatment; b) high magnification image of the corrugated sheets displaying several GQDs; c) two GQDs joined (highlighted in yellow) together. Reproduced from ref. [202] by permission of The Royal Society of Chemistry 47

Figure 24: HRTEM image of dialysed GQDs dispersion obtained after 30 minutes of laser ablation. Reproduced from ref. [202] by permission of The Royal Society of Chemistry 49

Figure 25: a) Electronic (solid line) and atomic temperature (dashed line) change during and after a 35 fs sec laser pulse; (b) peak atomic temperature (solid line) and average atomic temperature change for a 90 minute fs sec laser irradiation simulation. Reproduced from ref. [202] by permission of The Royal Society of Chemistry.....50

Figure 26: Schematic for the formation of the GQDs. In the first step the sp^2 carbon atoms are oxidized to sp^3 by the H_2O_2 formed during the water breakdown induced by fs ablation; in the second step the sp^3 carbon atoms are converted to CO_2 upon reaction with O_2 generated by fs ablation. In the final step the reduction and fragmentation of the GO sheets due to the formation of CO_2 lead to the synthesis of GQDs 52

Figure 27: XPS of GO solution before (a) and after PLA at 1.3W for (b) 5, (c) 15, (d) 30 and (e) 60 minutes respectively. Reproduced from ref. [202] by permission of The Royal Society of Chemistry ..53

Figure 28: Raman spectra of GO dispersion before (black spectrum) and after 5 minutes (light blue line), 15 minutes (purple line), 30 minutes (green line), and 60 minutes (dark blue line) of laser ablation. Reproduced from ref. [202] by permission of The Royal Society of Chemistry 54

Figure 29: TEM images of dispersions obtained performing PLA at 2.4 W for 5 (a), 15 ($b_{1,2}$), 30 ($c_{1,2}$), and 60 ($d_{1,2}$) minutes. Reproduced from ref. [202] by permission of The Royal Society of Chemistry.....56

Figure 30: (1) Raw and (2) binned size distribution Size distribution of the GQDs obtained at 2.4W after (a) 5, (b) 15, (c) 30, and (d) 60 minutes of laser ablation. Reproduced from ref. [202] by permission of The Royal Society of Chemistry 57

Figure 31: GQDs diameter as a function of the laser ablation time at different laser ablation powers using (a) absolute values and (b) Gaussian fit values from binned size distribution. Reproduced from ref. [202] by permission of The Royal Society of Chemistry 58

Figure 32: a) SEM image of the solution after 60 minutes of ablation at 2.4W. Some tubular structures are observable within the damaged sheets; b) TEM and HRTEM (inset) images of the tubular structures. These structures are made up of folded sheets where some GQDs are found to be embedded in. Reproduced from ref. [202] by permission of The Royal Society of Chemistry 59

Figure 33: PL spectra of GQDs dispersion obtained after 30 minutes of laser ablation of GO sheets. The GQDs showed a strong emission peak at 410nm with an excitation wavelength of 300 nm. Reproduced from ref. [202] by permission of The Royal Society of Chemistry 60

Figure 34: PL spectra of GQDs solutions obtained after 5, 15, 30 and 60 minutes of laser ablation of GO. The PL spectra were recorded at an excitation wavelength of 300 nm. The laser treated solutions showed blue luminescence at 410 nm, while the starting GO did not show any luminescence. Reproduced from ref. [202] by permission of The Royal Society of Chemistry 61

Figure 35: Photographs of (a) water and (b) dialysed GQDs dispersion obtained after 30 minutes of laser ablation at 1.3W under 365 nm UV light Reproduced from ref. [202] by permission of The Royal Society of Chemistry.....62

Figure 36: Optical image of (a) AgNPs printed patterns and (b) GQDs@AgNP printed patterns; (c) and (d) SEM images of AgNPs and GQDs@AgNP patterns, respectively. Reproduced from ref. [202] by permission of The Royal Society of Chemistry 63

Figure 37: Schematic of femtosecond laser ablation experiment setup consisting of (A) optical table, (B) Ti-sapphire laser, (C) mirror system, (D) focusing lens, (E) container containing stir bar and TiO2 solution, and (F) stir plate. Reproduced from ref. [139] by permission of The Royal Society of Chemistry 68

Figure 38: Schematic of femtosecond laser ablation setup for laser patterning consisting of (A) optical table, (B) Ti-sapphire laser, (C) mechanical shutter, (D) neutral density filter, (E) focusing lens, (F) patterned substrate, (G) motorized stage, and (H) computer. Reproduced from ref. [139] by permission of The Royal Society of Chemistry 70

Figure 39: Raman spectra of P25 dispersions after 5, 15, 30, 60, and 120 minutes of laser ablation. For comparison, Raman spectra of anatase, rutile and P25 as purchased powders have been included. Reproduced from ref. [139] by permission of The Royal Society of Chemistry 72

Figure 40: Integrated Raman peak intensity ratio as a function of laser ablation time of P25 dispersion. After 5 minutes of laser ablation the nanoparticles are in the anatase form (red circle), while after 20 minutes the transformation to rutile starts to occur (green circle). After 60 minutes of laser ablation the particles transformed to rutile (blue circle), however increasing the ablation time (90 min), the particles start to transform to anatase (green circle) and after 120 minutes the particles possess anatase phase (red circle). Reproduced from ref. [139] by permission of The Royal Society of Chemistry 73

Figure 41: TEM images of P25 powders before (a) and after 5 (b), 15 (c), 30 (d), 60 (e), 90 (f) and 120 (g) minutes of laser ablation. Reproduced from ref. [139] by permission of The Royal Society of Chemistry 75

Figure 42: Schematic illustrating the two events responsible for the formation of spherical rutile nanoparticle in the focused area and the formation of smaller anatase particle in the irraditaed area.....76

Figure 43: HRTEM images of TiO2 powder with d-spacing profiles (a) before laser ablation and after (b) 5, (c) 15, and (d) 30 min of laser ablation. Reproduced from ref. [139] by permission of The Royal Society of Chemistry.....77

Figure 44: HRTEM images of TiO_2 powder with d-spacing profiles after (a, b) 60, (c) 90, and (d) 120 min of laser ablation. Reproduced from ref. [139] by permission of The Royal Society of Chemistry 78

Figure 45: Size distribution of P25 aqueous suspensions laser treated at: (a) 0 min, (b) 5 min, (c) 15 min, (d) 30 min, (e) 60 min, (f) 90 min, and (g) 120 min. (h) P25 diameter as a function of laser irradiation time. Reproduced from ref. [139] by permission of The Royal Society of Chemistry 80

Figure 46: XRD analysis of the as prepared P25 dispersion and f-after laser treatment. Reproduced from ref. [139] by permission of The Royal Society of Chemistry 82

Figure 47: (a) UV-Vis of TiO_2 suspension ablated at different ablation time; (b) Plot of $(\alpha h\upsilon)^2$ versus photon energy for direct transition and (inset) plot of energy bandgap values as a function of ablation time. Reproduced from ref. [139] by permission of The Royal Society of Chemistry 83

Figure 48: (a) Top-bottom view and (b) surface profile of P25/ FTO contained femtosecond laser produced lines of varying power. Reproduced from ref. [139] by permission of The Royal Society of Chemistry.....84

Figure 49: SEM images of (a-c) non-patterned and (d-f) laser patterned P25 on FTO. Reproduced from ref. [139] by permission of The Royal Society of Chemistry 85

Figure 50: (a) Raman mapping line of the laser patterned P25 on FTO, (b) Raman spectra of the area outside (black spectrum) and inside (red spectrum) the laser patterned area. Reproduced from ref. [139] by permission of The Royal Society of Chemistry 86

Figure 51: (a) Schematic of a typical RRAM device, (b) I-V curve typical of a bipolar resistive switching device 91

Figure 52: (a) Arc discharge setup employed for the synthesis of polyynes. The arc discharge was maintained between two graphite electrodes for 10 minutes; (b) UV-VIS spectrum of polyynes obtained

upon arc discharge of two graphite electrodes in water. Reprinted from [15], with permission from Elsevier 94

Figure 53: (a) Schematic design of the structure of the Al/CNWs/FTO device, (b) schematic of the apparatus for the EPD of polyynes in order to obtain the CNWs. Reprinted from [15], with permission from Elsevier.....96

Figure 54: a) SEM image of the surface morphology of the CNWs prepared by EPD of polyynes. b) Magnification of the CNWs surface morphology. c) C1s XPS and (d) Raman spectrum of the CNWs. Reprinted from [15], with permission from Elsevier 97

Figure 55: (a) TEM image of the CNWS and (b) HRTEM of the carbon nanowalls displaying an interlayer distance of 0.34 nm, which is the d-spacing of graphite. Reprinted from [15], with permission from Elsevier.....98

Figure 56: a) I-V curve of Al/CNWs/FTO device for first and 150 cycles of voltage sweeping. Arrows and numbers indicate the direction and sequence for the I–V scan. b) Endurance results of the device for over 150 cycles at 0.4V. c) Retention result over 5×10^4 seconds at a read voltage of 0.4V. Reprinted from [15], with permission from Elsevier 99

Figure 57: SCLC I-V characteristics of the Al/CNWs/FTO device plotted in double-logarithmic scale for the a) postive and b) negative bias. Reprinted from [15], with permission from Elsevier.....101

Figure 58: Schematic showing the RS mechanism of the Al/CNWs/FTO device. (a) The LRS after applying a positive bias. The electrons flow along the filled oxygen vacancies from the bottom FTO electrode to the top Al electrode without the requirement of a forming step. (b) Transitioning from LRS to HRS caused by a de-trapping process of electrons from the oxygen vacancies upon application of a negative bias. Reprinted from [15], with permission from Elsevier 102

Figure 59: a) Resistive switching characteristic after 1 and 20 cycles of the Al/CNWs/FTO device heat treated in air. b) C 1s XPS spectrum of the CNWs heat treated in air. Reprinted from [15], with permission from Elsevier 103

Figure 60: a) I-V characteristics after 1 and 20 cycles at a sweeping voltage of 2 V. b) retention of the device at 0.2 V. c) XPS spectrum of C 1s. Reprinted from [15], with permission from Elsevier 105

Figure 61: (a) Schematic of the three-electrode quartz cell employed for the oxidation of the carbon structures. (b) CV of Cs@FTO in 1 M Na_2SO_4 aqueous solution. the scan rate is 20 mV/s. (c) Electrochemical oxidation of the FTO substrate without the deposition of the carbon structures. It is possible to notice that the FTO surface has not been oxidized. 107

Figure 62: (a-b) schematic of the bottom up synthesis of Cs upon deposition of polyynes and (c) electrochemical oxidation of the synthesized Cs; (d, f, h) C 1s XPS spectra, SEM and TEM images of the Cs before and (e, g, i) after the electrochemical oxidation. In In (h-i) it is possible to notice that the d-spacing of the as-prepared Cs is 0.34 nm, which increases to 0.5 nm upon oxidation. 108

Figure 63: (a) TEM-Cross section of the Al@Cs@FTO device. (b-e) composition maps of Al, C, O and Sn, respectively. 110

Figure 64: (a) TEM-Cross section of the Al@OCs@FTO device. (b-e) composition maps of Al, C, O and Sn, respectively. 111

Figure 65: Raman spectra of as-prepared Cs (black curve) and the Cs after electrochemical oxidation (blue curve). 112

Figure 66: (a) I-V curve of Al/Cs@FTO and Al/OCs@FTO devices after 1 cycle of voltage sweeping. (b) Endurance of the Al/OCs@FTO device for over 50 cycles. (c) Retention results of the Al/OCs@FTO device over 10x103 seconds at a reading voltage of -0.4V. (d) Distribution of the SET and RESET voltages of the Al/OCs@FTO device. 113

Figure 67: I-V curves of Al/OCs@FTO device plotted in a double logarithmic scale under negative (a) and positive (b) voltages. 115

Figure 68: (a) OCs on the bottom electrode. (b) Pristine Ocs device after depsotion of the Al top electrode. (c) Drifting of the postively charged oxygen vacancies towards the bottom electrode upon application of a negative voltage and formation of the conductive filaments wich switch the device ON . (d) During the reset process the oxygen vacancies are repelled back from the Al top electrode causing the rupture of the conductive filaments and the switch of the device to the OFF state. 116

Figure 69: XPS spectrum of the Cs after 3 (a) and 6 (b) oxidation/reduction/oxidation cycles, respectively. (c) I-V curve of Al/3OCs@FTO and Al/6OCs@FTO devices after 1 cycle of voltage sweeping. 117

Figure 70: (a) XPS spectra of the 3MOCS, (b) current response under a voltage sweep of 20V, (c) 3 level memory profile upon application of 15V and a reset bias of -21V, (d) current response under 32 voltage cycles from 0V → 15V →0V. 119

Figure 71: (a) SEM image of ZnO top surface, (b) magnification of the ZnO rods obtained upon cathodic deposition, (c) TEM image of ZnO rods showing good crystallinity demonstrated by SAED analysis (inset), (d) HR-TEM showing the d-spacing of the ZnO rods 125

Figure 72: (a) Raman spectrum; (b) Zn 2p core-levels and (c) O1s region of the as-grown ZnO rods. .126

Figure 73: (a) I-V curves of the Ag/ZnO rods/FTO (inset) in dark condition and (b) under UV irradiation with a sweeping voltage of 4V for 1 cycle (black curves) and after 40 cycles (red curves).....128

Figure 74: Resistive switching mechanism of the Ag/ZnOrods/FTO device. (a) Initially the device is in the HRS, upon application of an electric field the oxygen vacancies start to pile up (b) and form conductive filaments, which switch the device to LRS. Under UV light illumination (c) more oxygen vacancies are formed, which lead to the formation of multiple conductive filaments. At reversed bias (d and e), the conductive filaments are broken and the device returns into the OFF state.....129

Figure 75: (a) 3-level current amplification of the device upon application of 4V and a rest bias of -6 V under UV irradiation and (b) in dark condition. 130

Figure 76: UV photoresponse time of the Ag/ZnO rods/FTO under constant (a) positive and (b) negative voltage.....132

Figure 77: UV photoresponse of the Au/ZnO rods/FTO device applying a positive (a) and (b) negative voltage.....133

Figure 78: (a) Photocurrent response at -1V of the Ag/ZnOrods/FTO device turning ON and OFF the UV lamp with 5 minutes and (b) 1 min intervals; (c) reproducibility of the photo-induced multilevel current amplification in dark and during UV irradiation 134

List of Tables

Table 1: Parameters of two-temperature model heat transfer equation. Reproduced from ref. [202] by permission of The Royal Society of Chemistry 36

Table 2: Absolute and Gaussian fit values for GQDs obtained at 1.3 W and 2.4W at four ablation time points: 5, 15, 30, and 60 minutes. Reproduced from ref. [202] by permission of The Royal Society of Chemistry 38

Table 3: Chemical composition of the dispersions before and after the laser treatment calculated from the deconvolutions of the relative XPS spectra. Reproduced from ref. [202] by permission of The Royal Society of Chemistry 53

Table 4: Electrical properties of the aerosol-jet printed patterns from different inks. Reproduced from ref. [202] by permission of The Royal Society of Chemistry 64

Table 5: One-Way ANOVA *p*-value post-hoc tests (OriginPro, α=0.05) for laser-treated P25. Reproduced from ref. [139] by permission of The Royal Society of Chemistry 81

Table 6: Energy gap values as a function of laser ablation time. Reproduced from ref. [139] by permission of The Royal Society of Chemistry 83

Table 7: CNWs band positions and I_D/I_G ratio. Reprinted from [15], with permission from Elsevier 98

Table 8: Surface composition of the Cs before and after electrochemical treatment.....118

Table 9: Advantages and disadvantages of the explored techniques 136

List of Abbreviations

0D	Zero-dimensional
1D	One-dimensional
2D	Bi-dimensional
3D	Tri-dimensional
AgNPs	Silver nanoparticles
CNWs	Carbon nanowalls
Cs	Carbon structures
EPD	Electrophoretic deposition
fs	Femtosecond
FTO	Fluorine-doped tin oxide coated glass
GO	Graphene oxide
GQDs	Graphene quantum dots
GQDs@AgNPs	Hybrid made of graphene quantum dots mixed with silver nanoparticles
PLA	Pulsed laser ablation
rGO	Reduced graphene oxide
SEM	Scanning electron microscopy
TEM	Transmission electron microscopy
TiO_2	Titanium dioxide
UV	Ultraviolet

UV-Vis	UV-Visible
XPS	X-ray photoelectron spectroscopy
XRD	X-ray diffraction
ZnO	Zinc oxide

“Research is to see what everybody else has seen and to think what nobody else has thought”

(Albert Szent-Gyorgyi)

Chapter 1. Introduction

1.1. Background

In the last decades, nanomaterials have been in the center of many researches for their applications in various fields such as photovoltaics, water treatment, nanoelectronics and so on. The development of new approaches for the synthesis, characterization and manipulation of these nanomaterials led to an exponential growth of nanotechnology. The methods used for the synthesis of nanomaterials can be classified in top-down and bottom-up approaches. In the top-down methods, the materials are obtained upon size reduction of larger structures, while the use of molecular precursors as building blocks for the fabrication of new nanostructures is usually referred as bottom-up synthesis.

The possibility of controlling the structures and the properties of the nanomaterials allowed the synthesis of new products with specific properties or designed for specific applications. Examples of materials that have attracted the interested of the scientific community are graphene-based materials and semiconductors materials such as titanium dioxide (TiO_2) and zinc oxide (ZnO). The possibility of synthesizing nanomaterials of different size and shapes enables their applications in various fields. Graphene, a two-dimensional (2D) sheet of carbon atoms with sp^2 hybridization [1], possesses outstanding properties, which render it a unique material that could be employed in several applications [2,3]. Many studies demonstrated that upon modification of graphene structure it is possible to obtain graphene-based materials with improved chemical, electrical or mechanical properties. These "new" nanomaterials can be employed for the design of new electrical devices, such as nanoscale transistors [4], molecular sensors [5], fuel cells [6], solar cells [7], electrodes for organic light-emitting diodes (OLEDs) [8], membranes for water treatment [9,10], conductive adhesives [11] and inks [12–14] or as active layer in resistive memory devices [15]. However, one of the issues limiting the use of graphene and graphene-based nanomaterials in current nanotechnology devices is the lack of eco-friendly and straightforward methods for the gram scale production of graphene-based devices and their structural modification.

Besides graphene-based materials, other semiconductor materials such as TiO_2 and ZnO have been used in photocatalysis for the removal of pollutants from wastewaters [16], in photovoltaic processes, for the fabrication of solar cells [17], in electronics for the fabrication of resistive

memory devices [18], for light emitting diodes and UV photodetectors [19–24]. TiO_2 exists in three polymorphs, which are rutile, anatase and brookite. Both anatase and rutile are used as photocatalyst; however anatase phase has a greater photocatalytic activity [25–27]. It has been reported that the use of a mixture made of anatase and rutile as photocatalyst, results more active than the pure anatase. Anatase nanoparticles are the main products obtained with the commonly used synthetic methods such as sol-gel [28], hydrothermal [29] and solvothermal [30] methods. For some applications a high-temperature processes of the anatase nanoparticles are required, however, upon heating a phase transformation to rutile occurs. Therefore, it is crucial to have a control of the conditions that affect the phase transformation of TiO_2. In particular, the phase stability of TiO_2 has a key role in the design of devices for certain type of applications such as gas sensors, and dye-sensitized solar cells.

1.2. Objectives

The motivation for this thesis was to gain a better understanding of the relationship between the synthetic methods developed during my doctoral studies and the properties of the materials fabricated. This work provides a study on alternative synthetic methods for the synthesis of different nanomaterials and it focuses on understanding the mechanisms for the modification and improvement of materials' structure, which can be employed in emerging applications such as electronics. From this knowledge, it has been possible to design and develop engineering solutions to control the materials composition and improve their mechanical and electrical properties. This study can be divided into two parts:

Part 1: investigation of femtosecond laser ablation of graphite and titanium dioxide (TiO_2) as an ecofriendly and straightforward technique to induce structural modification of the materials ablated. It has been shown that laser ablation is a versatile tool and the study of the process mechanisms highlighted that the structure of the fabricated materials can be tailored with a proper control over the laser parameters, such as ablation time and laser power.

Part 2: development of electrochemical processes for the fabrication and improvement of resistive switching devices. In this study carbon structures and ZnO rods were fabricated by electrophoretic deposition and their electrical performances were tested. The work focused on the study of the process-structure and electrical properties relationship of the electrodeposited

materials varying their chemical composition and/or under ultraviolet illumination, in order to improve their performances.

1.3. Organization of the thesis

The thesis is divided into 9 Chapters and the major results are divided in two parts. An overview of the research carried out during my doctoral studies cis summarized in the following block diagram.

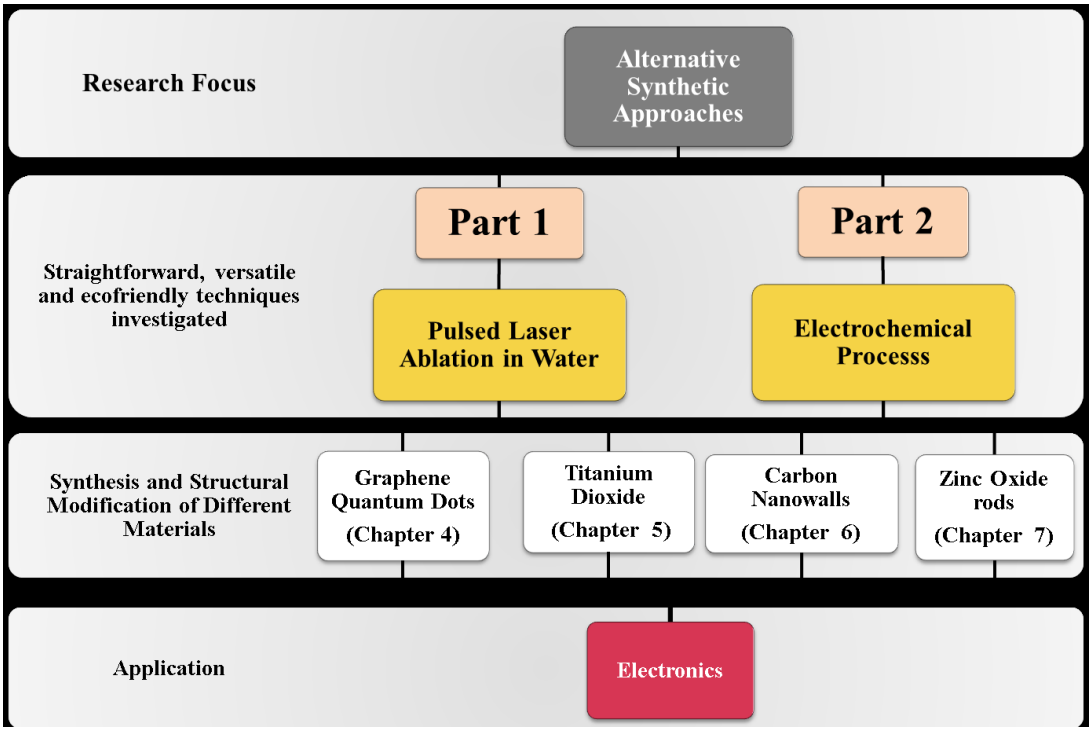

Figure 1: Block Diagram illustrating the research carried out during the doctoral studies.

A detailed overview of the contents for each chapters is given below:

- **Chapter 1** describes the motivation, objectives and the organization of the current thesis work
- **Chapter 2** contains a literature review of graphene, graphene-based nanomaterials, titanium dioxide and zinc oxide nanomaterials. The chapter focuses on the different methods employed for the synthesis of these materials and their properties will be outlined.

- **Chapter 3** will give general information on the main techniques employed for the characterization of the nanomaterials mentioned in Chapter 2.

Part 1: This part is focused on the laser ablation as alternative green and time effective technique for the synthesis and modification of nanomaterials' structure and composition. Chapters 4 and 5 will focus on this technique. In particular:

- **Chapter 4** describes the synthesis of graphene quantum dots, which are graphene-based nanomaterials, by femtosecond laser ablation of graphene oxide sheets dispersions. Results on the fabrication of a conductive ink made mixing the laser-synthesized graphene quantum dots with silver nanoparticles will be presented.
- **Chapter 5** will focus on the use of femtosecond laser for the phase transformation of titanium dioxide nanoparticles suspended in water and deposited on a conductive substrate.

Part 2: This part focuses on the electrochemical processes as alternative routes for the synthesis of different nanomaterials for their applications in electronics. Chapters 6 and 7 will focus on this technique. In particular:

- **Chapter 6** will describe the use of electrophoretic deposition combined with arc discharge for the synthesis of carbon-based devices for their application in future non-volatile memory devices. In this chapter, it will be shown that anodic oxidation can be used as a technique to engineer the chemical composition of the carbon structures synthesized, which will enhance their electrical performances.
- **Chapter 7** will focus on the use of cathodic deposition for the growth of ZnO for the fabrication of memory devices. The devices show better stability and multilevel current amplification upon exposure to ultraviolet light.
- **Chapter 8** reports the main conclusions and outlooks for future investigation
- **Chapter 9** lists the author's contribution to research

Chapter 2. Literature Review

The focus of this chapter is to give general information on the properties and synthesis of graphene, graphene-based nanomaterials, titanium dioxide and zinc oxide nanomaterials.

2.1. Graphene and Graphene-Based Nanomaterials

Carbon possesses an electronic configuration of $1s^2$ $2s^2$ $2p^2$ with 4 electrons in the valence shell, which form three types of hybridization: sp, sp^2 and sp^3. Carbon can form different allotropes in all dimensions. Diamond and graphite (Figure 2a-b) are the most known allotropes in three-dimension (3D); however in the last decades various carbon materials with different dimensionality have been discovered or produced.

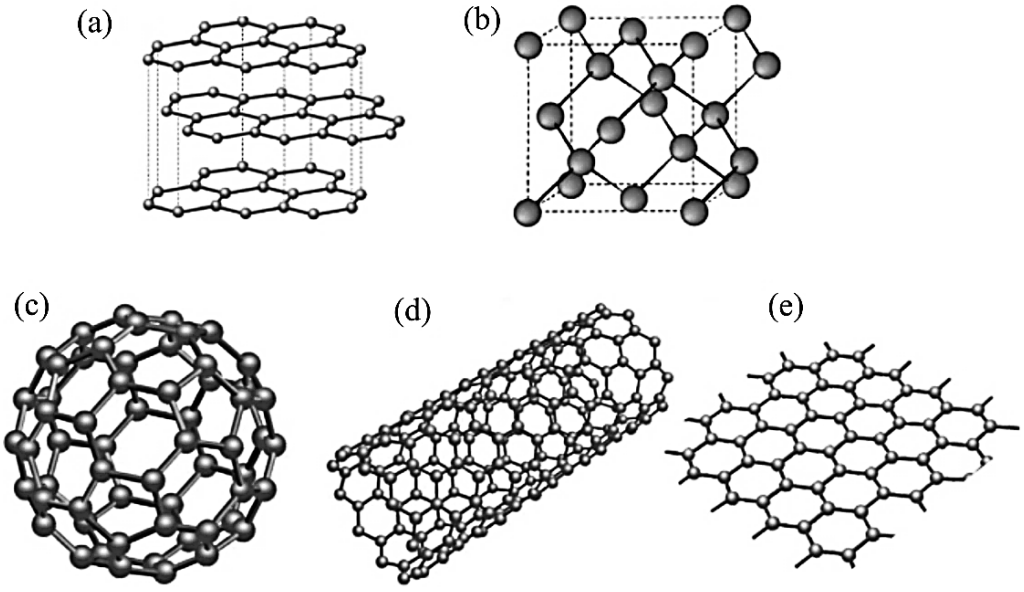

Figure 2: (a) Graphite structure; (b) diamond structure; (c) fullerene structure; (d) carbon nanotube structure and (e) graphene structure. From Ref. [31]

In 1985, Kroto and Smalley firstly reported the synthesis of the first zero-dimensional (0-D) carbon allotrope, the C_{60} molecule [32]. The C_{60} molecule, shown in Figure 2c, consists of 60 carbon atoms arranged in 20 hexagons and 12 pentagons. Its structure is similar to the geodetic domes built by the architect Buckminster Fuller, and for this reason the C60 is also known as buckminsterfullerene or simply fullerene. Graphene quantum dots (GQDs) represent another example of 0-D carbon allotrope and it will be discussed in section 2.1.3. Examples of one-dimensional carbon allotropes are carbon nanotubes (CNTs) and polyynes (or carbynes). CNTs, shown in Figure 2d, were discovered in 1991 by Ijiima [33] and can be considered as the result

of the rolling up of one or more graphene layers, while polyynes discovered in 1967 [34] are linear chains of carbon atoms. Graphene, discovered in 2004 [35] represents the carbon allotrope in two dimensions (2D), its structure is shown in Figure 2e.

2.1.1. Graphene

Graphene can be defined as a flat monolayer of sp^2 carbon atoms packed into a 2D honeycomb lattice and it can be considered as the basic building block for the fabrication of other carbon nanomaterials with different dimensionality. According to this description, fullerenes can be considered as the result of the wrapping of graphene, while CNTs are the products of the folding of graphene sheets in cylindrical shapes. In a similar way, graphite can be regarded as a tridimensional structure obtained from the stacking of several graphene layers along the z-axis, where the interlayer forces are of the van der Waals type.

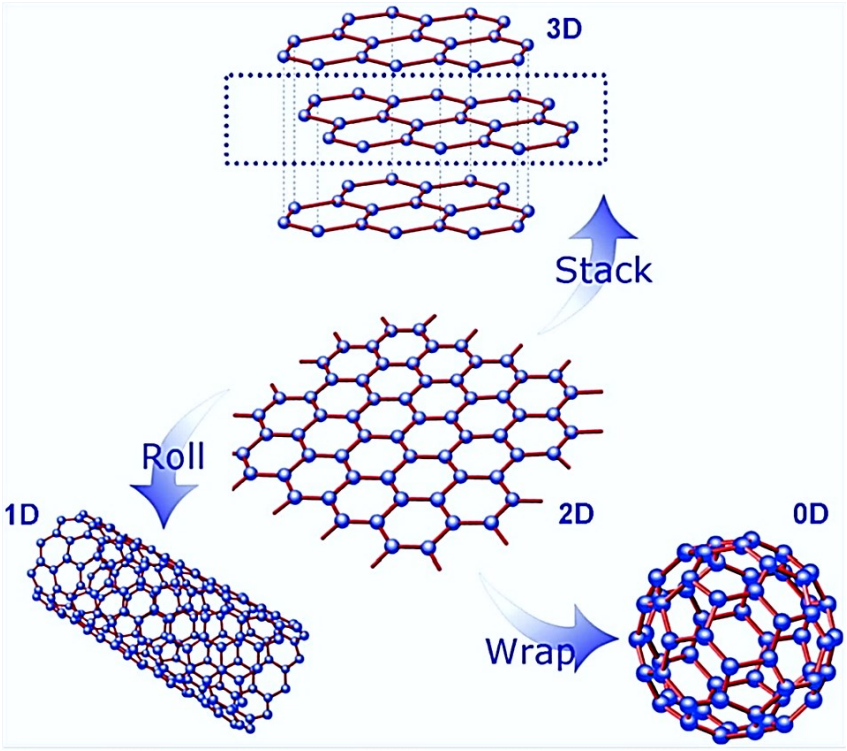

Figure 3: Graphene can be employed as building block for the synthesis of carbon nanostructures with different dimensionality . Reproduced from ref. [40] open access article distributed under the Creative Commons Attribution License

Graphene (or "2D graphite") has been studied since 1947 [36] and widely used for describing properties of various carbon-based materials. Graphene was presumed not to exist in the free-state, being described as an "academic" material and believed to be unstable with respect to the

formation of curved structures such as soot, fullerenes and nanotubes. This common wisdom was disproved in 2004 by the experimental discovery of graphene [35] and other free-standing 2D atomic crystals for example, carbon nanowalls [37,38] and boron nitride [39]. These crystals could be obtained on top of non-crystalline substrates, in liquid suspension and as suspended membranes. Importantly, the 2D crystals were found not only to be continuous but to exhibit high crystal quality.

2.1.2. Graphene Oxide

The graphene oxide's structure is still under debate [41], however it is widely accepted that graphene oxide can be described as the oxidized form of graphene in which carbon atoms possess sp^2 and sp^3 hybridization, due to their bonds with hydroxyl and epoxy functionalities [42]. In the last years, graphene oxide (GO) has attracted the interest of the scientific community, because it offers an alternative cheap way for the production of graphene [43,44]. In particular, for certain types of applications, such as energy storage, large quantities of graphene are necessary [41]. Gram scale production of graphene oxide can be produced from the oxidation of graphite, which will produce graphite oxide, followed by its exfoliation [45], as described in Section 2.3.1.3. It was further demonstrated that reduction of graphene oxide can lead to graphene oxide with different degree of reduction showing similar electrical, thermal, and mechanical properties of pure graphene [41,46].

2.1.3. Graphene Quantum Dots

Graphene quantum dots (GQDs), as mentioned in Section 2.1, are zero-dimensional (0D) nanomaterials and they have attracted the attention of many research groups for their outstanding properties such as chemical stability, strong luminescence and biocompatibility [47,48]. These characteristics make GQDs suitable nanomaterials for the design of different devices in electronic [49], bio imaging and photovoltaic applications [50–52]. As a consequence, several methods for the production of GQDs have been developed so far with the goal of producing electronic devices, such as transistors, supercapacitors, and sensors [49]. The approaches utilised in the fabrication of GQDs can be categorized as top-down or bottom up methods [53]. GQDs can be considered small fragments of graphene sheets with dimensions less than 30 nm [54],

therefore top-down approaches have involved the hydrothermal and solvothermal cutting of graphene oxide (GO) [55,56] sheets, or are derived from the photo-Fenton reaction of GO [57]. The resulting GQDs due to the presence of remaining oxygen containing groups are dispersible in water and show different colours of luminescence as a function of their sizes [58]. Researchers who reported the synthesis of GQDs through bottom-up approaches involved either organic synthesis by oxidation of polyphenylene dendritic precursors [59], by pyrolysis of glucose [60] or they were obtained from the opening of fullerenes C60 [41,47]. Some of these synthetic methods will be discussed in section 2.3.3.

2.1.4. Graphene Nanowalls

Graphene nanowalls (GNWs) are two-dimensional nanomaterials composed of stacked graphene layers, which are vertically oriented on a substrate. A schematic of the graphene nanowalls structure is shown in Figure 3. GNWs were first synthesized in 1997 by Ando and coworkers during an experiment for the fabrication of carbon nanotubes [37]. Graphene nanowalls possess a large surface area and due to their unique structure they are good candidates as catalyst supports, field emitters, electrochemical capacitors and Li-ion batteries [62–65].

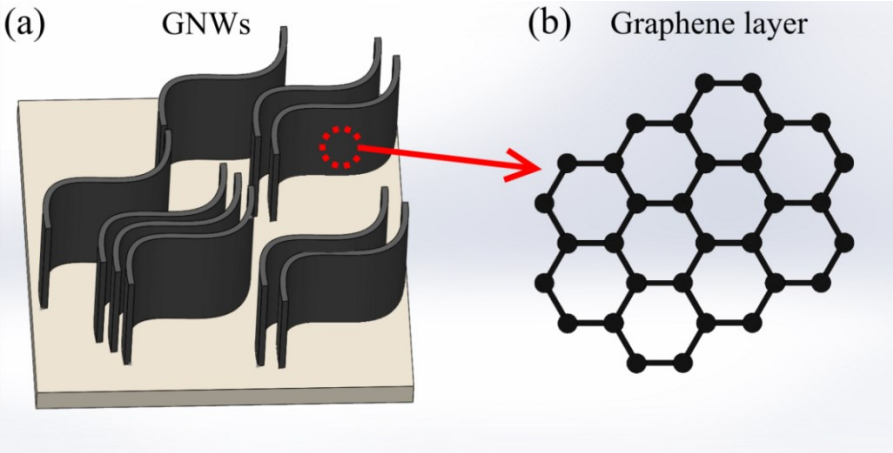

Figure 4: (a) Schematic view (top) of graphene nanowalls structure obtained from the stacking of many graphene (b) layers.

GNWs are obtained thorough bottom-up approaches by either plasma-enhanced chemical vapor deposition or electric field-assisted laser ablation of graphite [66–69]. Both these techniques will be discussed in the following sections.

2.1.5. Carbynes

Carbynes, 1D carbon allotropes, are linear carbon chains and they exist in two isomeric forms: polycumulene and polyynes.

The difference between the two forms is the conjugation of the carbon atoms. In the polycumulene's structure the carbon atoms are doubly bonded $(= C = C =)_n$, while polyynes have bonded carbon atoms with alternating single and triple bonds $(-C \equiv C -)_n$. The first reports on the discovery of carbynes date 1967 [34,70–72], however due to their structure these 1D carbon allotropes are unstable and tend to be easily oxidized or undergo chain-chain cross-linking reactions forming more stable 2D graphene-like structures [73,74]. Polyynes or carbynes can be obtained from the dehydropolycondensation of acetylene, laser ablation (in vacuum or in liquids) of graphite or by arc discharge of graphitic electrodes [75–81].

2.2. Properties of Graphene and its Derivatives

The outstanding properties of graphene arise from its particular structure. As mentioned before, graphene has been defined as a single-two-dimensional hexagonal sheet of carbon atoms (Figure 5a) composed of two equivalent triangular carbon sublattices. The stacking of several graphene layers along the z-direction forms the graphite structure (Figure 5b). Graphene is made of carbon atoms with sp^2 hybridization, where 2s orbitals superimpose with the $2p_x$ and $2p_y$ orbitals, which lie in the graphene plane, are oriented 120º to each other and form the energetically stable and localized σ-bonds with the three nearest-neighbor carbon atoms in the honeycomb lattice, as shown in Figure 5c. The remaining free $2p_z$ orbital for each carbon atom lies perpendicular to the plane and presents π symmetry orientation.

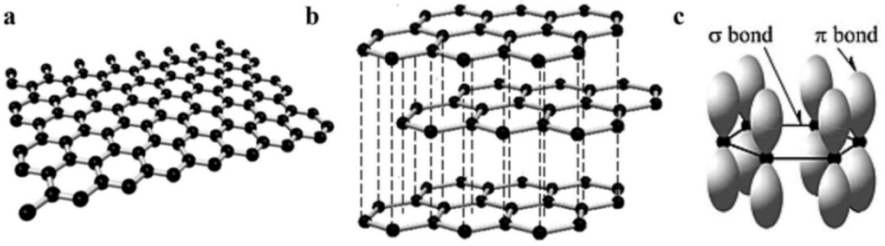

Figure 5: (a) Graphene structure; (b) graphite structure as a result of the stacking of graphene layers (c) schematic of the in-plane σ bonds and the π orbitals perpendicular to the plane of the graphene sheets. Reproduced from ref. [82] with permission of The Royal Society of Chemistry.

In Figure 6 it is displayed the band structure of graphene, where it is possible to observe that the conduction and valence bands touch each other at the so called *Dirac point*, set at 0 eV.

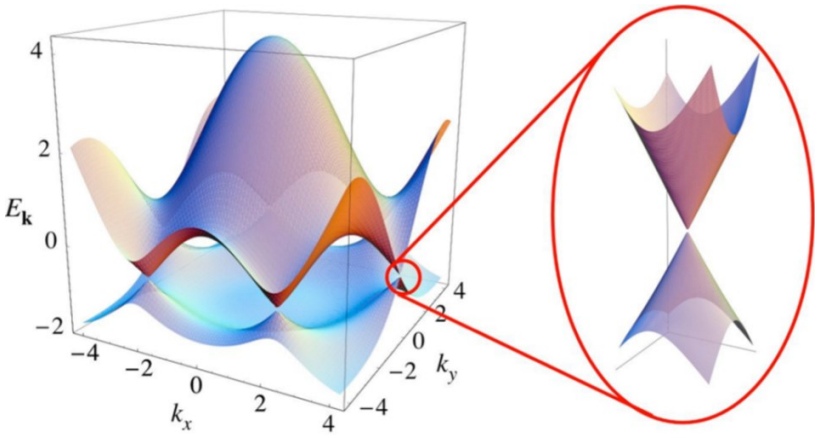

Figure 6: On the left the electronic dispersion in graphene in shown, while on the right a zoom in of the energy bands close to one of the Dirac points is displayed. Reprinted with permission from ref. [83] by the American Physical Society.

The absence of a band gap between the conduction and valence bands makes graphene a semimetal material or a zero-gap semiconductor [84], which limits its use in nanoelectronics [85,86], and for this reason researchers studied different ways to induce a band gap opening of graphene by doping [85], chemical functionalization [87,88], and introduction of defects [83]. Several study, have demonstrated that an opening of bandgap can be achieved upon reduction of graphene oxide [86,89–92] and this is one of the reason for the increasing interest towards the synthesis and modification of graphene oxides. Besides the electronic properties, graphene is defined as the strongest material ever measured. Lee and coworkers measured the elastic properties and intrinsic breaking strength of free-standing monolayer graphene membranes by nanoindentation in an AFM and reported a value of Young's modulus of 1 TPa [93]. Size reduction of graphene sheets lead to the formation of graphene quantum dots, as mentioned in section 2.1.3. One of the most attractive properties of GQDs is their strong luminescence and biocompatibility [60,94,95] that can enable their applications in biology and medical science [96]. It was demonstrated that GQDs photoluminescence strongly depends on their dimensions and shape [58], in particular GQDs can emit blue [55,97,98], green [95,99,100] and white [58,101] photoluminescence.

2.3. Synthesis of Graphene and Graphene-based nanomaterials

In the next paragraphs, some of the methods employed for the synthesis of graphene and graphene-based nanomaterials are described.

2.3.1. Synthesis of Graphene

2.3.1.1. Mechanical Exfoliation

Graphite can be considered as the result of the stacking of several graphene layers along the z-axis. The interplanar distance is 0.335 nm, and the carbon atoms in the hexagonal plane are covalently bonded, while the forces between the stacked layers are of the van der Waals type. This can explain the lubrication properties of graphite and the ease of exfoliation. From this consideration, the idea of producing graphene by the exfoliation of graphite aroused. The first recognised method employed for the synthesis of graphene was precisely the mechanical exfoliation of graphite by scotch tape technique [35]. It has been reported that the force necessary to exfoliate graphite and obtain a single-layer of is ~ 300 nN/μm^2 [102] and this force can be overcome by an adhesive tape. In the method employed by Geim and Novoselov, a piece of highly oriented pyrolytic graphite (HOPG) was peeled off with a scotch tape. The peeled material was then transferred onto a suitable substrate, a substrate of silicon with a certain thickness of silicon dioxide. This approach led to the fabrication of graphene films with dimensions in the range of ~ 80 μm in length and ~20 μm in width, as shown in Figure 7.

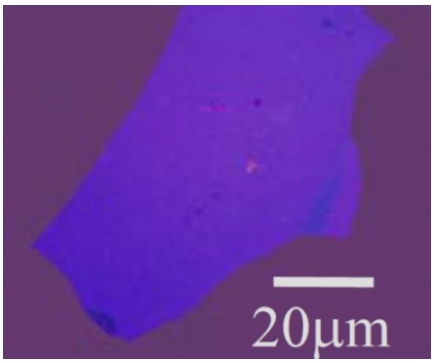

Figure 7: Optical image of graphene sample obtained from mechanical exfoliation of graphite. From ref. [103] reprinted with permission from AAAS.

The mechanical exfoliation of graphite is an inexpensive approach to obtain high quality graphene sheets, however a drawback of this technique is the impossibility to obtain a high yield required for various investigations and applications.

2.3.1.2. Chemical Exfoliation

The idea of obtaining graphene by chemical exfoliation of graphite and graphite oxide is similar to the mechanical exfoliation technique. In the chemical exfoliation, in order to weaken the van

der Walls forces between the graphene layers and achieve their detachment, intercalating compounds, surfactants and chemical functionalization are employed [104] together with sonication that helps the exfoliation. The chemical exfoliation of graphitic oxide can be easily achieved by sonication in water, due to the presence of the oxygen moieties the interlayer distance in GO is larger and this enables the intercalation of water molecules and other molecules within the graphene oxide layers [104]. Upon sonication the exfoliation of the graphitic oxide is achieved, producing single layer and multilayer of graphene oxide, that results dispersible in water [45]. The chemical exfoliation of graphite, compared to the graphite oxide one, results more difficult due to the tighter interlayer spacing, to the hydrophobicity of graphene sheets that requires the use of surfactants when the exfoliation is performed in water [104]. The method proposed by Hernandez of dispersing and sonicating pristine graphite in N-methyl-pyrrolidone (NMP) appears to provide the best thermodynamic stabilization [104,105].

2.3.1.3. Synthesis and Reduction of Graphene Oxide

Graphene can be chemically synthesized from the oxidation of graphite to graphite oxide followed by its reduction with different reducing agents [5,41,106–109]. There are different methods that can be employed for the oxidation of graphite [41], however the most employed one is the Hummers method [110], and in the last years, this method has been improved [111]. Generally, graphite oxide can be obtained mixing graphite with sodium nitrite, sulfuric acid, and potassium permanganate. The obtained graphite oxide is then sonicated in order to obtain single and few-layers of graphene oxide. The reduction with hydrazine [112], or ascorbic acid [106] or UV-light [108] leads then to the synthesis of the reduced graphene oxide.

2.3.2. Synthesis of Graphene Quantum Dots

2.3.2.1. Hydrothermal and Solvothermal Methods

The most employed methods for the synthesis of GQDs are the hydrothermal and the solvothermal cutting of graphene oxide sheets. The hydrothermal cutting of graphene sheets, was first reported by Pan in 2010 [55] and the technique was then improved by the same group in 2012 [99]. Pan and coworkers developed a three-step synthesis of GQDs, where reduction of graphene oxide takes place in the first step, followed by a further oxidation of the materials obtained. The synthesis of GQDs is obtained after the hydrothermal deoxidization of oxidized

sheets synthesized during the second step [99]. The authors pointed out that the temperature at which the hydrothermal process takes place, plays a key role in the quality of GQDs synthesized. In particular, at low temperature disordered GQDs were obtained [55], while hydrothermal treatment at high-temperature led to the production of well-crystallized GQDs showing strong green photoluminescence [99]. Blue and green photoluminescent GQDs, where synthesized by Zhu and coworkers by a two-step solvothermal process [113]. For the synthesis of GQDs, graphene oxide was dispersed in dimethylformamide (DMF) and after sonication, the mixing was placed in an autoclave and heated at 200 °C for 8h.

2.3.2.2. Cage-opening of fullerene C_{60}

Hydrothermal and solvothermal methods belong to the top-down approaches employed for the synthesis of GQDs [53]. As mentioned in section 2.1.3, another route for their production is trough bottom-up approaches where, atoms or clusters are used as building blocks. Cage-opening of fullerenes, belongs to this category of synthetic methods and it has been successfully employed for the synthesis of GQDs with well-defined dimensions [54,61]. In particular, since fullerenes C_{60} are employed as starting material, GQDs with average dimensions of ~2-3 nm can be obtained [54]. Lu [61] and Chua [54] reported the synthesis of GQDs through a ruthenium catalyzed opening of C_{60} and through a strong oxidation of fullerenes, respectively. The first approach requires sophisticated equipment; as a consequence the cage-opening of fullerenes with strong oxidation, proposed by Chua is preferable. In their method, Hummers method [110] was used to achieve the oxidation and cage-opening of the fullerenes.

2.3.3. Synthesis of Graphene Nanowalls

The main chemical vapor deposition (CVD) approaches employed for the synthesis of GNWs are the microwave plasma-enhanced CVD (MWPECVD), the radio-frequency plasma-enhanced CVD (rf-PECVD), the hot filament CVD (HFCVD) and the electron beam excited plasma-enhanced CVD (EBEPECVD). Wu et al, first synthesized the GNWs by MWPECVD employing a preheated NiFe-catalyzed substrate in hydrogen plasma and flow gases composed of methane (CH_4) and hydrogen (H_2) [38]. In an another work, the GNWs were obtained without catalyst using rf-PECVD assisted by H atom injection and the carbon source gas was made of fluorocarbon/hydrogen mixtures (C_2F_6,CH_4, CF_4, and CHF_3) [68]. Larger production scales of the graphene nanowalls have been obtained by HFCVD. In particular, in the work reported by

Shang et al, the synthesis of the GNWs is carried out heating a tungsten filament up to 2000-2200°C, which is used to decompose a mixture of hydrocarbons and hydrogen. The nanomaterials deposition occurred, at pressure of 1-100 Torr, onto an heated substrate placed at ~ 5 mm from the filament [114]. Mori and co-workers reported the fabrication of GNWs at lower temperatures (570°C) by EBEPECVD using a mixture of CH_4 and H_2 [115].

2.4. Alternative Method for the Synthesis of Graphene-based Nanomaterials

In the previous section, the most employed methods for the synthesis of graphene and graphene-based nanomaterials have been presented. Except for the mechanical exfoliation of graphite, for all the fabrication methods discussed above, the synthesis of graphene and its derivatives is achieved by multiple step reactions with strong acids that can be time consuming and harmful for the environment and/or involve the use of high pressures and temperatures. Consequently, alternative routes for the synthesis of graphene and graphene-based nanomaterials have been investigated.

2.4.1. Pulsed Laser Ablation

Pulsed laser ablation technique in the last decades has been successfully employed as a green and straightforward technique for the synthesis of different types of nanomaterials (metals, alloys, oxides etc.) either in gases or liquid media [116]. Generally, pulsed laser ablation is the process of material removal from solid target caused by nano-, pico- and femto-second lasers [117]. The product of laser ablation comes directly from the condensation of the plasma plume generated by the laser pulse irradiating the surface of the solid target. The ablation mechanism depends on the type of material with which the photons are interacting. The ablation mechanisms causing the generation of the plasma plume are different for the nanosecond, picosecond and femtosecond laser pulses [118]. For the ablation of the nanosecond laser, the material ejection is likely to be dominated by thermal processes [118]. Photons will couple into the available electronic or vibrational states in the material [119] leading to an electron-electron coupling which results in an immediate rise in the electron temperature causing the vaporization of the target. When the ablation is induced by ultrashort laser pulses (femtosecond and picosecond), since the pulse duration is shorter than the electron- lattice interaction (which is in the order of several

picoseconds), the laser energy deposited primarily in the electronic system cannot be transferred to the lattice [117]. Consequently, heating, plasma plume formation and material ejection occur after the pulse has ended [118].

In 1993, Cotton [120] reported the synthesis of colloidal solutions of different metal nanoparticles obtained upon laser ablation of pure metal targets submerged in water and other solvents. A schematic of the pulsed laser ablation in liquid (PLAL) setup employed by Cotton for the synthesis of nanoparticles is shown in Figure 8.

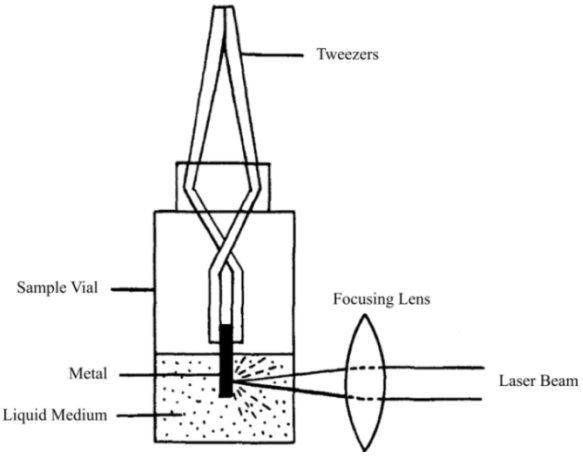

Figure 8: Schematic of the setup employed by Cotton for the synthesis of metal nanoparticles by PLAL. Adapted from ref. [120]

It should be noted that in PLAL, the target, whether a solid or a liquid one, plays a key role in the type of nanostructures that can be synthesized [118]. For instance, stable colloids of silver and gold nanoparticles can be obtained by ablating silver and gold thin plates in water, respectively [121,122]. Moreover, by laser ablation of a graphite target in water and in organic solvents, the synthesis of polyynes with 10-16 carbon atoms per chain [123,124] has been achieved.

2.4.1.1. Graphene from laser exfoliation of graphite

In 2001 Jeschke [125] reported about the possibility to induce the exfoliation of graphite films by femtosecond laser pulses. The theoretical study reported by Jeschke and coworkers, based on molecular dynamics simulation, revealed that graphite, due to its layered structure possess two different ablation thresholds (Figure 9). The low fluence ablation threshold (0.21 J/cm^2) being below the disruption threshold of the graphite planes leads to the exfoliation of graphite, while at higher fluence ablation threshold (0.35 J/cm^2) bond breaking processes inside the graphite layers occur, which lead to the expansion of the structure [125].

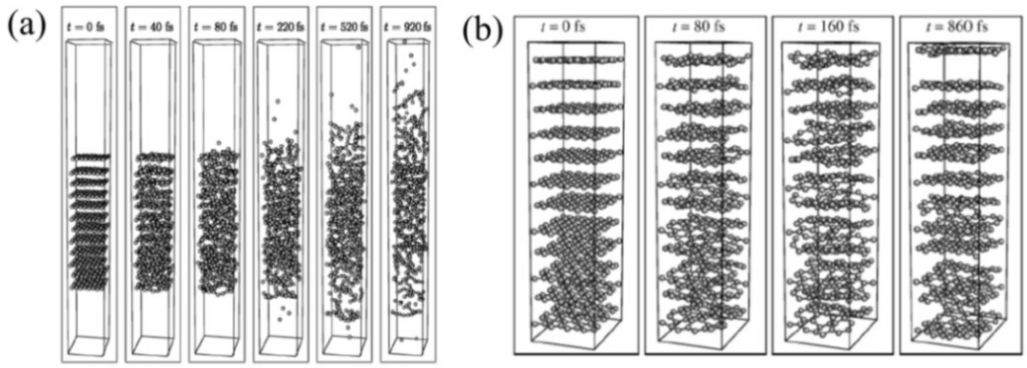

Figure 9: (a) high and (b) low fluence ablation thresholds in graphite. Reprinted with permission from ref. [125] by the American Physical Society.

The laser pulse induces strong vibrations of the graphite planes, which lead to collisions of the planes, which cause the removal of the planes at the top and at the bottom. This theoretical study conducted by Jeschke can be considered as the first model for the exfoliation of graphene induced by femtosecond laser ablation. Other theoretical study on the exfoliation of graphite for the synthesis of graphene, where then reported in 2008 and 2010 by Carbone [126] and Miyamoto [127], respectively. In 2010 Qian et al., reported the synthesis of graphene layers by exfoliation of graphite (HOPG) with a nanosecond laser in vacuum [128]. In particular, the authors demonstrated that by a proper control of laser fluences different types of carbon nanostructures, ranging from amorphous carbon, graphene and thin graphite films can be obtained. More recently, Compagnini et al., reported on the synthesis of large sheets of reduced graphene oxide (r-GO) by pulsed laser ablation of a graphite target (HOPG) in water using pulses from a Nd:YAG laser, with 532 nm as radiation wavelength, 5 nsec pulse duration, and operating at 10 Hz repetition rate [129]. Scanning electron miscopy (SEM) and Atomic Force microscopy (AFM) images of the laser exfoliated graphene sheets are shown in Figure 10.

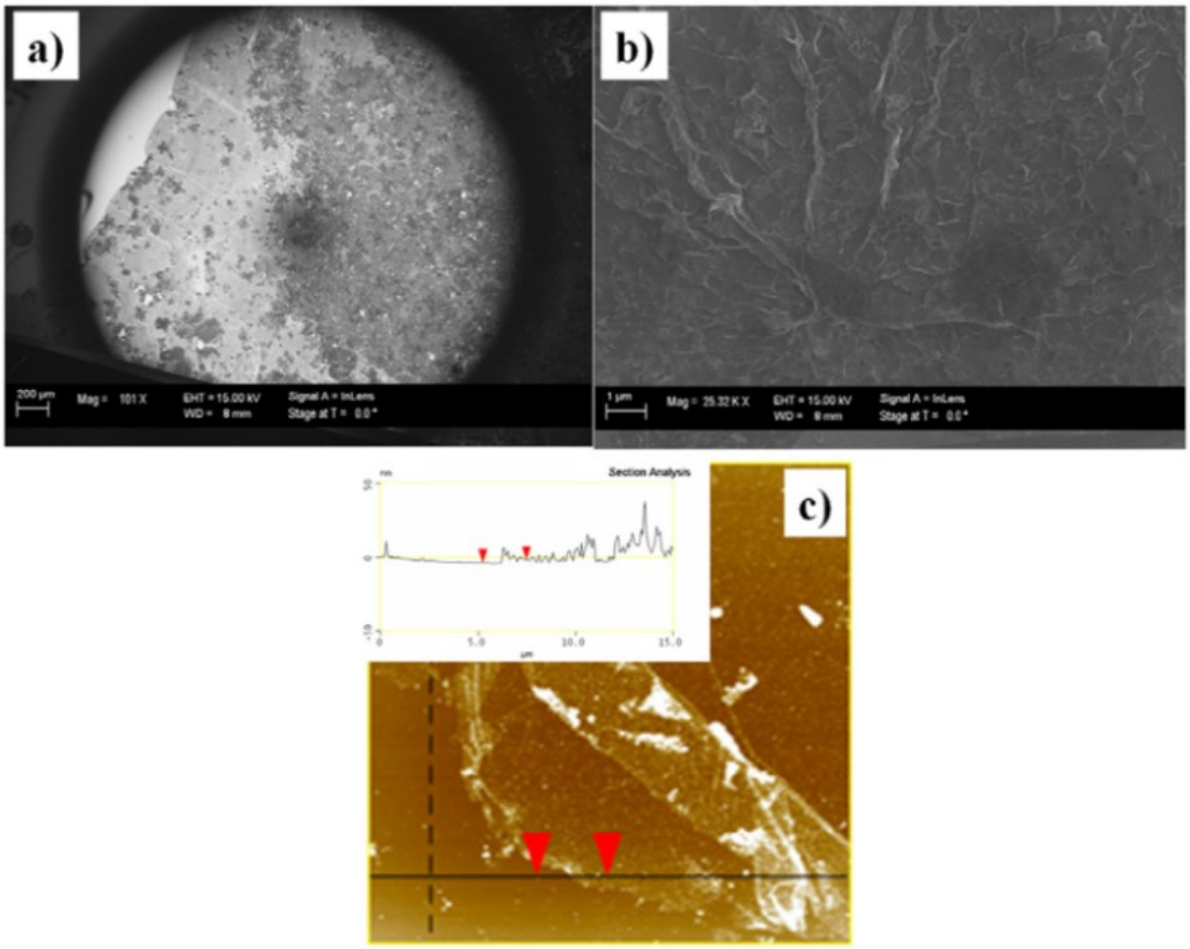

Figure 10: (a) low and (b) high magnification SEM images of r-GO layers obtained upon nanosecond laser exfolitiaon of HOPG in water; (c) AFM of the detached layer showing a heigth step of 1.56 nm. From ref. [129] © IOP Publishing. Reproduced with permission. All rights reserved

2.4.1.2. Graphene from laser reduction of graphene oxide

In section 2.3.1.3 it was mentioned that graphene can be obtained upon oxidation of graphite followed by its exfoliation and reduction with hydrazine [112], or ascorbic acid [106]. However, hydrazine is toxic and the deoxygenating processes are time consuming and complicated [130]. An alternative route, that permits a green and single-step synthesis of graphene is the laser irradiation of graphene oxide dispersions reported by Spano` and coworkers[130]. It has been reported that laser irradiation of solutions with unfocused laser beam can induce shape and size modification [116,131,132]. Spano` demonstrated that upon laser irradiation of graphene oxide dispersion with a Nd:YAG laser, with 532 nm as radiation wavelength, 5 nsec pulse duration, and operating at 10 Hz repetition rate, it is possible to achieve the reduction of GO. Moreover, it was shown that the degree

of the graphene oxide reduction could be tuned by the time of exposure of the graphene oxide dispersions to the laser beam.

2.4.2. GNWs by Electric Field-Assisted Laser ablation of Carbon in Water

The CVD methods described in section 2.3.3 are bottom-up approaches, which employ CH_4, C_2H_2, C_2F_6 as building blocks for the growth of the graphene nanowalls. An alternative eco-friendly and time effective method for the synthesis of these nanomaterials was developed by Compagnini and co-workers [69]. The GNWs were synthesized from the electrophoretic deposition of polyynes produced by the laser ablation of a graphite target submerged in water. The polyynes were used as the building blocks for the growth of the GNWs. In particular, once the polyynes are transported to the cathode by the electric field, due to their tendency to undergo crosslink reactions [73,74] they start to form more stable sp^2 carbon structure, which grow perpendicular to the electrode's surface leading to the formation of the GNWs.

2.5. Semiconductor nanomaterials: Titanium Dioxide and Zinc Oxide

Titanium dioxide (TiO_2) and zinc oxide (ZnO) materials are wide bandgap semiconductors, which due to their chemical stability, non-toxicity have been widely employed in photocatalysis, photovoltaics and memristors devices [18–21,133–137]. In the following paragraphs it will be discussed about the structure, the properties and the synthesis methods of these materials.

2.5.1. TiO_2

TiO_2 is an n-type semiconductor and in nature exists in three crystalline polymorphs, which are anatase, brookite and rutile. Due to the differences in their lattice structures [138], TiO_2 polymorphs possess different bandgap values. In particular, anatase and brookite have a bandgap of 3.2 eV and 2.96 eV, respectively, while rutile's bandgap is 3.0 eV [139]. Anatase has a greater photocatalytic activity compared to rutile; therefore, it is the most used polymorph for photocatalysis. In the past years, it has been demonstrated that a higher photocatalytic activity is reached when anatase is mixed with rutile in certain proportions, in particular P25 Aeroxide™, which is made of 70% of anatase and 30% of rutile, is an example [138,139].

2.5.2. ZnO

ZnO is a wide gap semiconductor (3.7 eV) and it has three main crystal structures: hexagonal wurtzite, zinc-blende and cubic rock salt. The latest structure is not very common since it is stable at pressure as high as 2GPa. Most of the ZnO structures possess the hexagonal wurtzite structure, since it is the most thermodynamically stable structure under ambient conditions [140]. ZnO structures have outstanding mechanical, electrical and optical properties [141]. In particular, ZnO materials are very sensitive to UV light and they are good candidates for light emitting diodes, photovoltaic and UV photodetectors applications [19–24]. Depending on the synthetic approach, ZnO materials with different morphologies can be obtained. Examples of ZnO structures are nanorods, nanoflowers, nanoplates, nanotubes and so on [140].

2.6. Synthesis of TiO_2

TiO_2 nanomaterials can be obtained by several methods and depending on the synthetic methods and experimental conditions it is possible to obtain TiO_2 nanoparticles, nanowires, nanorods and so on. In the following sections, the most employed methods for their production will be described.

2.6.1. Hydrothermal Synthesis

TiO_2 nanoparticles and nanowires can be obtained by the hydrothermal method [18,142,143]. In particular, for the synthesis of anatase and rutile nanoparticles, Cheng and coworkers employed titanium tetrachloride ($TiCl_4$) as stating material in an alkaline solution [142]. It was reported that, depending on the $TiCl_4$ concentration, pH of the solution and temperature TiO_2 nanoparticles with different phases can be produced. In particular, at higher values of pH anatase particles were obtained, while higher acidity is in favor of rutile ones. The temperature during the synthesis influences the size of the particles, it was reported that grain size decreases lowering the temperature, however agglomeration of the grains occurs [142].

TiO_2 nanowires can be grown *via* hydrothermal route, on titanium foil followed by heat treatment as reported by Hu and coworkers [143]. The synthesis was performed in an autoclave with a solution of sodium hydroxide (NaOH) and other organic solvents. The products obtained were titanate nanowires, which after heat treatment at 700 °C were transformed into TiO_2 anatase phase.

2.6.2. Sol-gel Method

The sol-gel method is employed for the synthesis of TiO_2 nanoparticles or films. In a typical sol-gel synthesis of TiO_2, an alkoxide titanium precursor in an alcohol solvent and water is hydrolyzed to titanium hydroxide. The obtained sol is transformed in a solid gel by polymerization reactions, which lead to the formation of Ti-O-Ti condensed bridge [28,144–146]. TiO_2 nanoparticles with different phase can be obtained varying the calcination temperature. For example in the work presented by Azizi and coworkers, it was reported that at a calcination of 400 °C anatase nanoparticles were obtained, at 500 °C a mixture of anatase and rutile particles were synthesized, while increasing the temperature the nanoparticles were in the rutile phase [145].

2.6.3. Laser Ablation of Titanium Target

Anatase TiO_2 nanoparticles can be obtained by pulsed laser ablation in water of a titanium metal plate. In the study performed by Liang and coworkers, spherical anatase nanoparticles with an average diameter of 3 nm were obtained upon ablation of a titanium target in water with the third harmonic (355 nm) of Nd:YAG laser [147]. The experiments were performed also in aqueous solutions of ionic surfactant in order to improve the stability of the colloidal suspensions. Anatase and rutile nanoparticles were obtained through laser ablation of metal titanium in water, using a continuous wave (CW) ytterbium doped fiber laser (Yb:YAG) operating at 1075 nm wavelength [148]. It was found that most of the nanoparticles were in the rutile phase, this because the particles ablated with CW laser are subjected to higher temperature, which promotes a phase transformation from the metastable anatase phase to the more stable rutile [148]. In another work, it was demonstrated that the crystalline phase of TiO_2 nanoparticles can be controlled varying the focusing conditions and the ablation fluence during the PLA [149]. In particular, rutile nanoparticles were obtained at high fluence at focus, while under defocused condition and at lower fluence the nanoparticles were in anatase phase [149].

2.7. Synthesis of ZnO

ZnO materials can occur in one (1D), two (2D) and three (3D) dimensional structures. Examples of 1D ZnO structures are nanorods, nanowires, while nanoplates and nanopellets are example of 2D ZnO nanomaterials. The most common 3D ZnO structures are the ZnO nanoflowers

[140,150]. As aforementioned, depending on the synthetic conditions ZnO structures with the above different dimensionality can be obtained.

2.7.1. Hydrothermal Synthesis

The hydrothermal method allows the synthesis of ZnO structures with different morphologies [151]. ZnO nanoparticles have been synthesised after placing an aqueous solution of zinc nitrate hexahydrate [$Zn(NO_3)_2 \cdot 6H_2O$], at pH 7.5, in autoclave at 120°C and post-annealing at 80°C [152]. A two-step hydrothermal route has been employed for the growth of ZnO rods in a neutral solution of zinc nitrate and methamine. In particular, in the first step of the synthesis a ZnO film was RF sputter on an ITO substrate, followed by the hydrothermal growth of the rods, with a wurtzite structure [153]. Regarding nanoflowers ZnO structures, it was reported that the hydrothermal synthesis using aqueous solutions of zinc acetate dehydrate and sodium hydroxide at 90°C led to flower-like structures composed of hexagonal ZnO rods [151].

2.7.2. Electrochemical Method

ZnO rods and ZnO films have been synthesized by electrochemical routes. Several researchers have reported the synthesis of ZnO rods *via* electrophoretic route employing ZnO seed layer obtained by radio frequency magnetron sputtering systems or by hydrothermal method [154–157]. For instance, Park and coworkers employed an hydrothermal-electrochemical method for the growth of the ZnO rods [155,158]. The ZnO seed layer for the growth of the nanorods was deposited by atomic layer deposition and it served as the working electrode. A platinum sheet was employed as counter electrode, while the reference electrode was a silver–silver chloride (Ag/AgCl) electrode. The electrochemical growth of the nanorods was achieved placing the three electrodes in a solution of zinc nitrate at 90°C in autoclave [158]. Similarly, Miao et al. reported the synthesis of ZnO films by electrophoretic deposition of ZnO colloidal suspensions. The authors performed the electrophoretic deposition of the ZnO nanoparticles employing a platinum sheet as the cathode, and ITO conductive glass as anode. It was reported the morphology and the microstructure of the deposited films and the possibility of having crack-free, and smooth films depends on several parameters, such as applied voltage, deposition time and suspension concentration [154].

2.8. Summary

From the above literature review, it is clear that graphene-based nanomaterials and semiconductors materials such as TiO_2 and ZnO are promising materials for the fabrication of electronic devices, devices for bioimaging, photovoltaic applications and UV photodetectors. The main synthetic methods of these nanomaterials have been presented, together with the description of alternative and less common methods such as the laser ablation and the electrochemical methods. The advantages of these alternative methods compared to the conventional fabrication processes are the possibility to achieve the synthesis and/or modification of different type of nanomaterials in an eco-friendly and time-effective way.
The following goals have been identified to be reached in the present study:

1) Experimental study of pulsed laser ablation of graphene oxide dispersions (Chapter 4) and TiO_2 nanoparticles (Chapter 5) as technique for their structural modification. The fabrication mechanisms will be studied in order to gain a better understanding how the processes can be controlled to induce specific structural modification of the materials to be employed in different applications. In particular, the laser modified graphene nanomaterials will be employed for the preparation of a conductive hybrid ink, when mixed with silver nanoparticles (Chapter 4). In Chapter 5, it will be shown that laser ablation can be used to induce and control the phase transformation of TiO_2 nanoparticles, which can be used in photocatalysis. The overall study relies on the sustainability of the laser ablation technique, since it involves the use of water as medium where to conduct modification of the nanomaterials involved, and on its time effectiveness, since PLA enables the synthesis/modification of nanomaterials in shorter time than other chemical approaches, like hydrothermal processes.

2) Experimental study on the synthesis of various materials by electrochemical process for the fabrication of memory devices. The work will focus on studying the resistive switching mechanisms of the devices fabricated and how the devices' electrical performances can be improved by engineering their chemical composition. In Chapter 6 will be discussed the resistive switching behaviour of carbon structures obtained by electrophoretic deposition and the improvement of their electrical performances by electrochemical oxidation. Chapter 7 investigates the electrical

performances, under ultraviolet (UV) light exposure, of ZnO rods produced by electrochemical process. This is the first study on the UV induced multilevel current amplification of ZnO rods memory devices.

Chapter 3. Characterization Methodologies

3.1. Optical Microscope

Optical microscope has been a cheap and non-destructive technique for the detection of single layer and multilayer graphene sheets deposited on a suitable substrate. It should be noticed that the identification of graphene layers by an optical microscope is possible only due to the different optical contrast between the graphene and the substrate, that arises from the interference of the reflected light beams at the air-to-graphene, graphene-to-dielectric, and (in the case of thin dielectric films) dielectric-to-substrate interfaces [159]. Consequently, a good identification of graphene layers can be achieved when graphene is deposited onto a silicon wafer with a layer of silicon dioxide (SiO_2) 300 nm thick [160]. Moreover, Blake demonstrated that not only the thickness of the substrate plays a key role in the identification of the graphene, but also the incident light [161].

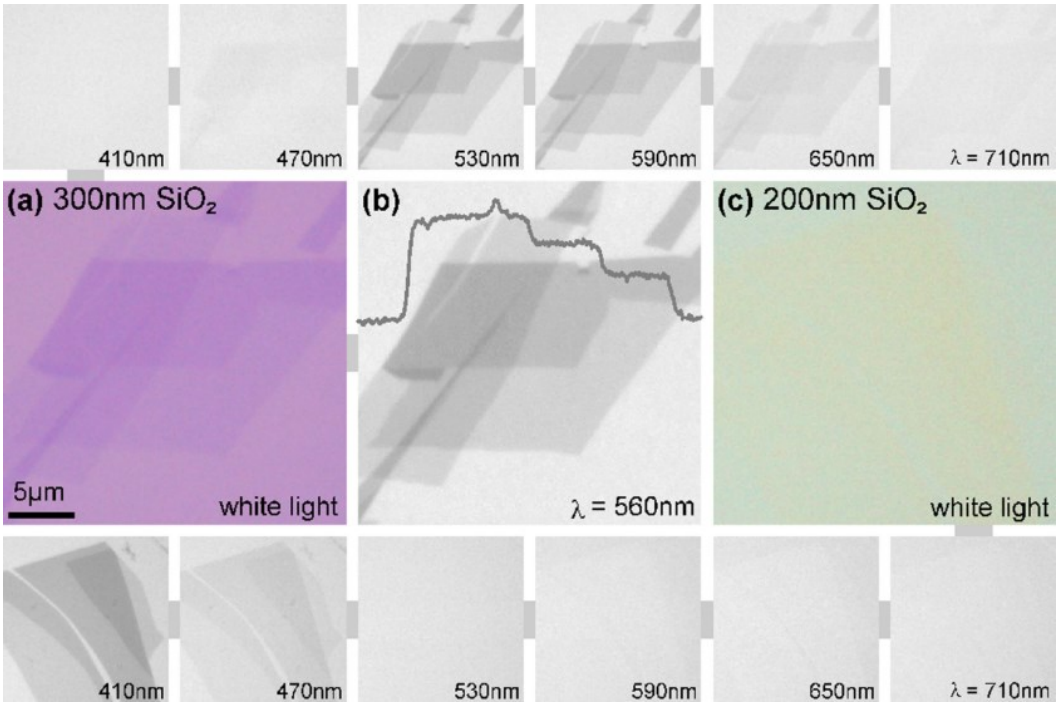

Figure 11: (a) Graphene layers deposited on 300 nm SiO_2 imaged with white light, (b) green light and (c) graphene sample on 200 nm SiO2 imaged with white light. The top and bottom panels represents the flakes shown in (a) and (c) illuminated with different bandpass filters. Reprinted from ref. [161], with the permission of AIP Publishing.

Indeed, when graphene layers are deposited onto 200 nm of SiO_2 and imaged by white light, their detection was not possible, while when the same samples were imaged with blue light, graphene samples were visible.

3.2. Raman Spectroscopy

3.2.1. Graphene-based materials

Raman spectroscopy is the most employed method for the characterization of carbon based materials. In particular, carbon-based nanomaterials possess unique Raman features, such as peak position, intensity and shape of the bands. From an accurate analysis of these characteristics it is possible to distinguish and characterize the different types of carbon allotropes [162–164]. Investigation of graphene by Raman spectroscopy permits the determination of the number of layers that compose the graphene samples and the study of defects present within the graphene structure [165–167]. In Figure 12a is displayed the typical Raman spectrum of a single defect free layer of graphene, and it is possible to notice that it is characterized by the presence of two main bands: the G band located at 1580 cm^{-1} and the 2D band at 2700 cm^{-1}. The presence of defects within the graphene structure can be monitored by the presence of a third band, the D peak at 1350 cm^{-1}. From the analysis of the intensity and shape of these bands it is possible to have information about the number of layers of graphene in the sample and the quality of graphene. Ferrari and coworkers [167] show that the evolution of the shape of the 2D band with the thickness (number of layers) of the graphene samples can be employed for the determination of the number of graphene layers. In particular, it was observed that a single layer of graphene is characterized by a sharp 2D band, with intensity higher than the G band. The Raman spectrum of a bilayer graphene is recognized by a broadening of the 2D band with intensity comparable to the G band. Upon increase of the number of graphene layers in the sample investigate, the Raman spectrum resembles the Raman spectrum of graphite. In Figure 12a the Raman spectra of graphite and graphene is shown, while in Figure 12b the evolution of the shape of the 2D band with the increase of the number of layers is displayed [167].

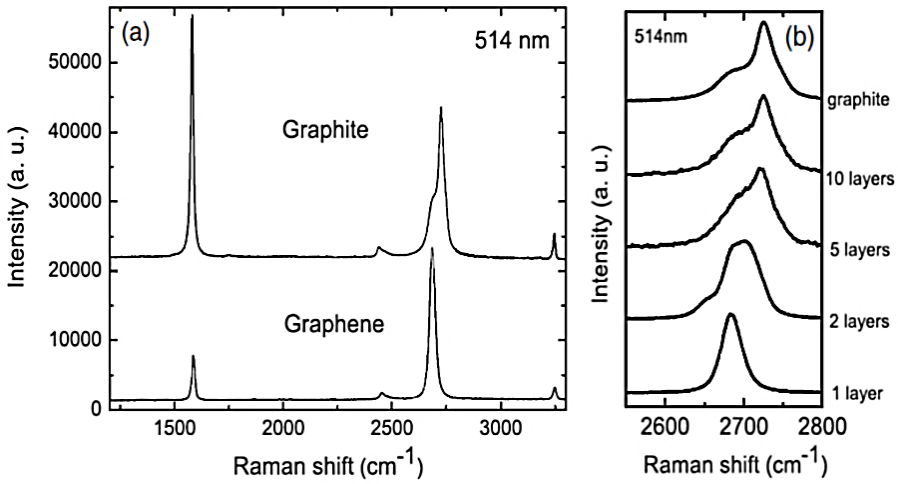

Figure 12: (a) Raman spectra of graphite and graphene; (b) evolution of the 2D increasing the number of graphene layers. Adapted from ref. [167].

The Raman spectrum of GO differs from the one of graphene. In particular, in the Raman spectra of GO, the intensities of the G band at 1600 cm^{-1} and the D band at 1367 cm^{-1}, are higher than the 2D band, as shown in Figure 13. Moreover, due to the presence of epoxy and hydroxyl groups a broadening of the G band is detected [168]. The 2D band appears at 2730 cm^{-1} and the other two combinational modes D+G at 2964 cm^{-1} and the 2G band at 3200cm^{-1} are visible.

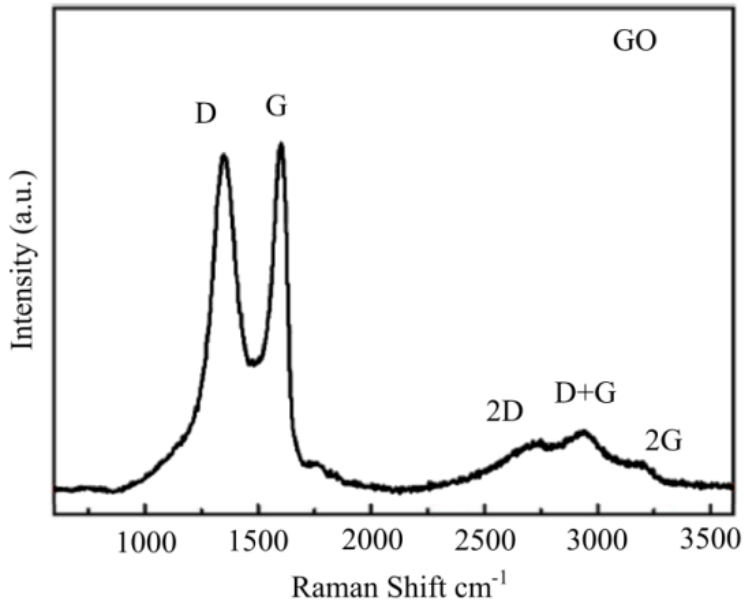

Figure 13: Raman spectrum of graphene oxide (GO). Adapted from ref. [169] open access article distributed under the Creative Commons CC-BY License http://creativecommons.org/

3.2.2. TiO_2

In section 2.5.1, it has been discussed that three crystalline structures are possible for titanium dioxide: anatase, rutile and brookite. Raman spectroscopy, allows to distinguish between these different phases, since each of them has a characteristic Raman spectrum [139,170–172]. In particular, anatase is characterized by four Raman active modes at 144 cm^{-1} corresponding to E_g, 399 cm^{-1} (B_{1g}), 513 cm^{-1} (A_{1g}) and the peak at 639 cm^{-1} corresponding to E_g. Rutile phase possesses three peaks at 143 cm^{-1} (B_{1g}), 447 cm^{-1} (E_g) and the peak at 612 cm^{-1} (A_{1g}), while brookite has 36 Raman active modes (9 A_{1g} + 9 B_{1g} + 9 B_{2g} + 9 B_{3g}) [171–174]. It has been reported that, Raman spectroscopy of titanium dioxide can be employed for the monitoring of the phase transformation of TiO_2 and its stoichiometry upon annealing or laser treatment, since the Raman active E_g modes are sensitive to oxygen deficiency, which will lead to a shift and broadening of these lines [139,170–172,174,175].

3.2.3. ZnO

The Raman active modes of ZnO are $A_1 + 2E_2 + E_1$, where the modes A_1 and E_1 have different frequencies for the transvers-optical (TO) and longitudinal-optical phonons (LO). The E_2 mode has two frequencies; one associated with the oxygen atoms E_2(high), while the other one, E_2(low), is associated with the Zn sublattice [176]. The frequencies of these Raman active phonon modes for ZnO bulk are: 102 cm^{-1} corresponding to the E_2 (low) mode, 379 cm^{-1} to A_1 (TO), 410 cm^{-1} to E_1 (TO), 439 cm^{-1} to E_2 (high), 574 cm^{-1} corresponds to the A_1 (LO) and the 591 cm^{-1} to E_1 (LO). It has been reported that these frequencies modes shift when ZnO nanostructures are analyzed and the position of the peaks varies depending on their morphology and size [176–178].

3.3. Atomic Force Microscopy (AFM)

The number of layer and the morphology of graphene samples can be investigated by Atomic Force Microscopy (AFM). In graphene samples, the number of graphene layers is determined by the height profile of the samples and considering that the interlayer distance in graphite is 0.35 nm. For the determination of number of layers in graphene oxide samples, it should be considered that the interlayer distance is greater than in graphene, due to the presence of oxygen groups; interlayer distance values of 0.75 and 1 nm have been reported for GO[89].

3.4. Scanning Electron Microscopy (SEM)

The morphology of graphene and graphene oxide can be studied by SEM. This technique can be employed as well for the determination of the number of layers. In particular, Hiura [179] reported a linear relationship between the number of graphene layers and the secondary electron intensity from the sample investigated.

3.5. Transmission Electron Microscopy (TEM)

3.5.1. Graphene-based nanomaterials

TEM can be employed to either observe morphological features in graphene and graphene-based nanomaterials or to determine the number of graphene layers. This because, the edges of the graphene films have the tendency to fold back, and this allow a cross sectional view of the films. These edges can be observed by TEM leading to an accurate calculation of the number of layers at multiple locations on the films.

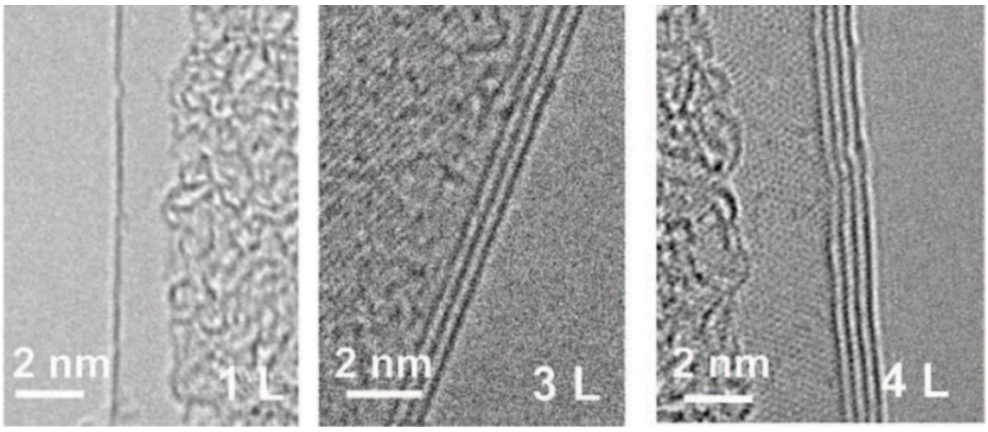

Figure 14: High-resolution TEM showing single-, three- , and four-layer graphene sheets. Adapted with permission from ref. [180] Copyright 2017 American Chemical Society.

Previous TEM studies conducted on graphene, have reported about the possibility of characterizing structural defects, in terms of mono-or multi-vacancies within the graphene plane, as shown in Figure 15 [181–183].

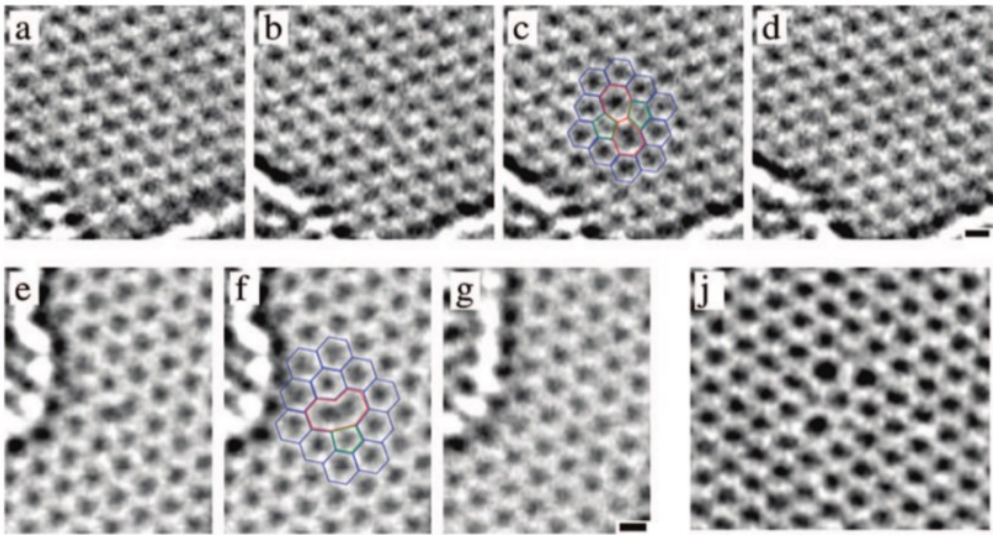

Figure 15: Defects detected in graphene by TEM. Adapted with permission from ref.[183] Copyright 2017 American Chemical Society.

3.5.2. TiO_2

The crystalline structure analysis of TiO_2 can be achieved by high resolution TEM (HRTEM). In particular, comparing the values of the interplanar distances obtained from the analysis of the HRTEM images with the crystallographic data of anatase, rutile and brookite it is possible to identify the different TiO_2 phases [148]. As an example, it has been reported that rutile nanoparticles have a d-spacing of 0.32 nm along the {110} family planes, while for the anatase ones is 0.35 nm along {101} [139].

3.5.3. ZnO

The crystallinity of ZnO nanostructures, the growth direction of ZnO rods and the particles size con be investigated by TEM [184–186]. The crystallinity of the samples is confirmed by a d-spacing of 0.26 ± 0.05 nm between adjacent lattice planes, which corresponds to the distance between (002) planes in the ZnO wurtzite structure. This lattice spacing confirms as well the [0001] as the preferential growth direction of ZnO rods and nanowires [185,187].

PART 1

Synthesis

by

Pulsed Laser Ablation

Chapter 4. Single-step synthesis of graphene quantum dots by femtosecond laser ablation of graphene oxide dispersions[250]

Overview

In this chapter, we investigated the femtosecond laser ablation of graphene oxide (GO) dispersions, as a technique for the straightforward and environmentally friendly synthesis of graphene quantum dots (GQDs). With proper control of laser ablation parameters, such as ablation time and laser power, it is possible to produce GQDs with average sizes of 2-5 nm, emitting a blue luminescence at 410 nm. We tested the feasibility of the synthesized GQDs as materials for electronic devices by aerosol-jet printing of an ink that is a mixture of the water dispersion of laser synthesized GQDs and silver nanoparticle dispersion, which resulted in lower resistivity of the final printed patterns. Preliminary results showed that femtosecond laser synthesized GQDs can be mixed with silver nanoparticles dispersion to fabricate a hybrid material, which can be employed in printing electronic devices by either printing patterns that are more conductive and/or reducing costs of the ink by decreasing the concentration of silver nanoparticles (Ag NPs) in the ink.

4.1. Introduction

Graphene, a two-dimensional (2D) sheet of sp^2-hybridized carbon atoms, was discovered in 2004 [35] and since then several approaches have been developed for its synthesis [180]-[188]. The increasing interest in graphene is to be attributed to its outstanding properties that render it one of the most promising materials for many applications [2], [3]. It was demonstrated by several research groups that modification of the graphene structure can improve its properties and lead to the production of new types of graphene-based materials, which can be employed for the manufacture of nanoscale transistors [4], molecular sensors [5], fuel cells [6], solar cells [7], electrodes for organic light-emitting diodes (OLEDs) [8], water treatment devices [10],[9] and conductive adhesives [11]. Among the many graphene-based materials that can be produced, graphene quantum dots (GQDs) which are zero-dimensional (0D) nanomaterials, have recently drawn the attention of many research groups for their outstanding properties such as chemical stability, strong luminescence and biocompatibility [47,48]. All these characteristics render GQDs suitable nanomaterials for electronic devices [49], devices for bioimaging and

photovoltaic applications [50–52]. Therefore, several methods for the production of GQDs have been developed so far with the goal of producing electronic devices, such as transistors, supercapacitors, and sensors [49]. The methodologies utilised in the fabrication of GQDs can be categorized top-down or bottom up approaches [53]. GQDs can be considered as small fragments of graphene sheets with dimensions less than 30 nm [54] so top-down approaches have involved the hydrothermal and solvothermal cutting of graphene oxide (GO) [55,56] sheets, strong acid-assisted cleavage of carbon nanomaterials [189] or are derived from the photo-Fenton reaction of GO [57]. The resulting GQDs due to the presence of remaining oxygen containing groups are dispersible in water and show different colours of luminescence as a function of their sizes [58]. Researchers who reported the synthesis of GQDs through bottom-up approaches involved either organic synthesis by oxidation of polyphenylene dendritic precursors [59] or obtained from the opening of fullerenes C_{60} [54],[61]. Many GQDs synthesis methods have been developed, however these methods are often time consuming, requiring more than 10 hours and multiple steps [55,189,190]. Additionally, these procedures are not environmentally friendly processes due to the use of strong acids, organic solvents, and high temperatures and pressures; a direct, simple and green process for the production of GQDs is still absent.

The novelty of this study relies on the development of an ecofriendly and straightforward process for the sole production of GQDs by femtosecond (fs) laser ablation of GO dispersions in water. Compared to the methods cited above, our process is environmentally friendly, since the synthesis is performed in water without the use of any chemicals. Furthermore, the ablation process is not time consuming, namely the production of GQDs is achieved in a single-step within a time window ranging from 15 to 60 minutes, depending on the laser parameters employed. Generally speaking, pulsed laser ablation in liquids (PLAL) is a powerful technique that permits the synthesis of different nanostructures. For example, stable colloids of silver and gold nanoparticles are obtained by ablating silver and gold thin plates in water, respectively [121], [191]. It should be stressed that the nature of the target, whether a solid or a liquid one, plays a key role in the type of nanostructures synthesized [118]. In literature, several groups successfully demonstrated the synthesis of carbon quantum dots (CQDs) by nanosecond laser ablation of nano-carbon in organic solvents [192], by nanosecond and femtosecond laser ablation of graphite powders dispersed in polyethylene glycol [193–195]. More recently luminescence

CQDs were synthesized upon laser irradiation of a solution of toluene, as carbon precursor [196] and by laser ablation in imidazolium ionic liquids [197]

In our previous work [198], we proved that upon fs laser ablation of a graphite target (HOPG), it is possible to obtain porous graphene sheets as primary products and GQDs as secondary products. However, it was not possible to have reliable control over the GQDs production or their separation from porous graphene.

In this study, we report the optimization of the developed process for the GQDs production employing GO dispersions as a starting material. To our knowledge, this is the first time that dispersions of GO are ablated with a fs laser for the primary synthesis of GQDs. Recently, only one other group has reported about the possibility of synthesizing different nanostructures by nanosecond laser ablation of GO dispersions as a starting material [199]. It is well-known [129,198] that the laser pulse duration employed for PLAL, such as femtosecond, picosecond and nanosecond lasers, plays a key role in the type of nanomaterials synthesized due to the different ablation mechanisms [200].

Additionally, we have demonstrated that with the optimization of laser parameters, such as ablation power and ablation time it is possible to achieve the synthesis of high quality GQDs in a simple manner. These GQDs were implemented as a conductive ink for printable circuits and we have shown that the laser treated GQDs dispersions mixed with silver nanoparticles (AgNPs) can be used, without any further purification, as a highly conductive and cost-effective ink for printed electronic devices compared to traditional AgNPs. To date, some reports show attempts towards developing more cost effective inks for printed electronics through decreasing the concentration of AgNPs by adding graphene sheets [12–14,201]. Graphene can enhance the charge transfer in AgNPs printed patterns or increase their conductivity [13,201]. Therefore, the addition of the laser synthesized water-based GQDs dispersion to AgNPs ink can result in cheaper or more conductive printable inks.

4.2. Experimental

4.2.1. GQDs synthesis

GO dispersion with a concentration of 500 mg/L in deionized water was purchased from Graphene Supermarket supplier. The concentration of the dispersions employed was 10 mg L^{-1} and was obtained by dilution of the purchased dispersion with deionized water and it was

employed as received without any further modification. The femtosecond laser ablation experiments were achieved employing a Ti-sapphire laser (Coherent, Inc.) with wavelength of 800 nm, repetition rate of 1 kHz and pulse duration of 35 fs with Gaussian beam distribution. The experiments were carried out at two different laser powers: 1.3 W (fluence = 25.87 J/cm^2) and 2.4 W (fluence = 47.77 J/cm^2). In our experimental setup a fixed volume of GO 10 mg L^{-1} dispersion was placed in a beaker and the laser ablation was performed from the top in order to avoid laser reflections through the glass walls. A scheme of the experimental setup is shown in Figure 16.

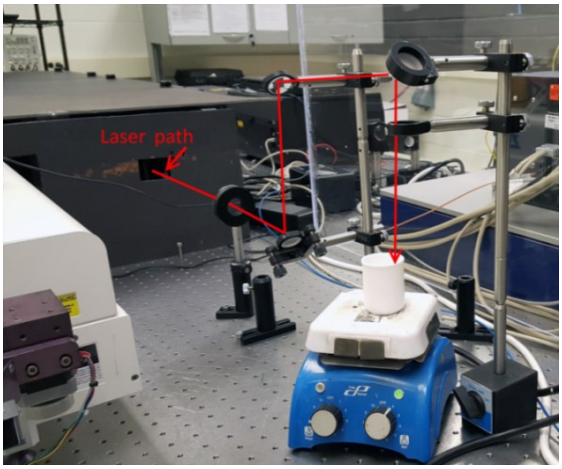

Figure 16: Picture of the laser ablation setup. Reproduced from ref. [202] by permission of The Royal Society of Chemistry

The laser beam was focused inside the dispersion at 5 millimeter from the liquid-air interface, and a magnetic stirrer was used to maintain a constant agitation of the dispersion during each experiment. The stirrer was kept far from the area of the focus beam in order to avoid the ablation of the magnetic stirrer, due to reflections. The GO dispersions, for each laser power chosen, were ablated at different times, 5, 15, 30 and 60 minutes. For each ablation time a new dispersion of GO 10 mg L^{-1} was employed to avoid a change of the concentration of the dispersion that could be caused by removal of the aliquots during the experiments.

4.2.2. Separation of the GQDs

The GQDs were separated from the reduced GO sheets through dialysis. In particular, a cellulose ester dialysis tube (Spectrum Labs Biotech CE Dialysis, 10 mm flat-width) with a Molecular Weight Cut-Off (MWCO) of 50kD was used. A 12 mm weighted dialysis tubing closure was clipped onto the bottom end of the dialysis tube A 1 mL solution containing laser processed GO

sheets with GQDs were pipetted into the dialysis tube and the remaining end was clipped with a non-weighted closure. The dialysis bag was placed in a beaker containing 100 mL of ultrapure water. The solutions were dialysed for 24 hours under magnetic stirring, in which GQDs diffuse out of the dialysis membrane into the bulk solution while GO sheets are retained in the bag. The GQDs solutions outside the dialysed bags were used for the TEM analysis and quantum yield efficiency measurements.

4.2.3. Preparation of the hybrid ink and of the hybrid ink printed patterns

In order to develop the GQDs@AgNP ink compatible with an aerosol-jet printing system, a Cabot AgNP (45-55 wt%.) solution (Cabot Superior Micro Powders in ethylene glycol ($C_2H_4(OH)_2$) and other compatible alcohols, Albuquerque, USA) was mixed with GQDs dispersion obtained after 30 min of laser ablation, without any further treatment, in a volume ratio of 1:3. The ink was then printed using the aerosol-jet printing system. To print GQDs@AgNP patterns with the width around 45 μm, sheath gas flow rate, atomizer flow rate, and ultrasonic atomizer power in the aerosol-jet printer were kept fixed at 50 ccm, 15 ccm, and 46 V, respectively. The patterns were printed with a speed of 0.2 mm/s. After printing the patterns with 4 deposition layers, the samples were left in the oven at temperatures of 180°C for 30 min in order to sinter the AgNPs and remove all the solvents from the ink.

4.2.4. Temperature profile simulation method

A two temperature model was employed to model the electronic and atomic temperature of the water molecules during laser irradiation and after the laser pulse until these two temperatures reach equilibrium conditions.

For this purpose, the simulation domain was proposed as a 10 μm ×10 μm ×10 μm cube. At the center of the simulation domain, another 300 nm × 300 nm × 300 nm cube was designed for laser irradiation. The central cube was divided to a 1×10^4 cubic mesh. The initial time step of this simulation was set to be one femtosecond with defined boundary conditions, in which the electronic and atomic temperatures of the outer surface of simulation domains were kept constant at 20°C during simulation. The energy of laser was homogenously distributed throughout the central meshed cube for 35 femtosecond. To find the temperature evolution, the governing

equations for this simulation (Equations 1 and 2) were simultaneously solved by finite element method and the time evolution of the electronic and atomic temperatures was calculated.

$$C_e(T)\frac{\partial}{\partial t}T_e(\boldsymbol{r},t) = \nabla\cdot\big(k_e\nabla T_e(\boldsymbol{r},t)\big) - g\big(T_e(\boldsymbol{r},t) - T_A(\boldsymbol{r},t)\big) + S(\boldsymbol{r},t) \quad (1)$$

$$C_A(T)\frac{\partial}{\partial t}T_A(\boldsymbol{r},t) = k_A\nabla^2 T_A(\boldsymbol{r},t) - g\big(T_A(\boldsymbol{r},t) - T_e(\boldsymbol{r},t)\big) \quad (2)$$

A specific term has been added to these two couple heat transfer equations to model energy transfer from electrons to atoms. In Equations (1) and (2), *r* is position and *t* is time, T_e and T_A are electronic and atomic temperatures, C_e and C_A are electronic and atomic heat capacity, k_e and k_A are electronic and atomic heat transfer coefficients, $S(\boldsymbol{r},t)$ is energy source, and g is the electron-phonon interaction coefficient. $S(\boldsymbol{r},t)$ is considered a uniform distribution of energy and has a user-defined efficiency for the laser pulse absorption in a medium, in this case, water. The atomic parameters are available from literature [203], while the electronic ones are estimated. In this study, we assumed that C_e =100×T_e $(Jm^{-3}k^{-1})$, k_e=$k_A T_e/T_A$, and g=1×10^{16} $(Wm^{-3}K^{-1})$[204]. The parameters employed for the two-temperature model heat transfer equations are listed in Table 1.

Table 1: Parameters of two-temperature model heat transfer equation. Reproduced from ref. [202] by permission of The Royal Society of Chemistry

C_e	100×T_e $\left(\frac{j}{m^3K}\right)$, T_e is electronic temperature
C_A	4200 $\left(\frac{j}{m^3K}\right)$
k_e	$k_A T_e/T_A$ $\left(\frac{W}{m^2K}\right)$
k_A	0.6 $\left(\frac{W}{mK}\right)$ at 293 K [176]
g	1×10^{16} $\left(\frac{W}{m^3K}\right)$

4.2.5. Instrumentation

For the SEM, AFM, XPS and Raman characterizations, drops of GO and laser treated dispersions were drop casted onto a substrate of silicon with a layer of SiO_2 ~300 nm in thickness. SEM analyses have been performed using a ZEISS LEO 1550 FE-SEM at an accelerating voltage of 5 kV. The GO and laser treated dispersions morphology was investigated

with an atomic force microscope (Parks system NSOM model). X-ray photoelectron spectroscopy (XPS) analysis was carried out using a multi-technique ultra- high vacuum imaging XPS microprobe spectrometer (Thermo VG Scientific ESCALab 250) with a monochromatic Al-Ka 1486.6 eV X-ray source. The spectrometer was calibrated by Au 4f7/2 (binding energy of 84.0 eV) with respect to the Fermi level. The chamber vacuum level was maintained below $2x10^{-10}$ Torr. Raman spectra were measured using a Renishaw micro-Raman spectrometer with a He/Ne laser at an excitation wavelength of 632.8 nm. HRTEM observation was conducted using a JEOL 2010F at the Canadian Centre for Electron Microscopy (Hamilton, Ontario, Canada). TEM samples were prepared by drop casting the dispersions onto lacey carbon grids and holey carbon copper grids (dialyzed solutions). Photoluminescence analyses were carried with a Carry Eclipse Instrument. The dispersions were scanned with different excitation wavelength from 260 nm to 400 nm in emission mode. The hybrid ink GQDs@AgNP was printed with an aerosol-jet printing system (Aerosol Jet technology, Optomec® Inc., Albuquerque, USA), and the printed patterns were heat treated in an oven (1100 Box Furnace, Lindberg/Blue M, Asheville, USA). A two-point probe station (M150 Measurement Platform, Cascade Microtech®, Beaverton, USA) and an atomic force microscopy (AFM) (Dimension 3100 AFM, Nanoscope Software, Veeco Instruments Inc., Plainview, NY, USA) were used to measure resistance and thickness of the printed patterns, respectively.

4.2.6. Size Distribution Analysis

Size distribution analysis was conducted using TEM images and particle count was conducted on ImageJ on a manual basis. The raw data was processed and a range of values were automatically binned – that is, the entire range of values was converted into specific intervals – using OriginPro 8 software, which automatically counts how many values fall into the interval. A Gaussian distribution was fitted and the mean ($\bar{x}_{std}$), standard deviation (σ_{std}), and coefficient of determination (R^2) was obtained. The mean ($\bar{x}_{abs}$) and mean absolute deviation (σ_{abs}) was also determined using the raw distribution data. The absolute values and Gaussian fit were tabulated in Table 2. All values reported in the discussion refer to the values obtained from the Gaussian fit; the absolute values from the raw distribution were calculated for reference.

Table 2: Absolute and Gaussian fit values for GQDs obtained at 1.3 W and 2.4W at four ablation time points: 5, 15, 30, and 60 minutes. Reproduced from ref. [202] by permission of The Royal Society of Chemistry

Ablation Time (min)	Power: 1.3 W					Power: 2.4 W				
	Absolute		Gaussian Fit			Absolute		Gaussian Fit		
	$\bar{x}_{abs}$	σ_{abs}	$\bar{x}_{std}$	σ_{std}	R^2	$\bar{x}_{abs}$	σ_{abs}	$\bar{x}_{std}$	σ_{std}	R^2
5	1.765	0.1398	1.672	0.0622	0.81	1.432	0.1176	1.461	0.2177	0.76
15	1.849	0.2336	1.825	0.0981	0.87	2.4057	0.5275	2.319	0.6246	0.92
30	2.275	0.5898	2.087	1.938	0.78	3.3785	0.8009	3.025	0.6826	0.93
60	3.923	0.7170	3.462	1.028	0.80	3.2632	0.5941	2.977	0.4207	0.93

*$\bar{x}_{abs}$ is the mean, σ_{abs} is the mean absolute deviation, $\bar{x}_{std}$ is the mean of the Gaussian fit, σ_{std} is the standard deviation, and R^2 is the coefficient of determination

4.2.7. Quantum Yield Measurements

Anthracene in ethanol (QY 30%) was chosen as the reference standard. The quantum yield of the dialyzed GQDs dispersions obtained at different laser ablation time was calculated according to Equation 3 [205]:

$$\Phi = \Phi_{st}(I/I_{st})x(\eta^2/\eta_{st}^2)x(A_{st}/A) \quad (3)$$

Where Φ is the quantum yield, I is the measured integrated emission intensity, η is the refractive index of the solvent (1.36 for anthracene and 1.33 for GQDs in water) and A is the optical density. The subscript "st" was used to indicate the reference standard with a known quantum yield. The excitation wavelength was 300 nm.

4.2.8. Calculation of the resistivity of the printed patterns

The resistivity of the printed GQDs@AgNP and AgNP patterns was calculated according to the Equation (4):

$$R=\rho L/A \quad (4)$$

Where ρ is the resistivity, L is the length which is the distance between the probe tips, R is the resistance measured by a two-probe station and A is area which is given by the width multiplied by the thickness of the patterns measured by AFM.

4.3. Results and Discussion

4.3.1. Morphology of fs laser processed GO dispersions at low power

Dispersions of GO in water were ablated with a fs laser at different ablation times and laser power to study how these parameters effect the type of materials obtained and consequently to optimize the process for the synthesis of GQDs. The experiments were performed in such a way that after the dispersions were ablated for the established time, a certain volume of the laser treated dispersions was collected for further characterization. The morphology and structure of the initial GO dispersion were investigated prior to the laser ablation by atomic force microscopy (AFM), scanning electron microscopy (SEM), transmission electron microscopy (TEM), UV-VIS spectroscopy and X-ray photoelectron spectroscopy (XPS), in order to have a clear understanding of the modifications induced upon laser treatment. In Figure 17(a-b), the topography of GO sheets together with the height profile, Figure 17c, is displayed. From the AFM analysis, the GO dispersion that was deposited on the substrate and dried at room temperature appeared folded on top of each other. However, it was possible to detect a single layer covered with another GO layer thus forming a bi-layer structure. This was established from the magnification of the area highlighted with a dashed rectangle in Figure 17a and from the section profile along the white line shown in Figure 17b. The height profile displayed in Figure 17c shows a double step profile with identical heights of ~1.020 nm, which indicates that the height of a single GO sheets in our dispersion is ~1 nm. This value is in agreement with the height value reported for a monolayer GO [89]. The random stacked structure of GO layers was further confirmed by SEM analysis. In Figure 17d, different free-standing layers are shown with sizes in the range of few micrometers lying on each other. Some of the GO layers did not appear flat since some ripples were seen either in the AFM (Figure 17a) or in the SEM images (*i.e.* right corner of Figure 17d, which was attributed to the deposition procedure onto the Si/SiO_2 substrate. As discussed in Section 4.2.1, the laser ablation experiments performed at the two different powers were carried out without interruption for 5, 15, 30 and 60 minutes.

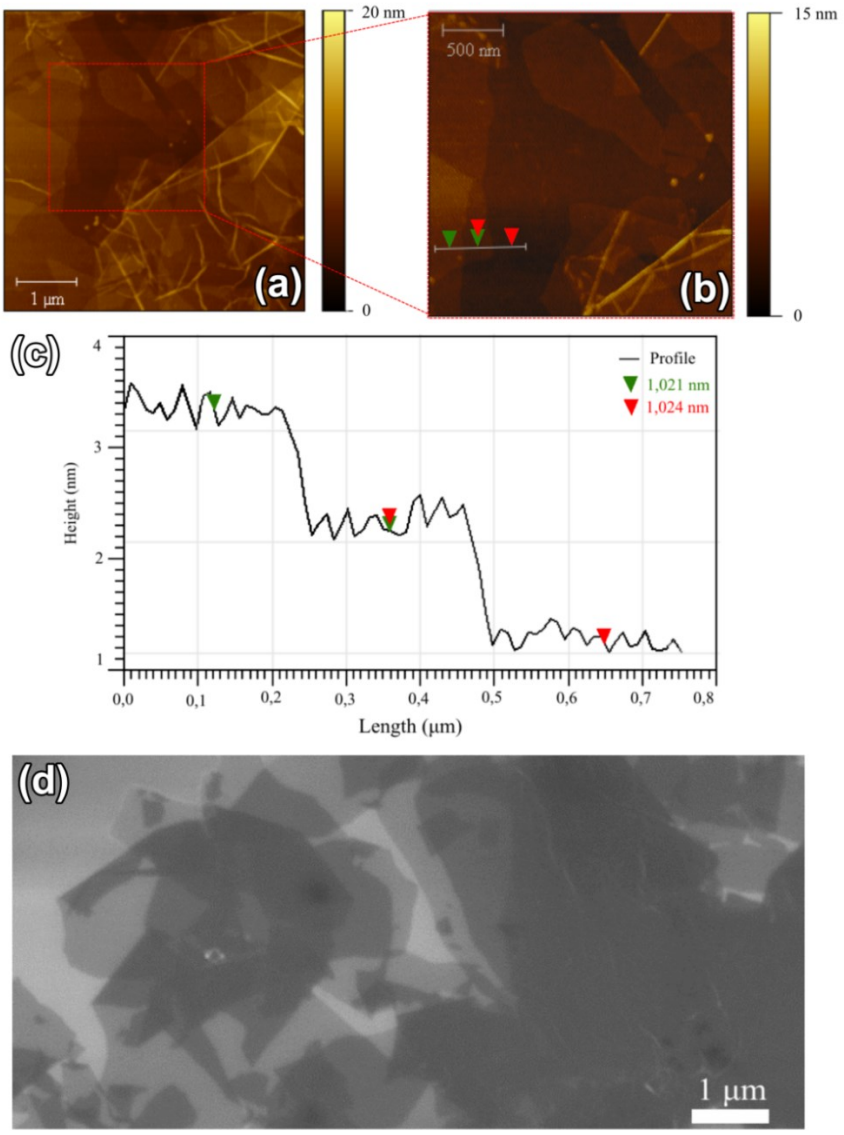

Figure 17: : a) AFM image of GO sheets deposited onto the Si/SiO2 substrate; b) magnification of the area highlighted with a dash rectangular in panel a); c) section profile along the white line in panel b); d) SEM image of GO sheets. Reproduced from ref. [202] by permission of The Royal Society of Chemistry

For the AFM, SEM and XPS characterization, the laser treated dispersions were drop casted onto Si substrates with a 300 nm SiO_2 passivation layer. In Figure 18, the SEM images of the dispersions obtained at 1.3 W after 5 min (Figure 18a), 15 min (Figure 18b), 30 min (Figure 18c) and 60 min (Figure 18d) of laser ablation are shown. From the comparison with the SEM image of non-treated GO dispersion (Figure 17d), it was possible to establish that structural modifications of the sheets started to occur within the first 5 minutes of laser ablation as shown

in Figure 18a, which depicts small fragmentized sheets that were distributed randomly along with larger sheets over the substrate.

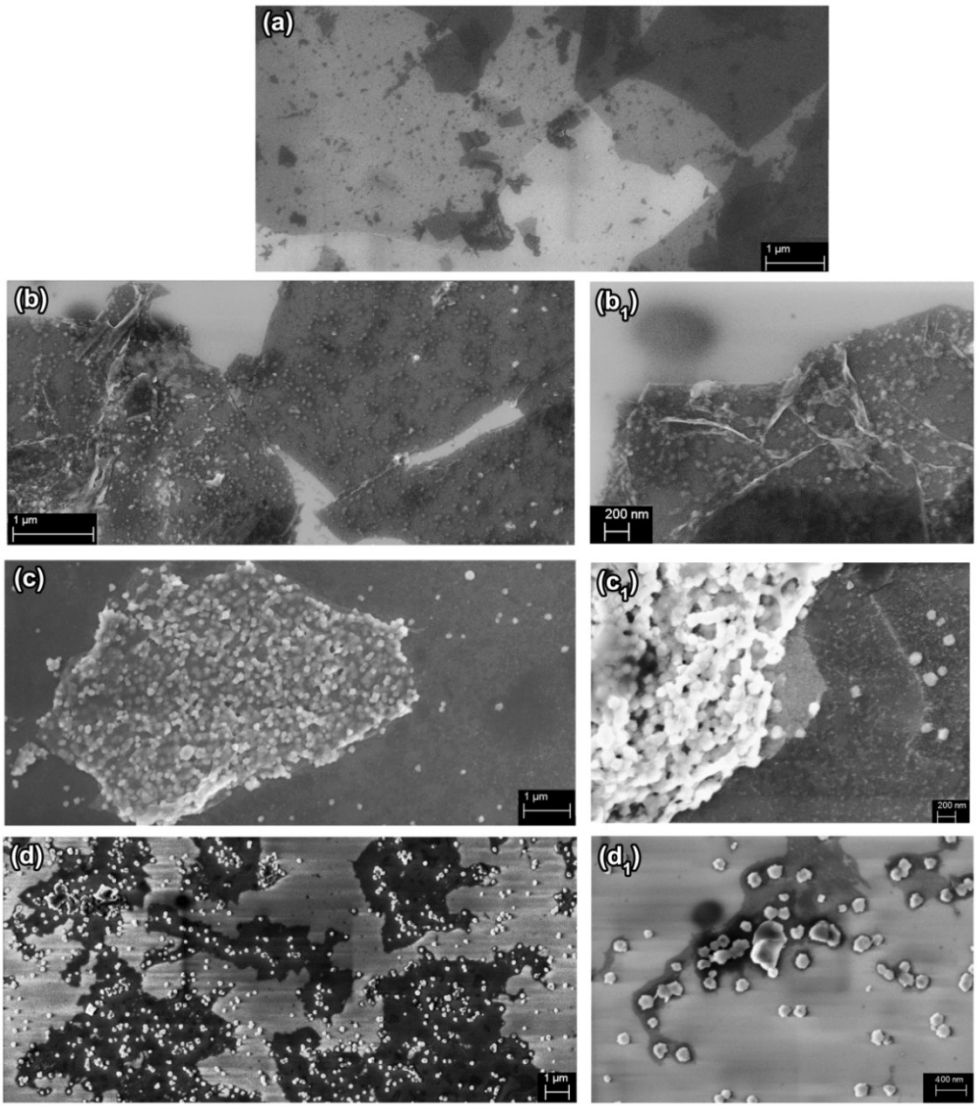

Figure 18: SEM images of GO dispersion after (a) 5, (b-b1) 15, (c-c1) 30 and (d-d1) 60 minutes of laser ablation. Reproduced from ref. [202] by permission of The Royal Society of Chemistry

It is evident that an ablation time of 5 minutes is not enough to induce a consistent modification of the sheets. Figure 18b shows how the increase of laser treatment time up to 15 minutes resulted in the formation of particles, which were found mostly on top of the larger sheets or small sheet fragments with well-defined edges. Dispersions obtained after 30 and 60 minutes of PLA showed significant changes. In particular, it was observed that after 30 minutes the sheets were fully covered by particles and the edges of the sheets appeared smoothed and, in some cases, were not easily distinguishable. Many of those particles were also found irregularly spread

throughout the substrate. After 60 minutes of laser ablation, particles were detected with an average size of 100 nm, larger than those found after 30 minutes of ablation. The particles were randomly dispersed in the entire sample; however, some of them were agglomerated. It should be noted that some sheets were still visible, though they appeared smaller in size with undefined borders compared to the sheets detected in the samples at lower ablation times.

The morphology of the laser treated solution was investigated by AFM. In Figure 19, the AFM images of the dispersion after laser ablation are shown.

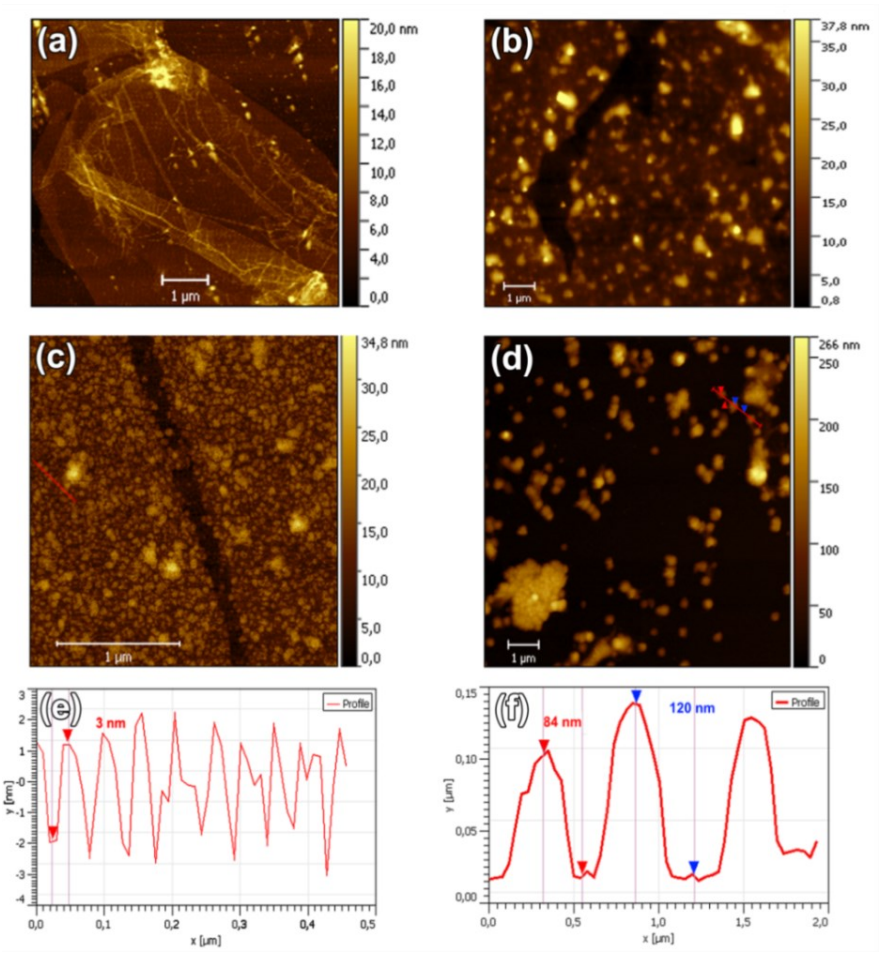

Figure 19: AFM images of the GO dispersions after (a) 5 minutes. (b) 15 minutes, (c) 30 minutes and (d) 60 minutes of laser ablation; (e) and (f) height profiles of image (c) and (d) respectively. Reproduced from ref. [202] by permission of The Royal Society of Chemistry

The analysis results are in agreement with the SEM images, namely at a longer ablation time, the GO sheets are covered by clusters of nanoparticles, as shown in Figure 19(c-d). The height profile displayed Figure 19e showed that the nanoparticles obtained after 30 minutes of laser treatment have an average height of 34 nm, however when the time of ablation is extended to 60

minutes, particles with a height of 80-120 nm were detected and start to agglomerate when increasing the ablation time. In order to investigate the structure of the particle obtained, the laser-treated dispersions and the untreated one were characterized by TEM. Figure 20, depicts the low magnification and HR TEM images relative to the non-treated GO (a, b) and the GO dispersions ablated at 1.3W for 5 (c, d) and 15 (e, f) minutes, respectively.

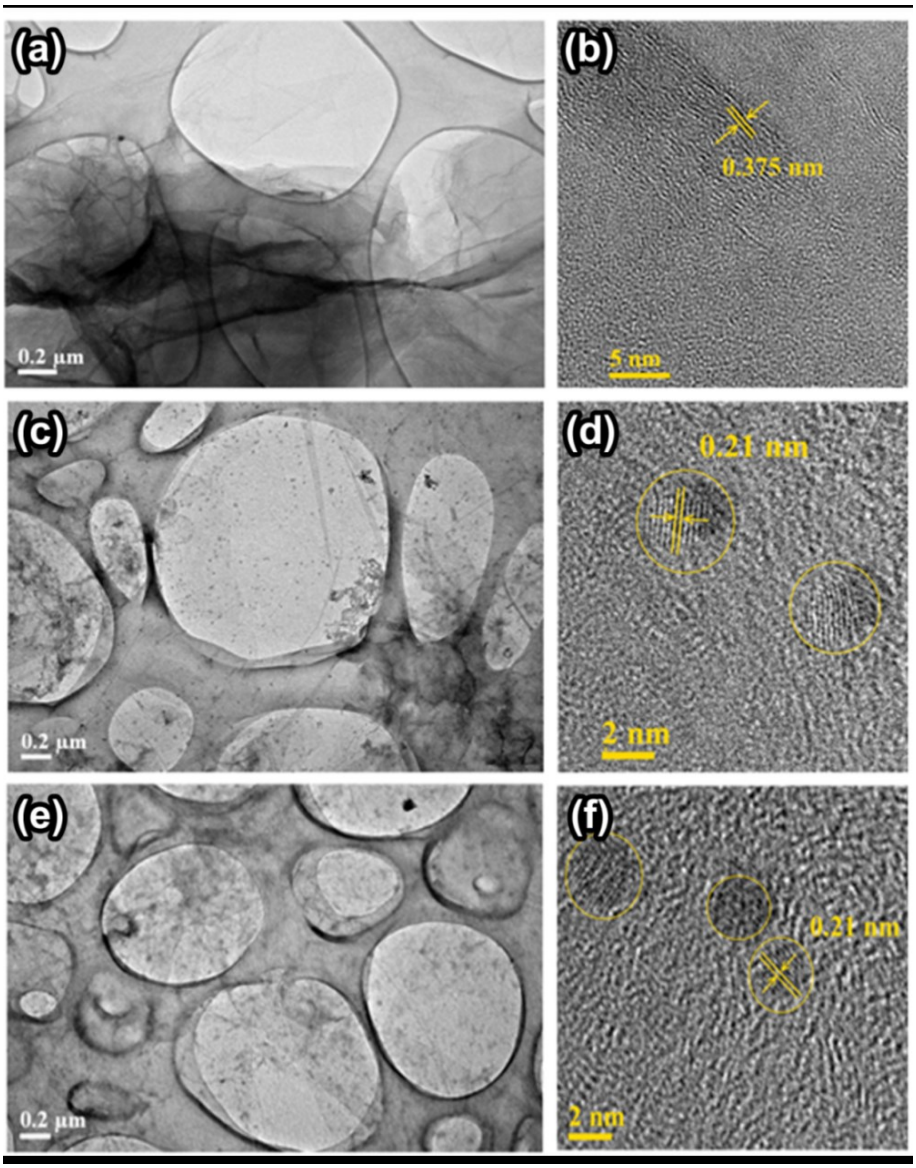

Figure 20: TEM images of a) non-treated GO solution and GO solution after (c) 5 minutes and (e) 15 minutes of laser ablation. In panel (b) HRTEM image of the non-modified GO sheets shows an interlayer d-spacing of 0.375 nm, which is larger than that of the graphite due to the presence of oxygen/containing groups. HR images (d) and (f), show the presence of few graphene quantum dots within the graphene oxide sheets after 5 and 15 minutes of laser treatment, respectively. Reproduced from ref. [202] by permission of The Royal Society of Chemistry

The interlayer spacing of the non-modified GO (Figure 20 (b) was found to be 0.375 nm, which is bigger than the value reported for bulk graphite, due to the presence of oxygen containing groups within the layers that increase the d-spacing [55]. As observed by SEM analysis, the GO sheets started to undergo structural modification after 5 minutes of laser treatment; however, graphene sheets with sharp edges were still detected after 15 minutes of ablation. HRTEM images of dispersions at 5 and 15 minutes of ablation show the presence of GQDs on GO sheets (Figure 20d and f) where GQDs possess a lattice spacing of 0.21 nm. This value of d-spacing agrees with that reported in the literature for a monolayer graphene [181], while the d-spacing calculated in carbon quantum dots is 0.35 nm, which is attributed to graphite-like layers [192]. Therefore, this result highlights that upon laser ablation of the GO dispersion the sheets underwent a reduction processes that caused the synthesis of these nanomaterials, which can be defined as graphene quantum dots. The average diameter of the GQDs found after 5 minutes of laser treatment was 1.67 ± 0.062 nm based on size distribution analysis in Figure 21a, whereas after 15 minutes the average diameter of GQDs was 1.82 ± 0.098 nm (Figure 21b).

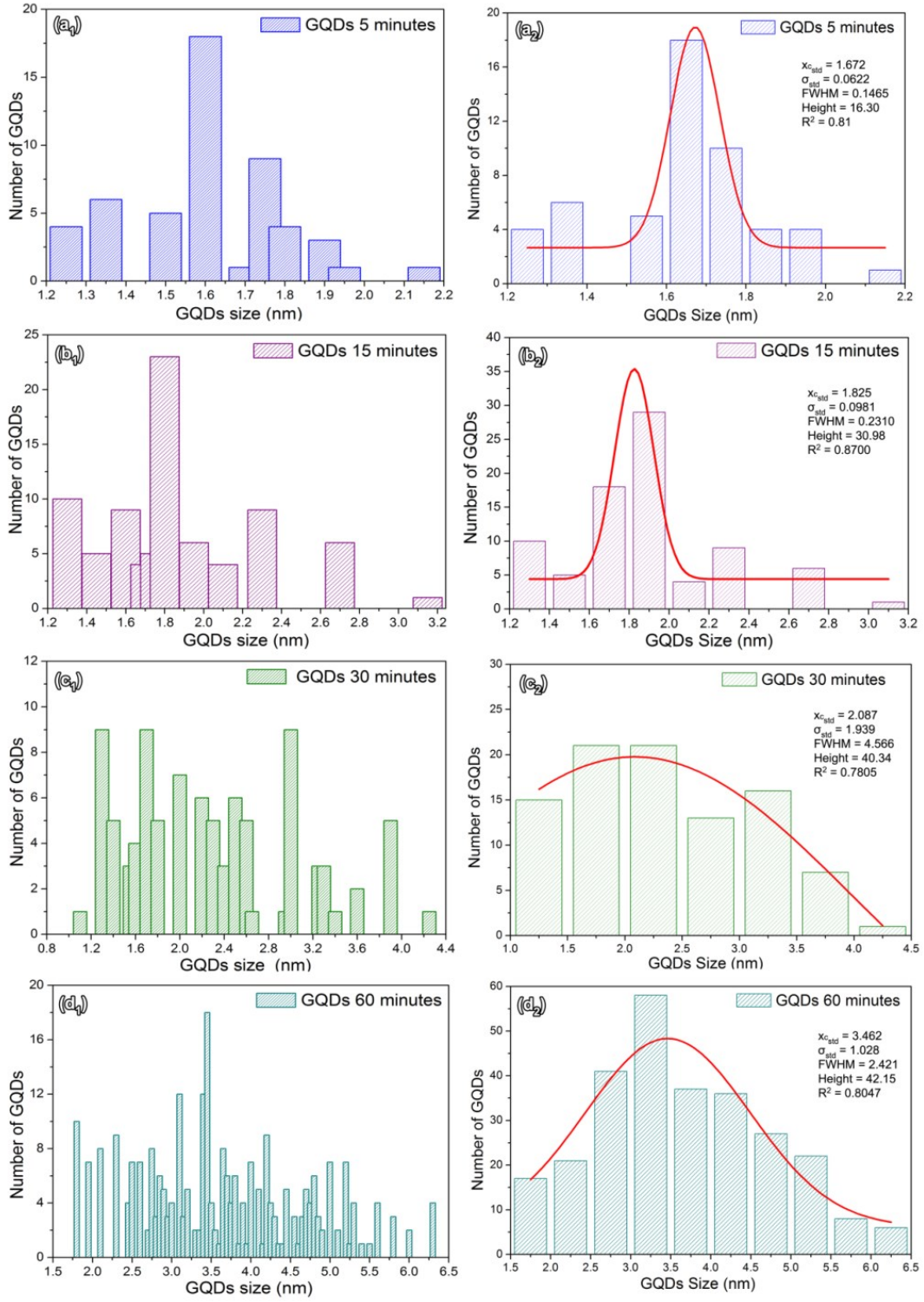

Figure 21: Raw and (2) binned size distribution of GQDs after (a) 5 minutes, (b) 15 minutes, (c) 30 minutes and (d) 60 minutes of laser ablation at 1.3W. Reproduced from ref. [202] by permission of The Royal Society of Chemistry

Further modification of the sheets took place after 30 minutes of PLA as seen from Figure 22a. In particular, the particles detected in the SEM image and shown in Figure 18c were clusters of nanostructures within the sheets.

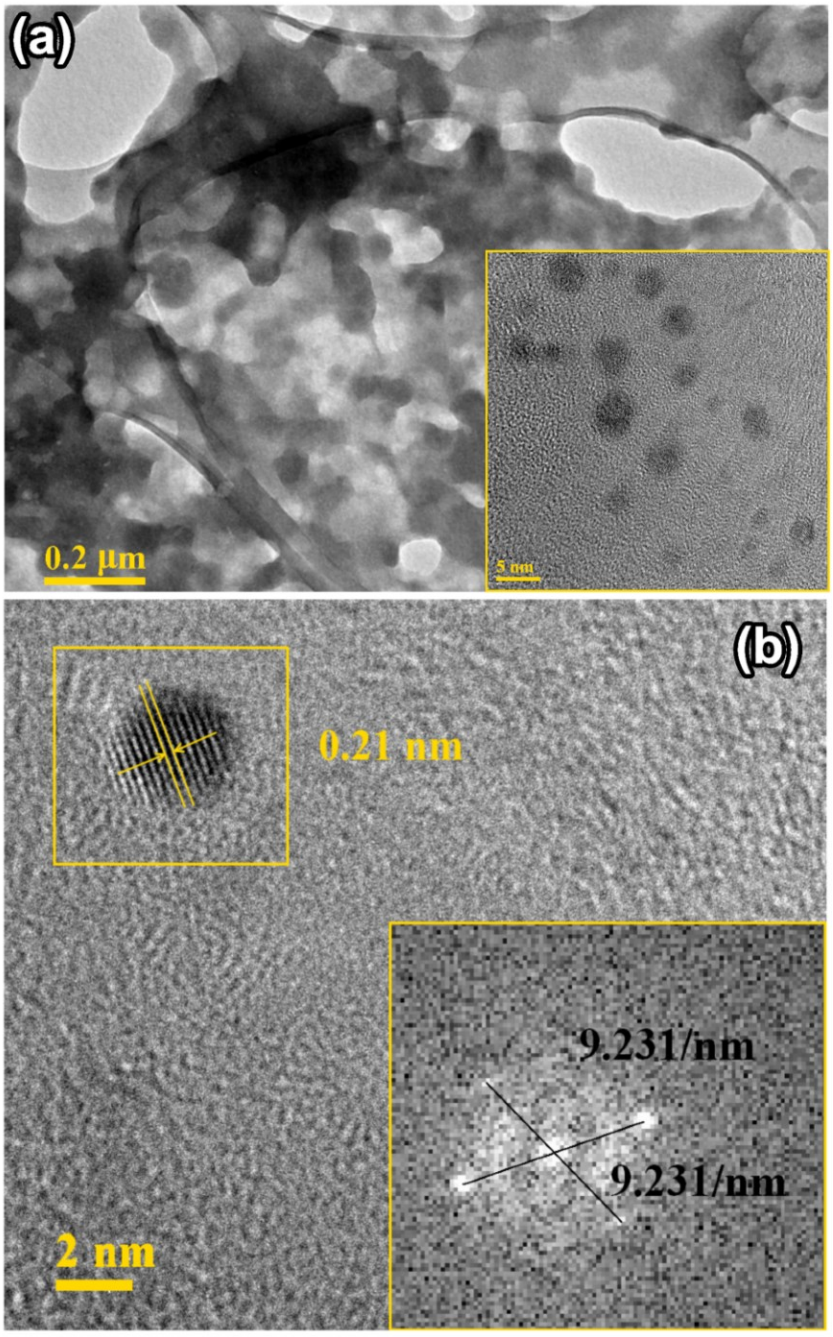

Figure 22: a) TEM image of GO sheets after 30 minutes of laser ablation, in the inset GQDs can be seen embedded in the residual GO sheets; b) HRTEM image of a GQDs and its relative FFT image showing a d-spacing of 0.21nm. Reproduced from ref. [202] by permission of The Royal Society of Chemistry

HRTEM analysis of these clusters, inset of Figure 22a, revealed the presence of some GQDs embedded in matrices, which we hypothesized are damaged and reduced GO sheets. Figure 22b shows the Fast Fourier Transform (FFT) taken from the high resolution image, which demonstrates the symmetry of hexagonal structure with an inter-planar d-spacing of 0.21 nm, typical of a monolayer of graphene [181]. The size distribution in Figure 21c suggests that the average size of the GQDs is 2.1± 1.9 nm, albeit GQDs much smaller and bigger than the average were detected. The standard deviation for this sample was much larger than at other laser ablation times TEM analysis of the dispersion after 60 minutes (Figure 23a) showed the complete modification of the GO sheets that were smaller in size compared to those ablated at shorter times and it was not possible to observe well-defined borders.

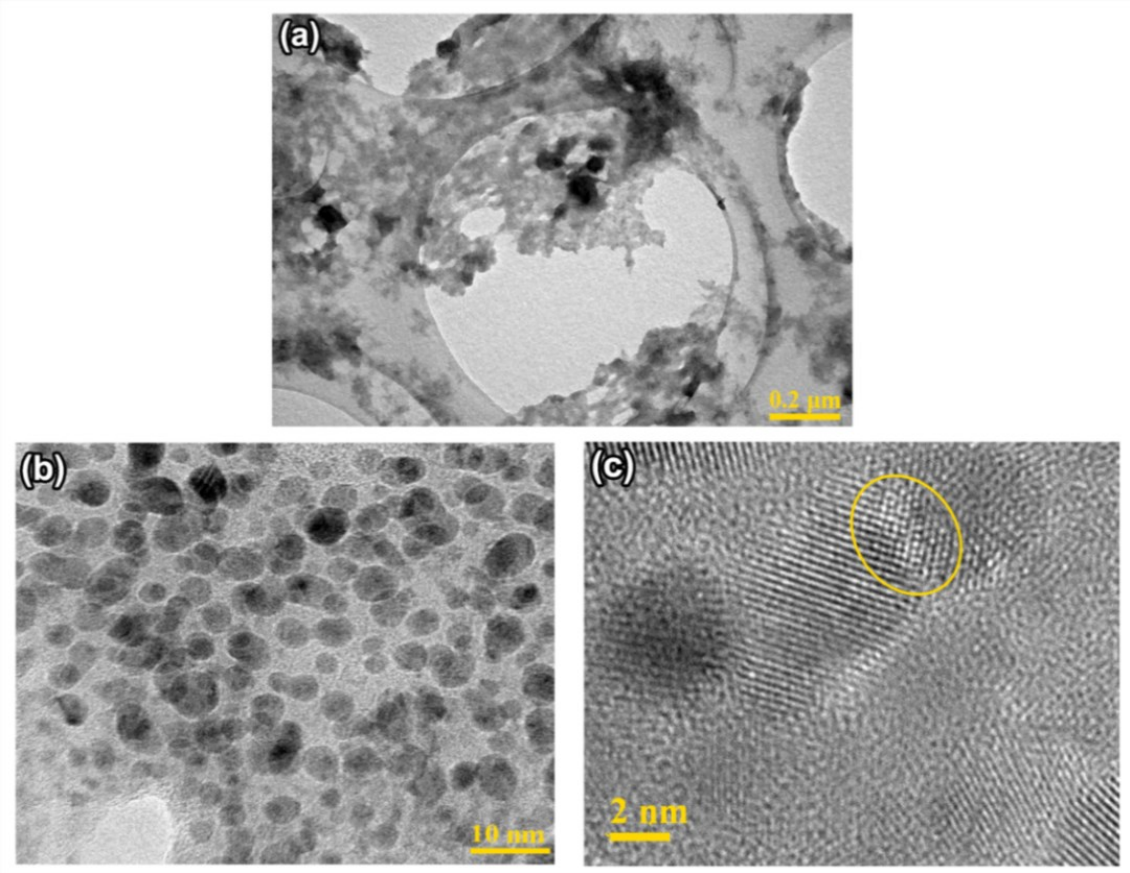

Figure 23: a) TEM overview of the GO sheets after 60 minutes of laser treatment; b) high magnification image of the corrugated sheets displaying several GQDs; c) two GQDs joined (highlighted in yellow) together. Reproduced from ref. [202] by permission of The Royal Society of Chemistry

Within the modified sheets, some black clusters of ~90 nm in size were detected as already identified by AFM and SEM characterization. High magnification images showed that after 60

minutes, there were more GQDs enclosed in the sheets compared to the sample at lower ablation time (Figure 23b). From the size distribution in Figure 21 (d), when compared to the GQDs produced at lower ablation time, most of the dots produced after one hour of laser treatment are 3.5 ± 1.0 nm in size; however, GQDs of 6 nm and 1.8 nm were found as well. The analysis performed on the black clusters revealed the presence of some GQDs with a crystalline elongated structure. We hypothesized that these structures may have originated from the joining of the GQDs upon laser treatment. In Figure 23c, joined GQDs have been highlighted with a yellow circle. Recently, the joining of graphene sheets under ultrafast laser irradiation has been demonstrated based on molecular dynamics simulations [206]. The study demonstrated that the dynamic thermal expansion and the dynamic fluctuation out of the plane provided the "driving power" for the possible joining process of the graphene sheets side-by side or out-of-plane, respectively [206]. The authors stated that in order to realize a joint between two graphene sheets, the presence of dangling bonds is necessary at the edges of the sheets. Based on this study, it was hypothesized that with 60 minutes of laser ablation, some GQDs might possess the right position relative to each other to be joined together. While the joining of graphene sheets has been reported either theoretically or experimentally using a CO_2 laser [207], no evidence of joints between GQDs has been demonstrated so far. However, more investigations are needed to determine the possibility of joining of GQDs at longer ablation times.

In order to separate the GQDs from the reduced GO sheets in which they are embedded, we dialysed the laser treated dispersions. The HRTEM image of the dispersion obtained after 30 minutes of laser treatment after dialysis is shown in Figure 24. For TEM analysis, drops of the dispersion were deposited onto holey carbon copper grids. GQDs were successfully separated by the reduced graphene sheets and the d-spacing was 0.21 nm.

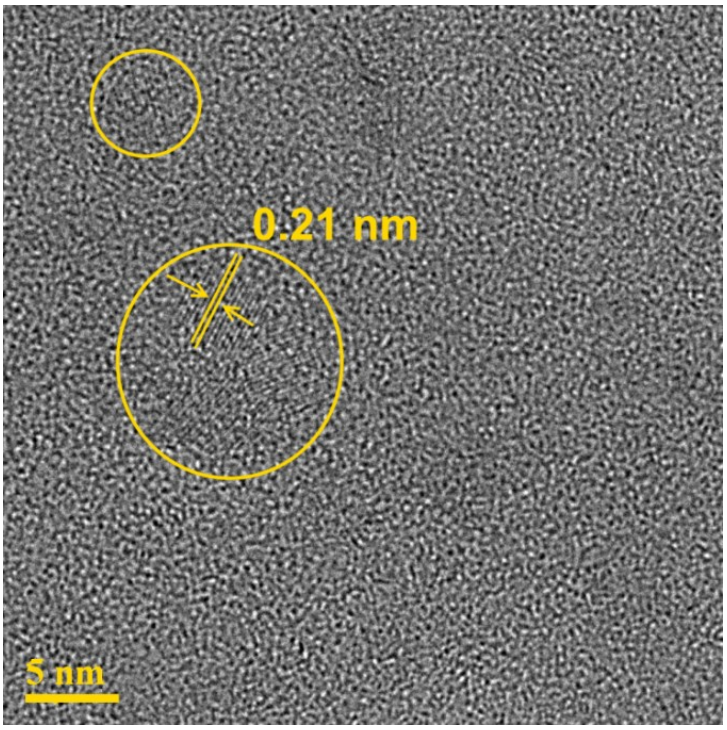

Figure 24: HRTEM image of dialysed GQDs dispersion obtained after 30 minutes of laser ablation. Reproduced from ref. [202] by permission of The Royal Society of Chemistry

4.3.2. Mechanism of GQDs formation on femtosecond laser ablated GO

The mechanism for the formation of the GQDs can be ascribed to a combination of effects induced directly and indirectly by the fs laser ablation process. Of note is that water is not completely transparent to laser irradiation and, especially when shorter laser pulses are used, a part of energy is absorbed by water [208]. The energy of the laser is absorbed by electrons and then transferred to the water molecules [209]. The time scale of the energy transfer from electrons to atoms is around one order of magnitude larger than the duration of the fs laser pulse [209–211]. Consequently, in fs laser, electronic and atomic temperatures are not in equilibrium with each other. This phenomenon can be simulated by two temperature model (described in Section 4.2.4) in which, the heat transfer equations are used to express the electronic and atomic temperature as a function of time, position, initial temperature and heat input to the system [212–214]. Equations 1 and 2 were simultaneously solved by finite element method to find time evolution of the electronic and atomic temperatures. Figure 25a demonstrates the electronic (solid line) and atomic temperature (dashed line) changes during and after an initial laser pulse, simulated using an absorption efficiency of 20%.

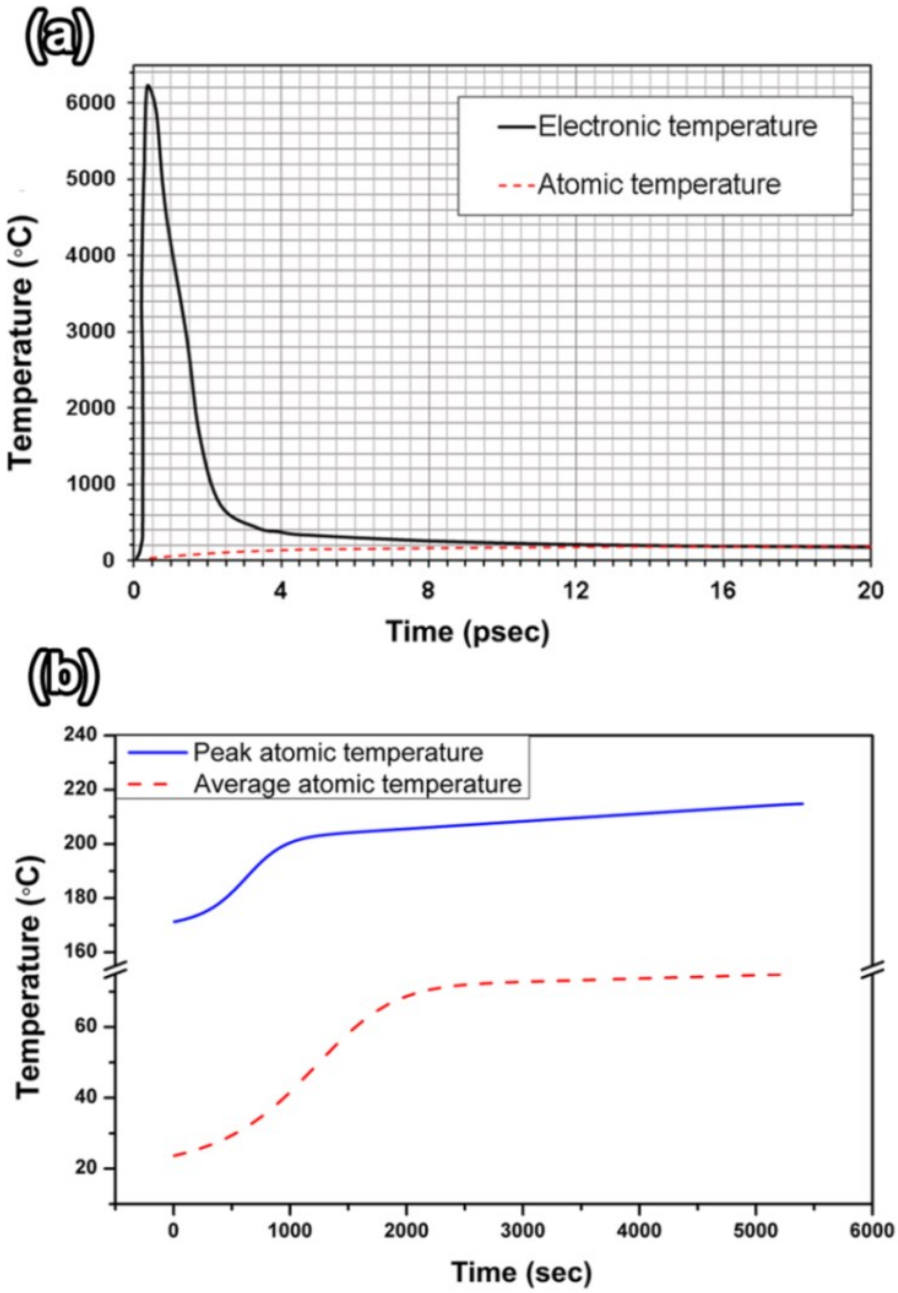

Figure 25: a) Electronic (solid line) and atomic temperature (dashed line) change during and after a 35 fs sec laser pulse; (b) peak atomic temperature (solid line) and average atomic temperature change for a 90 minute fs sec laser irradiation simulation. Reproduced from ref. [202] by permission of The Royal Society of Chemistry

During one fs pulse, the electronic temperature will increase rapidly above 6000°C and start to decrease immediately after the pulse, while the atomic temperature will increase to 177°C. After 15 ps, the electronic and atomic temperatures become equal and the system is in equilibrium as shown in Figure 25a. When the system reaches this equilibrium condition, conventional heat transfer takes place and the temperature distribution can be found by solving a conduction heat

transfer problem [215]. To find the overall temperature of the system over a long irradiation time, in this case 90 minutes, a multiscale heat transfer simulation was designed. In the simulation, the temperature profile of the meshes, which were irradiated by the laser, was simulated by a two-temperature model for 15ps followed by a conduction heat transfer up to 1ms. Afterwards, a temperature profile was obtained from the central meshes of the simulation domain, the section irradiated by laser; this temperature profile was then applied to the system to find the temperature evolution for a larger time scale (90 minutes). The electronic heat transfer coefficient k_e was calculated at each time step; for changes greater than 10%, the proposed temperature profile was recalculated for every 1 ms. Figure 25b displays the peak temperature (solid line) of the central mesh and the average temperature (dash line) of the irradiated meshes of the simulation domain. During the entire duration of fs laser ablation, 60 minutes in our experiments, the peak atomic temperature reached was around 210°C (Figure 25b). During the laser pulse irradiation (Figure 25a) the electronic temperature of the system increases due to the higher kinetic energy of the electrons and can be excited to higher energy states. This excitation may lead to the breakdown of the chemical bonds in water leading to the generation of the reactive species, such as H•, O• and HO• radicals, as shown in Equation 5 [198,216].

$$6H_2O \xrightarrow{Femtosecond\ laser} 8H^{\blacksquare} + 2O^{\blacksquare} + 4HO^{\blacksquare} \quad (5)$$

$$6H_2O \xrightarrow{Femtosecond\ laser} 4H_2 + O_2 + 2H_2O_2 \quad (6)$$

The recombination of these radicals leads to the formation of H_2, O_2 and H_2O_2 (Equation 6) and heat energy, which will increase the peak atomic temperature to approximately 200°C, initiating the processes responsible for the synthesis of GQDs. These processes include: 1) the oxidation of sp^2 carbon atoms to sp^3 carbon atoms due to the presence of H_2O_2 (Equation 6); 2) the O_2(g), formed by photo-dissociation reactions induced by fs ablation (Equation 6), react with the sp^3 carbon atoms of GO sheets, in a way similar to the coal gasification of solid carbon; and 3) the reduction and fragmentation of GO sheets due to the removal of carbon atoms as CO_2(g) and CO(g), as demonstrated in our previous work [198]. These three steps for the formation of the GQDs can be summarized with the following schematic.

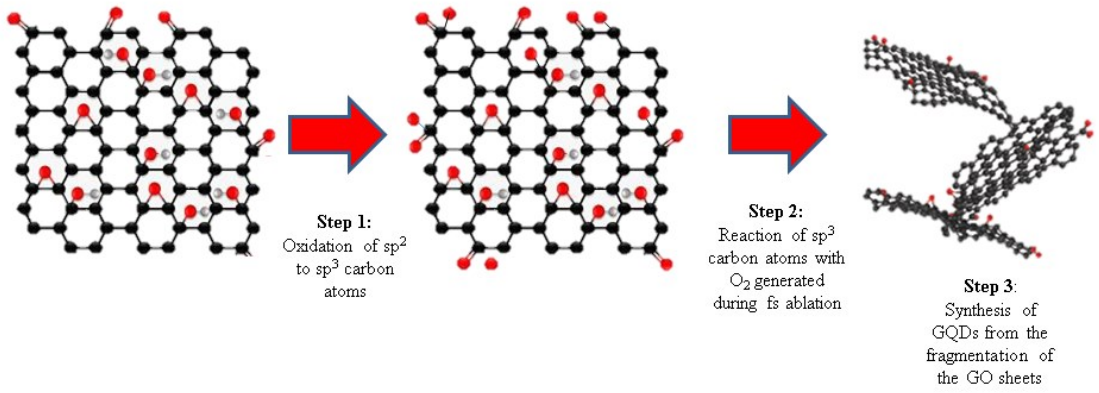

Figure 26: Schematic for the formation of the GQDs. In the first step the sp^2 carbon atoms are oxidized to sp^3 by the H_2O_2 formed during the water breakdown induced by fs ablation; in the second step the sp^3 carbon atoms are converted to CO_2 upon reaction with O_2 generated by fs ablation. In the final step the reduction and fragmentation of the GO sheets due to the formation of CO_2 lead to the synthesis of GQDs

The water breakdown which generates O_2 or H_2O_2 and the peak atomic temperature reached during the laser ablation are responsible for the synthesis of the GQDs, through a mechanism similar to the hydrothermal cutting of GO sheets [55,217], which does not involve the use of strong oxidizers. Consequently, we succeeded in the optimization of the laser ablation of graphene oxide dispersions as top-down approach for the solely synthesis of GQDs.

In order to investigate the chemical composition of the dispersions at different ablation time, XPS analysis of the samples was performed before and after the laser treatment. The results are presented in Figure 27.

Figure 27a shows the XPS spectrum of the untreated GO dispersion, where the C1s peak has been fitted to four components which are located at 284.50 eV, attributed to the fraction of sp^2 carbon atoms (C=C); 286.60 eV and 285.67 eV to (C-O-C) and (C-OH) groups, respectively; and 288.30 eV ascribed to (O-C=O) groups [41,218,219]. The composition of the XPS spectra contained 62.83% of C1s and 37.17 % of O1s. From the comparison of the XPS spectra obtained analysing the dispersion at increasing laser ablation time from 5 min (Figure 27b) up to 60 min (Figure 27e), it is evident that the reduction of the GO dispersion is occurring during the laser ablation process. This result was consistent with the *d* spacing of 0.21 nm, typical of graphene monolayer, obtained from TEM analysis (Figure 20 and Figure 22b).

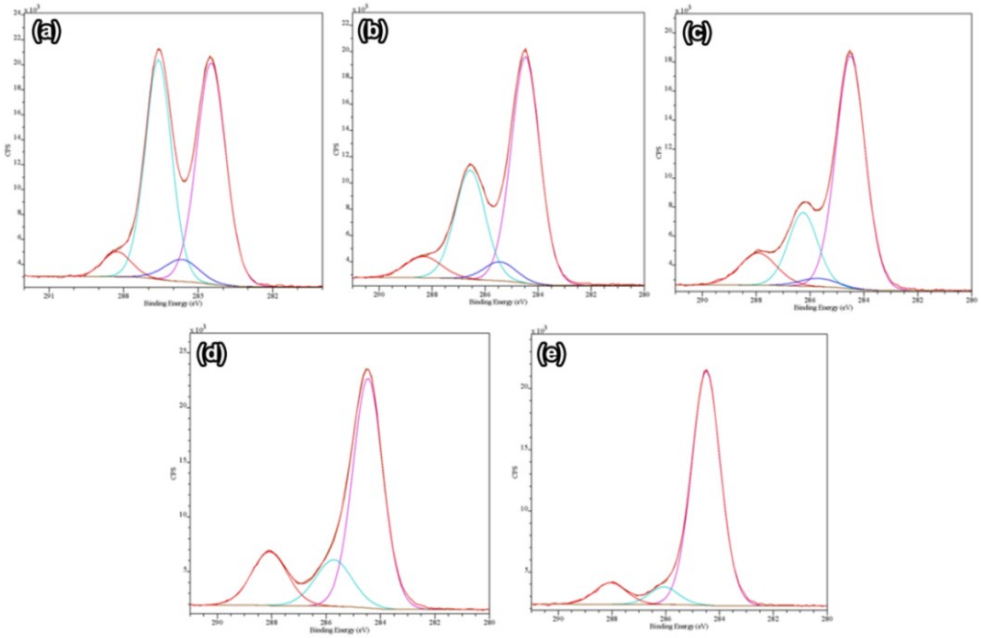

Figure 27: XPS of GO solution before (a) and after PLA at 1.3W for (b) 5, (c) 15, (d) 30 and (e) 60 minutes respectively. Reproduced from ref. [202] by permission of The Royal Society of Chemistry

The deconvolutions of the XPS spectra, summarized in Table 3, showed that the percentage of the sp^2 carbon atoms fraction (peak at 284.50 eV) increased from 47.03% up to 84.70% after 60 minutes of ablation due to the restoring of the aromatic graphene structure as a consequence of the reduction of the GO sheets induced by the laser ablation process.

Table 3: Chemical composition of the dispersions before and after the laser treatment calculated from the deconvolutions of the relative XPS spectra. Reproduced from ref. [202] by permission of The Royal Society of Chemistry

		After Laser Ablation (min)			
	GO	**5**	**15**	**30**	**60**
C=C (%)	47.03	58.04	65.12	65.57	84.70
C-OH (%)	5.57	5.49	2.93	16.32	6.49
C-O-C (%)	42.19	29.58	20.63	//	//
(C=O)-OH (%)	5.21	6.89	11.32	18.11	8.81

However, together with an increase of C=C percentage there was a slight increase of the percentage of hydroxyl groups and (C=O)-OH groups, peaks at 285.37 eV and 288.30 eV, respectively. We hypothesized that these groups were due to residual oxygen-containing groups

of the GO sheets and they were bonded to the edges of the GQDs making the GQDs dispersible in water.

4.3.3. GO dispersion defect density as a function of laser ablation time

The Raman spectra of GO dispersions before and after the laser ablation are shown in Figure 28. The most prominent features in graphene-based materials are the D peak at 1328 cm^{-1} and the G band at 1598 cm^{-1}. The peak intensity ratio, I_D/I_G, is commonly used for the characterization of disorder in carbon-based materials. Here, it was found that the I_D/I_G ratio increased from 1.43 of GO up to 1.53 after 15 minutes of laser ablation of the GO dispersions. This behaviour is usually attributed to the decrease in size of the graphitic domains together with an increase in the number of sp^2 domains [220], and is indicative of a "low" defect regime. The increase of sp^2 was confirmed by the XPS analysis, as described previously. After 15 minutes of laser ablation the percentage of sp^2 carbon atoms increased from 47.03% to 65.12% (Table 3) because of the reduction of GO sheets and the formation of the GQDs upon laser treatment.

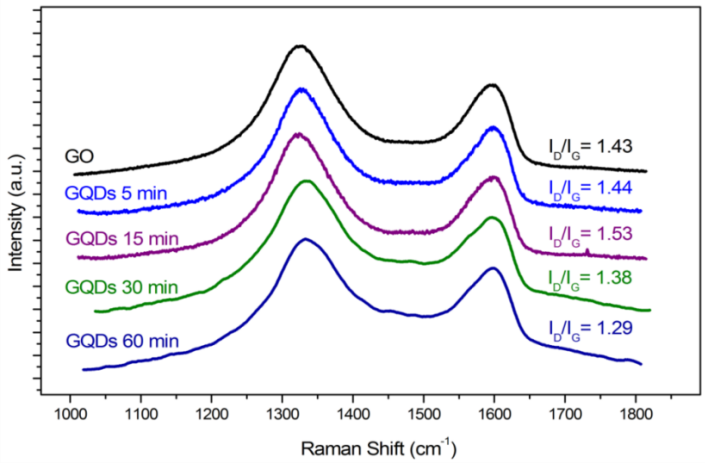

Figure 28: Raman spectra of GO dispersion before (black spectrum) and after 5 minutes (light blue line), 15 minutes (purple line), 30 minutes (green line), and 60 minutes (dark blue line) of laser ablation. Reproduced from ref. [202] by permission of The Royal Society of Chemistry

However, after 30 minutes of laser ablation the intensity ratio I_D/I_G decreased to 1.38 and reaches the value of 1.29 after 60 minutes of laser treatment. This regime is indicated as "high" defect density regime, in which the intensity ratio I_D/I_G starts to decrease on increasing the defect density [221,222]. Recently, Kim and coworkers [223] reported that the Raman-scattering in GQDs was a function of their sizes. It was shown, that for GQDs with an average size of 5 nm the value of I_D/I_G was 1.3, which is in good agreement with the 3.6 nm average size detected in

the samples obtained after 60 minutes of laser treatment. It was also observed a blue shift of the G peak increasing the laser ablation time. It has been demonstrated by Kim [224], that a shift of the G peak at higher wavenumber can be interrelated to an increase of the GQDs diameters. From the size distribution analysis shown in Figure 21, an increase of the GQDs diameters occurs increasing the laser ablation time, which explains the shift of the G peak observed in the Raman spectra displayed in Figure 28.

4.3.4. GQDs nanostructure dependence on laser type and frequency

Recently, T.N. Lin and coworkers [199] reported the synthesis of different nanostructures by laser ablation of GO dispersions. Similarly to our results, T.N. Lin observed a reduction of the GO with the laser ablation time, while we observed the formation of GQDs and the reduction of the GO. It should be noted that Lin and coworkers used a nanosecond laser with a wavelength of 415 nm, while an fs laser (λ=800nm) was used in our work. As mentioned previously, due to the different physical ablation mechanisms induced by nanosecond laser and femtosecond laser it is possible to produce different nanomaterials employing the same starting material. In particular, as discussed in Section 4.3.2, upon fs laser ablation the water breakdown occurs which generate H_2, O_2 and H_2O_2, which lead to the fragmentation of the GO sheets, i.e. synthesis of the GQDs. The water breakdown does not occur upon ns laser ablation, and this might be the reason why GQDs are obtained using the fs laser. The laser pulse duration plays a key role in the synthesis of the GQDs. The reduction of the GO occurred either with the ns laser or the fs laser; therefore it is independent from the laser pulse duration and laser wavelength. The novelty of this work consists in the demonstration that, GQDs can be produced by femtosecond laser ablation of GO and their synthesis can be attributed to the different pulse duration.

4.3.5. Effect of high laser power (2.4 W) on the morphology of GO dispersions

In this study, we demonstrated that with a proper control of ablation time it is possible to obtain high quality GQDs in a green and single-step process. However, the laser ablation power should also be considered. In order to study the effects of the laser power, we performed the experiments at higher (2.4W) power maintaining the same ablation time (*i.e.* 5, 15, 30 and 60

minutes). In Figure 29, TEM images of the dispersions obtained after 5 (a), 15 ($b_{1,2}$), 30 ($c_{1,2}$) and 60 ($d_{1,2}$) minutes of ablation at 2.4W, are displayed.

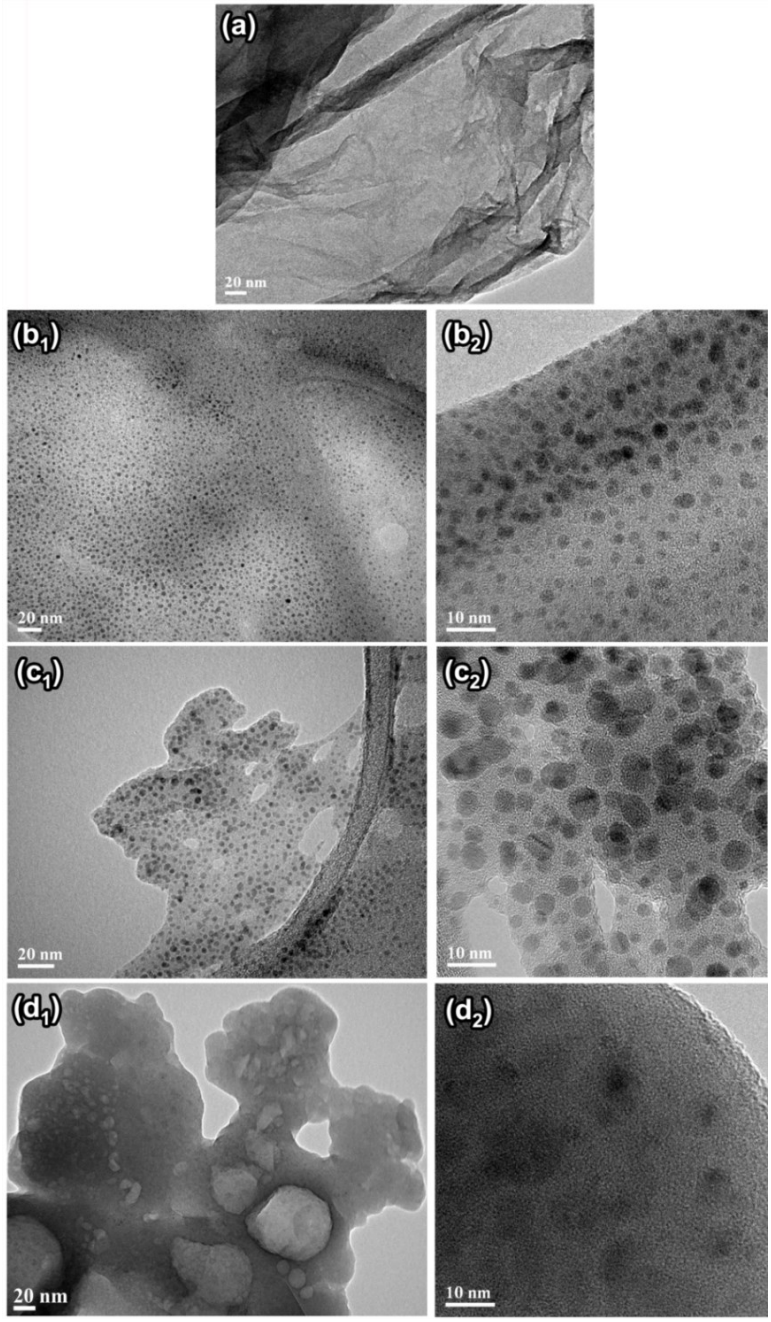

Figure 29: TEM images of dispersions obtained performing PLA at 2.4 W for 5 (a), 15 ($b_{1,2}$), 30 ($c_{1,2}$), and 60 ($d_{1,2}$) minutes. Reproduced from ref. [202] by permission of The Royal Society of Chemistry

It was observed that at higher power, in the same way as the experiment performed at 1.3W, 5 minutes of laser ablation were not enough to induce strong modifications of the sheets. However, a different behaviour was found for the dispersions ablated for longer time. In particular, as

shown in Figure 29b_1-b_2, after 15 minutes of PLA many GQDs were found. In Figure 30b, the size distribution of the GQDs after 15 minutes of laser ablation is shown. The average size of the GQDs obtained was 2.3± 0.6 nm, which was larger than the average size of GQDs obtained after 15 minutes of PLA at lower power.

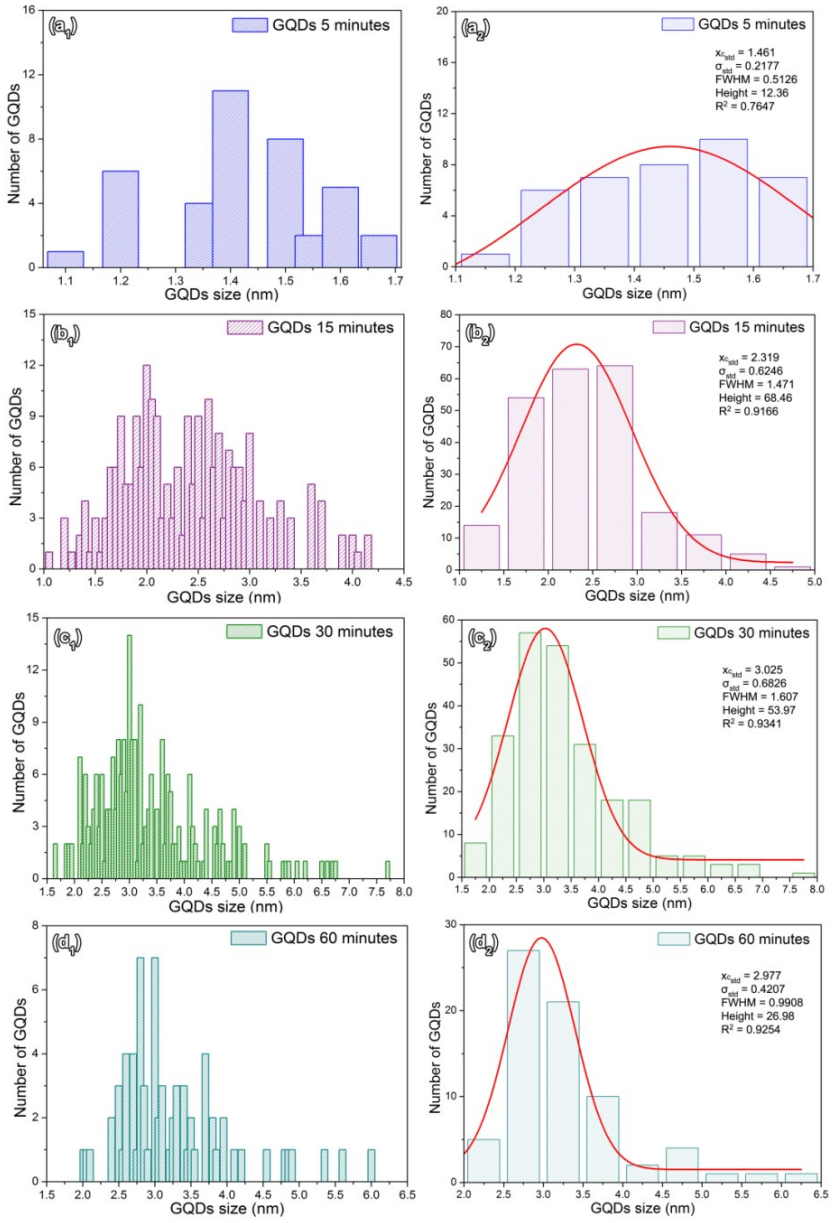

Figure 30: (1) Raw and (2) binned size distribution Size distribution of the GQDs obtained at 2.4W after (a) 5, (b) 15, (c) 30, and (d) 60 minutes of laser ablation. Reproduced from ref. [202] by permission of The Royal Society of Chemistry

The dispersion ablated for 30 minutes showed an increase of size of the particles up to 3.0 ± 0.7 nm (Figure 30b). A further increase of the ablation time up to 60 minutes resulted in the formation of a second type of nanostructure together with GQDs. Noteworthy, the average size of GQDs synthesized after 60 minutes was found to be 3.0 ± 0.4, which has less variance than GQDs obtained after 30 min of laser ablation. A trend of the average GQDs' size as function of laser power is shown in n Figure 31. At a lower ablation power (1.3W) the average size increases slowly with the ablation power and for higher laser ablation power (2.4W) the GQDs' size rapidly increases after 15 minutes of PLA reaching a value of 3.0 ± 0.7 nm after 30 minutes. The resulting GQDs had a larger mean size and lower variance than the one synthesized at the same ablation time but at lower power (2.1 ± 1.9 nm). After 1 hour of ablation at 2.4 W the average size did not change, staying at 3.0 ± 0.4 nm. Generally, the GQDs size distribution increased as the laser ablation time increased at both laser powers until 30 minutes of ablation. The GQDs size distribution lowered at an ablation time of 60 min due to formation of other nanostructures.

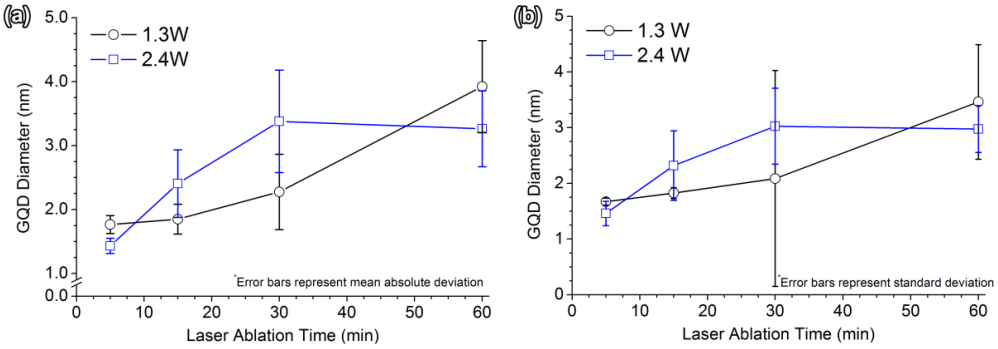

Figure 31: GQDs diameter as a function of the laser ablation time at different laser ablation powers using (a) absolute values and (b) Gaussian fit values from binned size distribution. Reproduced from ref. [202] by permission of The Royal Society of Chemistry

After 60 minutes of laser ablation at 2.4W, tubular nanostructures were detected; they were analyzed by SEM and TEM and the results are displayed in Figure 32a-b, respectively. The HRTEM image (inset of Figure 32b) showed that the tubular structures were made of an assembly of sheets that contained some GQDs. The formation of these structures is not quite clear and further investigation needs to be conducted on these systems.

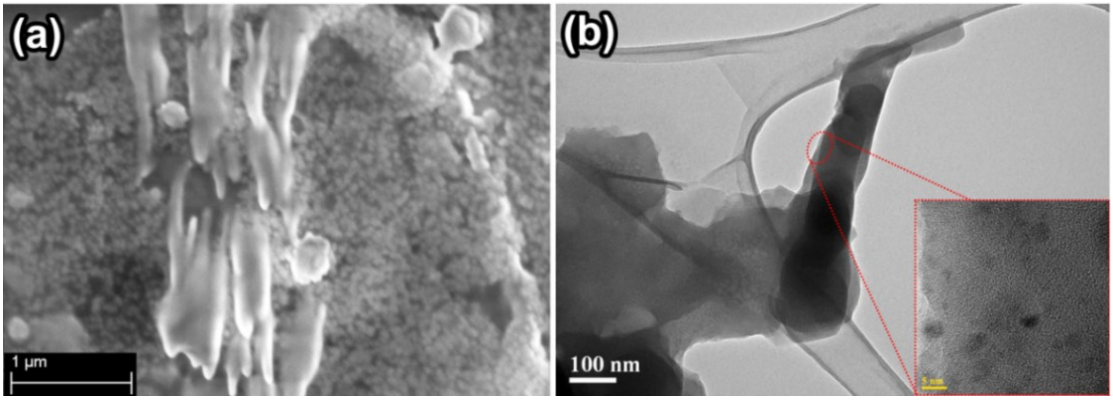

Figure 32: a) SEM image of the solution after 60 minutes of ablation at 2.4W. Some tubular structures are observable within the damaged sheets; b) TEM and HRTEM (inset) images of the tubular structures. These structures are made up of folded sheets where some GQDs are found to be embedded in. Reproduced from ref. [202] by permission of The Royal Society of Chemistry

The shape of these materials was similar to the ones reported by Lin and coworkers [199], after nanosecond irradiation of GO dispersion. The authors described those materials as irregular GO sheets; however, no explanation for their formation has been given yet.

4.3.6. Photoluminescence of femtosecond laser processed GO dispersions

One of the most intriguing properties of GQDs is their luminescence. Many studies have demonstrated that GQDs photoluminescence (PL) depends on many parameters, including size, shape, and surface states [58,225–227]. As a consequence, the PL behaviour of GQDs can be tuned and these nanomaterials can show blue and green PL [189]. In Figure 33, PL spectra of the GQDs dispersion obtained after 30 minutes of ablation at 1.3W are displayed. The PL behaviour is excitation-dependent [227], and a strong peak at 410 nm (blue emission) was obtained employing an excitation wavelength of 300 nm. It was found that the emission wavelength of these GQDs was lower than the one reported by other groups [228],[229].

According to the quantum confinement effect (QCE) of conjugated π-domains in GQDs, when the size of sp^2 domains gets smaller, there is a blue shift of the PL energies [225].

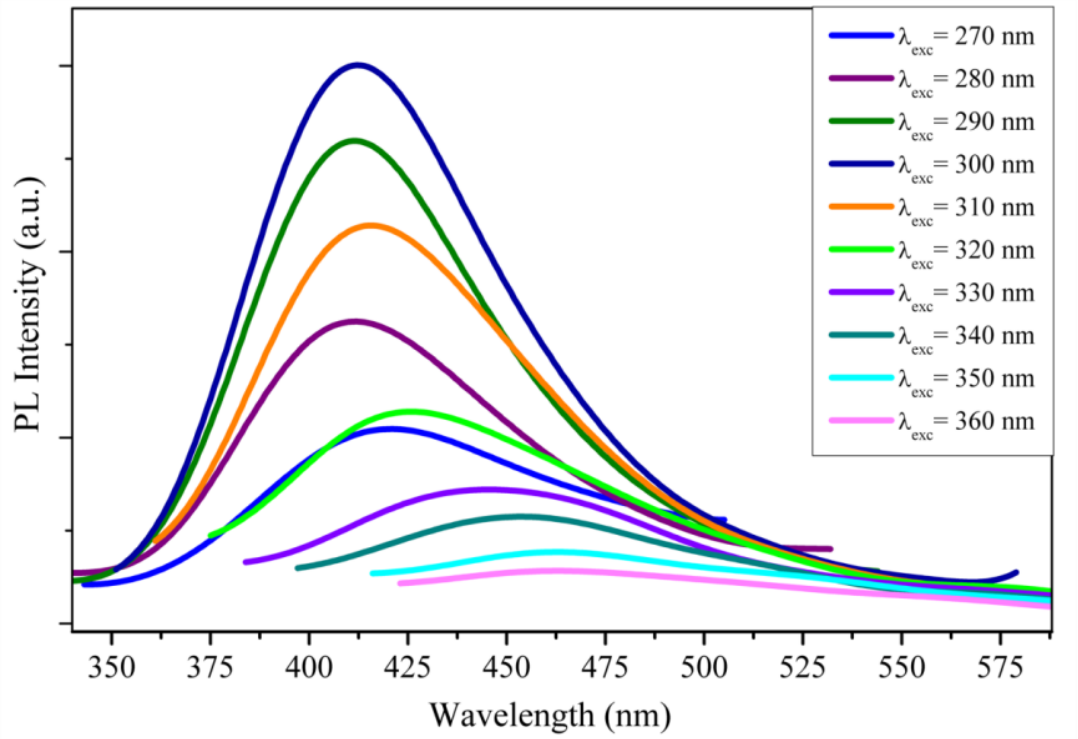

Figure 33: PL spectra of GQDs dispersion obtained after 30 minutes of laser ablation of GO sheets. The GQDs showed a strong emission peak at 410nm with an excitation wavelength of 300 nm. Reproduced from ref. [202] by permission of The Royal Society of Chemistry

Since the dimensions of the GQDs we synthesized at different laser ablation time range between 1.5 nm and 4 nm in size, we hypothesized that this might be the reason for the emission at 410 nm. The dispersions obtained after 5, 15 and 60 minutes of ablation, showed a strong emission peak at ~410 nm with an excitation wavelength of 300 nm, however the only difference was the PL intensity of the emission peak. In particular, the emission peak of the dispersion obtained after 5 min of laser ablation was found to be more intense than that of the other dispersions. This is due to the fact that, after 5 min of laser ablation, the GO sheets undergo reduction leading to the removal of oxygen containing groups and formation of new sp^2 islands as reported in Table 3. The percentage of the sp^2 carbon atoms fraction (peak at 284.5 eV) increased from 47.03% up to 58.04%. Moreover, it was reported that a relative intensity increase of the emission peak could be attributed to the intrinsic PL of graphene fragments [230], confirming that a reduction of GO sheets is occurring in the first 5 minutes of laser ablation. There was a decrease in the intensity of the PL peak upon further laser ablation. It has been reported that the π–π stacking between graphene and GQDs can lead to the luminescence quenching of GQDs by graphene [231]. Upon increasing the laser ablation time, a reduction of the GO sheets takes place and the percentage of

the sp^2 carbon atoms fraction increased from 47.03% up to 84.70% as shown in Table 3. The GQDs were embedded in reduced graphene sheets (Figure 22) and it was hypothesized that the decrease of PL intensity may be due to the π–π stacking between graphene and GQDs as the ablation time was increased. The PL spectra obtained at 300 nm excitation wavelength of the GQDs dispersion at different ablation time is displayed in Figure 34.

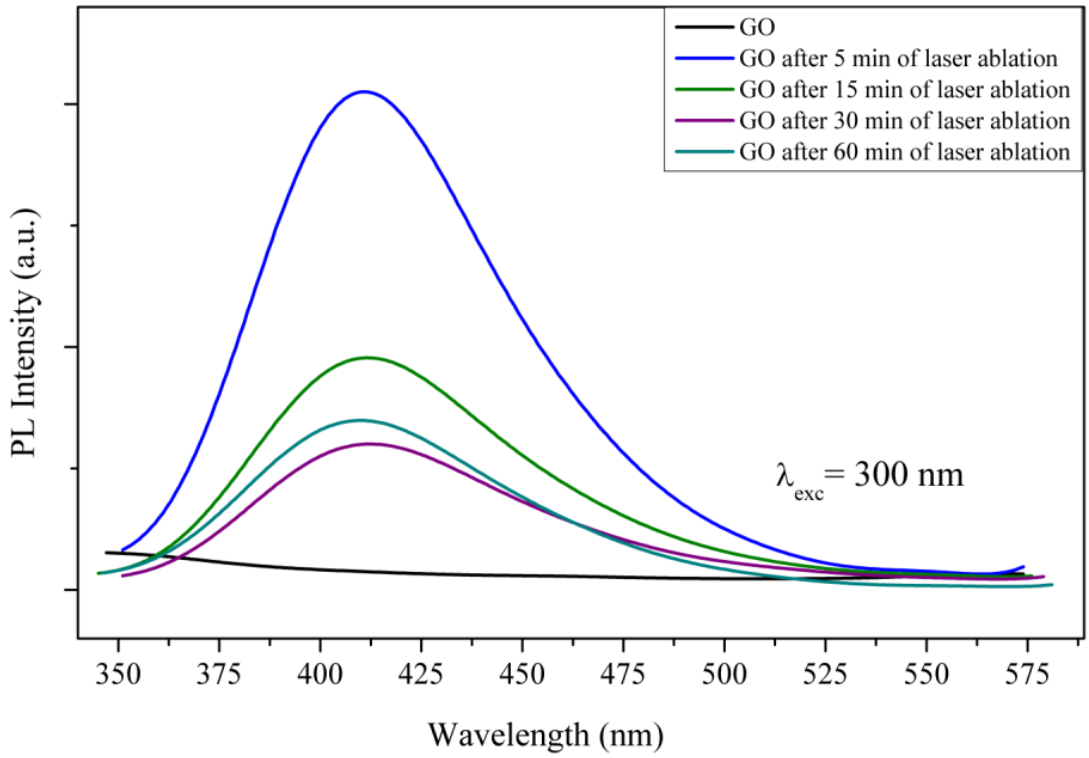

Figure 34: PL spectra of GQDs solutions obtained after 5, 15, 30 and 60 minutes of laser ablation of GO. The PL spectra were recorded at an excitation wavelength of 300 nm. The laser treated solutions showed blue luminescence at 410 nm, while the starting GO did not show any luminescence. Reproduced from ref. [202] by permission of The Royal Society of Chemistry

We investigated the optical efficiency of the GQDs obtained at 1.3W at different laser ablation time, measuring the quantum yield efficiency (QY) of the dialyzed dispersions. For the QY measurements, anthracene in ethanol was used as reference (QY 30%). The QY calculated for the dialysed dispersion obtained after 30 minutes of laser ablation is 2.10%. It is widely known that the quantum yield of GQDs is affected by different factors, such as size, fabrication method, doping, surface chemistry [47,232,233], however a value of QY of 2% was reported for unpassivated GQDs [234]. Consequently, the QY of 2.10% we calculated for the GQDs obtained after 30 minutes may be ascribed to the novel fabrication method and to the unpassivation of the

synthesized GQDs. An image of the dispersion's luminescence obtained after 30 minutes of ablation at 1.3W after dialysis compared with pure water, is shown in Figure 35.

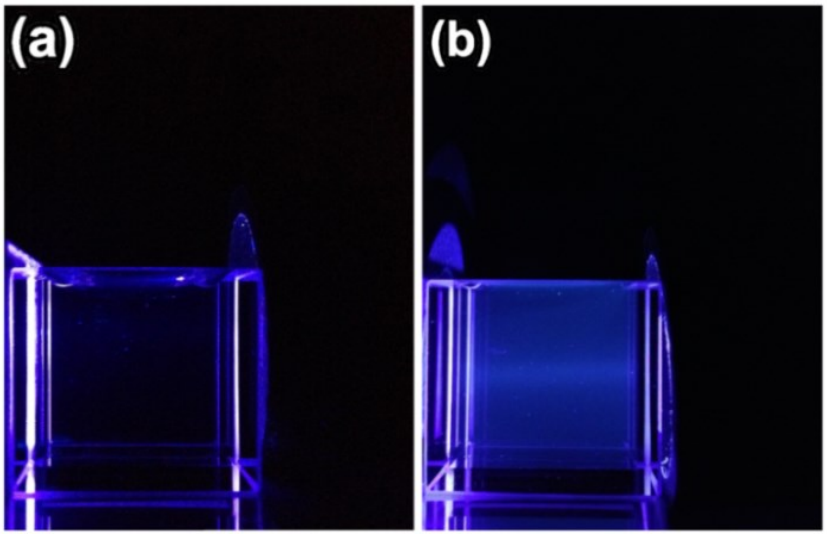

Figure 35: Photographs of (a) water and (b) dialysed GQDs dispersion obtained after 30 minutes of laser ablation at 1.3W under 365 nm UV light Reproduced from ref. [202] by permission of The Royal Society of Chemistry

4.3.7. Application: Conductive ink using GQDs in GO dispersion

In order to investigate the performance of the unpurified femtosecond laser synthesized GQDs from the initial GO dispersion as candidate materials for electronic applications, a hybrid ink of GQDs and silver nanoparticles (GQDs@AgNP ink) was developed to be compatible with an aerosol-jet printing system. In particular, an AgNPs solution was mixed with GQDs dispersion obtained after 30 min of laser oblation, without any further purification, in a volume ratio of 1:3. Details on the aerosol-jet printing system have been already reported in previous publications of the authors [235,236]. After printing the patterns with 4 deposition layers, the samples were left in the oven at temperatures of 180°C for 30 min in order to sinter the AgNPs and remove all the solvents from the ink. The resistivity of the printed GQDs@AgNP patterns was calculated using the resistance and thickness of the printed patterns measured by a two-probe station and an AFM, respectively. For comparison, we calculated the resistivity of the AgNPs printed patterns, which were prepared with the same procedure employed for the hybrid ink, *i.e*. 4 deposition layers. The results obtained are listed in Table 4, while the optical and SEM images of the AgNP and GQDs@AgNP printed patterns are shown in Figure 36.

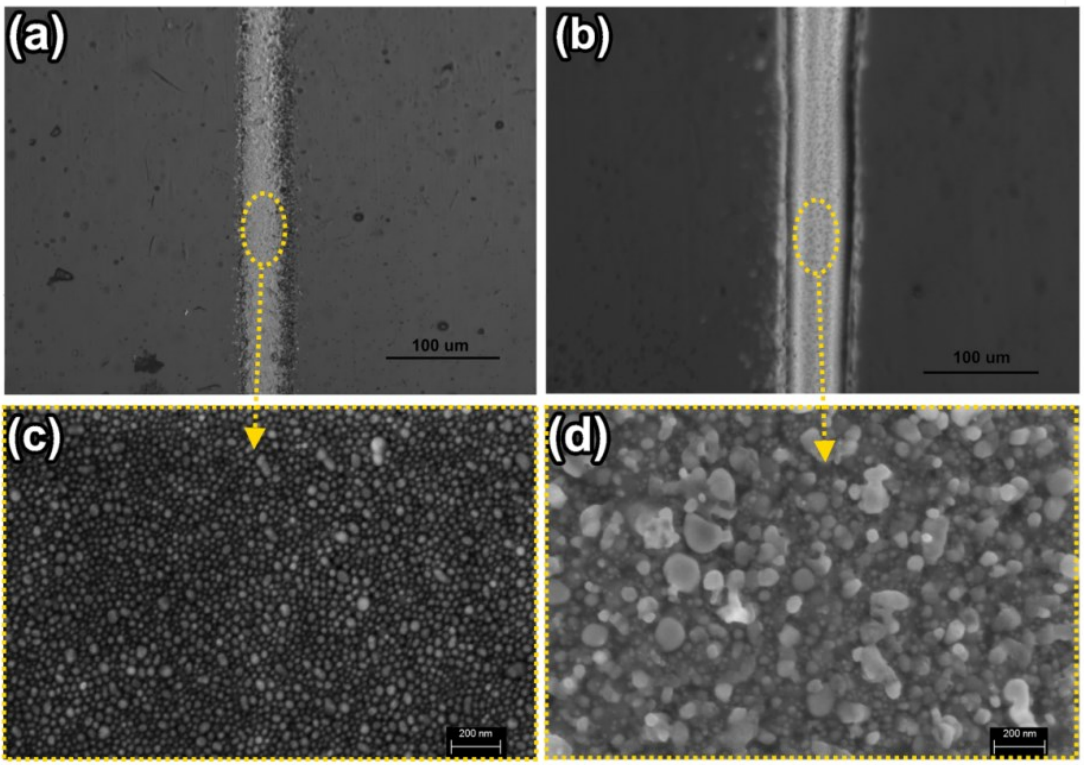

Figure 36: Optical image of (a) AgNPs printed patterns and (b) GQDs@AgNP printed patterns; (c) and (d) SEM images of AgNPs and GQDs@AgNP patterns, respectively. Reproduced from ref. [202] by permission of The Royal Society of Chemistry

The results indicate that the calculated resistivity of the GQDs@AgNP patterns is two times less than the resistivity of the AgNP patterns. Moreover, it shows that the GQDs, as the connectors between the AgNPs, can improve the movement of the electrons [14]. The calculated resistivity of the composite pattern is two orders of magnitude of that of printed graphene sheets from work published elsewhere by E. Jabari [237,238]. The graphene sheets have higher resistivity due to contact resistance between graphene sheets that are aggregated causing increased number of edges and random joints. Recently, Meschi and co-workers demonstrated that the use of graphene as filler in electrically conductive adhesive (ECA) decreased the percolation threshold of silver content from 40 wt% to 10%, improving the electrical conductivity of ECA [11].

Table 4: Electrical properties of the aerosol-jet printed patterns from different inks. Reproduced from ref. [202] by permission of The Royal Society of Chemistry

Inks	Mean resistivity of the printed patterns (Ω.cm)	*Reference*
AgNP	$(3.14 \pm 0.15) \times 10^{-4}$	**This work**
GQDs@AgNP	$(1.53 \pm 0.23) \times 10^{-4}$	This work
Graphene	$(2.25 \pm 0.23) \times 10^{-2}$	[237,238]

Therefore, for the first time we demonstrated that adding the as-prepared laser-ablated dispersion of GQDs to AgNP ink could either increase the conductivity of the AgNPs inks or decrease their cost by reducing the required concentration of the AgNPs in the ink.

4.4. Summary

In this chapter, we have reported the development of a straightforward, eco-friendly and time-effective process for the synthesis of GQDs by fs laser ablation of GO dispersions. Compared to the other synthetic methods of GQDs (strong acid-assisted cleavage of carbon nanomaterials [189] or derived from the photo-Fenton reaction of GO [57]), our process is environmentally friendly, since the synthesis is performed in water without the use of any chemicals. Furthermore, the ablation process is not time consuming, namely the production of GQDs is achieved in a single-step within a time window ranging from 15 to 60 minutes, depending on the laser parameters employed. It has been demonstrated that with a control over the ablation time and laser power is possible to modify the structure of these graphene-based nanomaterials. In particular, through the study of the relationship between these two key parameters and the structure of the GQDs, it has been found that nanomaterials with different size and nanostructure could be obtained. The laser synthesized GQDs possess a blue luminesce and the calculated QY of 2% is similar to the one reported for the unpassivated GQDs. Moreover, for the first time we demonstrated that the GQDs synthesised by femtosecond laser ablation of GO can be employed for the fabrication of a hybrid conductive ink. The developing of more cost effective inks is nowadays in the focus of many research groups and the preliminary results reported in this study

revealed that the resistivity of the hybrid ink (GQDs@AgNPs) patterns resulted to be two times lower than the resistivity of the pure AgNP printed patterns. We can conclude that the advantages of the method presented here, are the possibility of synthesizing and modifying GQDs in a straightforward and green route, and that the dispersion of GQDs, mixed without any further purification, with silver nanoparticles can be employed as conductive ink. In particular, the resistivity measurements showed that the addition of the laser synthesised water-based GQDs dispersion to AgNPs ink can result in cheaper or more conductive printable inks.

Chapter 5. Phase Transformation of TiO_2 Nanoparticles by Femtosecond Laser Ablation in Aqueous Solutions and Deposition on Conductive Substrates[139]

Overview

In this chapter, we will discuss the femtosecond laser ablation of titanium dioxide nanoparticles. The focus of this study is to demonstrate that laser ablation is a versatile technique for the synthesis and modification of different materials. In particular, besides the synthesis of graphene quantum dots (**Chapter 4**), laser ablation can be used for the phase engineering of TiO_2 nanoparticles with a proper control over the laser parameters. Moreover, it is observed that laser ablation time is a key parameter allowing the bandgap engineering of TiO_2 nanoparticles, since it was found that upon increase of the ablation time of the TiO_2 dispersion in water a bandgap widening occurred.

5.1. Introduction

The pulsed laser ablation in liquids has been widely employed in the ablation of titanium targets for the synthesis of TiO_2 nanomaterials with different shape, size and phases [239–245] depending on the laser parameters employed such as the laser wavelength [175,242,246], laser pulse energy [243,245,247,248] and the type of liquid medium employed [147,240,242,249]. Titanium dioxide has been extensively researched for its photocatalytic properties and applications. In 1972, Fujishima and Honda reported the splitting of water under illumination using a rutile TiO_2 photoanode and Pt counter electrode [250]. Since then, due to its chemical stability, low cost, and non-toxicity, TiO_2 has been used in a wide range of applications such as removing conventional and emerging organic contaminants in water [16,251], photocatalytic [134,252–256] processes, sensor devices [135,257], and solar cells [17,258]. In Section 2.5.1, we described the three crystalline polymorphs being rutile, anatase and brookite.

Under ambient conditions, rutile is the most stable crystal phase in bulk, while the other two polymorphs are considered as metastable phases, and upon heating an irreversible phase transformation to rutile occurs [259]. Several studies demonstrated that the particle sizes play a key role in the determination of phase stability [138,260]. For particle sizes less than 11 nm, anatase will be the most thermodynamically stable phase, while for dimensions between 11-35

nm, brookite is the most stable phase. When the sizes are greater than 35 nm, rutile is the most stable phase [138]. In Section 2.6 we described that anatase nanoparticles may be obtained using several processes, which include sol-gel [28], hydrothermal [29] and solvothermal [30] methods. Heat treatment of these nanoparticles will produce rutile nanoparticles at a specific phase transformation temperature.

The possibility to control the conditions that affect the phase transformation is important. The phase stability of titania has a key role in the design of electronic devices because the properties and the performance of these materials may be affected [261,262] by the alteration of the crystalline phase [261,263]. It is commonly believed that the reason for the phase transformation from anatase to rutile should be attributed to the increase in the particle size induced by the sintering process that takes place at elevated temperatures [260]. However, more studies should be done in order to better understand the physical and chemical processes involved in the phase transformation, as well as the mechanisms to promote or inhibit it [264–267].

In this work we studied the phase-transformation of a dispersion of TiO_2 (P25, AerodixdeTM) induced by femtosecond laser ablation under two conditions: (i) in aqueous solution and (ii) deposited on fluoride-doped tin oxide (FTO) substrate. To the best of our knowledge, few studies have been performed on the effects of the femtosecond laser ablation of a dispersion of TiO_2 in water. For instance, in a recent report it was studied the ablation of rutile powder in water with a femtosecond laser [268] which led to the formation of rutile, anatase and brookite nanoparticles [268]. It has been also reported the laser ablation of TiO_2 powders with a YAG:Nd3+ solid state laser [269], where the powders were deposited onto a glass substrate and then laser ablated in air. In the study presented here, we report on the phase-transformation of TiO_2 nanoparticles by femtosecond ablation of P25 either as a suspension or deposited by electrophoretic deposition on FTO glass. The results of the experiments carried out showed that the laser ablation process of the P25 suspension in water induces the phase transformation from anatase to rutile and back again to anatase increasing the ablation time. Moreover, the bandgap of the material can be controlled, leading to the possibility of employing PLA of TiO_2 for bandgap engineering. Ablation of the deposited P25 on FTO resulted in transformation from anatase to rutile phase of the patterned area, making this technique suitable for laser patterning. Rutile, a higher refractive crystal phase, can scatter light more efficiently than anatase, and this opens the possibility of

using these patterned substrate in various applications such as silicon solar cells, energy-harvesting devices, and dye-sensitized solar cells (DSSC) [270,271].

5.2. Experimental

5.2.1. Laser ablation of TiO_2 in water

A schematic of the setup employed for the laser ablation experiments is shown in Figure 37.

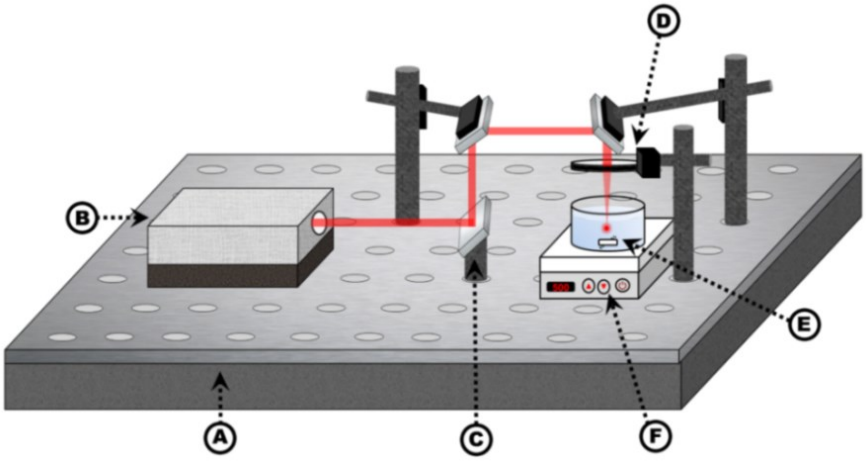

Figure 37: Schematic of femtosecond laser ablation experiment setup consisting of (A) optical table, (B) Ti-sapphire laser, (C) mirror system, (D) focusing lens, (E) container containing stir bar and TiO2 solution, and (F) stir plate. Reproduced from ref. [139] by permission of The Royal Society of Chemistry

In our experiments, 10 mg of P25 powder (Aeroxide^{TM}) was suspended in 10 ml of water and stirred with a magnetic stirrer for the entire duration of the experiments. Femtosecond laser ablation experiments were conducted using a Ti-sapphire laser (Coherent, Inc.) with a wavelength of 800 nm, repetition rate of 1 kHz, and pulse duration of 35 fs with Gaussian beam distribution. The laser ablation experiments were performed from the top in order to avoid laser reflections through the glass walls. The laser beam (80 μm in diameter) was focused inside the TiO_2 dispersion at 5 mm from the dispersion-air interface. The experiments were carried out at a power of 1.3 W (25.8 J/cm^2) and at different laser ablation times, in order to study the laser effects on the TiO_2 crystal structure as a function of the ablation time.The P25 dispersions were ablated for 5, 15, 30, 60, 90 and 120 minutes and then the resulting ablated suspensions were characterized. Scanning electron microscopy (SEM) images of the dispersion deposited onto silicon substrate were taken using a ZEISS LEO 1550 FE-SEM at an accelerating voltage of 10 kV. The crystal phase and structure of the ablated material was investigated by Raman

spectroscopy and transmission electron microscopy (TEM). Raman spectra were measured using a Renishaw micro-Raman spectrometer with a He/Ne laser at an excitation wavelength of 632.8 nm. HRTEM observation was conducted using a JEOL 2010F at the Canadian Centre for Electron Microscopy (Hamilton, Ontario, Canada). The TEM samples were prepared by drop casting the dispersions onto lacey carbon grids. Ultraviolet-visible (UV-VIS) analysis of the laser ablated dispersions was carried out with a Shimidazu UV-2100 PC spectrophotometer over a spectral range of 190–600 nm.

5.2.2. Deposition of TiO_2 onto FTO substrates (P25/FTO)

TiO_2 films were fabricated by electrophoretic deposition of P25 on fluoride-doped tin oxide (FTO) glass, followed by annealing. The TiO_2 dispersion was made by dispersing 1 g of P25 nanoparticles in 250 mL ethanol, 15 mL acetylacetone, 4 mL acetone, 2 mL water, and 27 mg iodine[272]. The dispersion was sonicated for 30 min and stirred for 1 hour. FTO glass (MTI Corp, 1" x 3" x 2.2 mm, TEC 7, R: 12-14 ohm/sq.) was used as a support and cathode for TiO_2 deposition, while a titanium sheet was used as the anode. The cathode and anode were connected to a DC voltage supply and immersed in the aforementioned TiO_2 dispersion. The electrophoretic deposition was conducted at a constant voltage of 30 V for 60 seconds and deposited onto 1"x1" of the FTO glass. The P25 deposited FTO substrate was dried in air and then heat-treated at 450^oC to improve adhesion.

5.2.3. Laser patterning of TiO_2 on FTO substrate

The patterning of P25 deposited on FTO substrate was performed using the Ti-sapphire laser system described in 5.2.1 and the setup was configured to pattern the substrate on a motorized stage controlled *via* computer, the experimental setup schematic used is shown in Figure 38. The sample was placed on a 2 axis stepper motor stage and a 5 cm line was patterned focusing the laser (80 μm in diameter) on the substrate at a speed of 1.5 mm/s. In total, 8 lines were patterned at increasing laser powers.

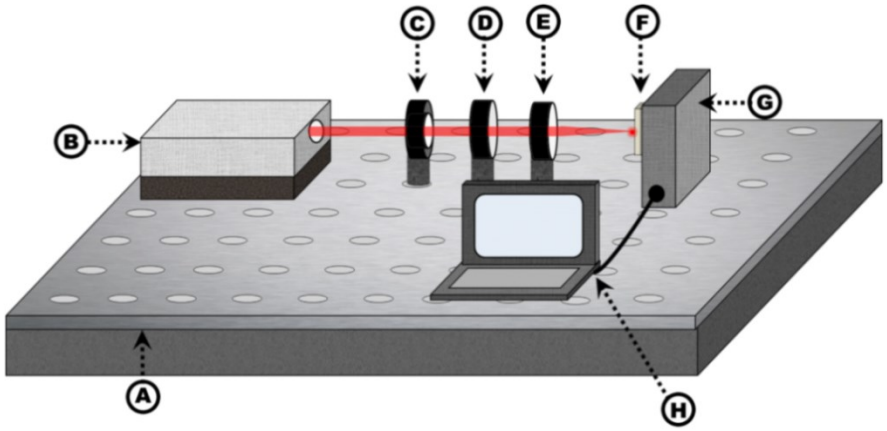

Figure 38: Schematic of femtosecond laser ablation setup for laser patterning consisting of (A) optical table, (B) Ti-sapphire laser, (C) mechanical shutter, (D) neutral density filter, (E) focusing lens, (F) patterned substrate, (G) motorized stage, and (H) computer. Reproduced from ref. [139] by permission of The Royal Society of Chemistry

5.3. Results and discussion

5.3.1. TiO_2 phase transformation upon laser ablation in water

The laser ablation study of the TiO_2 nanoparticles was conducted by increasing the ablation time. After 15 minutes of irradiation the color of the dispersions changed from white (as-purchased P25 Aeroxide^{TM}) to blue. The color change can be attributed to the formation of Ti^{3+} species that will lead to the formation of rutile TiO_2 nanoparticles [240,268]. The mechanisms underlying the formation of TiO_2 nanoparticles upon laser ablation of a Ti target have been widely discussed. The mechanism may be summarized in three steps, in which (1) the high temperature and pressure generated by the laser-matter interaction will produce a plasma plume; (2) the plasma plume undergoes ultrasonic adiabatic expansion, which causes a rapid cooling of the plume and formation of titanium clusters; and (3) the titanium ions and clusters react with water molecules at the interfacial region between plasma and liquid, leading to the formation of rutile nanoparticles.[240,242,273]

Increasing the ablation time to 120 minutes led to dispersions that were less blue in intensity. In order to investigate whether a structural modification of the P25 nanoparticles was occurring during the laser ablation, the ablated dispersions were investigated using Raman spectroscopy which is widely used for the characterization of TiO_2 polymorphs since it allows to distinguish between the different phases of TiO_2 [170,172,174]. The most prominent Raman features of anatase are the peaks centered at 144 cm^{-1} (E_g), 197 cm^{-1} (E_g), 399 cm^{-1} (B_{1g}), 513 cm^{-1} (A_{1g}),

519 cm^{-1} (B_{1g}), and 639 cm^{-1} (E_g), while the Raman active modes of rutile phase are at 143 cm^{-1} (B_{1g}), 447 cm^{-1} (E_g), 612 cm^{-1}(A_{1g}) and 826 cm^{-1} (B_{2g})[274]. The Raman spectrum of P25 possesses peaks containing the anatase and rutile phases, since it is made of 70-75% of anatase and 30-25% of rutile phases. The main peaks are centered at 636 cm^{-1} (E_g), 515 cm^{-1} (B_{1g}), 443.17 cm^{-1} (E_g), and 394.52 cm^{-1} (B_{1g}). It has been reported that, Raman spectroscopy can be employed for the monitoring of the phase transformation of TiO_2 and its stoichiometry upon annealing or laser treatment, since the Raman active E_g modes are sensitive to oxygen deficiency, which will lead to a shift and broadening of these lines [139,170–172,174,175]. In this study, Raman analysis was performed after depositing the laser treated dispersions onto glass slides and letting them dry in air under ambient conditions. The acquired spectra are shown in Figure 39 and compared to commercial anatase, rutile and P25 powders. The laser-treated samples are compared to the as-received P25 in aqueous solution. After 5 minutes of laser treatment of dispersed P25, the peak centered at 636.4 cm^{-1} blue-shifted by 1.59 cm^{-1}. From the comparison of the Raman spectra, structural modification of P25 started to take place after 15 minutes of laser ablation, as depicted from the spectrum (purple line), which depicts peak shifting in Figure 39. In particular, a blue-shift of 11.11 cm^{-1} of the Raman mode at 636.4 cm^{-1} was detected along with the peak broadening. Additionally, the intensity of the peak at 515.06 cm^{-1} decreased, while the intensity of the peak at 443.17 cm^{-1} increased and blue-shifted by 2.65 cm^{-1}. The peak at 394.52 cm^{-1} red-shifted by 8.73 cm^{-1} and the intensity of the peak decreased. The two peaks at 394.52 cm^{-1} and 443.17 cm^{-1} are relative to the Raman active modes (B_{1g}) and (E_g) of anatase and rutile phases, respectively, and are of note. After 15 minutes of laser treatment, these two peaks give rise to a unique peak and the spectrum results to be similar to the Raman spectrum of rutile, suggesting a phase transformation from mainly anatase to mainly rutile nanoparticles. This evidence is further supported if we take into consideration the earlier observation of the color change of the dispersion to blue, which is attributed to the formation of rutile nanoparticles [240,268]. This result is in agreement with the mechanisms occurring during the laser ablation of titanium dioxide discussed earlier, which cause the formation of a plume containing titanium ions which upon expansion and successive cooling will form titanium clusters leading to the formation of rutile nanoparticles. The phase transformation to rutile is more apparent after 30 minutes of laser ablation, in which a peak shift to 614.98 cm^{-1} occurs, which is within the reported for rutile (611 cm^{-1}).

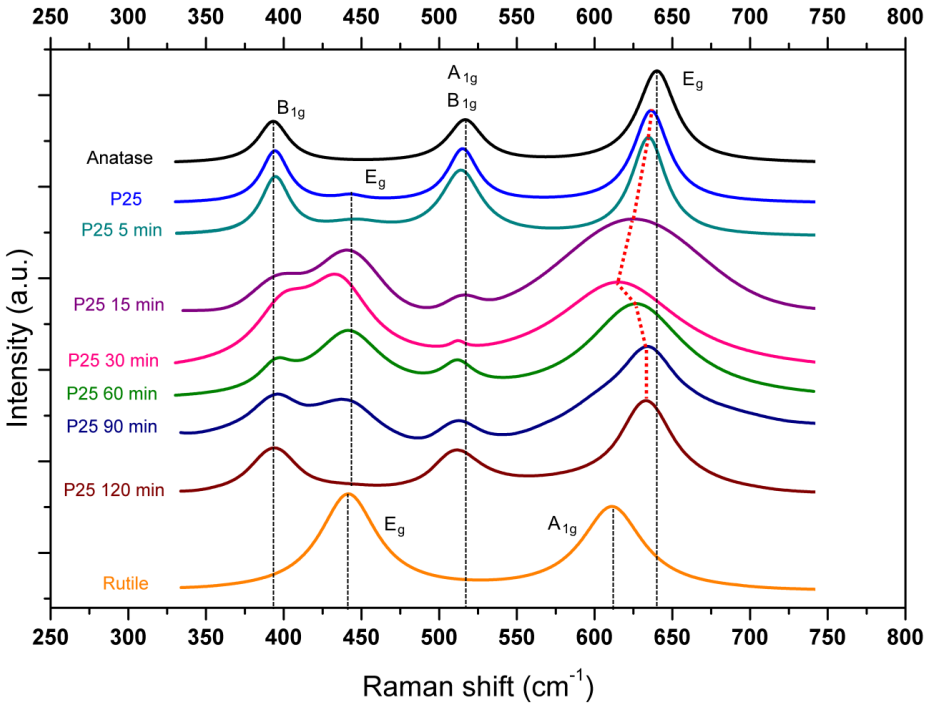

Figure 39: Raman spectra of P25 dispersions after 5, 15, 30, 60, and 120 minutes of laser ablation. For comparison, Raman spectra of anatase, rutile and P25 as purchased powders have been included. Reproduced from ref. [139] by permission of The Royal Society of Chemistry

Furthermore, the intensity of the peak at 511 cm^{-1} decreases and the separation between the two peaks at 394.52 cm^{-1} and 443.17 cm^{-1} is reduced compared to the P25 treated for 15 minutes. When the laser ablation is performed for 60 minutes, a redshift of 11.9 cm^{-1} occurred and the peak center was found at 626.88 cm^{-1}, the intensity of the peak at 511.89 cm^{-1} increased, and the separation between the two peaks at 397.7 cm^{-1} and 441.31 cm^{-1} is more evident. This suggests of the TiO_2 nanoparticles are of mixed phase composition containing rutile and anatase. It should be noted that the existence of a mixed phase upon laser ablation of Ti target has been already reported by Tian et al. and it is a consequence of the rapid change of temperature and pressure during ablation [275]. The increasing of the laser ablation time up to 90 minutes causes either a decrease of the intensity of the band of rutile phase at 437 cm^{-1}, or increase of the band intensity relative to the anatase phase at 394.52 cm^{-1}. This indicates that the predominant phase of the nanoparticles is the anatase one. After 120 minutes of laser ablation there is a clear phase transformation to anatase occurred. In literature, the ratio of the integrated Raman peak intensity of the peak of rutile at 447 cm^{-1} to that of anatase at 399 cm^{-1} is used for the measure of the weight ratio of rutile to anatase [276,277]. Figure 40, depicts the integrated Raman peak intensity

ratio as function of laser ablation time in order to visualize the anatase-to-rutile and rutile-to-anatase conversion as a function of laser ablation time. The commercial P25 and the nanoparticles ablated for 5 minutes showed a I_{446}/I_{396} ratio of 0.2 indicating the presence of mostly crystalline anatase, which is in agreement with the recorded Raman spectra and with the I_{446}/I_{396} value reported in literature [278].

Increasing the ablation time causes an increase of the I_{446}/I_{396} ratio to 1.1 which can be related to the formation of rutile nanoparticles. After 60 minutes of laser ablation, the I_{446}/I_{396} reaches 1.8 indicating that the nanoparticles produced were predominantly rutile, which has been already demonstrated by the Raman spectrum analysis. The increase of the ablation time up to two hours introduced a phase transformation from rutile to anatase and this can be seen as a decrease in the I_{446}/I_{396} ratio to 0.8 after 90 minutes and to 0.2 after 120 min, which is the value recorded for the un-treated P25, where anatase is the predominant phase.

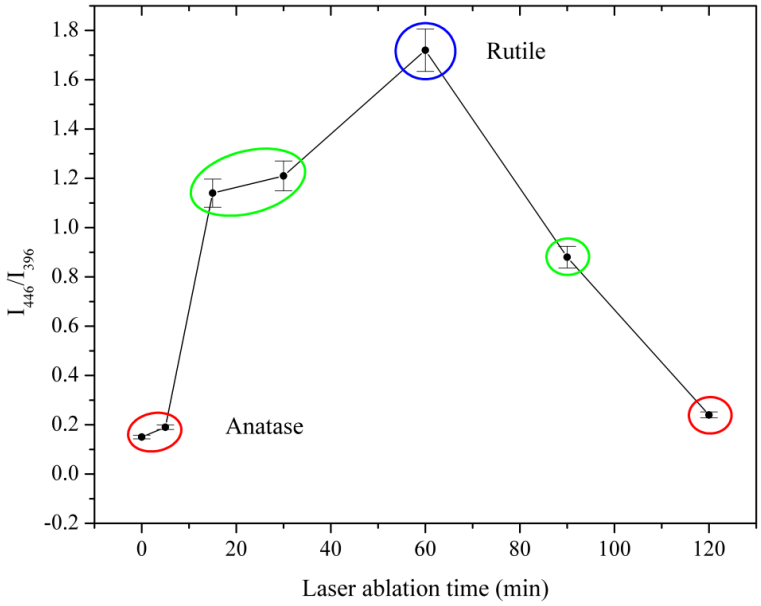

Figure 40: Integrated Raman peak intensity ratio as a function of laser ablation time of P25 dispersion. After 5 minutes of laser ablation the nanoparticles are in the anatase form (red circle), while after 20 minutes the transformation to rutile starts to occur (green circle). After 60 minutes of laser ablation the particles transformed to rutile (blue circle), however increasing the ablation time (90 min), the particles start to transform to anatase (green circle) and after 120 minutes the particles possess anatase phase (red circle). Reproduced from ref. [139] by permission of The Royal Society of Chemistry

The trend shown in Figure 40 is in agreement with the information obtained from the Raman spectrum analysis, in which one hour of laser ablation of P25 nanoparticles induces the

formation of rutile nanoparticles; however, for prolonged ablation times a phase transformation to anatase takes place.

As previously described, the laser ablation in water causes the melting of the material and the generation of a plasma plume, which contains atoms, molecules, electrons, ions, and expands into the surrounding liquid, cools down and finally lead to the formation of the nanoparticles. It was reported from Koshizaki et al. that spherical nanoparticles are obtained when laser ablation is performed in a liquid environment [132]. The phase transformation from rutile to anatase is thermodynamically irreversible, however when the sizes of the particles decrease the phase stability reverses [138]. This is corroborated by studies that have reported about the size reduction of nanoparticles upon laser irradiation of nanoparticles using an unfocused laser beam [131,132]. On the basis of the current literature and on the experimental results, we hypothesize that upon laser ablation of P25 aqueous suspension with a focused laser, two events might occur which lead to the phase transformation from rutile to anatase nanoparticles. The first process involves the generation of spherical particles from a localized volume that is ablated from as-received P25 nanoparticles that appear square-like. Only the TiO_2 nanoparticles that cross the focus will melt and upon cooling spherical particles start to form. The formation of spherical particles is shown in Figure 41(a-g), which represent the nanoparticles obtained at different ablation time.

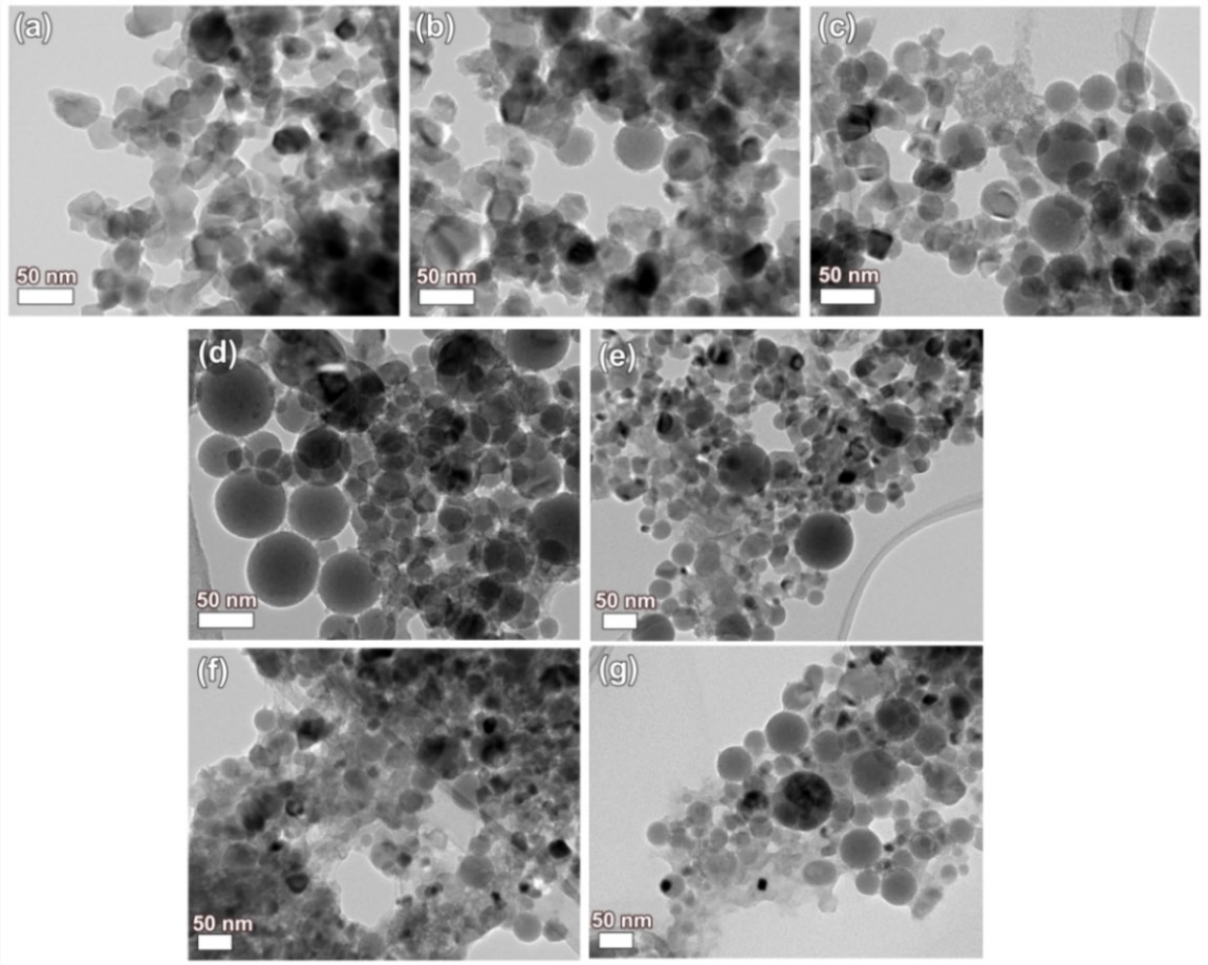

Figure 41: TEM images of P25 powders before (a) and after 5 (b), 15 (c), 30 (d), 60 (e), 90 (f) and 120 (g) minutes of laser ablation. Reproduced from ref. [139] by permission of The Royal Society of Chemistry

The second process that occurs is a decrease in the size of spherical nanoparticles with laser ablation time. As previously stated, a decrease in size of the nanoparticles could reverse the phase stability and this could be the reason for the transformation of rutile nanoparticles to anatase nanoparticles. The mechanism underlying the decrease in size could be explained if we consider that during the laser ablation not all the particles dispersed in the solution will cross the laser focus, consequently most of them will be irradiated by the laser causing the size reduction [279–281]. The decrease of the nanoparticles size can be attributed to fragmentation [273] that occurs during the laser treatment. Alnassar et al. reported about the decrease of size as a function of the pulse energy [273], but it is also time-dependent [280].

A schematic of the two events is shown in Figure 42.

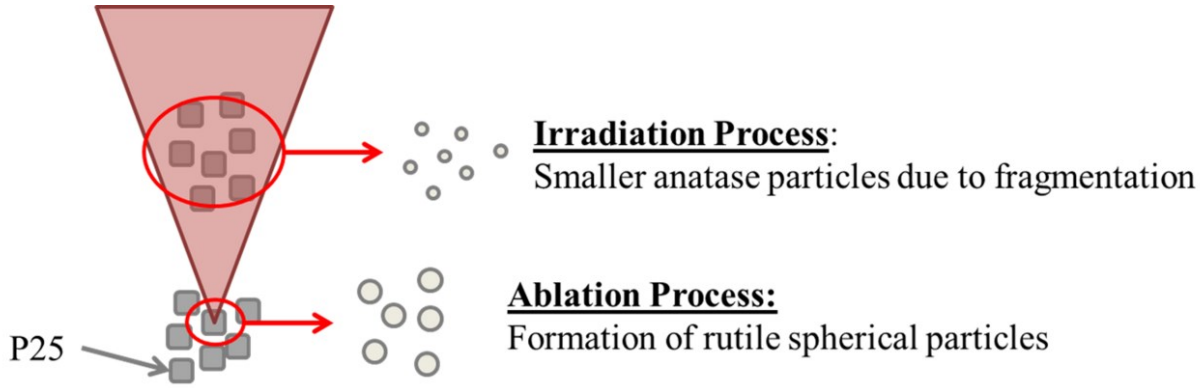

Figure 42: Schematic illustrating the two events responsible for the formation of spherical rutile nanoparticle in the focused area and the formation of smaller anatase particle in the irraditaed area

We observed that, after 15 and 30 minutes of PLA, there are more particles that have a size above 30 nm and it has been reported that when TiO_2 particles are bigger than 35 nm, the rutile phase is thermodynamically more stable than the anatase phase. In Figure 43 and Figure 44, are shown the HRTEM images with the d-spacing profiles of the samples at different ablation time. From the analysis of the d-spacing it was confirmed that after 15 and 30 minutes of laser ablation, the particles are mainly rutile with a d-spacing of 0.32 nm (110) plane, as shown in Figure 43(c-d) respectively. This result is in accordance with the Raman analysis which showed an increase of the rutile phase after 30 minutes of laser processing. Increasing the ablation time to 60 minutes led the formation of particles with diameters over 35 nm, however smaller particles with diameters in the range of 9-20 nm are abundant. These particles are in the anatase form with a d spacing of 0.35 nm (101) plane, as showed from the HRTEM images in Figure 44b, however rutile nanoparticles are also present (Figure 44a).

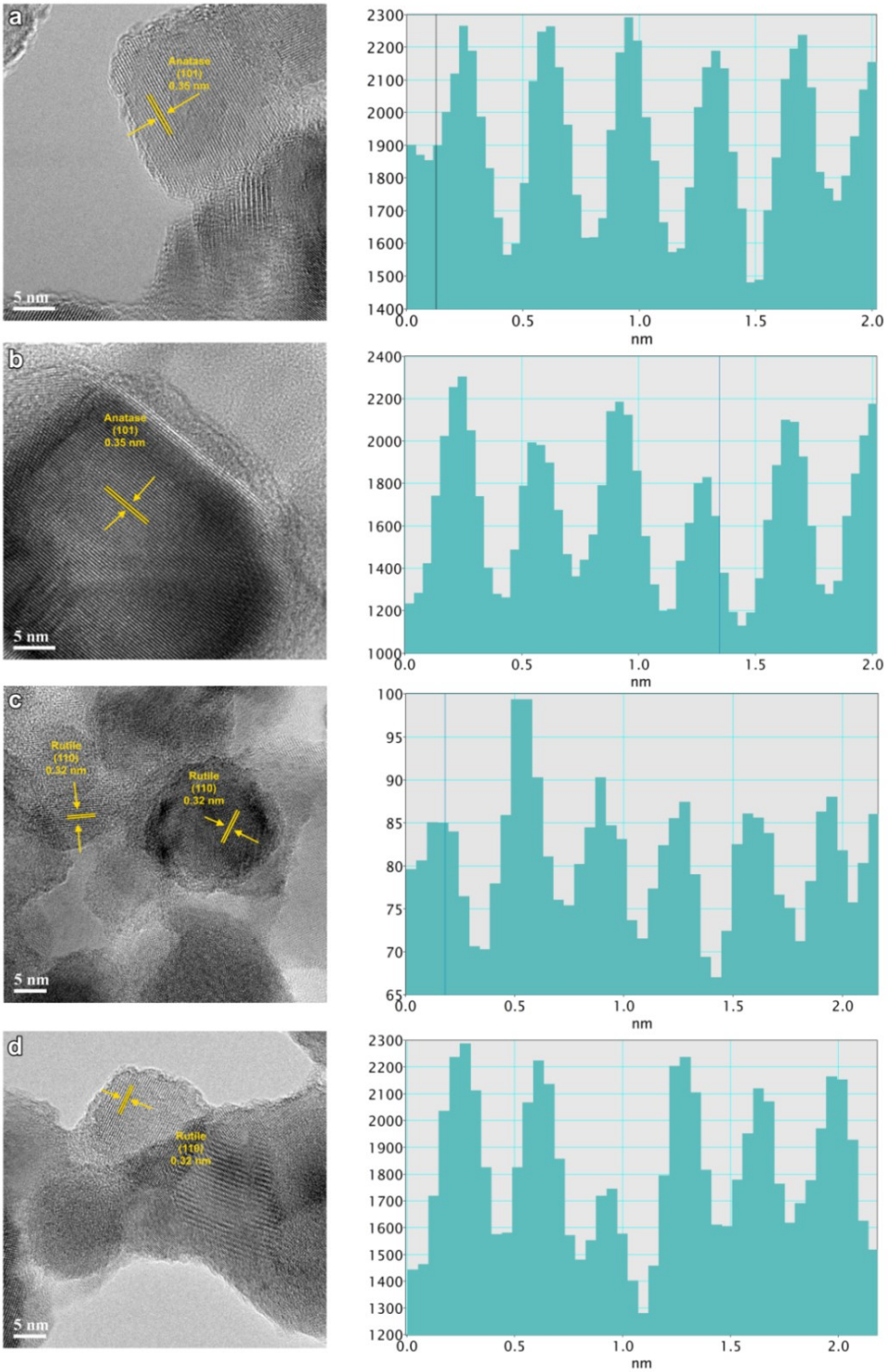

Figure 43: HRTEM images of TiO2 powder with d-spacing profiles (a) before laser ablation and after (b) 5, (c) 15, and (d) 30 min of laser ablation. Reproduced from ref. [139] by permission of The Royal Society of Chemistry

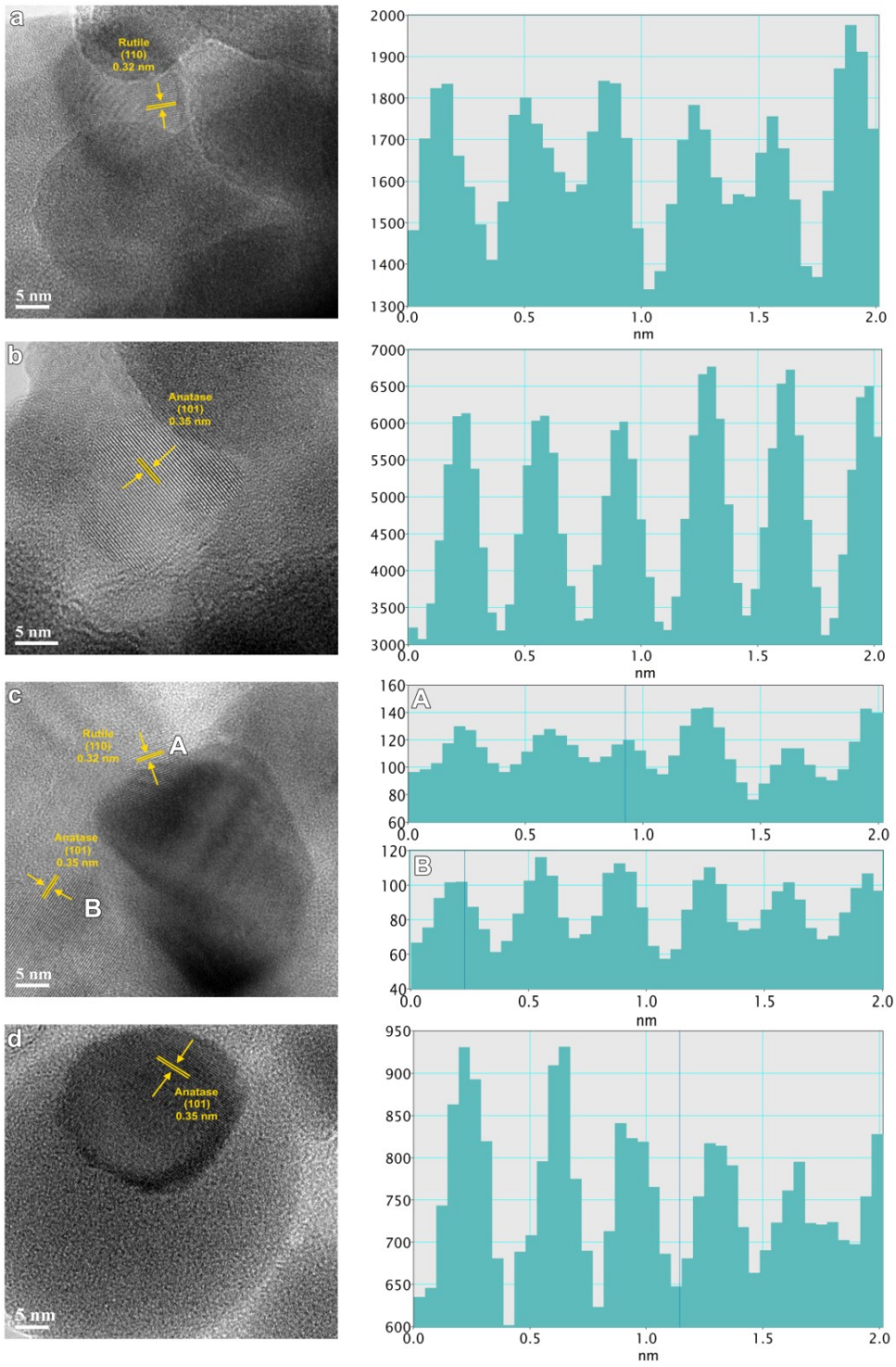

Figure 44: HRTEM images of TiO_2 powder with d-spacing profiles after (a, b) 60, (c) 90, and (d) 120 min of laser ablation. Reproduced from ref. [139] by permission of The Royal Society of Chemistry

The coexistence of the small anatase particles and the bigger rutile ones can be explained on the basis of the two events that we hypothesized are occurring during the laser ablation process. The first event leads to the formation of the rutile nanoparticles with diameters of 35 nm, while the irradiation causes the size decreasing and reverse of the phase stability, leading to a broadening of the size distribution. After 90 and 120 minutes of laser ablation the nanoparticles formed have a similar dimensions of the nanoparticles obtained after one hour of laser ablation, but there is evidence that anatase nanoparticles have been produced, as shown by the HRTEM image in Figure 44d and confirmed by Raman spectroscopy. From these results, it is evident that the laser ablation of P25 induced the formation of rutile particles mixed with smaller anatase nanoparticles. The size distribution analysis was conducted on the HRTEM images for laser ablated samples from 0 min to 120 min (Figure 45). One-way ANOVA statistics were conducted on P25 samples (Table 5). All laser ablated P25 samples showed a significant increase in diameter ($p < 0.01$) compared to the untreated P25 sample. In general, increasing irradiation time did not increase the diameter significantly. However, when the irradiation time was increased to 120 min, the diameter was higher than P25 samples irradiated at 5 min (p=0.003) and 90 min (p=0.0121).

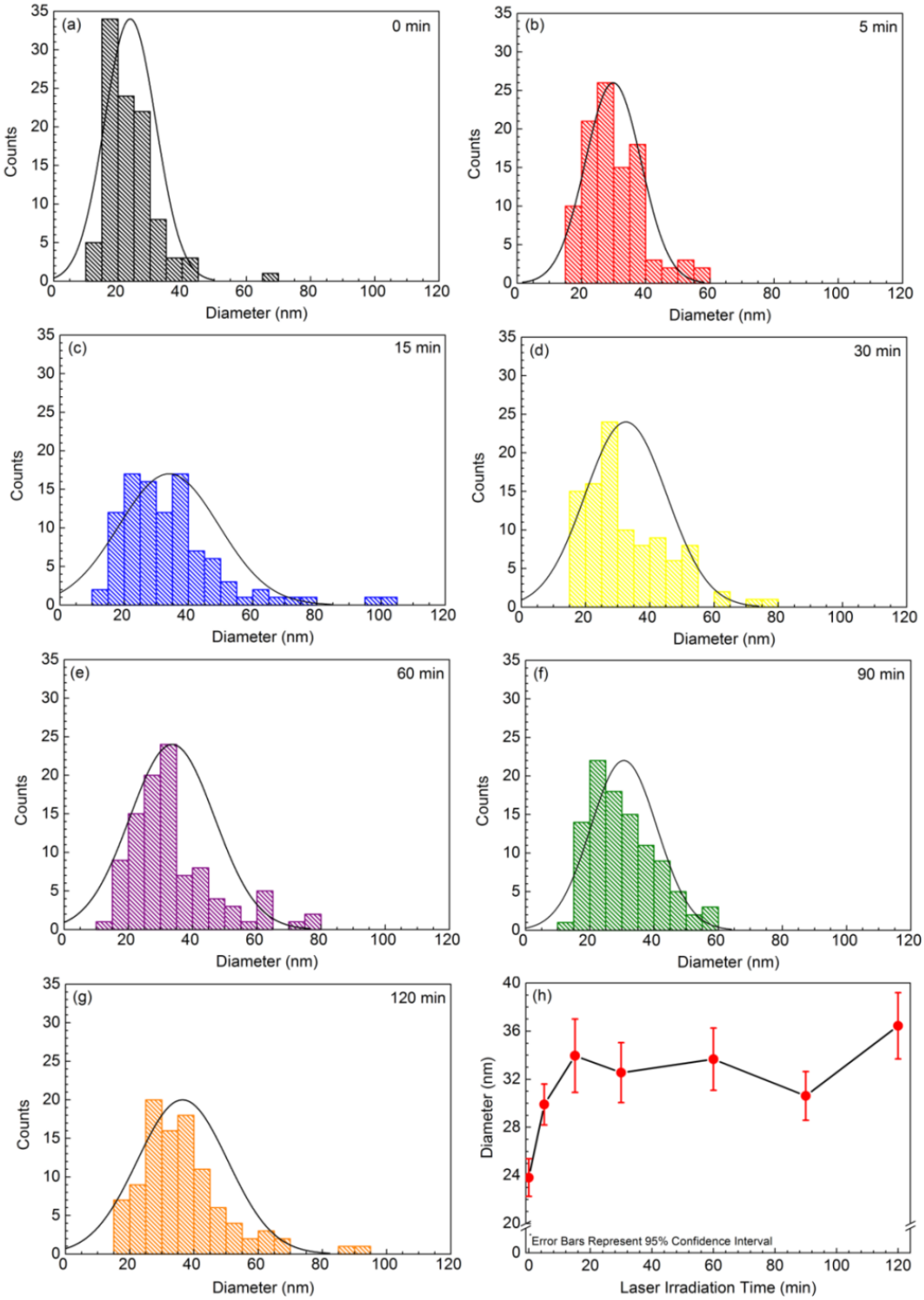

Figure 45: Size distribution of P25 aqueous suspensions laser treated at: (a) 0 min, (b) 5 min, (c) 15 min, (d) 30 min, (e) 60 min, (f) 90 min, and (g) 120 min. (h) P25 diameter as a function of laser irradiation time. Reproduced from ref. [139] by permission of The Royal Society of Chemistry

Table 5: One-Way ANOVA *p*-value post-hoc tests (OriginPro, α=0.05) for laser-treated P25. Reproduced from ref. [139] by permission of The Royal Society of Chemistry

A	B	p-value	Significance (α=0.05)
5min	0min	0.0073	YES
15min	0min	<0.0001	YES
15min	5min	0.2111	NO
30min	0min	<0.0001	YES
30min	5min	0.7137	NO
30min	15min	0.9825	NO
60min	15min	<0.0001	YES
60min	5min	0.2967	NO
60min	15min	1.0000	NO
60min	30min	0.9951	NO
90min	0min	0.0015	YES
90min	5min	0.9996	NO
90min	15min	0.4441	NO
90min	30min	0.9180	NO
90min	60min	0.5610	NO
120min	0min	<0.0001	YES
120min	5min	0.0027	YES
120min	15min	0.7711	NO
120min	30min	0.2558	NO
120min	60min	0.6631	NO
120min	90min	0.0121	YES

*Post-hoc tests (multiple comparisons) were conducted when a statistical significance was detected using Holm-Sidak method with overall statistical significance level of 0.05.

In order to confirm the polymorphism and crystallinity of the laser treated P25 dispersions, we performed the XRD analysis of the samples before and after 5 and 60 minutes of laser ablation. The results are displayed in Figure 46.

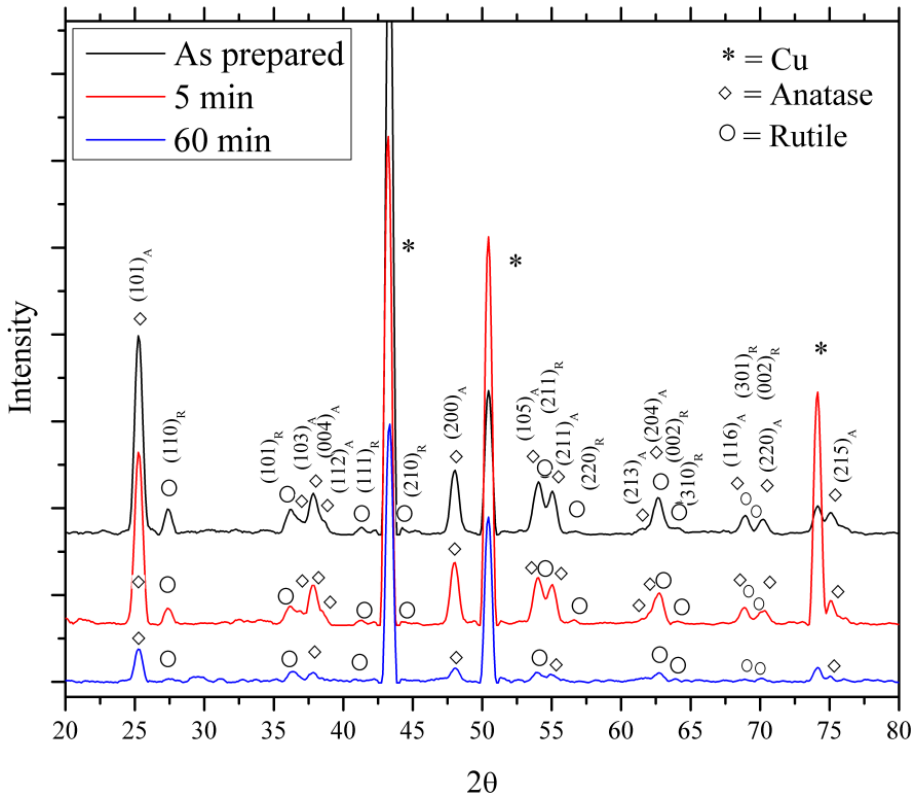

Figure 46: XRD analysis of the as prepared P25 dispersion and f-after laser treatment. Reproduced from ref. [139] by permission of The Royal Society of Chemistry

After laser treatment the dispersions showed the presence of both phases (anatase and rutile), as demonstrated by Raman spectroscopy and HRTEM analysis. The degree of crystallinity was calculated using the ratio of the intensity (I_A/I_R) of the strongest anatase reflection to the strongest rutile reflection, (101) and (110) respectively [282]. The equation employed is given below [282].

$$X_C = \frac{1}{1+1.265\left(\frac{I_R}{I_A}\right)} \times 100\ [\%] \qquad (1)$$

The as prepared dispersion and the ones laser treated for 5 and 60 minutes, have degree of crystallinity equal to 85.98%, 89.14% and 82.31%, respectively. It can be observed that the laser treatment did not change the level of crystallinity of the materials and the polymorphism is still present.

The energy bandgap of the ablated dispersions were investigated. The optical bandgap of TiO_2 nanoparticles was calculated using Tauc's law in which the direct band gap and indirect band gap follow the Equations (2) and (3), respectively [274]:

$$(\alpha h\upsilon) \propto (h\upsilon\text{-}E_{gap})^{1/2} \qquad (2)$$

$$(\alpha h\upsilon) \propto (h\upsilon - E_{gap})^2 \quad (3)$$

where α is the absorption coefficient, h the Planck's constant, υ is the frequency and E_{gap} is the energy bandgap. As reported in literature, anatase is an indirect band gap semiconductor and the energy band gap value of 3.2 eV is attributed to $\Gamma_3 \rightarrow X_{1b}$ transition [274]. Figure 47a, it is shown that the normalized UV-Vis spectra of the TiO_2 suspensions ablated at different ablation times.

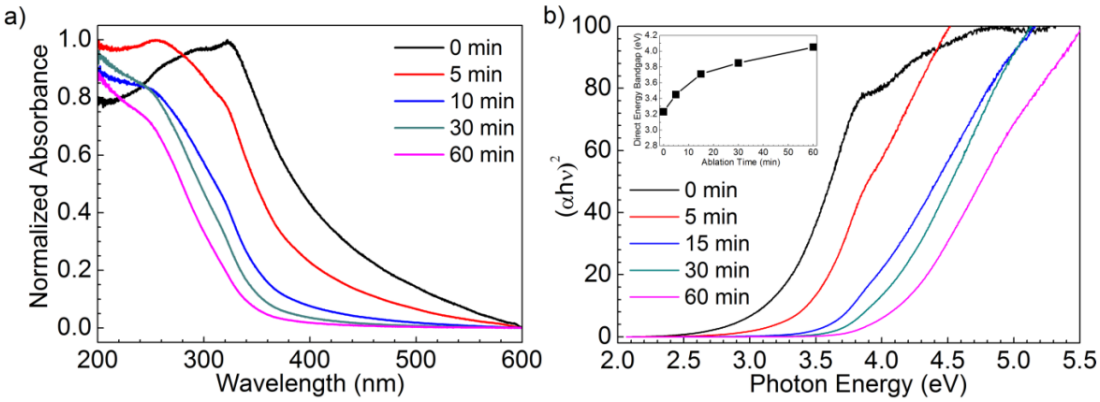

Figure 47: (a) UV-Vis of TiO_2 suspension ablated at different ablation time; (b) Plot of $(\alpha h\upsilon)^2$ versus photon energy for direct transition and (inset) plot of energy bandgap values as a function of ablation time. Reproduced from ref. [139] by permission of The Royal Society of Chemistry

Based on our absorption results the plots of $(\alpha h\upsilon)^{1/2}$ versus photon energy, for indirect transitions, displayed no linear relationships. However, when the spectral data were plotted as $(\alpha h\upsilon)^2$ versus photon energy, a linear relationship was obtained, suggesting the occurrence of a direct band transition in an indirect bandgap semiconductor [283].

In Figure 47b, the Tauc plot is shown. The energy bandgap (E_{gap}) values of the solutions ablated at different times have been obtained by extrapolation to α=0, and the inset plot of the energy bandgap as a function of the laser ablation time is shown. The E_{gap} values are reported in Table 6.

Table 6: Energy gap values as a function of laser ablation time. Reproduced from ref. [139] by permission of The Royal Society of Chemistry

Laser Ablation Time (min)	Direct Energy Bandgap $(\alpha h\upsilon)^2$
0	3.2 eV
5	3.35 eV
15	3.7 eV
30	3.85 eV
60	3.9 eV

It was found that increasing the ablation time, an increase in the direct energy bandgap occurred. Based on the study carried out by Nath [274], the energy band gap value of 3.8 eV of TiO_2 nanoparticles after 60 minutes of laser ablation, may be attributed to either the direct interband transition of rutile phase or to a decrease in size of the TiO_2 nanoparticles [284]. This result is in accordance with both Raman and TEM results, which showed the phase transformation from anatase to rutile and particle size decrease occurred after 60 minutes of laser ablation.

With proper control of the ablation time, it is possible to synthesize TiO_2 nanoparticles with different sizes or induce phase transformations, which lead to TiO_2 nanoparticles with different values of energy bandgap. This opens the possibility of using PLA as technique for bandgap engineering of TiO_2, such as its use in future electronic devices [285,286].

5.3.2. Laser ablation of P25/FTO substrates

Femtosecond laser ablation was performed on P25/FTO substrates in order to compare the results from the ablation of P25 carried out in an aqueous dispersion with the ablation of P25 deposited on a substrate. The experiments were performed varying the laser power in order to study the phase transformation as a function of the laser power and in total 8 lines were patterned, as shown in Figure 48.

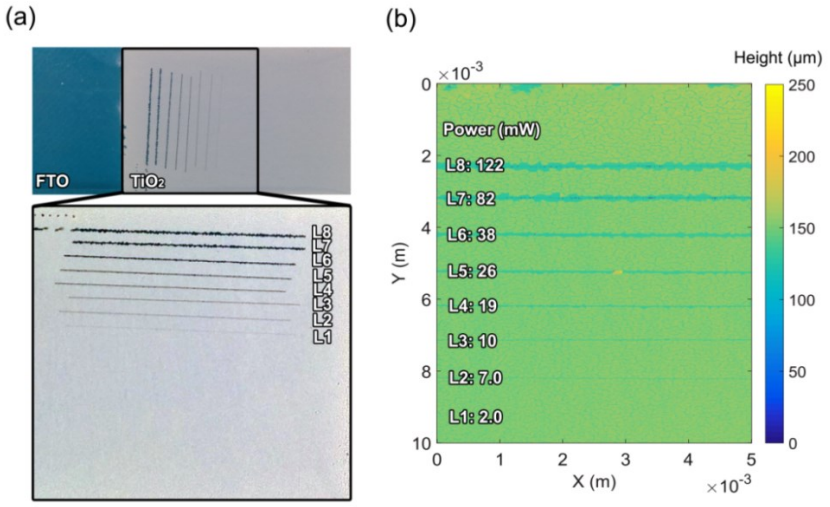

Figure 48: (a) Top-bottom view and (b) surface profile of P25/ FTO contained femtosecond laser produced lines of varying power. Reproduced from ref. [139] by permission of The Royal Society of Chemistry

The eight lines, 1.5 cm long, were ablated at powers of 2.0, 7.0, 10, 19, 26, 38, 82, and 122 mW (Figure 48b). The estimated fluence was calculated using the following Equation (4):

$$F = \frac{P}{1000Hz \times \pi r^2} \quad (4)$$

where P is the power (W) and r is the radius of the beam spot (cm). The beam diameter is 80 μm and the estimated fluences tested were 39.8, 139.3, 204.9, 378.0, 517.3, 756.0, 1600, and 2700 mJ cm^{-2}. In Figure 48a, lines from 3 to 8 (L3-L8) depict TiO_2 that is completely removed due to spallation from the femtosecond laser ablation process and only FTO glass remains on the surface, as can be seen from the surface profile (Figure 48b). The lines patterned at powers of 2.0 and 7.0 mW (L1-L2) showed no removal of TiO_2, suggesting that lower powers are preferable in order to achieve the laser patterning of the P25 on FTO/glass. The line 2 (L2) was then characterized by SEM and Raman in order to determine the morphological and crystal phase changes of TiO_2 after the laser interaction.

In Figure 49, SEM images of the non-laser patterned (a, b, and c) and laser patterned (d, e, and f) regions of P25 onto FTO are shown. The electrophoretic deposition of P25 onto FTO did not form a uniform layer of P25; instead some cracks are clearly visible, as shown in Figure 49a. This occurs when the deposition layer is thick.

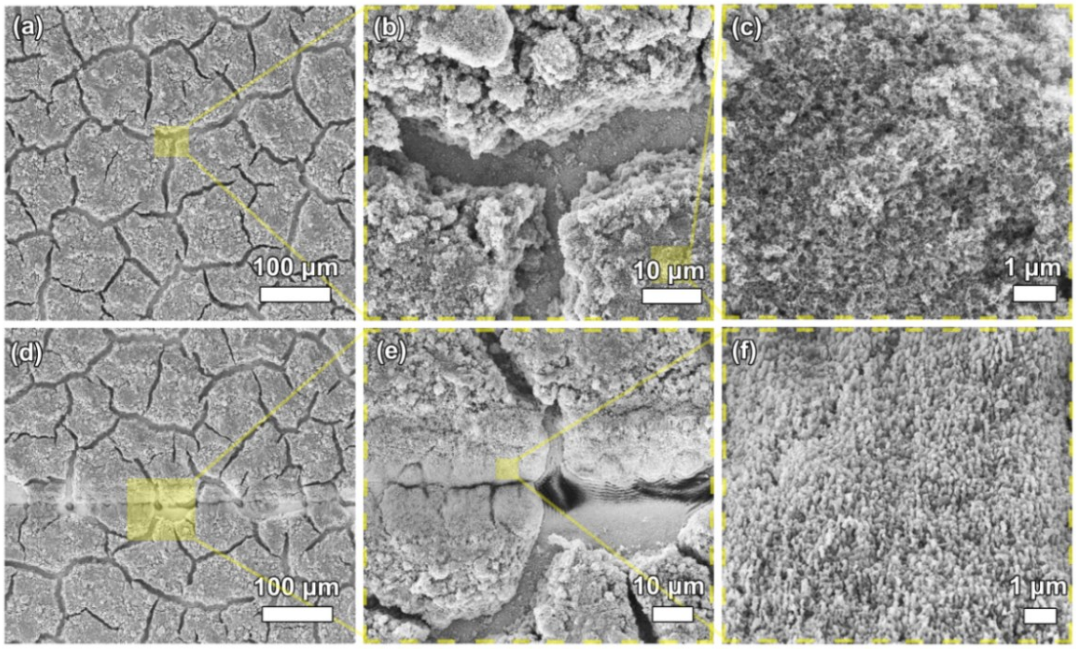

Figure 49: SEM images of (a-c) non-patterned and (d-f) laser patterned P25 on FTO. Reproduced from ref. [139] by permission of The Royal Society of Chemistry

A closer look at the untreated P25 film in Figure 49b reveals the presence of a porous-like structure. Upon laser irradiation of the P25 film, a structural change occurs, but the conductive substrate did not interfere with the absorption processes. Pseudo-spherical nanoparticles with sizes of 100-300 nm are formed (Figure 49f), which are much larger particles than the non-

treated regions (Figure 49c) in which average particle size are 21 ± 5 nm. The formation of larger particles can be understood considering the underlying ablation mechanisms discussed earlier. In particular, due to the laser-matter interaction, the local increase of temperature and pressure will take place leading to the melting and coalescence of the material and production of larger nanoparticles [175,241,245]. In order to study the effects of the laser patterning on the crystal phase of the P25, Raman line mapping was performed perpendicularly from the ablated line.

The Raman line mapping is shown in Figure 50a, while in Figure 50b the Raman spectra of the region outside the laser patterned (black spectrum) and in the middle of the laser patterned area (red spectrum) are shown. The phase transformation tends towards rutile upon laser patterning of P25 on FTO. In particular, the non-patterned P25 Raman spectrum (Figure 50b black spectrum) shows the characteristic anatase peaks at 143 cm^{-1}, 395 cm^{-1}, 511 cm^{-1}, and 630 cm^{-1}.

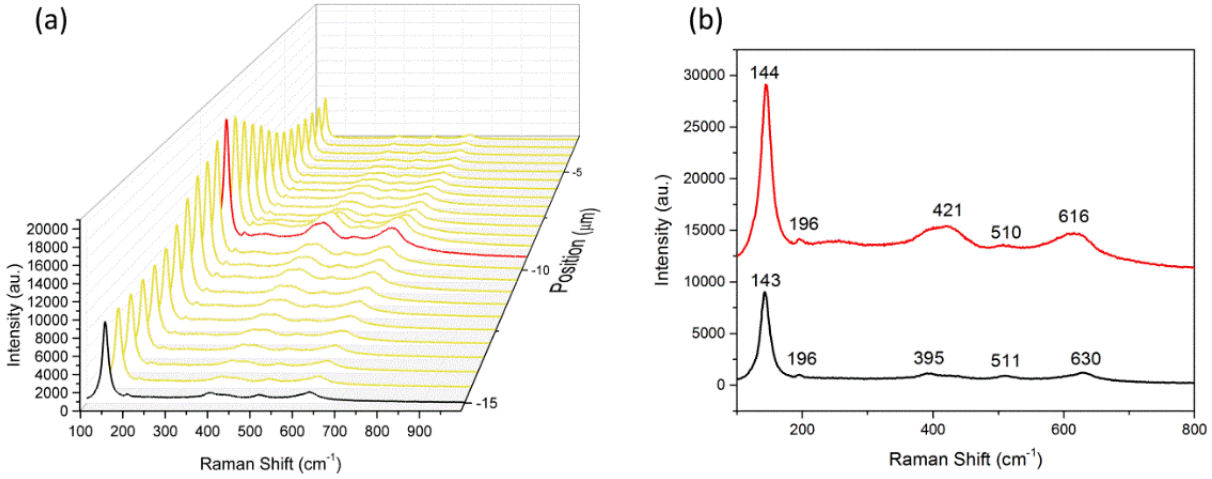

Figure 50: (a) Raman mapping line of the laser patterned P25 on FTO, (b) Raman spectra of the area outside (black spectrum) and inside (red spectrum) the laser patterned area. Reproduced from ref. [139] by permission of The Royal Society of Chemistry

From the Raman scan line analysis, Figure 50a, it can be seen that approaching the ablated center of the laser patterned line, a redshift in the 143 cm^{-1} peak occurs, and the overall spectrum shifts towards rutile-like spectrum (red). At the ablated center of the laser patterned line, broadened peaks start to appear at 421 cm^{-1} and 616 cm^{-1}, and anatase peaks at 421 cm^{-1}, 395 cm^{-1} and 630 cm^{-1} are suppressed, confirming that phase transformation of P25 to a rutile-like phase occurs along with increasing particle size in the laser affected area. It has been reported that phase transformation of TiO_2 crystal rutile to anatase can occur upon femtosecond laser irradiation [241,245], however in order to achieve the transformation high temperatures and pressures are

required. In our case, when the P25 substrate is irradiated in air the power employed during the laser pattering is not high enough to trigger the phase transformation to anatase. Therefore, the laser patterning induces a local increase of temperature and pressure that leads to the melting and coalescence of the material and production of larger rutile nanoparticles [175,241,245].

The rutile phase has a higher refraction of index (n=2.9) and can scatter light more efficiently than the anatase phase (n=2.4) [287–289]. This phase transformation obtained by laser patterning of TiO_2 films on FTO with a femtosecond laser, can open the possibility of using femtosecond laser patterned substrates in various applications such as light trapping layers in silicon solar cells, energy-harvesting devices, and dye-sensitized solar cells (DSSC) [270,271]. From these results, it is clear that femtosecond laser can be used to pattern TiO_2 films and by thermodynamic phase transformation, changing the crystal phase from anatase to rutile. The cross sectional profile and depth of these ablated zones can be controlled by varying the power, ablation time, scanning speed, and focus spot size.

5.4. Summary

In this chapter we studied the effects of femtosecond laser ablation of P25 powders dispersed in water and electrophoretic deposited onto a FTO conductive substrate.

1) The experiments indicated that when laser ablation is performed in water, depending on the laser ablation time, it is possible to induce a phase transformation of the P25 nanoparticles from anatase to rutile and then back to anatase. Although, the phase transformation from rutile to anatase is thermodynamically impossible, when the sizes of the nanoparticles decrease, a change in the phase stability occurs. In particular, for particle sizes less than 11 nm, anatase will be the most thermodynamically stable phase. When the sizes are greater than 35 nm, rutile will result the most stable phase. At short ablation times, the particles size increased to slightly larger particle. After prolonged laser exposure up to 2 hours, the particles size start to decrease and consequently anatase particles were formed.

2) Together with phase transformation of the TiO_2 nanoparticles, an increase of energy band gap upon increase of the laser ablation time occurred. Through the investigation of the effects of the laser ablation on the TiO2 structure, it has been

found that the size of the nanoparticles could be controlled by varying the laser ablation time. These results highlight the possibility of using the laser ablation of TiO_2 as a tool for the bandgap engineering of these nanomaterials, which can be potentially employed in photocatalysis.

3) Phase transformation also occurs upon laser of P25 powder deposited onto FTO glass. Preliminary results showed that P25 powder can be patterned and due to phase transformation to rutile, the patterned areas possess a higher refraction index leading to the possibility of using these patterned substrates for the fabrication of light trapping layers.

PART 2

Synthesis

by

Electrochemical

Processes

Chapter 6. Carbon Materials for Next Generation Resistive Switching Memory Devices[15]

Overview

In the following chapter, is reported the study on the synthesis and modification of carbon-based memory devices by electrochemical processes. The aim of this study is to demonstrate that the electrophoretic deposition of carbon nanomaterials is an alternative straightforward and time effective technique for the fabrication of carbon-based devices, which can be employed as future non-volatile memory devices. The fabrication process we developed could overcome the current complex fabrication process of this type of memory devices, which impede their large-scale development. For the first time we reported about the resistive switching behavior of a new type of device made of carbon nanostructures electrophoretic-deposited on fluorine-doped tin oxide (FTO) substrate. This new device shows a forming-free bipolar resistive switching behavior, with a low operating voltage of 2 V and long retention time ($5x10^4$ s). The obtained results demonstrate the good reproducibility of the device's production process. The study of the resistive switching mechanisms of the fabricated carbon-based devices highlighted a relationship between chemical composition and electrical properties. It has been demonstrated that the device's electrical performances can be engineered with a control over fabrication process, which allows tailoring the materials' structure and composition. In particular, it has been shown for the first time that electrochemical oxidation is an engineering solution for the specific modification of the electrophoretic-deposited carbon structures. The oxidation of the carbon materials resulted to improve their electrical performances enabling multilevel current amplification behavior.

6.1. Introduction

Currently, much attention is being paid to resistive switching random access memory (RRAM) devices as alternatives for the next generation of non-volatile memories. The most common structure of a RRAM device consists of an insulator/semiconductor layer sandwiched between two metallic electrodes, a schematic of a typical RRAM device is shown in Figure 51a .

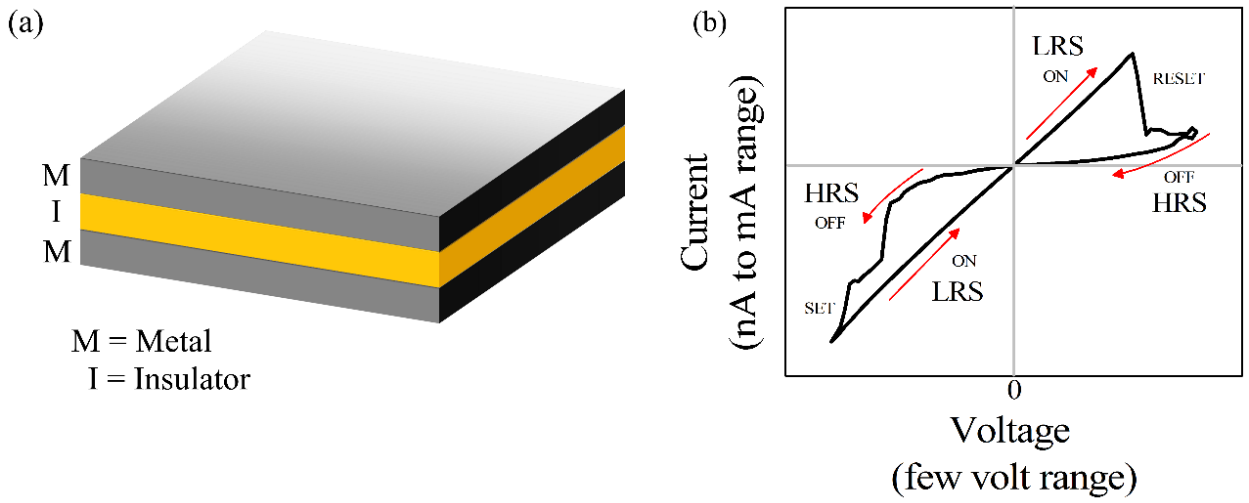

Figure 51: (a) Schematic of a typical RRAM device, (b) I-V curve typical of a bipolar resistive switching device

The resistive switching (RS) behavior in this type of device is due to a resistance change between high resistance state (HRS) and low resistance state (LRS) when a voltage across the electrodes is applied [290–295]. Bipolar switching devices display a characteristic hysteresis loop in their current-voltage curves, as displayed in Figure 51b. Initially the device is in its high-resistance state (OFF) and it is switched (SET) into a low-resistance state (ON) applying a certain voltage. The RESET into the OFF state takes place at reversed voltage polarity.

Different types of RRAM have been fabricated based on the different chemical composition of the insulator/semiconductor layer and the different type of electrodes used. The materials that have been used for RRAM devices span from perovskites to transition metal oxides such as TiO_2, NiO, and ZnO to chalcogenides and recently organic dielectric materials have been used [18,296–308]. Carbon materials, such as graphene oxide (GO) [309,310], reduced graphene oxide (rGO) [311,312] and carbon nanotubes (CNTs) [313,314] are attracting growing interest in nanoelectronics as alternatives to traditional silicon-based electronics due to their unique electrical characteristics, optical transparency and flexibility [315–318]. It has been reported that tetrahedral amorphous carbon films, graphene oxide and carbon nanotubes show resistive switching behavior, opening the possibility for their application for next-generation non-volatile memory devices [314,319–324], due to their high operation speed and scalability [309,325–327]. The underlying resistive switching mechanisms in RRAM devices depend on how the electron transport takes place in the sandwiched structure, which can be attributed to a large variety of physical and/or chemical phenomena. The mechanisms can be divided depending on whether the

dominant contribution derives from a thermal, an ionic or an electronic effect [328,329]. It has been widely demonstrated that the presence of lattice defects in the switching layer plays a key role in the resistive switching performance of the RRAM devices [329]. The most common resistive switching mechanisms proposed in the current literature are: formation and rupture of conductive filaments induced by redox reactions [312,330], Schottky emission, space-charge-limited conduction (SCLC) controlled by the presence of defects in the materials, i.e. oxygen vacancies, which create charge-carrier traps, Pool-Frenkel emission [331–333], and trap-assisted tunneling where the RS originates from the electronic charge injection and/or charge displacements effects [290,292,293,328,334,335]. Recently, Ageev and coworkers published an interesting study on the resistive switching behavior of vertically aligned carbon nanotubes (VA CNT) under scanning tunneling microscopy (STM), induced by a distortion of the nanotubes upon the application of a voltage [313,314]. It was reported that the resistance ratio between the HRS and LRS was voltage dependent and reached 25 when 8 V was applied to the STM probe/VA CNT. However, no further studies on the main electrical performance parameters (i.e. endurance, retention time) have been carried out on VA CNT. In this connection, carbon nanowalls (CNWs) are two-dimensional nanomaterials made of graphene layers that instead of being rolled up as in VA CNT; they are vertically stacked onto a substrate leading to the formation of graphene "walls" [336]. These nanomaterials possess the characteristic properties of graphene together with unique characteristics induced by the presence of sharp edges and high surface area, which enable CNWs to be employed as field emitters, catalyst support, capacitors and in Li-ion battery fabrication [62,64,65,337–339]. Moreover, it is well known that graphene-like systems possess high electrical conductivity along the basal plane, and the CNWs, due to their perpendicular orientation structure, possess an enhanced electrical conductivity compared to graphene which promises to be employed for devices fabrication [340]. To the best of our knowledge, no studies have been performed on whether CNWs can be employed for the application of memory devices. In this study, we report for the first time the resistive switching behavior of a new type of device made of electrophoretic-deposited CNWs on FTO substrates. As aforementioned, carbon-based RRAM are promising candidates for non-volatile memory applications [309–312,318,332,333,341], however, one of the disadvantages that hamper their development on a large scale is their fabrication processes, which involve high temperatures and pressures and the use of chemicals harmful for the environment [317]. Consequently, a new,

simple, fast, cost effective and eco-friendly method for the fabrication of carbon-based electronics is needed in order to enable their broad production. The study presented here, shows that CNWs devices can be fabricated by electrophoretic deposition of a solution of polyynes obtained by arc discharge on FTO substrates. This resulted to be a straightforward, time effective and green approach for the fabrication of carbon-based devices. The Al/CNWs/FTO device shows a forming-free bipolar RS behavior, with a low operating voltage of 2 V and long retention time (5×10^4s). The results demonstrate the good reproducibility of the device's production and that the electrical performances can be tailored with a systematic control of the fabrication parameters. In particular, the electrical properties of the carbon-based devices could be improved if a control over the chemical composition of the carbon material is performed. Preliminary results suggested that the electrochemical oxidation of the electrophoretic-deposited carbon structures lead to a device with improved electrical performances. The electrochemical treatment has been widely used as a technique to study the redox processes involved in the resistive switching mechanisms of different types of RRAM [342–344] and to increase the electrochemical capacitance of carbon materials by the introduction, on the surface of materials, of oxygen functional groups at room temperature [345,346]. To our best knowledge, it has not been used as a tool to improve the electrical performances of carbon-based RRAM devices. Here, we demonstrate that with a proper control over the chemical composition of the carbon materials by electrochemical route it is possible to engineer their structure in order to improve their electrical performances, confirming their potential as a resistive switching material. Moreover, we demonstrate that, since the material we synthesized is easier to obtain than the widely used GO, this approach can be helpful for the large-scale development of carbon-based memory devices and can be extent to be used to tailor the chemical composition of other carbon materials such as graphene, carbon nanotubes and so on.

6.2. Experimental

The carbon nanowalls were obtained upon electrophoretic deposition of a solution of polyynes, which are linear carbon chains containing sp-carbon atoms [347]. The polyynes acted as building blocks for the fabrication of the carbon nanowalls and a similar fabrication method has been already published employing polyynes obtained by laser ablation of a graphite target and then

deposited by electrophoresis [69]. The details about the synthesis of polyynes and their EPD for the synthesis of the CNWs are given below.

Synthesis of the polyynes: In this work the polyynes were obtained by arc discharge in water between two graphite electrodes having a diameter of 10 mm and length 70 mm [81,347,348].

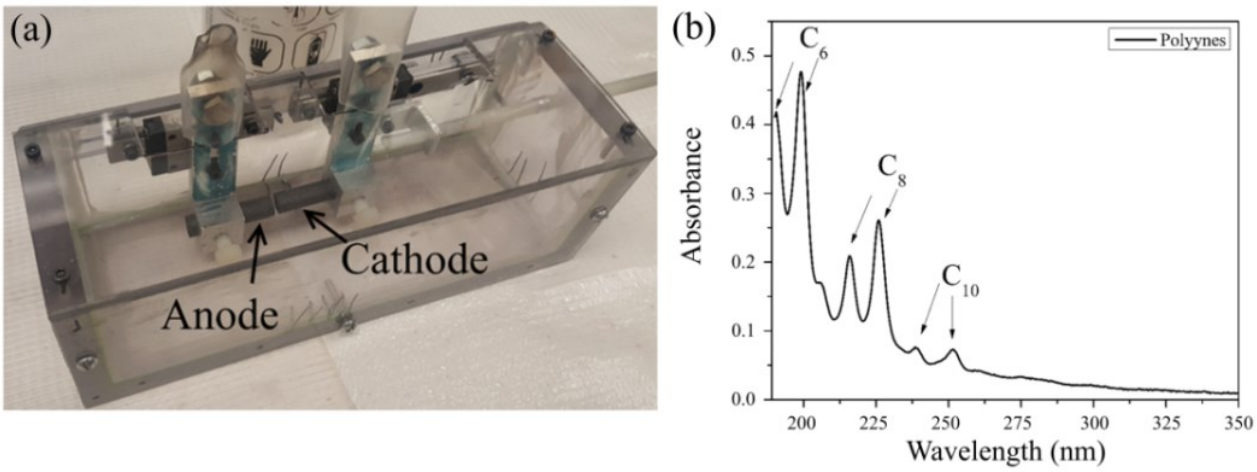

Figure 52: (a) Arc discharge setup employed for the synthesis of polyynes. The arc discharge was maintained between two graphite electrodes for 10 minutes; (b) UV-VIS spectrum of polyynes obtained upon arc discharge of two graphite electrodes in water. Reprinted from [15], with permission from Elsevier

The arc discharge between the electrodes was maintained for 10 minutes at a voltage of 30 V. In Figure 52a the picture of the arc discharge setup is displayed while in Figure 52b is shown the UV/VIS spectrum of the obtained polyynes. In particular, polyynes containing 6, 8 and 10 carbon atoms per chain were produced [349].

Synthesis and deposition of the carbon nanowalls: The polyynes solution was transferred in a glass beaker and two pieces of FTO/glass substrate were used as electrodes and submerged in the polyynes solution. The distance between the two electrodes during the electrophoretic deposition was kept at 5 mm. The FTO substrates, with a resistance of ~10 Ω sq^{-1}, before the polyynes deposition and fabrication of the CNWs, were cleaned in acetone, ethanol and isopropyl alcohol respectively and dried under nitrogen gas flow. The CNWs deposition occurred at the cathode upon application of a voltage of 30 V at the electrodes for 1 hour. The CNWs/FTO substrate was then annealed at 150°C for 1 h in Argon gas, in order to remove the trapped water. Three types of heat treatments of the CNWs have been carried out: heat treatment at 150°C in argon, in air and in argon followed by heat treatment in air.

Fabrication of the memory device: Al top electrodes with 100 nm thickness and 1 mm diameter were deposited by an e-beam evaporation process on the CNWs surface.

6.2.1. Instrumentation

Scanning Electron Microscopy (SEM) analyses have been performed using a ZEISS LEO 1550 FE-SEM at an accelerating voltage of 5 kV. The X-ray photoelectron spectroscopy (XPS) analysis was carried out using a multi-technique ultra- high vacuum imaging XPS microprobe spectrometer (Thermo VG Scientific ESCALab 250) with a monochromatic Al-Ka 1486.6 eV X-ray source. The spectrometer was calibrated by Au 4f7/2 (binding energy of 84.0 eV) with respect to the Fermi level. The chamber vacuum level was maintained below $2x10^{-10}$ Torr. The carbon nanowalls were analyzed using a Renishaw In Via micro-Raman spectrometer, employing an excitation laser with a wavelength of 633 nm, and the spectra were acquired with a 50x objective at a laser power of 0.1 mW. HRTEM observation was conducted using a JEOL 2010F at the Canadian Centre for Electron Microscopy (Hamilton, Ontario, Canada). TEM samples were prepared by scratching the samples onto lacey carbon grids. Electrical measurements have been performed with a Keithley 2602A source meter at ambient conditions.

6.3. Results and Discussion

The new CNWs-memory devices were fabricated in three steps using arc discharge and electrophoretic deposition (EPD) for the synthesis and deposition of CNWs on FTO substrate, respectively. Arc discharge in water of two graphite electrodes was employed for the production of a solution of polyynes, which are linear carbon chains of sp-carbon atoms [81,347,348]. These nanomaterials were then used as building blocks for the synthesis of the CNWs; indeed polyynes have a strong tendency to interchain crosslinking. The EPD was used for the synthesis/deposition of CNWs on FTO substrate, since it has been demonstrated as an excellent method to deposit carbon nanomaterials for forming free RRAM devices [327]. FTO substrates were used as electrodes and immersed in the polyynes solution. Upon application of the electric field, the polyynes are transported at the cathode and undergo interchain crosslinking reactions leading to the formation of hexagonal-graphene like sp^2 carbon structures perpendicular to the electrode's surface, *i.e.* the CNWs [74,350]. After heat treatment in Argon at 150 °C for 1 hour, the final step of the fabrication process was the deposition of Al top electrodes on the CNWs/FTO substrate by e-beam evaporation. The production method we developed is more user-friendly, cost-effective and eco-friendly compared to the current fabrication methods employed for the synthesis of carbon-based electronic devices, since no high temperatures or high pressures and

poisonous chemicals are needed [317]. Figure 53a displays a schematic of the structure of the Al/CNWs/FTO devices fabricated, while in Figure 53b a schematic of the EPD process is displayed.

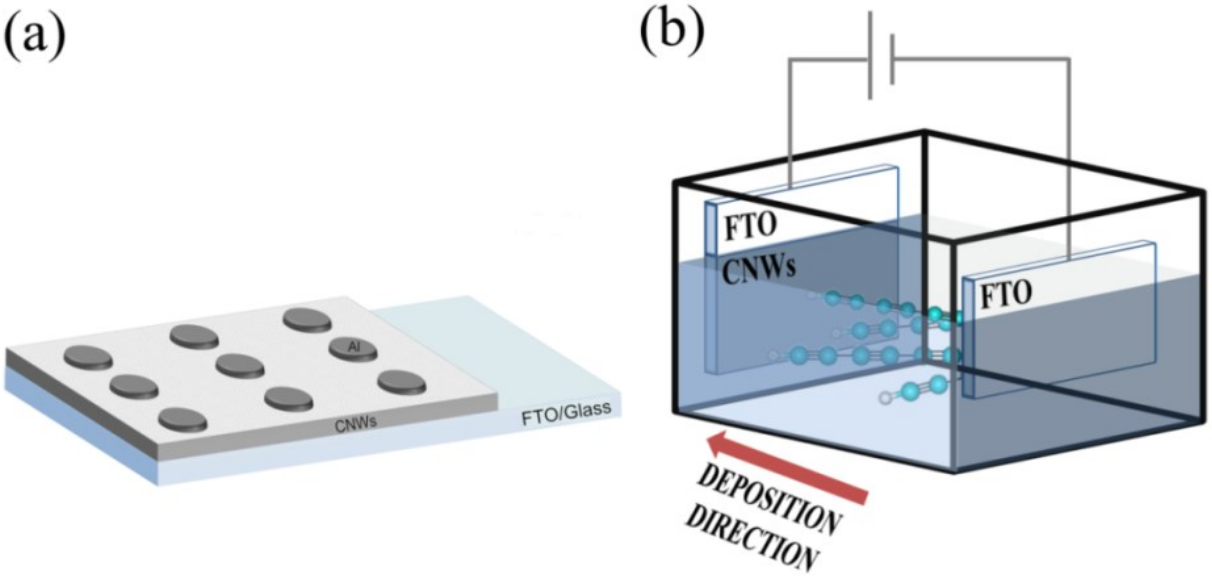

Figure 53: (a) Schematic design of the structure of the Al/CNWs/FTO device, (b) schematic of the apparatus for the EPD of polyynes in order to obtain the CNWs. Reprinted from [15], with permission from Elsevier

The top-view SEM image of the CNWs obtained after the EPD of polyynes on FTO substrate is shown in Figure 54a, which confirmed that the CNWs are uniformly distributed over the substrate area.

In Figure 54b is displayed the magnified SEM image of the CNWs. The SEM images show the typical morphology of the carbon nanowalls, where the branched 2-dimensional carbon sheets are clearly shown.

Figure 54c presents the C1s XPS spectrum of the electrophoretic fabricated CNWs. The C1s peak was fitted using a Gaussian-Lorentzian curve to four components in which the peak located at 284.35 eV indicates the presence of sp^2 carbon atoms (C=C), the peak at 285.04 eV is attributed to sp^3 carbon atoms (C-C), while the peaks at 286.03 eV and 287.87 eV can be ascribed to (C-OH) and (-O-C=O) groups respectively [69,351]. As shown in the inset in Figure 54c, the percentage of sp^2 carbon atoms is 56.46 %, while the ratio relative to sp^3 carbon atoms is 19.01 %, due to the presence of defect sites or edges [352]. The presence of 10.34 % of hydroxyl groups and 14.19 % of (-O-C=O) groups also suggest that a mild oxidation of the carbon nanowalls occurs during the fabrication process. The formation of defects and presence of

oxygen-containing groups upon fabrication of CNWs by EPD is crucial for the resistive switching behavior of the device [328,329]. The CNWs were analyzed by Raman spectroscopy with an excitation wavelength of 633 nm and the relative spectrum is displayed in Figure 54d.

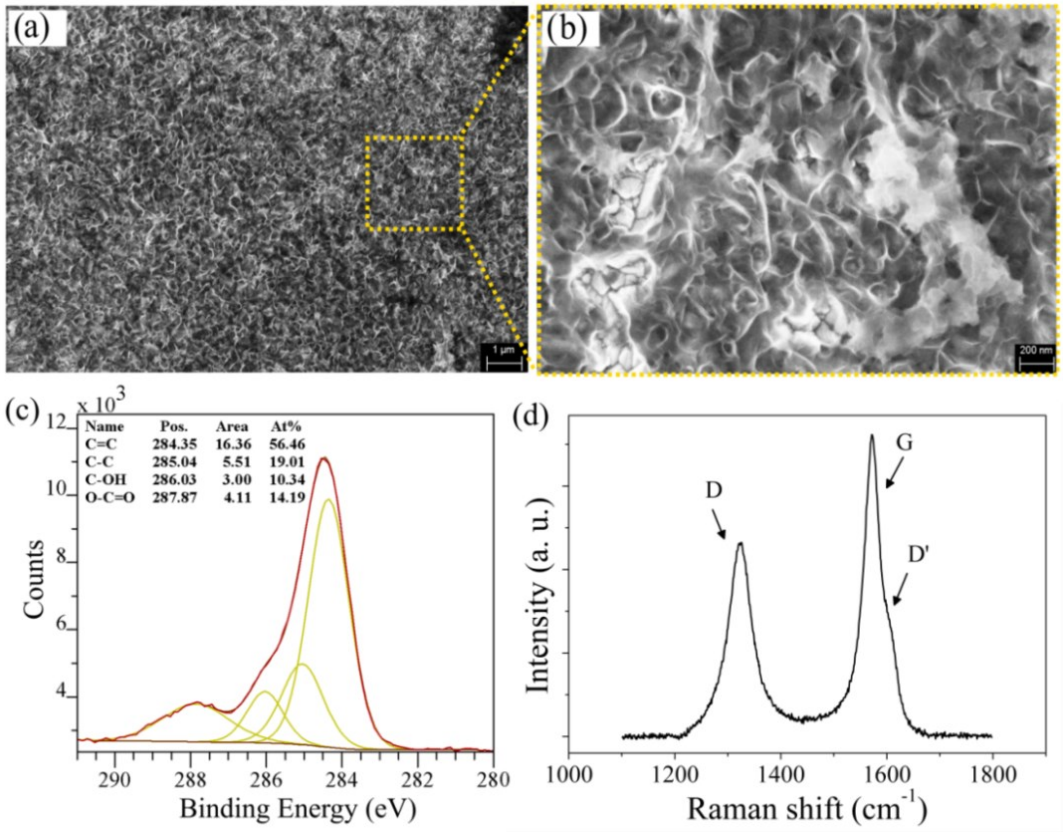

Figure 54: a) SEM image of the surface morphology of the CNWs prepared by EPD of polyynes. b) Magnification of the CNWs surface morphology. c) C1s XPS and (d) Raman spectrum of the CNWs. Reprinted from [15], with permission from Elsevier

It is possible to notice, that the Raman spectrum obtained is the one characteristic of CNWs, as reported by Kurita and Wang [353,354]. In particular, it can be observed the characteristic D band originated by the presence of defects and the G band, which arises from the in-plane vibration of sp^2 carbon atoms. As reported by Kurita [353], the narrow G band (~37 cm^{-1}) is due to the presence of nanowalls made of small crystallites with high degree of graphitization. In addition to these bands, a weak band is also observed corresponding to D' band originated by the presence of disorder. The length of the carbon nanowalls can be correlated to the I_D/I_G ratio, since it increases with decreasing the CNWs [353]. The I_D/I_G ratio of the CNWs is 0.95 (see Table 7) and based on the literature the length of our CNWs should be around 1.8 μm [353]. It is also reported that a decrease of the I_D/I_G ratio occurs upon addition of O_2 [66,354]. From Figure

54b it is possible to notice that the CNWs are smaller in length than 1.8 μm, therefore the low I_D/I_G ratio could be attributed to the presence of oxygen groups which induce a mild oxidation of the CNWs.

Table 7: CNWs band positions and I_D/I_G ratio. Reprinted from [15], with permission from Elsevier

	D band	G band	D' band	I_D/I_G
Position	1324 cm^{-1}	1572 cm^{-1}	1607 cm^{-1}	0.95
Width (FWHM)	53	37	20	

From the TEM results displayed in Figure 55it is possible to notice that, the CNWs are made of 8-10 graphene layers with a d-spacing of 0.34 nm, which is the interlayer distance in graphite.

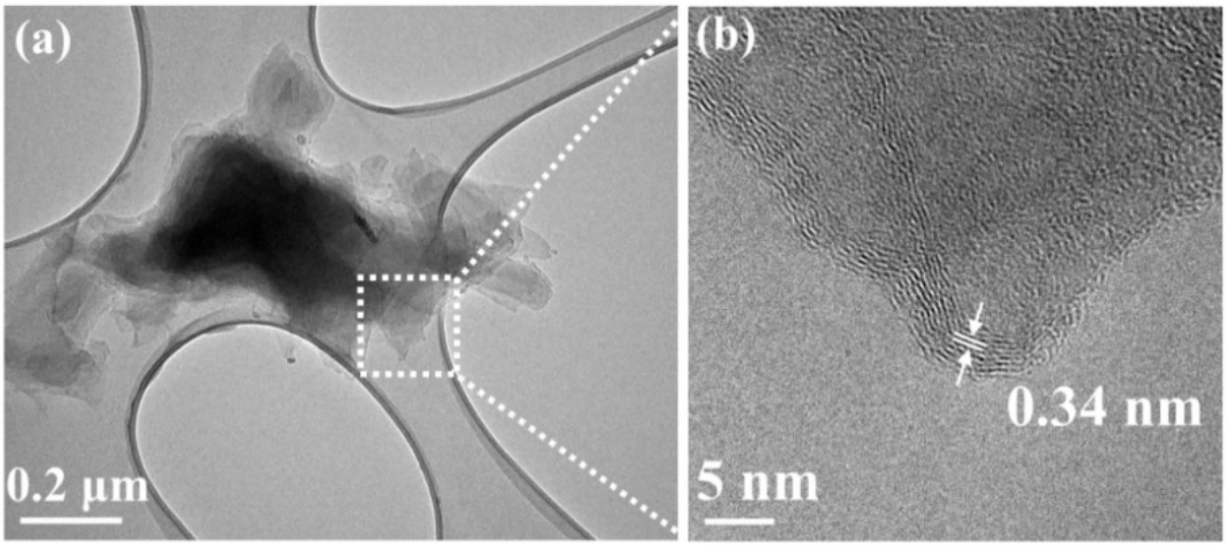

Figure 55: (a) TEM image of the CNWS and (b) HRTEM of the carbon nanowalls displaying an interlayer distance of 0.34 nm, which is the d-spacing of graphite. Reprinted from [15], with permission from Elsevier.

These results together with the SEM and Raman analysis, confirm the synthesis of carbon nanowalls. The electrical performance of the fabricated Al/CNWs/FTO devices was investigated by applying the sweep voltages of 0V → 2V → 0V→ -2V → 0V. Figure 56a demonstrates the typical bipolar resistive switching behavior of the new developed device obtained under direct sweeping operations for 1 and 150 cycles. It was found that the Al/CNWs/FTO device was initially in the LRS and the device maintained this state during the voltage sweeping from 0 to 2V. The reason might be due to the dominance of sp^2 carbon atoms over the sp^3, providing high

conducting channels in the CNWs [310], as confirmed by XPS study in Figure 54c. Moreover, as aforementioned, the vertical orientation of the CNWs parallel to the electrons flow causes a higher conductivity [340], leading to the initial LRS in our I-V current response. The device switches to the HRS during the voltage sweeping from 2 V to 0 V, which means that the RESET process occurs. The HRS remained after the negative voltage was applied until the negative voltage is high enough to transition the device from HRS to LRS. It should be noted that the resistive switching performance for our devices does not require the commonly used electroforming step [310], desirable for the ReRAM devices due to the simplifying electrical operation.

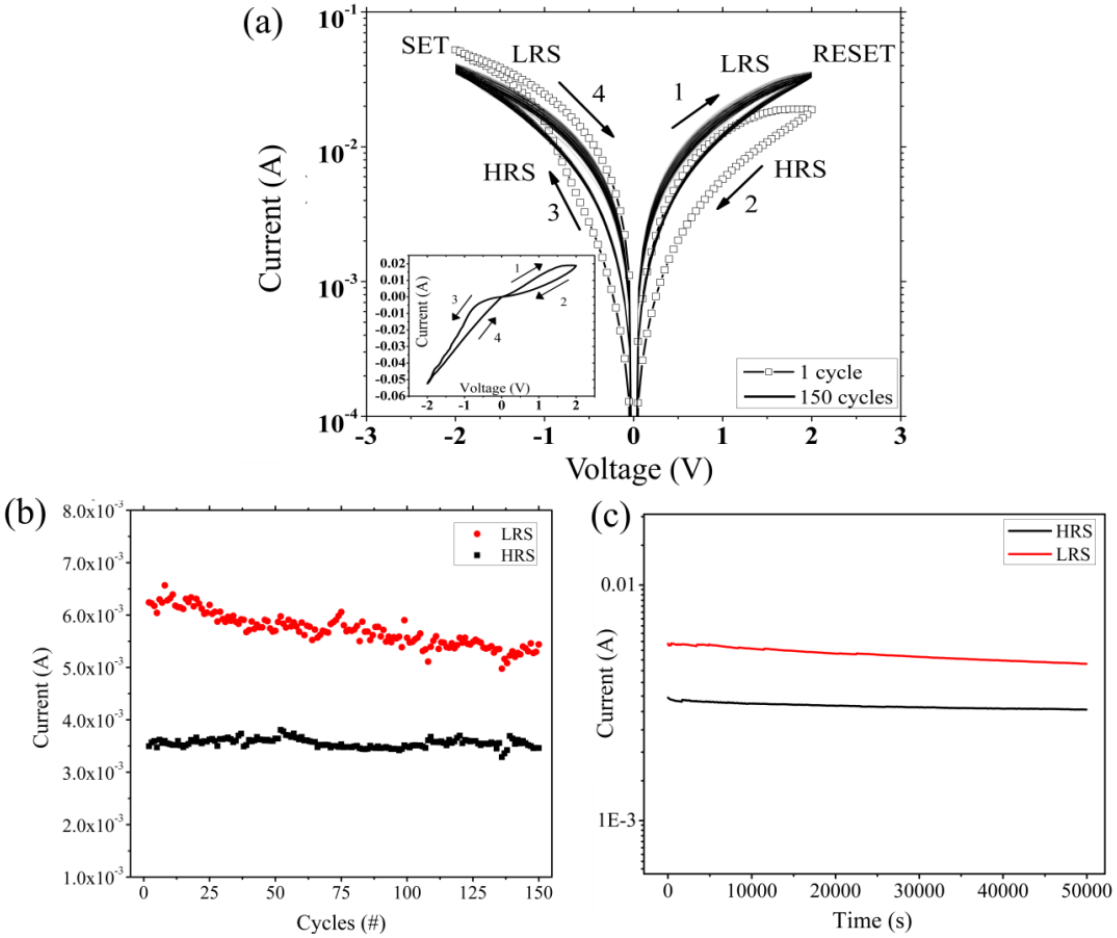

Figure 56: a) I-V curve of Al/CNWs/FTO device for first and 150 cycles of voltage sweeping. Arrows and numbers indicate the direction and sequence for the I–V scan. b) Endurance results of the device for over 150 cycles at 0.4V. c) Retention result over 5×10^4 seconds at a read voltage of 0.4V. Reprinted from [15], with permission from Elsevier

We have observed that the I-V curve obtained after 150 cycles is different from the one obtained after only one cycle and we hypothesize this could be attributed to a rearrangement of the oxygen

atoms in the CNWs structure induced by the first voltage sweep. The reset and set currents slightly changed after the first cycle and stabilized with increasing the number of cycles. After 150 cycles it was still possible to distinguish the LRS and HRS, suggesting that this new type of device could be employed as RRAM in future memory devices. The results of the cycling performance are shown in Figure 56b at the read voltage of 0.4V. Over 150 cycles we found that the difference between the LRS and HRS firstly decreased but the difference remained constant with increase in the number of cycles probably as a consequence of the stabilization of CNWs structure, suggesting a promising durability of the new device. Figure 56c shows the retention results measured at room temperature. Over the time period of 5×10^4 seconds, the currents for HRS and LRS, respectively measured at 0.4 V were stable, confirming the non-volatile nature of the device.

It is important to explore the origin of the RS effect in this new type of CNWs-based device. Based on the type of the dielectric layer sandwiched between the electrodes, the RS behavior has been explained with different types of mechanisms [292,295,334]. In order to study the RS mechanism in our device, the I-V curves have been fitted to the different mechanisms and among them, we found that the trap-controlled SCLC mechanism, which is controlled by the presence of defects, best fit our device. The structural defects are related to the following mechanism for the formation of the CNWs upon EPD of polyynes. As aforementioned, polyynes are characterized by an extremely high reactivity with oxygen and a strong tendency to interchain crosslinking. Therefore, when polyynes are transported at the surface of electrode upon application of the electric field, interchain crosslinking reactions occur leading to the synthesis/deposition of CNWs [74,350]. The deposition process and the crosslinking reactions might lead to the formation of defective carbon structures (pentagon rings) with missing carbon atoms, which results in the formation of defect sites in the CNWs. The presence of defect sites and oxygen is confirmed by the observation of the peak at 285.04 eV attributed to sp^3 carbon atoms (related to the presence of defect sites) and the peaks at 286.03 eV and 287.87 eV (related to oxygen containing carbon groups), as seen in the XPS spectrum in Figure 54c. Therefore, we hypothesize that due to the presence of structural defects and oxygen in the CNWs, the RS effect observed in our new device can be explained with the trap-controlled SCLC mechanism. In order to verify this hypothesis, we replotted the I-V curves of the device heat treated in argon in double-logarithmic scale as shown in Figure 57.

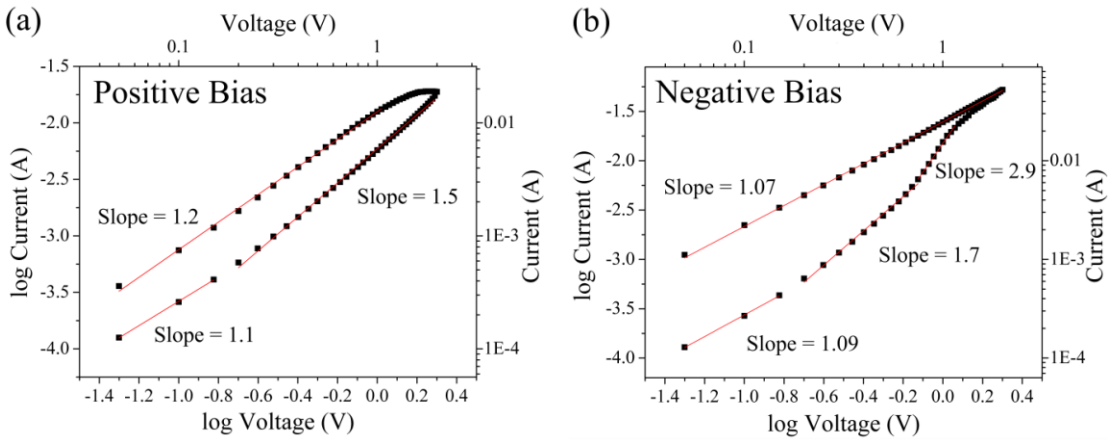

Figure 57: SCLC I-V characteristics of the Al/CNWs/FTO device plotted in double-logarithmic scale for the a) postive and b) negative bias. Reprinted from [15], with permission from Elsevier

The I-V curve characteristic of trap-controlled SCLC can be easily recognized since the HRS consists of three portions: (i) Ohmic region ($I \propto V$) observed at low field; (ii) the Child's Law region ($I \propto V^2$); (iii) steep current increase observed at high field [334].

It can be seen that the I-V curves are in agreement with the trap-controlled SCLC mechanism. In particular, under positive voltage the LRS follows the Ohm's law conduction mechanism with a slope ~1, i.e., current varies linearly with applied voltage, while the HRS consists of two regions. At low voltage the current conduction follows the Ohm's law with a slope of ~1 and at higher voltage the Child's law conduction mechanism is dominant, suggesting that the switching mechanism is controlled by the trap-controlled SCLC. The slope value is lower than the one reported for the Child's law mechanism, however lower slope values have been recorded in case of conjugated polymers and CNWs are made of conjugated carbon atoms [355]. Under negative voltage, the LRS was found to follow the Ohm's law, while the HRS showed three regions: at low voltage the conduction mechanism followed the Ohm's law with a slope of 1. The intermediate region represents the transition between Ohm's and Child's law conduction mechanisms [356]. The third region with slope 2.9 was seen to correspond to the Child's law region [356].

From the above results, we determined that the initial state of the device is LRS due to: (i) existence of defects sites, i.e. oxygen vacancies, which act as trap centers for the electrons and (ii) the perpendicular orientation of the CNWs on the FTO substrate, which enhances the electrical conductivity. Therefore, upon the application of a positive bias the electrons could flow along the filled oxygen vacancies from the bottom FTO electrode to the top Al electrode without

the requirement of a forming step. Upon the application of negative bias, a de-trapping process of electrons from the oxygen vacancies occurs, which causes the device to transition from LRS to HRS. A schematic of the RS mechanism is shown in Figure 58**.**

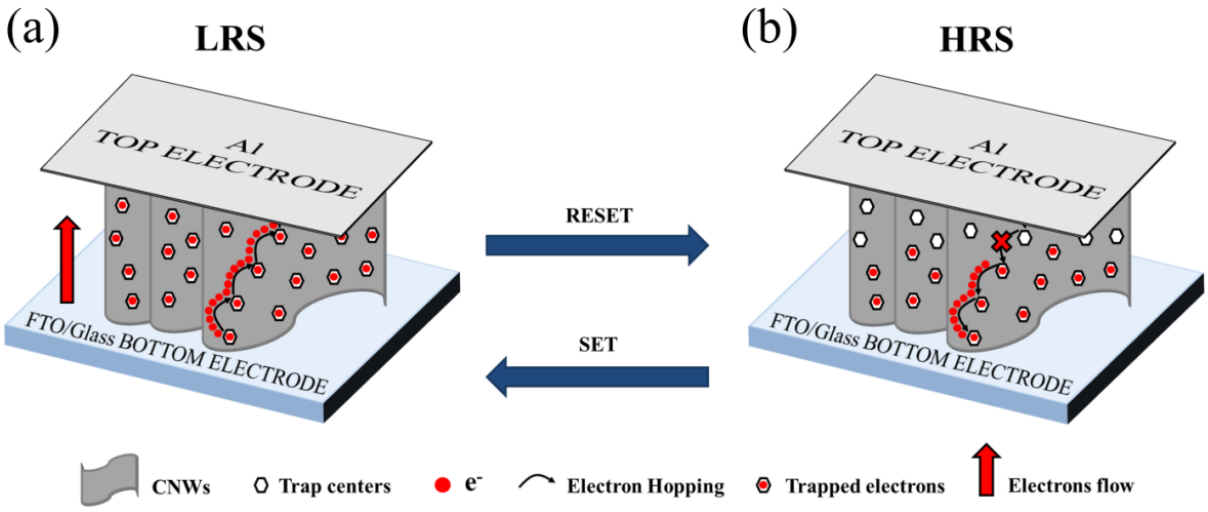

Figure 58: Schematic showing the RS mechanism of the Al/CNWs/FTO device. (a) The LRS after applying a positive bias. The electrons flow along the filled oxygen vacancies from the bottom FTO electrode to the top Al electrode without the requirement of a forming step. (b) Transitioning from LRS to HRS caused by a de-trapping process of electrons from the oxygen vacancies upon application of a negative bias. Reprinted from [15], with permission from Elsevier

These preliminary results indicated that the morphology of CNWs plays a key role in the electrical performance of the device. In particular, we showed that the presence of defects sites, i.e. oxygen vacancies, is vital for the RS behavior of the CNWs based devices. Therefore, it was of interest to try to engineer the concentrations of defects in the CNWs structure and study how the RS performance is affected. Heat treatment of carbon nanomaterials is a way that can be employed for the modulation of oxygen containing groups [46], which might affect the RS behavior. Therefore, after 1 hour of deposition of CNWs by EPD on FTO substrate, the substrate was heat treated at 150 °C in air at ambient pressure. The electrical performance was then investigated and compared to the sample heat treated in argon at 150 °C. In Figure 59 are shown the I-V characteristics of the device heat treated in air under the voltage sweep of 2V.

Figure 59a shows that the RS behavior is similar to the device heat treated in argon, with the device initially in the LRS state.

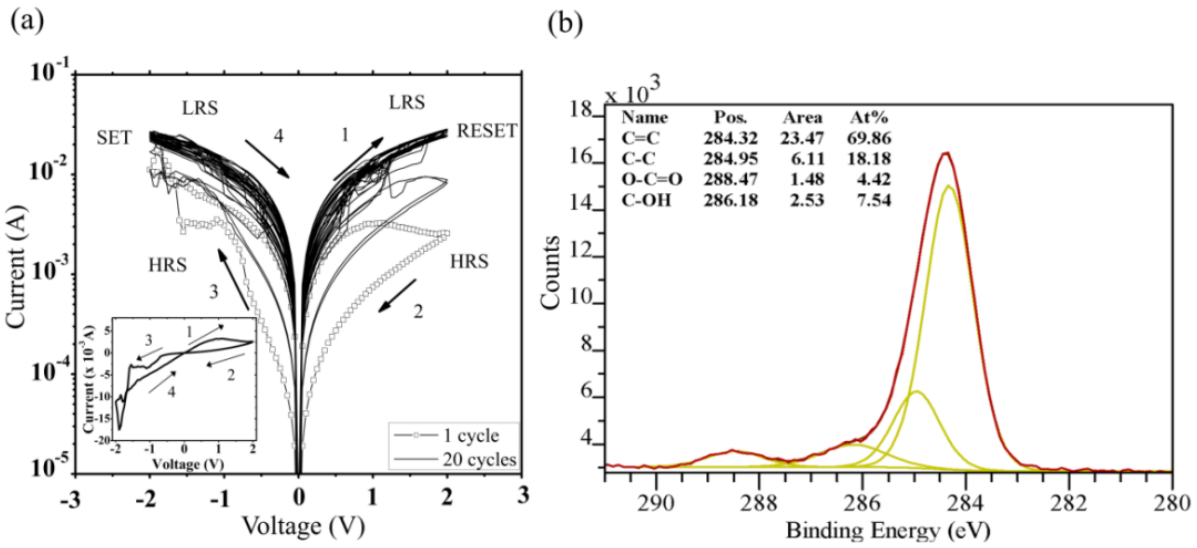

Figure 59: a) Resistive switching characteristic after 1 and 20 cycles of the Al/CNWs/FTO device heat treated in air. b) C 1s XPS spectrum of the CNWs heat treated in air. Reprinted from [15], with permission from Elsevier

Noteworthy, the LRS/HRS ratio after one voltage sweep at 2 V was higher for the sample heat treated in air than the one heat treated in argon (LRS/HRS of 7 and 3 respectively at the read voltage of 0.4V); however, the device did not show a good endurability. In particular, after few cycles the device became unstable and the LRS and HRS became undistinguishable, as displayed in Figure 59a. Clearly, this demonstrates that the heat treatment conditions after the deposition process play a key role in the stability of the device. The reason for the instability of the device might be the presence of a higher percentage of sp^2 carbon atoms and a lower percentage of oxygen containing carbon groups after the treatment in air atmosphere. In Figure 59b the XPS spectrum of C1s is displayed together with the atomic percentages (inset) of carbon atoms and carbon groups detected in the sample. It was found that compared to the XPS spectrum of the sample heat treated in argon (Figure 54c), in the sample treated in air the percentage of sp^2 carbon atoms increased by ~ 24%, while the percentage of hydroxyl groups and carboxyl groups were 7.54% and 4.42%, respectively. This result suggests, supported by the current literature, that the heat treatment in air at 150 °C induced a reduction of the CNWs [357], leading to a restoration of the sp^2 hybridization and a decrease in the oxygen containing groups. The heat treatment in air leads to more conductive and less defective CNWs in term of oxygen containing groups compared to the CNWs heat treated in argon and this could be the reason for the instability of the device. In particular, as aforementioned, the presence of defects, i.e. oxygen vacancies, plays a key role in the RS behavior of our device and the fact that the heat treatment

in air led to CNWs with less content of oxygen and higher content of sp^2 carbon atoms might affect the RS behavior. This result leads us to the hypothesis that the fabrication of CNWs with a smaller percentage of sp^2 carbon atoms and higher percentage of oxygen containing carbon groups could lead to more stable devices [310].

In order to confirm our hypothesis a preliminary experiment was carried out with heat treatment of the CNWs first in argon, in order to remove the trapped water molecules, followed by heat treatment in air at 150°C. In Figure 60a, the I-V characteristics after sweeping a voltage of 2 V for 1 cycle and after 20 cycles are displayed. We noticed that after one cycle the LRS/HRS ratio reached a value of 9, however the device was not very stable and after few cycles the LRS and HRS collapsed. The retention experiment carried out at a voltage of 0.2 V showed that the device was able to maintain the LRS and HRS up to 2000 seconds with a ratio of ~10. Compared to the device heat treated only in argon and only in air, we found that the new type of heat treatment increased the LRS/HRS ratio but it did not result in an increase of stability in terms of endurability of the device. The XPS analysis (Figure 60c) showed that the heat treatment in argon and in air increased the sp^2 percentage compared to the CNWs heat treated only in argon, as well as the percentage of oxygen containing groups. From these preliminary results, we can assess that the control of the content of sp^2 carbon atoms and oxygen groups is crucial for the stability of the CNWs device. In particular, on one side a higher content of sp^2 carbon atoms leads to devices with a higher LRS/HRS ratio, which promise to be employed for the fabrication of high-density memory devices [295]. On the other side it seems that the increase of sp^2 carbon atoms together with the decrease of oxygen containing groups affect the RS behavior due to a decrease in the concentration of charge-carrier traps, which are vital for the RS behavior.

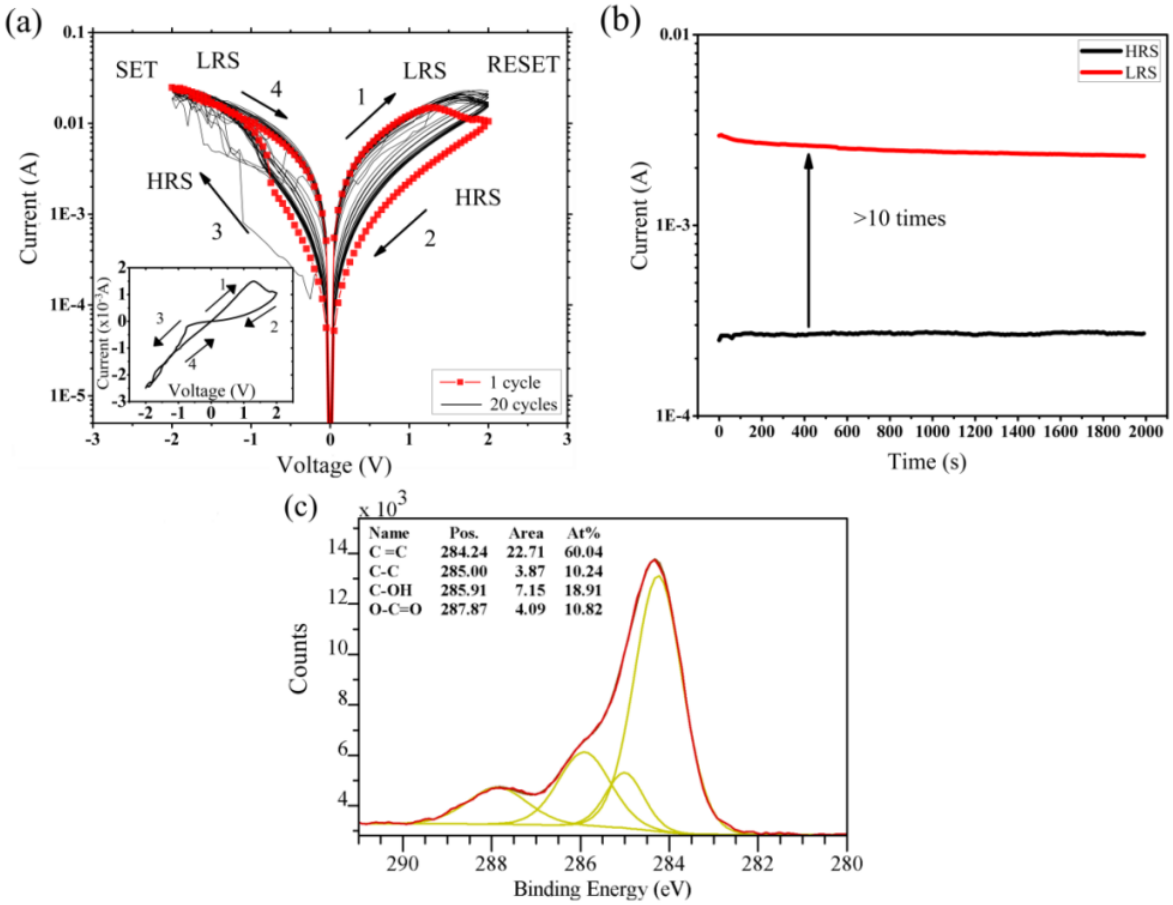

Figure 60: a) I-V characteristics after 1 and 20 cycles at a sweeping voltage of 2 V. b) retention of the device at 0.2 V. c) XPS spectrum of C 1s. Reprinted from [15], with permission from Elsevier

Therefore, our hypothesis is that highly oxidized carbon nanowalls, with a lower percentage of sp^2 carbon atoms might be employed for the fabrication of more stable memory devices.

For the first time we demonstrated the resistive switching behavior of a new type of device made of carbon nanowalls on FTO substrates via EPD. The electrical measurements indicate that the Al/CNWs/FTO device shows a forming-free bipolar RS behavior, with a low operating voltage of 2 V and long retention time (5×10^4s), confirming the non-volatile nature of the device. It has been demonstrated that oxygen vacancies play a key role in the resistive switching mechanism of this type of device acting as traps for the electrons. Indeed, the RS effect has been attributed to the trap-controlled SCLC mechanism. The fabrication method of CNWs by EPD is worthy of attention. Here we demonstrated that arc discharge in water followed by EPD can be employed for the synthesis of CNWs under environmentally friendly and timesaving conditions. It is clear that the device is still in its early stage of development, and we found out that heat treatment of

the deposited layer of CNWs plays a key role in the stability of the device. In particular, based on the experiments we found a dependence of the stability of the device on the oxygen content in CNWs. Therefore, we hypothesize that higher oxygen content might lead to much more stable electrical performance and with proper control of this parameter, this new type of materials can be employed for non-volatile memory devices and other carbon-based electronics.

Consequently, we performed new experiments were, after EPD of carbon structures (Cs) on FTO substrates, we studied the effect of the anodic oxidation on the electrical performances of the carbon-based devices.

6.4. Synthesis of the Cs

The Cs were prepared following the procedure described in Section 0 and 0. However, the deposition of the Cs on FTO was performed for 2 hours at a voltage of 30 V and current of 0.01 A. The Cs obtained at the cathode (Cs@FTO) were let dry at room temperature.

6.5. Electrochemical oxidation of the Cs

The as-prepared Cs@FTO samples were oxidized through anodic oxidation applying a potential in the range of [0-0.8] V vs. a saturated calomel electrode (S.C.E.) in 1 M sodium sulfate (Na_2SO_4) aqueous solution at room temperature. The electrochemical oxidation was carried out using a potentiostat/galvanostat (Gamry Potentiostat, Series 300) with a scan rate of 20 mV/s. The experiments were performed in a three-electrode quartz cell with the Cs@FTO sample as working electrode, a platinum wire as counter electrode and the S.C.E. as the reference electrode. After the electrochemical oxidation, in order to remove salt residues, the oxidized Cs (OCs@FTO) were rinsed with deionized water and dried at room temperature.

6.6. Results and discussion

Figure 61a shows the schematic of the three-electrode quartz cell employed for the oxidation of the Cs, while Figure 61b displayed the cyclic voltammogram (CV) curve of the Cs@FTO in the range [0-0.8] V at a scan rate of 20 mV/s.

The curve obtained in Figure 61b is independent of substrate material. Thus, the electrochemical oxidation of FTO substrate without the Cs deposition showed no oxidation peaks in the [0-0.8] V range, as displayed in Figure 61c. Therefore, the changes in the CV shape of the Cs have been

attributed to their structural modification, due to the oxidation of their surface. In particular, it is possible to notice a peak at a potential of 0.2 V, which is attributed to the formation of hydroxyl groups (-OH) upon electrochemical oxidation occurring at carbon defects sites according to the following reaction [358,359]:

$C + H_2O \leftrightarrow COH + H^+ + e^-$ E=0.207 V (1)

$C + H_2O \leftrightarrow CO + 2H^+ + 2e^-$ E=0.518 V (2)

The broad peak in the range of [0.3 - 0.5] V can be attributed to the formation of carbonyl, carboxyl (HO-C-C=O-), epoxy (O-C-O) groups at the surface of the Cs [345,359–361].

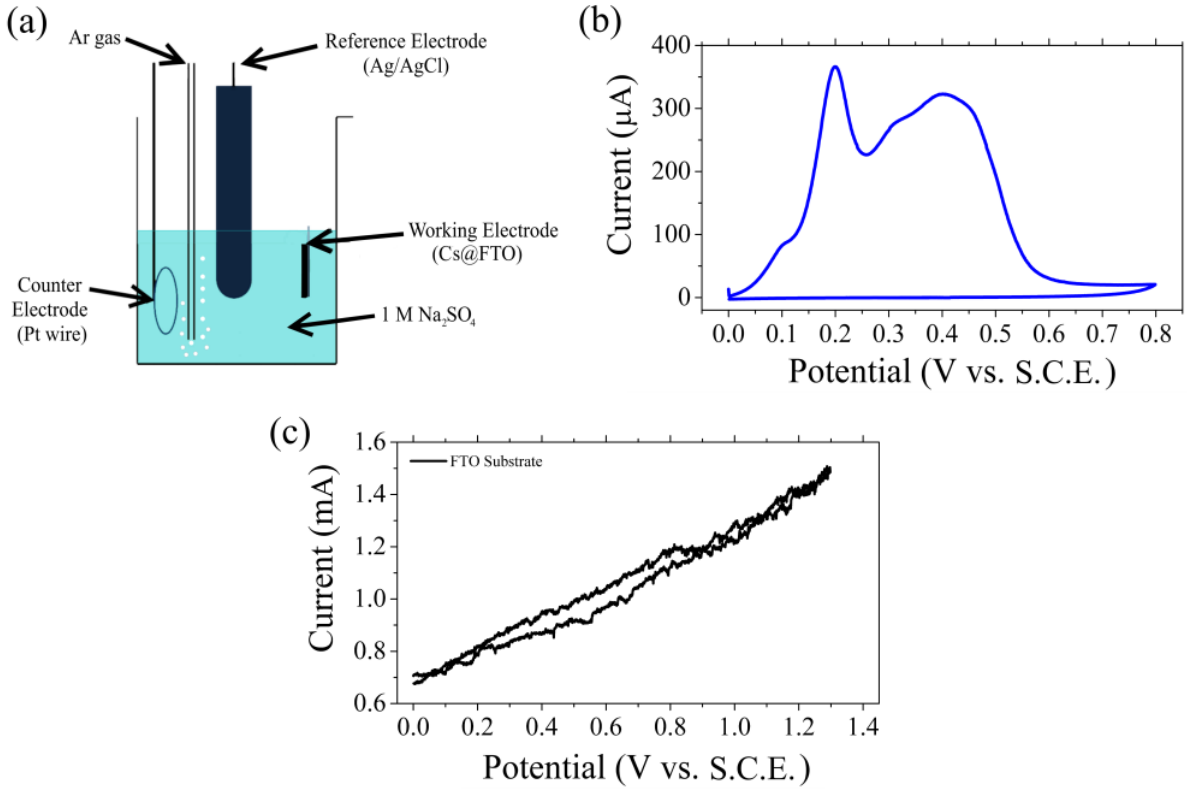

Figure 61: (a) Schematic of the three-electrode quartz cell employed for the oxidation of the carbon structures. (b) CV of Cs@FTO in 1 M Na_2SO_4 aqueous solution. the scan rate is 20 mV/s. (c) Electrochemical oxidation of the FTO substrate without the deposition of the carbon structures. It is possible to notice that the FTO surface has not been oxidized.

A schematic of the fabrication and modification process of the CN is displayed in Figure 62(a-c). Figure 62a shows the electrodeposition of the polyynes on the FTO substrate, which leads to the synthesis of the Cs through a bottom up approach (Figure 62b).

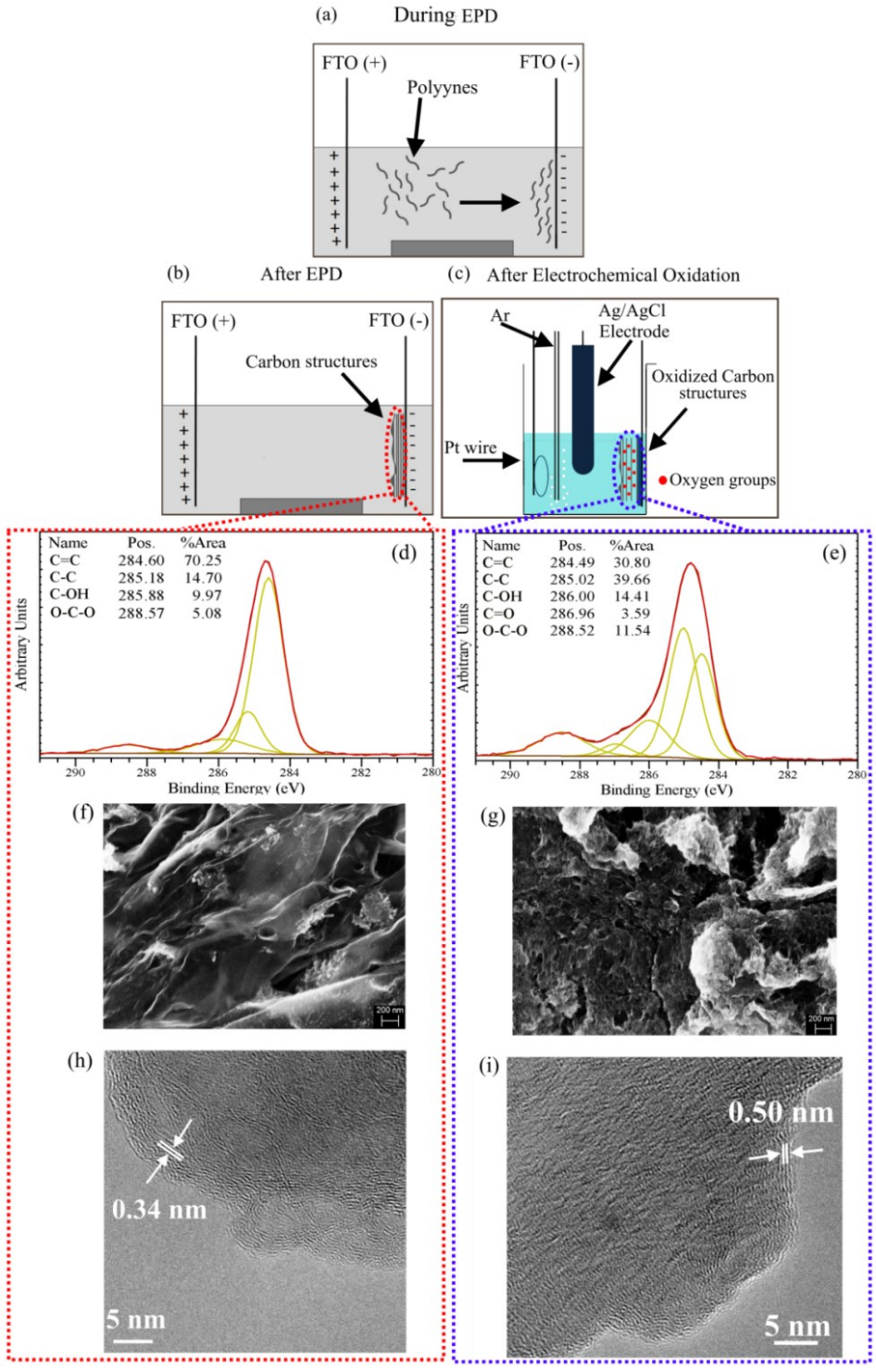

Figure 62: (a-b) schematic of the bottom up synthesis of Cs upon deposition of polyynes and (c) electrochemical oxidation of the synthesized Cs; (d, f, h) C 1s XPS spectra, SEM and TEM images of the Cs before and (e, g, i) after the electrochemical oxidation. In In (h-i) it is possible to notice that the d-spacing of the as-prepared Cs is 0.34 nm, which increases to 0.5 nm upon oxidation.

In order to confirm the structural modification of the Cs induced by the electrochemical oxidation (Figure 62c), we performed XPS, SEM and TEM characterization analysis on the samples before and after the oxidation treatment. The results are displayed in Figure 62(d-i). It is seen that as a result of the electrochemical oxidation a modification of the chemical composition of the Cs occurred. It should be noted, that the as-prepared Cs samples have a mild oxidation, probably due to their deposition by EPD [15]. The peak at 284.60 eV is attributed to C=C bonds, while the C-C bonds give rise to the peak at ~ 285 eV. The as prepared sample contains hydroxyl and epoxy groups and the related peaks are situated at 285.88 eV and 288.57 eV, respectively. The electrochemical oxidation, gives rise to the appearance of a new peak at 286.96 eV, which can be attributed to the presence of carbonyl group. From the comparison of the XPS spectra before (Figure 62d) and after (Figure 62e) the electrochemical treatment, it can be observed a decrease of the percentage of sp^2 carbon atoms attributed to C=C bonds and an increase of the percentage of sp^3 carbon atoms attributed to C-C bonds as a consequence of the oxidation of the Cs. Moreover, the percentage of hydroxyl groups and epoxy groups increased together with the appearance of the peak attributed to the carbonyl groups. These evidences are in agreement with the results obtained from the CV curve in Figure 61b.

The morphology and structure of the Cs before and after electrochemical treatment was investigated by SEM and TEM, as shown in Figure 62f-g and Figure 62h-i, respectively.

From the characterization analysis, it is possible to notice that the electrochemical oxidation of the Cs induced a transformation of the structure. In particular, it was observed that the oxidation of the Cs induced a modification of the morphology and an increase of the d-spacing from 0.34 nm, typical of graphitic structures, to 0.50 nm due to the presence of oxygen groups within the graphene layers, as sketched in Figure 62c by the red dots between the layers [362,363].

The TEM cross section analysis, displayed in Figure 63 and Figure 64 further confirmed the oxidation of the Cs.

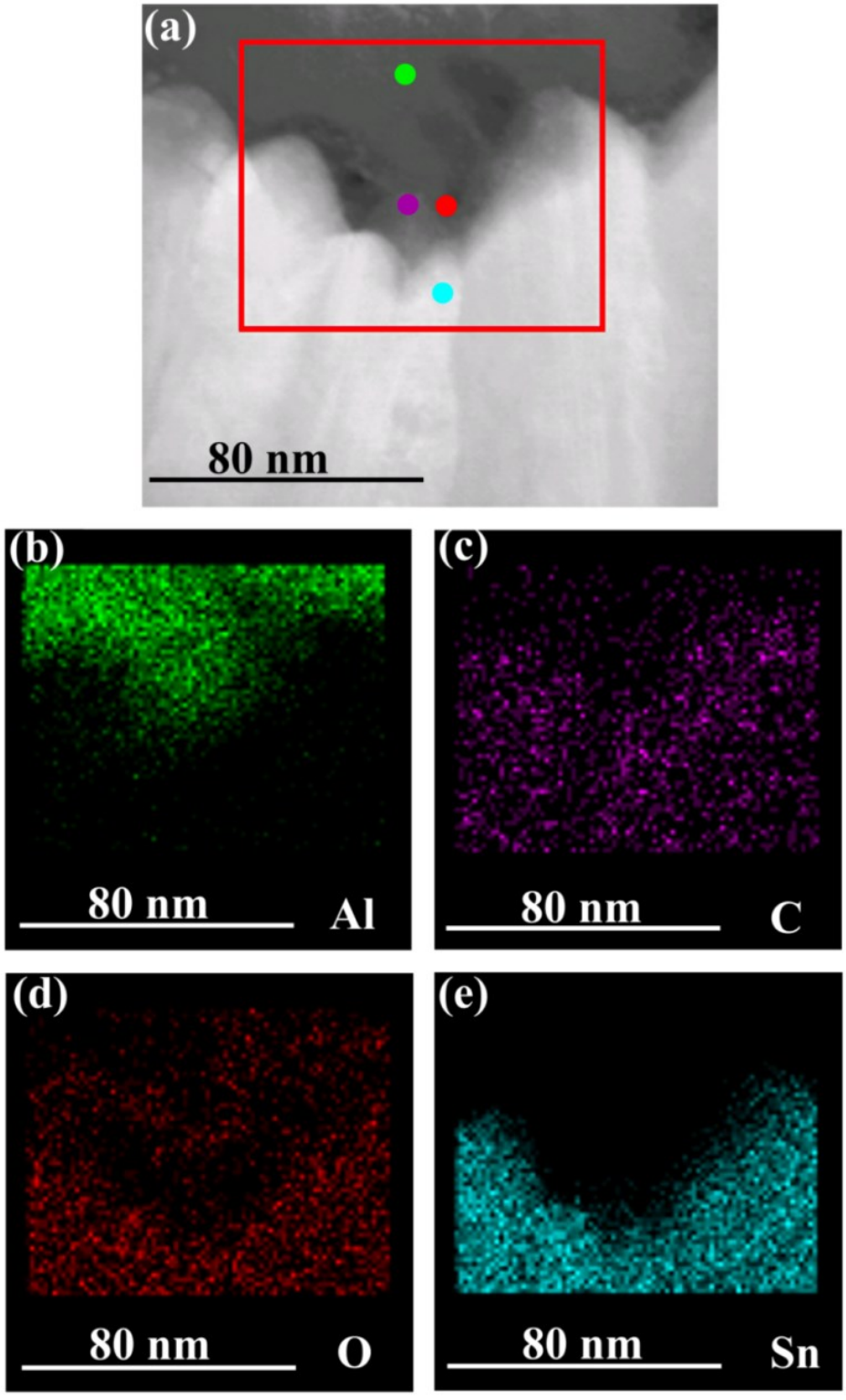

Figure 63: (a) TEM-Cross section of the Al@Cs@FTO device. (b-e) composition maps of Al, C, O and Sn, respectively.

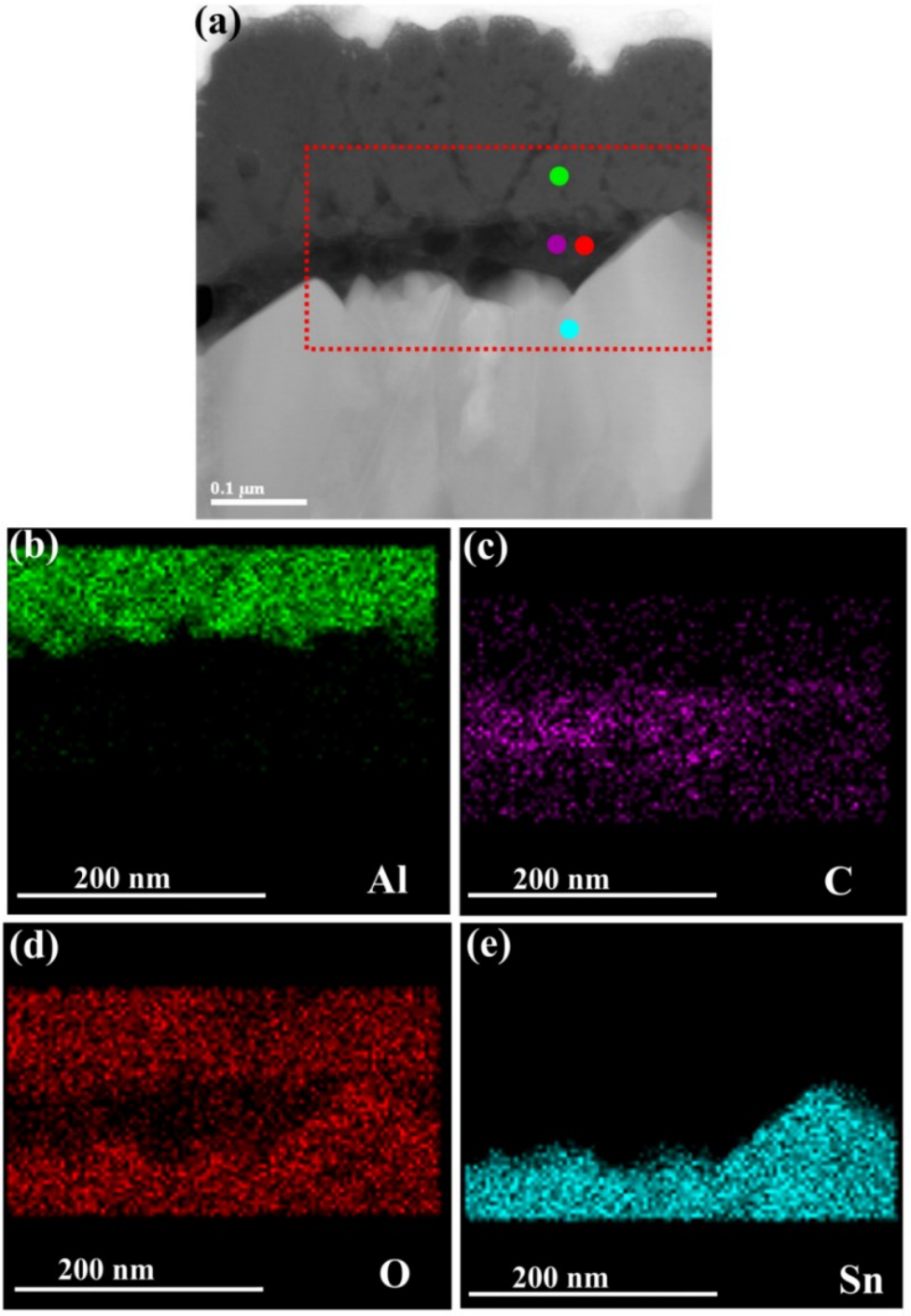

Figure 64: (a) TEM-Cross section of the Al@OCs@FTO device. (b-e) composition maps of Al, C, O and Sn, respectively.

In Figure 65 is displayed the Raman spectra of the samples before and after the electrochemical treatment. The main characteristic bands of carbon-based materials are the D band induced by defects in the crystalline structure and it is related to the size of the in-plain graphitic (*i.e.* sp^2) domains [364]. The G band arises from the in-plane vibration mode of sp^2 carbon atoms, while 2

D and D+G bands are originated by second order Raman vibration modes [166,365]. The I_D/I_G and I_{2D}/I_G ratio is often used to get information on the presence of defects in the carbon materials and it has been reported that the I_D/I_G and I_{2D}/I_G ratio decreases as the crystallinity of the material improves [366]. It has been extensively reported the I_D/I_G ratio can be employed for the investigation of the reduction of graphene oxides [9,364,366,367].

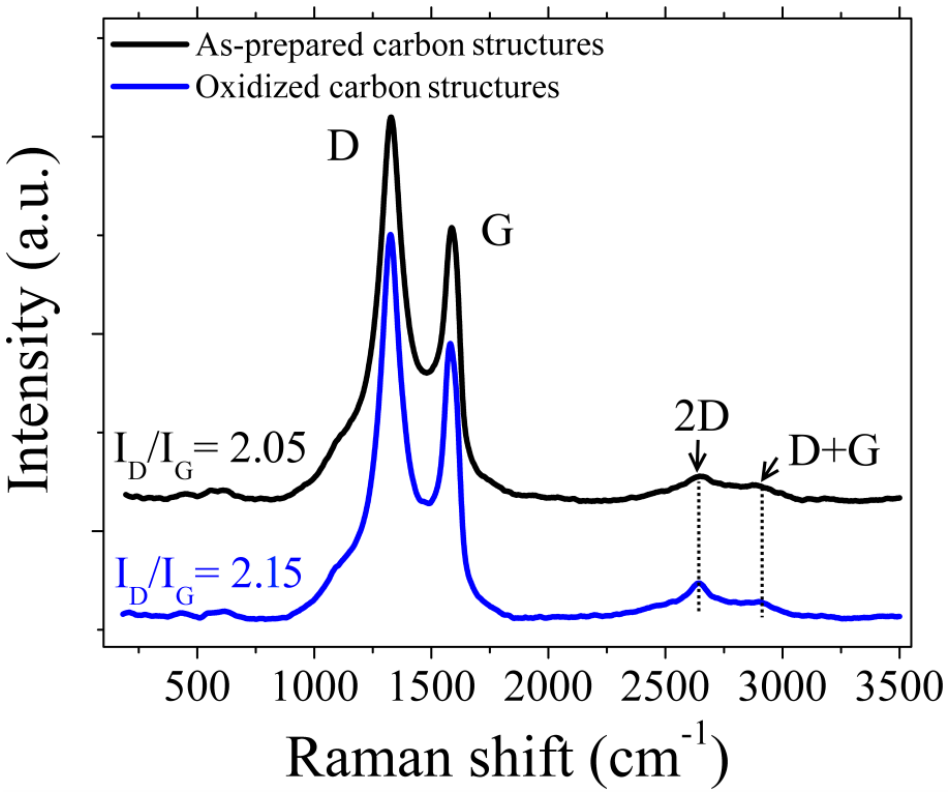

Figure 65: Raman spectra of as-prepared Cs (black curve) and the Cs after electrochemical oxidation (blue curve).

In particular, upon reduction of the GO the I_D/I_G ratio increases due to a reduction in the average of the sp^2 domains, since it is inversely proportional to the average size of the sp^2 domains [364]. Conversely, a decrease of the I_D/I_G is expected in oxidized carbon materials [317]. It is possible to notice that upon the electrochemical treatment the I_D/I_G ratio decreased, thus confirming the oxidation of the Cs. This is further supported by the decrease of the I_{2D}/I_G ratio from 0.28 to 0.20, indicating a decrease of sp^2 domains [346].

The Al/Cs@FTO and Al/OCs@FTO devices were then fabricated following the procedure described in 0, and a schematic of the Al/OCs@FTO device is shown as inset in Figure 66b. The electrical performances of the devices were studied applying sweeping voltages of 0V → -2V → 0V→ 2V → 0V. The Al/Cs@FTO and Al/OCs@FTO devices, after 1 cycle of voltage sweeping

showed bipolar resistive switching behavior as can be observed from the current-voltage (I-V) curves displayed in Figure 66a.

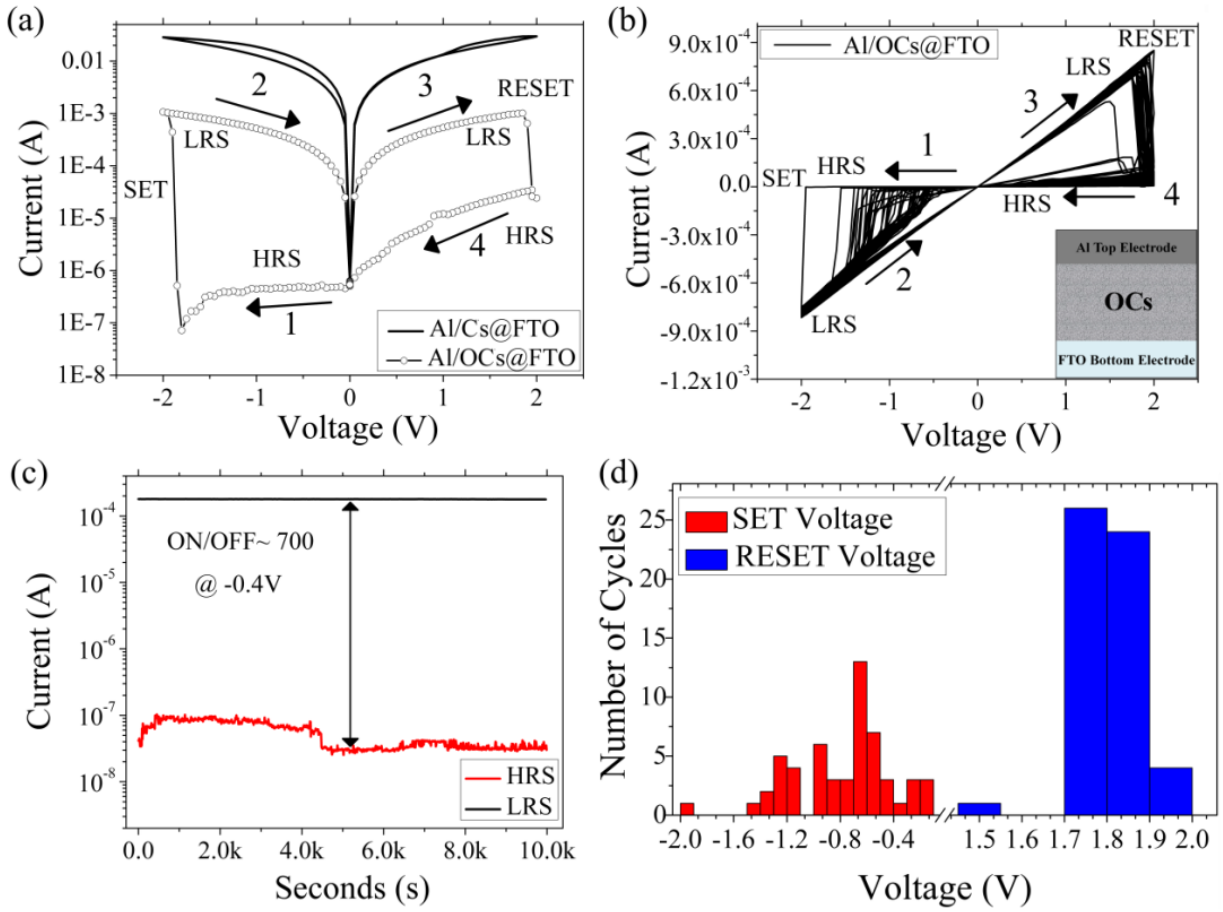

Figure 66: (a) I-V curve of Al/Cs@FTO and Al/OCs@FTO devices after 1 cycle of voltage sweeping. (b) Endurance of the Al/OCs@FTO device for over 50 cycles. (c) Retention results of the Al/OCs@FTO device over 10x103 seconds at a reading voltage of -0.4V. (d) Distribution of the SET and RESET voltages of the Al/OCs@FTO device.

It is possible to notice that the Al/Cs@FTO device is initially in the LRS due to presence of higher percentage of sp^2 carbon atoms, which provide high conductive channels, as already reported in our previous study [15]. The device is then switched to the HRS upon application of a voltage from -2 V to 0 V. This state is maintained up to 2V, where the RESET process occurs and the device is switched again to the LRS state. The I-V curve of the Al/OCs@FTO device is different. In particular, the devices are initially in the HRS state, due to the presence of a higher percentage of sp^3 carbon atoms [333] as a result of the electrochemical oxidation and in agreement with the XPS spectra in Figure 62(d-e). As the negative voltage increases the devices are switched to the ON (LRS) state, which corresponds to the SET process. The ON state is maintained upon application of a positive voltage. At 2 V the RESET process occurs and the

devices are switched to the OFF (HRS) state. From the comparison of the I-V curves for the Al/Cs@FTO and Al/OCs@FTO devices it is possible to notice that the ON/OFF ratio value for the device fabricated with the oxidized Cs is ~10^2 times higher than the Al/Cs@FTO device. It was observed that the Al/OCs@FTO device could sustain different sweeping cycles, as displayed in Figure 66b; however, a change in the SET and RESET voltages was recorded as shown in Figure 66d. This phenomenon can be attributed to the rupture, in different locations, of the conductive filaments, as will be discussed later. In Figure 66c the retention characteristics of the Al/OCs@FTO device at -0.4V is displayed. The HRS and LRS states can retain up to $1x10^4$ seconds confirming the non-volatile nature of the Al/OCs@FTO device.

To better understand the conduction mechanism in the Al/OCs@FTO resistive switching device, we fitted the I-V curve of the LRS and HRS in a double logarithmic scale and the results are better described by the SCLC mechanism. Figure 67a shows the I-V curves during the SET operation, while in Figure 67b the I-V curves during RESET are plotted. Under negative and positive voltages the LRS states follow the Ohm's law conduction mechanism with a slope ~1, while the negative and positive HRS states with a slope ~2 are governed by the Child's law conduction mechanism according to the relationship $I(V) = \alpha V + \beta V^2$, which represents the SCLC mechanism. These results are in agreement with the current literature regarding GO-based RRAM [312,331–333]. From the I-V curves it is possible to notice that the resistive switching behavior in the OCs takes place through the formation of conductive filament paths built from the oxygen vacancies and structural defects. It should be noted that this type of mechanism has been reported by several works [312,368–370]. Therefore the Al/OCs@FTO device can be classified as oxygen vacancies based (VO) RRAM [371], where the resistive switching mechanism can be described by formation and rupture of oxygen vacancies conductive filaments.

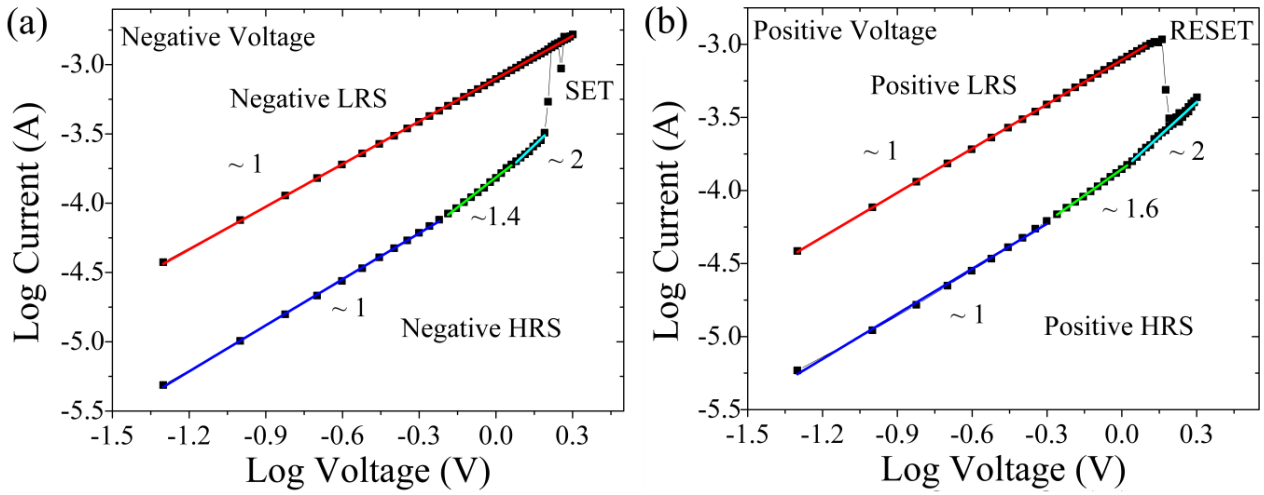

Figure 67: I-V curves of Al/OCs@FTO device plotted in a double logarithmic scale under negative (a) and positive (b) voltages.

In Figure 68(a-d), a schematic of the proposed resistive switching mechanism is displayed. As recently reported by Pradhan [312] and Sung [326], aluminum has an high affinity to oxygen, therefore it reacts with the oxygen ions desorbed from the OCs forming an oxygen-rich region near the top electrode. This will induce the creation of oxygen-deficient regions (i.e. oxygen vacancies) in the OCs matrix due to the removal of oxygen from the OCs (Figure 68b). This is in agreement with the EDS maps displayed in Figure 64(b-e), where it can be observed a higher concentration of oxygen in the Al region compared to C region. Due to the difficulties in performing XPS analysis after the deposition of the Al top electrode, we could not confirm the percentage of oxygen-containing groups remaining in the carbon structures, which requires more attention.

When a negative voltage is applied on the Al top electrode, the oxygen vacancies move towards the cathode and they start to be cluster leading to the formation of conductive filaments (Figure 68c) that will switch the device from the OFF to the ON state, *i.e.* SET process. During the RESET process, the positive bias pushes back the oxygen vacancies [310,312], which lead to the breakage of the conductive filaments and consequently the device is switched to the HRS state, Figure 68d. It was observed that the SET voltage changed with the number cycles (Figure 66d). This might be attributed to the fact that during the RESET process the conductive filaments can break at various locations, leading to a distribution of SET voltages. From the electrical measurement results, it is evident that the electrochemical oxidation of the Cs enhanced the electrical performances. This is because the presence of oxygen functional groups and defects

plays a key role in resistive switching behavior in RRAM devices [298,316–318,330,331,334,372].

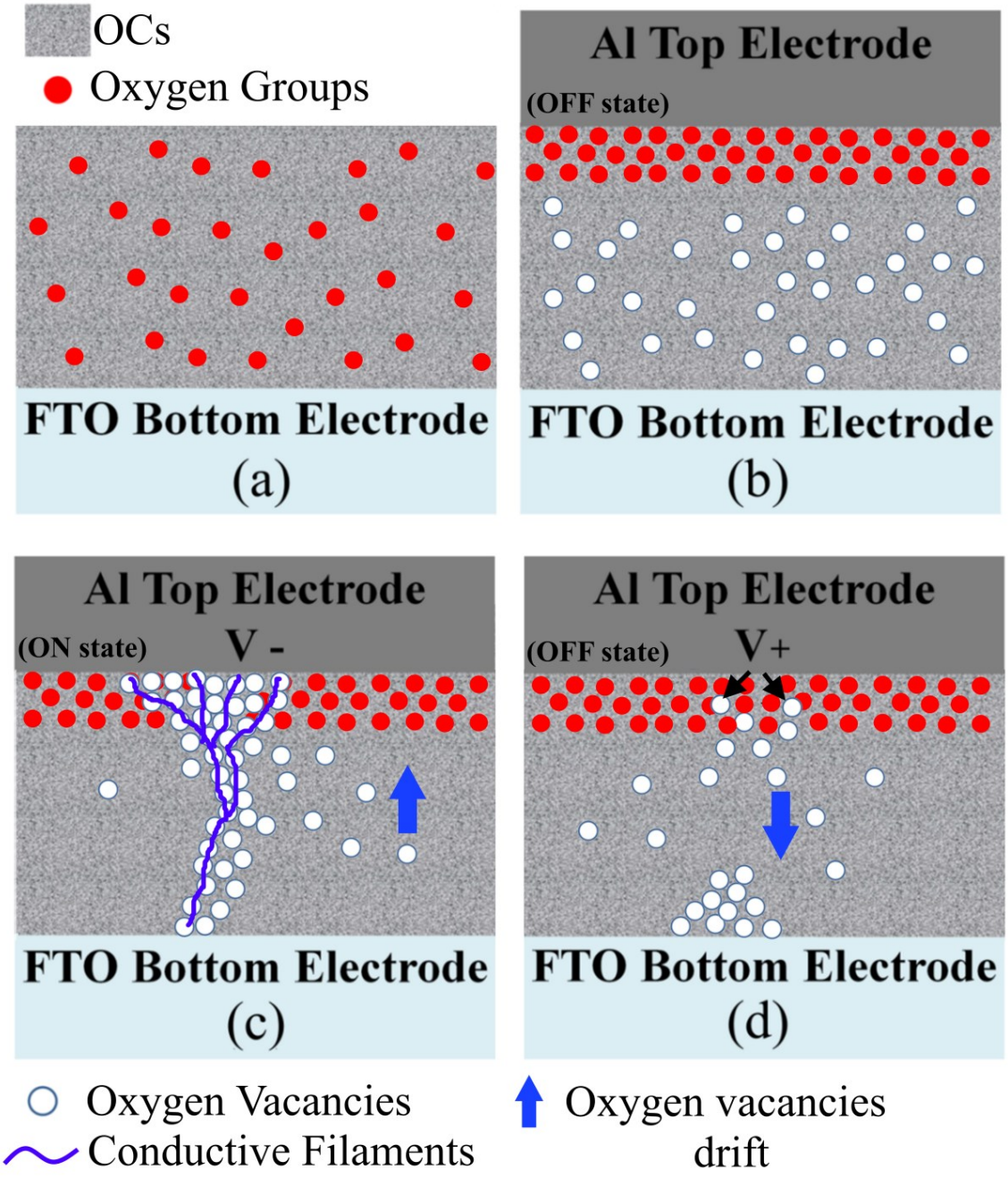

Figure 68: (a) OCs on the bottom electrode. (b) Pristine Ocs device after depsotion of the Al top electrode. (c) Drifting of the postively charged oxygen vacancies towards the bottom electrode upon application of a negative voltage and formation of the conductive filaments wich switch the device ON . (d) During the reset process the oxygen vacancies are repelled back from the Al top electrode causing the rupture of the conductive filaments and the switch of the device to the OFF state.

In order to investigate how the degree of the Cs oxidation influences the electrical performances, we fabricated two devices with different electrochemical oxidation/reduction/oxidation cycles. In particular the devices were first oxidized applying a voltage in the range [0-0.8] V, then reduced by the application of a negative voltage from 0V to -0.8V followed by a further anodic oxidation from 0V to 0.8V. The devices were fabricated in a way, that the number of oxidation/reduction/oxidation cycles was 3 and 6, respectively. These devices will be referred as 3OCs and 6OCs, where the number refers to the number of anodic oxidation cycles the device undergoes. The XPS spectra of these devices are shown in Figure 69(a-b).

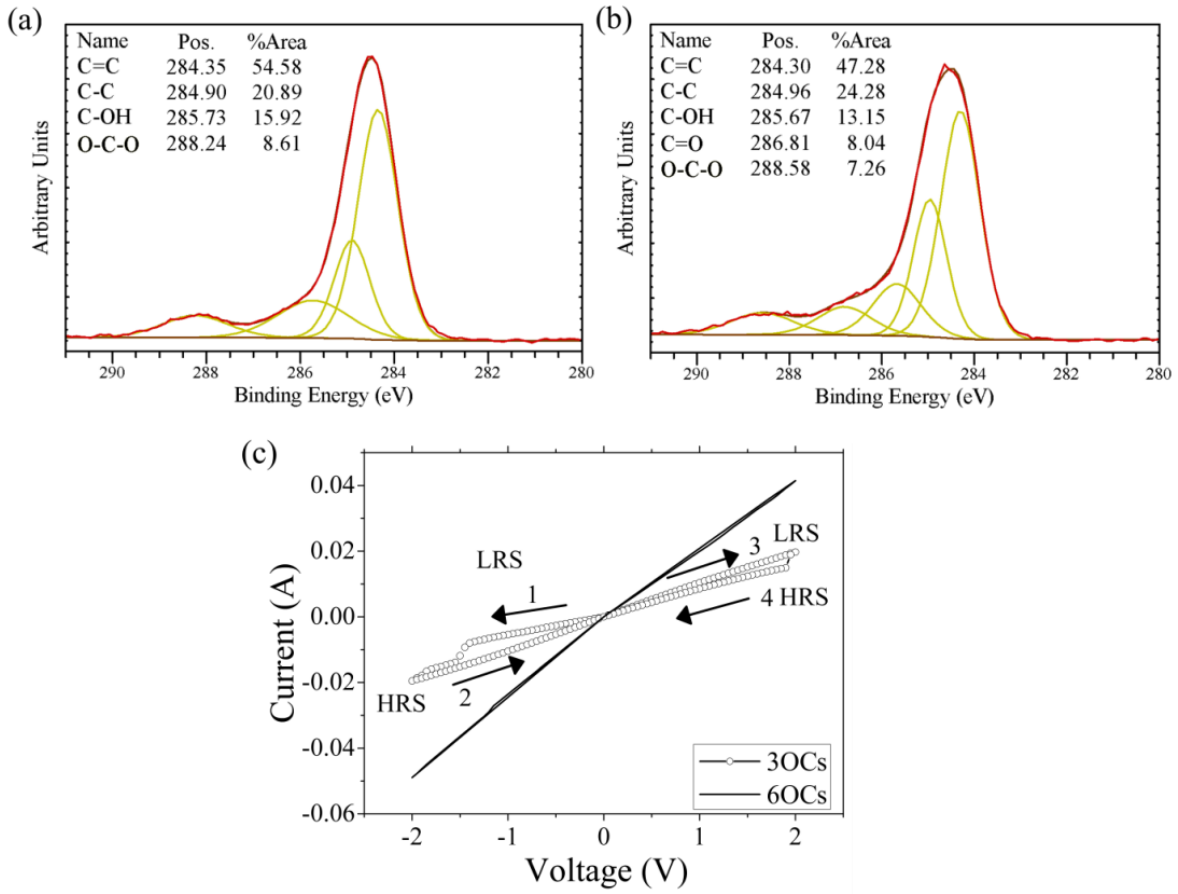

Figure 69: XPS spectrum of the Cs after 3 (a) and 6 (b) oxidation/reduction/oxidation cycles, respectively. (c) I-V curve of Al/3OCs@FTO and Al/6OCs@FTO devices after 1 cycle of voltage sweeping.

In Table 8, the surface concentrations of the Cs before and after electrochemical treatment are displayed. It is possible to notice that increasing the cycles of oxidation/reduction/oxidation the percentage of sp^2 carbon atoms increases compared to the Cs oxidized with only one anodic oxidation. Furthermore, the percentage of epoxy groups is higher in the OCs compared to the 3OCs and 6OCs samples.

Table 8: Surface composition of the Cs before and after electrochemical treatment.

Sample	C=C (%)	C-C (%)	C-OH (%)	C=O (%)	O-C-O (%)
Cs	70.25	14.70	9.97	//	5.08
OCs	30.80	39.66	14.41	3.59	11.54
3OCs	54.58	20.89	15.92	//	8.61
6OCs	47.28	24.28	13.15	8.04	7.26
3MOCs	27.49	47.80	9.57	9.02	6.12

The I-V curves of Al/3OCs@FTO and Al/6OCs@FTO devices are displayed in Figure 69c, and it is possible to observe that the electrical performances do not improve *via* increasing the number of oxidation/reduction/oxidation. The Al/3OCs@FTO electrical behavior is similar to the Al/Cs@FTO device; the device is initially in the LRS due to the higher percentage of sp^2 carbon atoms and switch to HRS upon application of a voltage from -2 V to 0 V. However, the device cannot maintain the HRS state and switch to LRS upon application of a positive voltage. The I-V curves for the 6OCs showed that this device behaves like a resistor, due to the presence of a higher concentration of sp^2 carbon atoms.

These results highlight that the degree of oxidation of the Cs strongly influences their electrical performances, *i.e.* a higher concentration of sp^3 carbon atoms together with the presence of carbonyl and epoxy groups improved the device's performances. Therefore, the possibility to have a control over the degree of oxidation is necessary for the fabrication of next generation RRAM devices.

In order to extent the study on the role of oxygen content in our materials, we carried out preliminary experiments performing the electrochemical oxidation increasing the salt concentration from 1M to 3M. In Figure 70a is displayed the XPS spectra of the OCs obtained, which will be indicated as 3MOCs. Compared to the OCs XPS spectra in Figure 62e, the 3MOCs show a lower percentage of sp^2 carbon atoms and hydroxyl groups, and a higher percentage of carbonyl groups, as reported in the table S1. From the I-V curve displayed in Figure 70b, it is possible to notice that compared to device oxidized employing a salt concentration of 1M, the

3MOCs required a higher voltage to switch the device from the OFF state to the ON state. This can be attributed to the higher percentage of sp^3 carbon atoms and carbonyl groups.

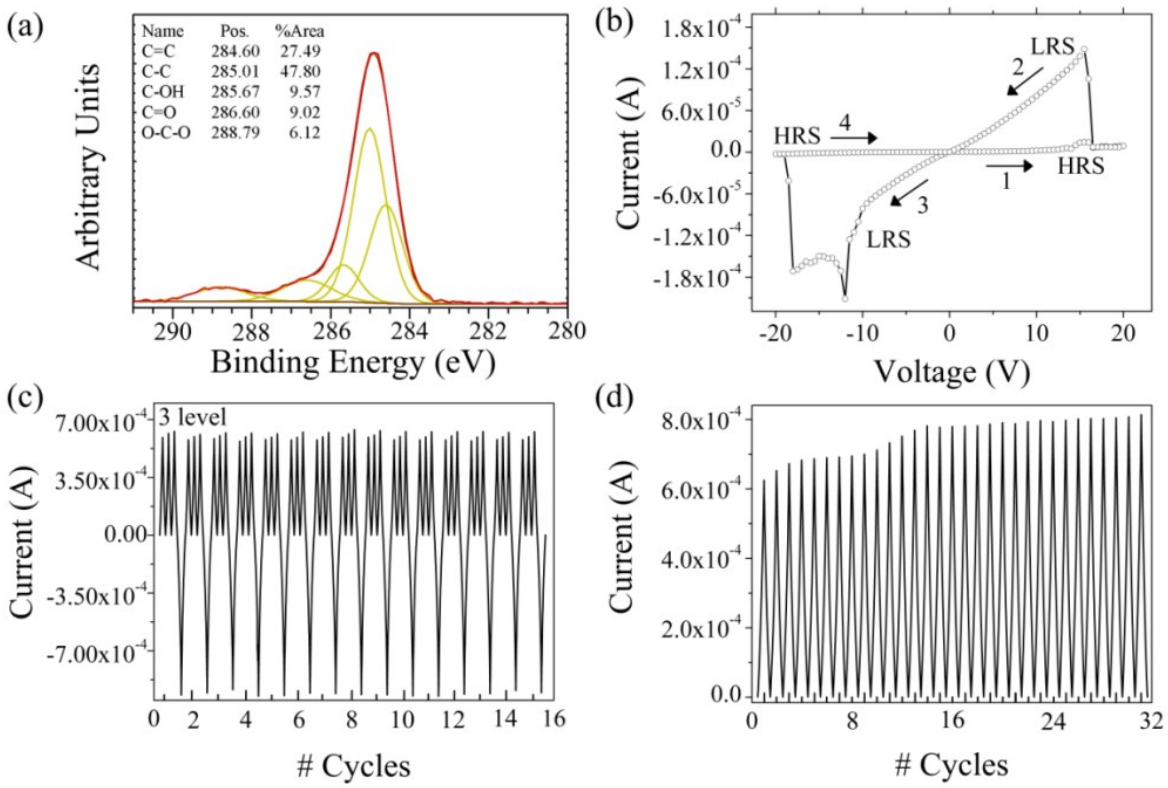

Figure 70: (a) XPS spectra of the 3MOCS, (b) current response under a voltage sweep of 20V, (c) 3 level memory profile upon application of 15V and a reset bias of -21V, (d) current response under 32 voltage cycles from 0V → 15V →0V.

Compared to the OCs device, the 3MOCs showed a 3 level current amplification memory effect, as can be seen from Figure 70c. Upon application of consecutive biasing of 15V, an accumulation of charged defects takes place leading to a current amplification, due to the creation of multiple conduction paths, which is known to occur in RRAM devices based on oxide materials [299,346]. A reverse erase bias of -21V, disrupts the conduction filaments and the device goes back to its original state, allowing a repeatable 3 level current amplification. It was observed thirteen-level amplification under continuous excitation with forward voltage cycles, as shown in Figure 70d. As the number of cycles increases the saturation of the current occurs and it stabilizes reaching a value of ~$8E^{-4}$ A [299]. It is evident from these preliminary results, that the electrochemical oxidation of the Cs could be used as a tool to engineer the electrical performances of this type of carbon-based devices. In particular, the possibility to control the chemical composition of the carbon material could lead to the fabrication of devices with

enhanced electrical performances, such as multilevel memory amplification for the storage of more than one bit per memory cell [373].

6.7. Summary

In this chapter, it has been demonstrated that electrochemical processes such as the electrochemical deposition and the anodic oxidation are straightforward and time-effective ways for the synthesis and modification of carbon materials. The ease of the method allows the deposition of the carbon materials directly on conductive substrates that have been used as the bottom electrodes of the carbon-based devices. The carbon nanowalls showed resistive switching behavior and from the study of the RS mechanisms it has been observed that their electrical performances can be improved modifying the materials' structure through a proper control of the fabrication process parameters, such as deposition time, heat treatment, and chemical composition of the carbon materials. Preliminary results demonstrated a good reproducibility of the devices and it has been discussed that the degree of oxidation plays a key role in the electrical properties of the devices. It has been determined that the electrochemical oxidation of carbon structures can be used to engineer the chemical composition of the Cs. It was observed that a proper control over the oxidation degree is vital for the Cs' resistive switching mechanism, since it is originated by the formation of conductive filament paths built from the oxygen vacancies and structural defects. The increase of the Cs' degree of oxidation led to devices with multilevel current amplification which enables the storage of more than one bit of information. The ease and time effectiveness of the method we developed is an engineering solution for the large-scale development of other carbon-based electronics.

Chapter 7. UV-induced multilevel current amplification memory effect in zinc oxide rods resistive switching devices.

Overview

In Chapter 6, it was demonstrated that the electrophoretic deposition of carbon materials could be employed as a straightforward and time-effective technique for the fabrication of memory devices and for the improvement of their electrical properties. This technique is very versatile and it can be used for the deposition of different materials. The aim of the study presented in this current chapter is to employ the EPD as the solely technique for the synthesis of ZnO rods for the fabrication of resistive switching (RS) devices. As mentioned in Section 2.7.2, electrochemical routes have been employed either for the growth of ZnO rods on ZnO films prepared by magnetron sputtering or for the deposition of ZnO films where the rods have been grown by hydrothermal method [154–157]. In this study, the cathodic deposition of zinc nitrate solution on FTO substrates is employed as technique for the synthesis of the ZnO seed layer and for the consecutive growth of the ZnO rods. The ZnO rods act as the active layers of the resistive memory structure, while the FTO serves as bottom electrode. From the analysis of the electrical measurements it has been found that upon exposure of the devices to ultraviolet (UV) light an increase of the device's stability occurs. Moreover, for the first time it has been observed a photo-induced multilevel current amplification, which is absent in dark conditions. From the study of the RS mechanisms, it has been demonstrated that RS behaviour in these devices can be attributed to the presence of conductive filaments composed of oxygen vacancies. The improved device's resistive switching behavior is due to the higher production of oxygen defects generated by UV light. The investigation of the photodecay processes carried out on the devices fabricated with different electrodes, showed that the nature of the interface metal/ZnO rods affects the surface barrier height, which influences the photodecay rate. It is shown that higher relaxation constants (slower photodecay rates), lead to the multilevel current amplification behavior which is triggered by the UV light.

7.1. Introduction

As already presented in Chapter 6, RRAM devices consist of an active layer sandwiched between two metallic electrodes (Scheme in Figure 51a). These type of devices rely on the

resistance change of the active material under application of an electrical stimulus, from a low resistance state (LRS or "ON") to a high resistance state (HRS or "OFF") and *vice versa*.[292,293,295,334] When a device is switched from HRS to LRS, the process is referred as the SET, while the RESET is the process of switching the device from LRS to HRS. Across the years different types of materials have been employed as a dielectric layer: chalcogenides, TiO_2, NiO, and carbon nanomaterials [15,18,136,304,308,310,324,331,344,356,373–378].

Among all, ZnO nanostructures, such as ZnO rods, because of their transparency in the visible region, low cost, wide direct band gap (3.34 eV), controllable electrical behavior, and chemical stability have been employed for the fabrication of different types of RRAM devices [137,379–385]. In ZnO RRAM devices, depending on the device's structure, RS effect can operate under unipolar and bipolar operation mode, where the SET and RESET processes occurs in the same or opposite bias polarity, respectively[386,387]. The resistive switching behavior underlying ZnO based RRAM can be attributed to the electrochemical metallization mechanism (ECM) induced by the formation and rupture of metallic filaments or to the valence change mechanism (VCM) where the conductive filaments are composed of oxygen vacancies defects [383]. Besides the resistive switching memories, ZnO nanostructures are very sensitive to UV light and they are good candidates for light emitting diodes, photovoltaic and UV photodetectors applications [19–24].

The RS and photoconductivity properties of ZnO nanostructures have been extensively studied, however only one group reported about the concurrent study of RS and photoconductivity of ZnO devices, in particular the study focused on the photo-stimulated RS in the ZnO rods devices. However, the authors did not observe a multilevel current amplification upon exposure of the device to ultraviolet light [24].

In this study, we investigated the RS mechanisms, in dark and under UV-light exposure, of ZnO rods obtained by two-step electrochemical deposition process. The advantages of the electrophoretic deposition employed in this study compared to the common hydrothermal and sol-gel routes rely on the time-effectiveness of the method [153,388,389]. This technique allows the deposition of materials on different type of substrates achieving large scale deposition [21,22,150,153,155,388–392]. In literature, several papers reported about the synthesis of ZnO seed layers on different type of substrates employing the electrophoretic deposition of an aqueous solution of zinc nitrate or ZnO powders [393–396]. Few researchers have reported the

synthesis of the ZnO rods *via* electrophoretic route employing ZnO seed layer obtained by radio frequency magnetron sputtering systems [154–157]. The synthesis of both ZnO seed layer and ZnO rods through electrophoretic deposition has been reported only by another group, where the rods have been deposited on indium indium-doped tin-oxide (ITO) [397]. Here, we will present and discuss the results obtained investigating the electrical performances of ZnO rods grown through cathodic deposition on FTO and we will discuss the possible mechanism of the multilevel current amplification effect induced by UV exposure. The novelty of our study relies on the simultaneous study of the photo-multilevel current amplification effect and the improved resistive switching behavior of ZnO rods devices under UV light illumination. To the best of our knowledge, the multilevel current amplification triggered by the UV light has never been reported in ZnO RS devices.

7.2. Experimental

7.2.1. Deposition of the ZnO seed layer

The ZnO seed layer was synthesized by electrodeposition approach in a three-electrode quartz cell [398–400]. The FTO substrates were purchased from Ossila Company, and they were cleaned ultrasonically in isopropanol, ethanol, and acetone, rinsed with deionized water and dried with air. A 0.1 M aqueous solution of zinc nitrate hexahydrate [$Zn(NO_3)_2 \cdot 6H_2O$] was used as the electrolyte solution and it was kept at 80°C during the electrodeposition. The FTO substrate was used as working electrode, and the counter electrode was Pt mesh. In order to deposit the ZnO seed layer a potential of -1.1 V vs. a saturated calomel electrode (S.C.E.) was applied for 1800 seconds. After the deposition of the ZnO layer, the substrate was dried in oven at 60°C for 1h.

7.2.2. Growth of the ZnO rods

The ZnO rods were grown trough an electrochemical deposition method in a three-electrode quartz cell [398]. The electrolyte solution for the growth of the rods was an equimolar (5 mM) aqueous solution of [$Zn(NO_3)_2 \cdot 6H_2O$] and hexamethylenetetramine (HMTA, $C_6H_{12}N_4$). The temperature of the bath was kept at 80°C and under continuous stirring. The seeded FTO substrate and Pt mesh were the working and the counter electrodes, respectively. The ZnO rods

were grown applying a potential of -0.95 V vs. S.C.E. for 1500 seconds. After the synthesis of the rods, the substrate was rinsed with deionized water and dried in air.

7.2.3. Device fabrication

Silver paint (High Purity Silver Paint from SPI-SUPPLIES) was used for the fabrication of the Ag top electrodes. A mask with patterned holes of 100 μm was attached to the ZnO rods/FTO and the silver paint was brushed in order to create the electrodes. For the preparation of the Au/ZnO rods/FTO devices, a mask with patterned holes of 100 μm was applied on the ZnO rods/FTO samples and the gold electrodes were deposited by gold sputtering.

7.2.4. Instrumentation

The ZnO seed layer and the ZnO rods were obtained using a Gamry Potentiostat (Series 300). The morphology of the rods was investigated by scanning electron microscopy (SEM). It has been employed a ZEISS LEO 1550 FE-SEM at an accelerating voltage of 7 kV. The structural characterization was investigate with TEM and the analysis has been carried out using a JEOL 2010F at the Canadian Centre for Electron Microscopy (Hamilton, Ontario, Canada). X-ray photoelectron spectroscopy (XPS) analysis was employed to study the surface chemical composition analysis and it was performed by using a multi-technique ultra-high vacuum imaging XPS microprobe spectrometer (Thermo VG Scientific ESCALab 250) with a monochromatic Al-Ka 1486.6 eV X-ray source. The ZnO rods spectrum was acquired with a 50x objective and laser wavelength of 633 nm at a power of 0.1 mW. The electrical measurements were performed with a Keithley 2602A source meter at ambient conditions. The measurements under UV light have been carried out with a UV-LED lamp with a wavelength 365 nm (LED Engin, 1 A forward current, 4.1 V forward voltage).

7.3. Results and Discussion

The mechanism for the growth of the ZnO rods thorough electrophoretic deposition has been well-reported and it is attributed to the reaction between the Zn^{2+} ions, dissolved in the growth solution, with the hydroxide (OH^-) ions generated upon application of an electric field.

The reactions involved in the growth of the ZnO rods can be described as follows:

$$Zn(NO_3)_2 \rightarrow Zn^{2+} + 2NO_3^- \quad (1)$$

$$NO_3^- + H_2O + 2e^- \rightarrow NO_2^- + 2OH^- \quad (2)$$

$$Zn^2 + OH^- \rightarrow Zn(OH)_2 \quad (3)$$

$$Zn(OH)_2 \rightarrow ZnO + H_2O \quad (4)$$

The HMTA reacting with water provides additional hydroxide ions according to the following reactions [156,399,401]:

$$C_6H_{12}N_4 + 6H_2O \rightleftarrows COH_2 + 4NH_3 \quad (5)$$

$$NH_3 + H_2O \rightleftarrows NH_4^+ + OH^- \quad (6)$$

The morphology and the structure of the ZnO rods were analyzed by scanning electron microscopy (SEM) and transmission electron microscopy (TEM). Figure 71a, shows the top SEM image of the ZnO rods on a seeded FTO substrate, while a magnified SEM image of the rods is displayed in Figure 71b.

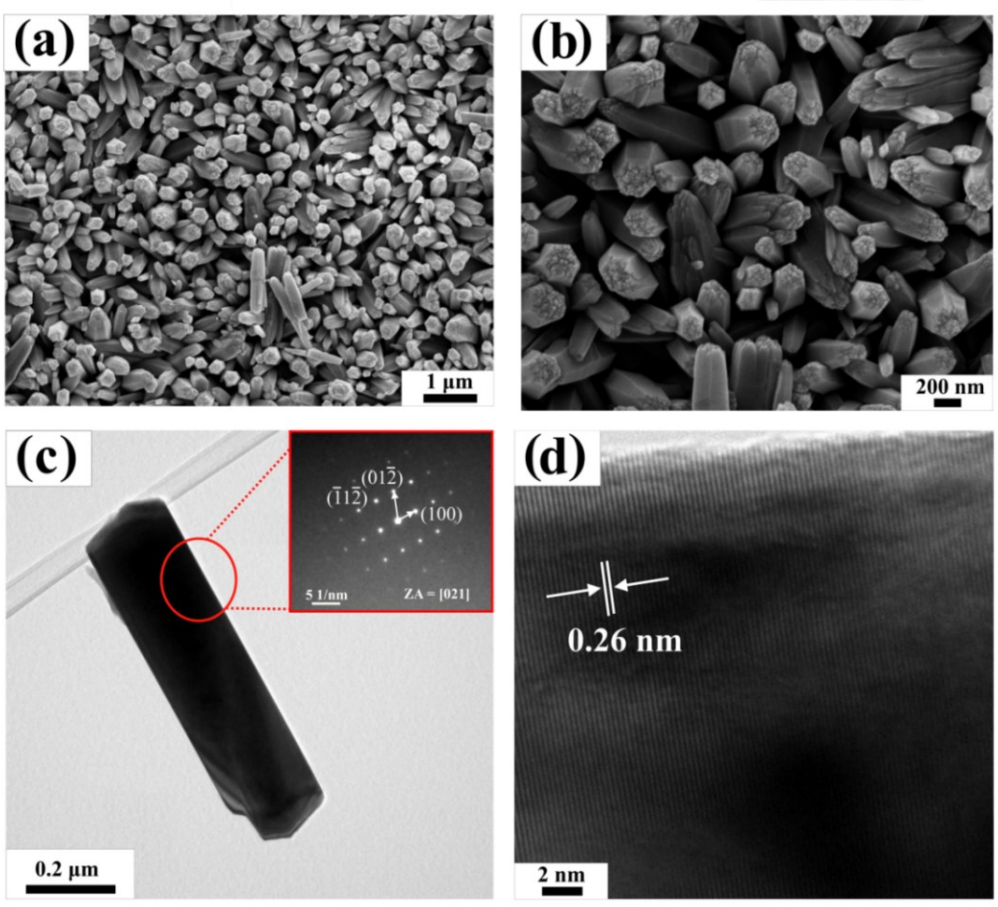

Figure 71: (a) SEM image of ZnO top surface, (b) magnification of the ZnO rods obtained upon cathodic deposition, (c) TEM image of ZnO rods showing good crystallinity demonstrated by SAED analysis (inset), (d) HR-TEM showing the d-spacing of the ZnO rods

It was possible to obtain a homogenous layer of ZnO rods with an average length of ~ 1 μm using solely cathodic deposition. In Figure 71(c-d), TEM images of the ZnO rods are displayed. The inset of Figure 71c displays the selected area electron diffraction (SAED) pattern of the ZnO rods, which confirms their single crystalline nature.

The high resolution TEM image in Figure 71d, reveals the lattice fringes with a d spacing of 0.26 nm, which match the inter-spacing of the (002) planes of the ZnO with wurtzite structure, thus confirming the growth direction of the ZnO rods is in the c-axis direction [155,402].Figure 72a displays the Raman characterization analysis of the ZnO rods. The main characteristic peaks of zinc oxide rods are associated to different vibrational modes. In particular, the peak at 379 cm^{-1} corresponds to A_1, while E_1 originates the peak at 410 cm^{-1}. The other two Raman active modes are the low frequency E_2 phonon mode originated from the Zn vibrations, and the peak at 437 cm^{-1}, which corresponds to the high frequency E_2 mode due to oxygen atoms in the structure [176–178] . It has been reported that the position of the E_2 (high) mode shifts towards lower frequencies as the amount of oxygen vacancies increases [403].

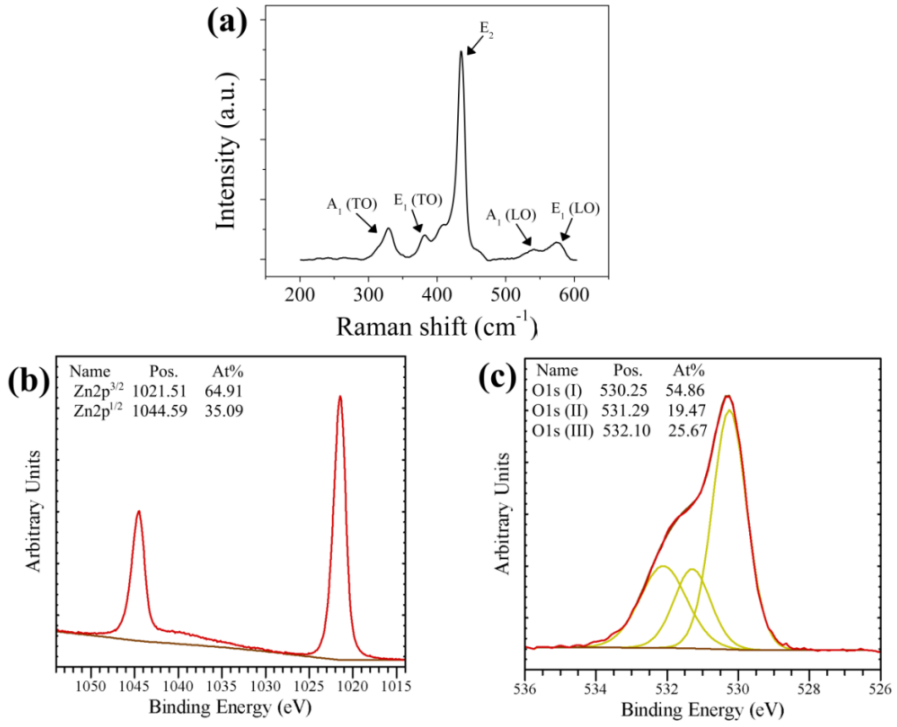

Figure 72: (a) Raman spectrum; (b) Zn 2p core-levels and (c) O1s region of the as-grown ZnO rods.

The position of the E_2 (high) peak in the Raman spectrum displayed in Figure 72a is shifted at lower frequencies located at 435 cm^{-1}, suggesting the presence of oxygen vacancies within the ZnO structure. In order to analyze the chemical composition and oxidation state of the ZnO rods,

we performed X-ray photoelectron spectroscopy (XPS) analysis. The high-resolution spectra of Zn 2p and O1s are shown in Figure 72b and c, respectively. The two peaks located at 1021.51 eV and 1044.59 eV are attributed to Zn $2p^{3/2}$ and Zn $2p^{1/2}$ of ZnO rods, which indicates a +2 valence state of the rods. Moreover, both the peaks were fitted to a single one Gaussian curve and the binding energy difference between the two Zn 2p core-levels is 23 eV, which is in agreement with the data reported in literature for ZnO rods [137,404,405]. The presence of oxygen vacancies and interstitial oxygen defects can be investigated through the chemical state of O 1s region [24,137,406]. In Figure 72c, the spectrum of the O 1s region is displayed and the peak was fitted to three Gaussian peaks located at (I) 530.25 eV, (II) 531.29 eV and (III) 532.10 eV. The peaks at the low and middle binding energies are attributed to O^{2-} ions in the Zn-O bonding in the ZnO rods wurtzite structure and to the O^{2-} ions in the oxygen deficient regions, respectively. The peak at higher binding energy is associated to chemisorbed oxygen. The very strong intensity of the peak at lower binding energy compared to the other two components indicates a good crystallinity of the samples, as further confirmed by the SAED pattern in the inset of Figure 71c and by the sharp and higher intensity of the E_2 (high) Raman peak in Figure 72a [178,406]. The intensity of the peaks located at middle and high binding energies is comparable, indicating the coexistence of oxygen vacancies V_o and chemisorbed oxygen, in agreement with previous reports [24,406].

In order to study the electrical performances of the ZnO rods, silver contacts were fabricated following the procedure described in the Experimental Section. A schematic of the Ag/ZnO rods/FTO device is displayed in Figure 73(a-b) as insets.

The electrical measurements were performed applying a sweeping voltage of 4V at the Ag top electrode, while the FTO was grounded. The electrical tests were carried in dark and under UV irradiation and the I-V curves are displayed in Figure 73a and b, respectively. In dark conditions, the device showed a bipolar resistance switching, however the device was not stable and after 40 sweeping cycles a decrease of the current occurred. The sweeping direction was 0→ 4V →0→ -4V, and it was found that the device is initially in the HRS and switched to the LRS during the voltage sweeping from 4V to 0V, due to the piling of oxygen vacancies, which creates the conductive filaments, as it will be discussed later. The I-V curve of the Ag/ZnO rods/FTO device under UV irradiation (inset Figure 73b) is displayed in Figure 73b, and the illumination conditions changed the electrical response. In particular, an increase of the measured current was

observed together with the improvement of the device's stability, which could sustain up to 40 sweeping cycles.

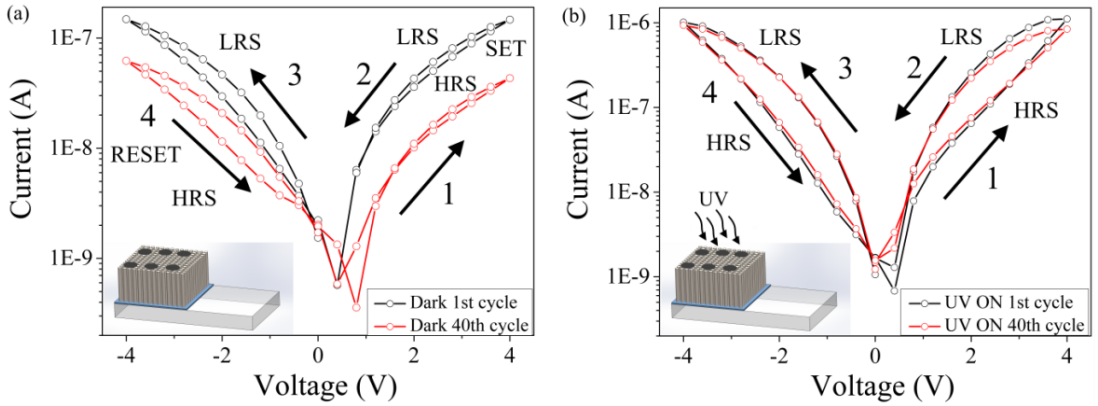

Figure 73: (a) I-V curves of the Ag/ZnO rods/FTO (inset) in dark condition and (b) under UV irradiation with a sweeping voltage of 4V for 1 cycle (black curves) and after 40 cycles (red curves).

The measured current under UV exposure was 20 times greater than the current in dark conditions. The increase of the conductivity of the Ag/ZnO rods/FTO device upon illumination, showed in Figure 73b can be explained as follows. ZnO is a n-type semiconductor extremely sensitive to the UV irradiation, and the mechanism for the photoconduction in the nanostructured ZnO has been extensively studied [21,23,407–409]. It is well known that in air, oxygen molecules chemisorb on ZnO surface and, by capturing the free electrons from the n-type ZnO conduction band, are converted to oxygen ions according to the following reaction:

$$O_{2(g)} + e^- \rightarrow O^-_{2(ad)} \quad (7)$$

Consequently, a low-conductivity depletion layer is formed near the surface. When the ZnO is illuminated by UV irradiation with photon energies above the semiconductor band gap, electron-hole pairs are photo-generated according to Equation 8:

$$h\nu \rightarrow e^- + h^+ \quad (8)$$

The photo-generated holes migrate to the surface react with the oxygen ions releasing oxygen molecules (Equation 9).

$$O^-_{2(ad)} + h^+ \rightarrow O_{2(g)} \uparrow \quad (9)$$

As a consequence the high-resistance depletion layer is reduced and the unpaired electrons, left behind by the photo-generated holes, increase the conductivity under an applied field [21,23,24,407,409]. The bipolar resistive switching (RS) behavior of the Ag/ZnO rods/FTO device and the increase of the device's stability upon UV exposure can be explained by the

oxygen vacancies conduction mechanism [23,24,137,409]. ZnO possesses intrinsic defects, *i.e.* oxygen vacancies V_o, which are homogeneously distributed in the ZnO nanostructure and the presence of these type of defects in our device has been confirmed by XPS analysis shown in Figure 72c, where the peak at 531.29eV is associated with O^{2-} ions in the oxygen deficient regions [24,410]. A schematic of the resistive switching mechanism of the ZnO rods in dark and under UV light is illustrated in Figure 74. Oxygen vacancies are doubly positively charged and upon application of a positive bias they drift towards the cathode (FTO bottom electrode) and start to connect with each other forming the conductive filaments responsible of the resistance switching of the device from HRS to LRS, as shown in Figure 74b.

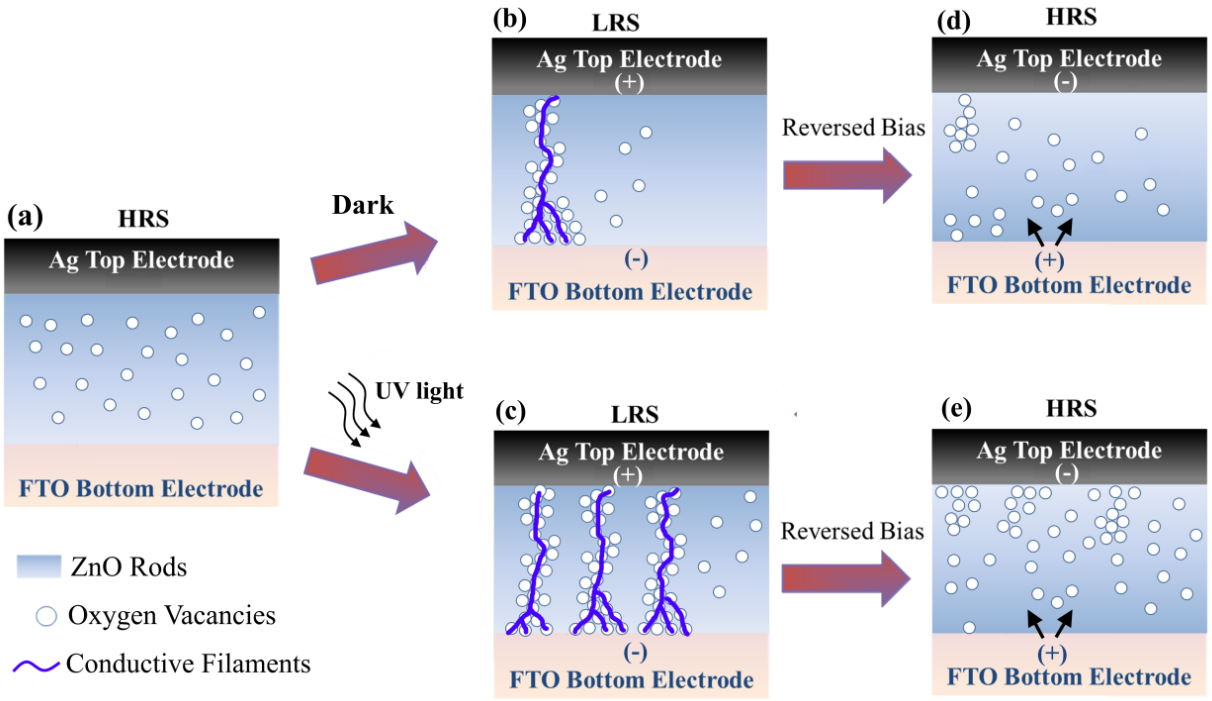

Figure 74: Resistive switching mechanism of the Ag/ZnOrods/FTO device. (a) Initially the device is in the HRS, upon application of an electric field the oxygen vacancies start to pile up (b) and form conductive filaments, which switch the device to LRS. Under UV light illumination (c) more oxygen vacancies are formed, which lead to the formation of multiple conductive filaments. At reversed bias (d and e), the conductive filaments are broken and the device returns into the OFF state.

The I-V curves of the device exposed to UV light showed an increase of stability compared to the ones obtained in the dark, which may be attributed to the higher production of oxygen defects and oxygen ions obtained during UV illumination [411,412]. It has been reported that under UV illumination of ZnO oxygen vacancies will be generated [411–414], therefore higher amount of defect sites will be present in the illuminated device compared to the one in dark conditions

(Figure 74c). The oxygen vacancies drift towards the cathode and they start to connect with each other forming multiple conductive filaments (Figure 74c), which are responsible of increase stability of the device.[21,23,407,415,416]. At reverse bias, either in dark (Figure 74d) or under UV light (Figure 74e), the oxygen vacancies are repelled back from the anode (FTO electrode) and as a consequence the conductive filaments are broken switching the device from LRS to HRS (Figure 74e) [137,417,418].

In Figure 75, the I-V curves of the Ag/ZnO rods/FTO device upon application of consecutive biasing of 4V under dark conditions and continuous UV irradiation are displayed. Under UV illumination (Figure 75a) the device showed a three-level memory current amplification, and when a reverse erase bias of -6V is applied the device goes back to its original state, allowing a repeatable 3 level current amplification.

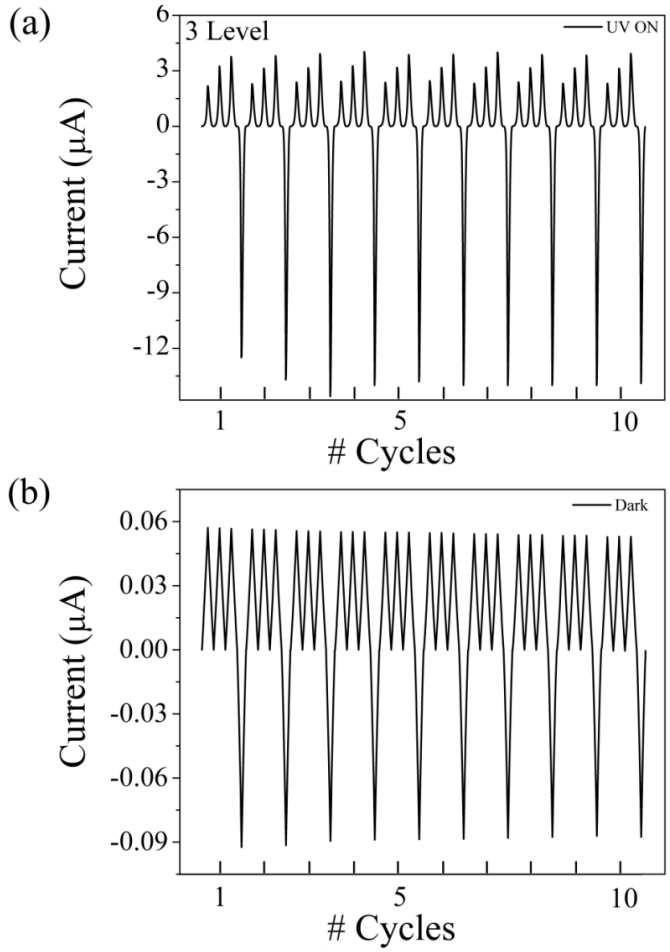

Figure 75: (a) 3-level current amplification of the device upon application of 4V and a rest bias of -6 V under UV irradiation and (b) in dark condition.

We can ascribe the multilevel current amplification of the ZnO device as a consequence of the multiple conductive paths created under UV light, which increases the number of oxygen vacancies. Indeed, it has been reported that the current amplification is due to the accumulation of charged defects[136]. The multilevel current amplification is not occurring under dark conditions (Figure 75b). Indeed, at each level the current is constant and the value of current reached is ~ 0.06 μA and decreased with the number of cycles. Whereas, under UV light the current reached ~ 4 μA, which is two orders of magnitude larger than the one in the dark, and the current values for each cycle are reproducible and stable. Despite the memory current amplification behavior it is well known to take place in RRAM devices based on oxide nanomaterials, it has not been reported to occur in the case of ZnO rods, as demonstrated from the results obtained under dark condition (Figure 75b) [299,346]. Generally, the current amplification is due to the accumulation of charged defects which lead to the creation of multiple conduction paths [136]. Based on the results obtained, the multilevel behavior in our devices is a direct consequence of the build-up of the charged defects and of the unpaired electrons left behind by the photo-generated holes upon UV irradiation [21,23,24,407,409].

As aforementioned, in dark conditions a low conductive depletion layer is formed near the ZnO surface because the oxygen molecules adsorbed on the ZnO surface are transformed to oxygen ions by capturing free electrons from the n-type ZnO surface (Equation 7). However, when the ZnO rods are exposed to UV light, electron-hole pairs are photogenerated (Equation 8), which leads to a fast increase of the current. The photogenerated holes discharge the adsorbed oxygen ions on the surface and the oxygen is desorbed from the ZnO surface leading to a decrease of the depletion layer width and to the increase of the current (Equation 9). When the UV light is turned off, an increase of the depletion layer's width occurs and the current value will reach the initial value of the dark current. The photo-response rate depends on the concentration of surface defects, surface captured oxygen and on the recombination rate of photo-generated electrons-holes pairs, which are separated by the surface barrier originated by the depletion layer. The lower concentration and lower barrier height leads to a faster photorecombination and therefore faster photo-response decay [23,419,420]. In order to investigate the photo-response time of our devices, we applied a constant positive and negative voltage of 1V to the Ag electrode while the FTO is grounded, and we exposed the device to the UV light for 50 minutes. In Figure 76(a-b)

the photoresponse performances of the device under positive (a) and negative (b) voltage are displayed.

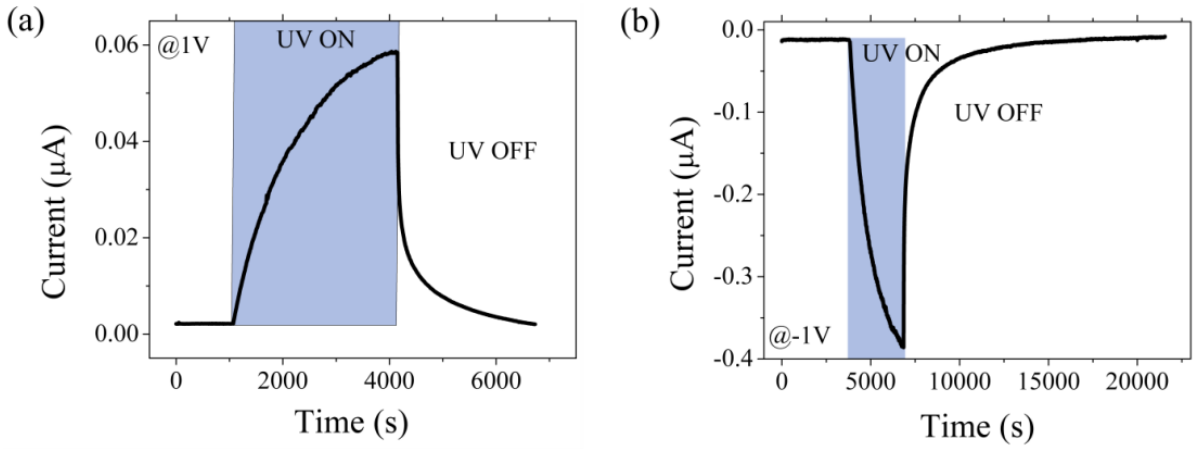

Figure 76: UV photoresponse time of the Ag/ZnO rods/FTO under constant (a) positive and (b) negative voltage.

The photo-decay process can be fitted with the following exponential relaxation equation:

$$I = I_0 + Ae^{-\frac{t}{\tau_1}} + Be^{-\frac{t}{\tau_2}} \qquad (10)$$

where the two relaxation time constant are indicated as τ_1 and τ_2. These relaxation time constants highlight the presence of two different mechanisms during the decay process, as reported in literature [23,421]. The time constant τ_1 is related to the band-to-band recombination in the bulk, while τ_2 depends on the presence of chemisorbed oxygen and oxygen vacancies, which give rise to the persistent photoconductivity in ZnO [23,421–423]. We observed that under a constant positive voltage, the time constants are τ_1= 42 s and τ_2= 828 s. These values are in agreement with those reported in literature [23,421–423], moreover, due to the presence of chemisorbed oxygen and oxygen vacancies within the ZnO structure in our device, a long τ_2 is expected. However, when a constant negative voltage is applied, we found higher time constant values. In particular, τ_1 resulted to be 154 s, while τ_2 is 1953 s. It is evident that, under negative voltage the recombination lifetime is increased. As aforementioned, the recombination rate depends on the concentration of chemisorbed oxygen, oxygen vacancies and surface potential barrier and is independent of voltage polarity. Based on our results, we hypothesize that the slower photorecombination rate under constant negative voltage could be attributed to the presence of higher concentration of chemisorbed oxygen, which lead to a higher barrier height. It is assumed that the Ag/ZnO rods interface is an ohmic contact and ZnO rods/FTO forms a Schottky barrier, based on the work function of the electrodes (4.3 eV for Ag and 4.7 eV for FTO) and the ideal

Fermi level of ZnO (4.2 eV) [424]. We hypothesize that when a negative voltage is applied, during UV illumination the decrease in the high-resistance depletion layer (barrier height) and increase of unpaired electrons' concentration lead to an enhancement of conductivity, as shown in Figures 6. However, when the UV irradiation is switched OFF, the Schottky barrier at the ZnO/FTO limits the electrons transport. Therefore, more electrons, compared to the case applying a positive voltage, will be trapped by the oxygen molecules forming oxygen ions (Equation 7), which lead to a higher barrier height (depletion layer's width) and promoting a spatial separation of the electrons and photogenerated holes, which lead to a slower photo-response [23]. In order to confirm this hypothesis, we fabricated a device with gold electrodes. In particular, in the case of Au/ZnO rods/FTO due to the higher work function of Au compared to Ag, in this device the Au/ZnO rods interface is assumed to form a sharper Schottky barrier [424]. Based on our hypothesis, when a positive voltage is applied to the gold electrode a slower photo-response is expected due to the higher Schottky barrier at the Au/ZnO rods interface.

In Figure 77(a-b) the photoresponse of this device under constant positive and negative voltage of 1V are displayed.

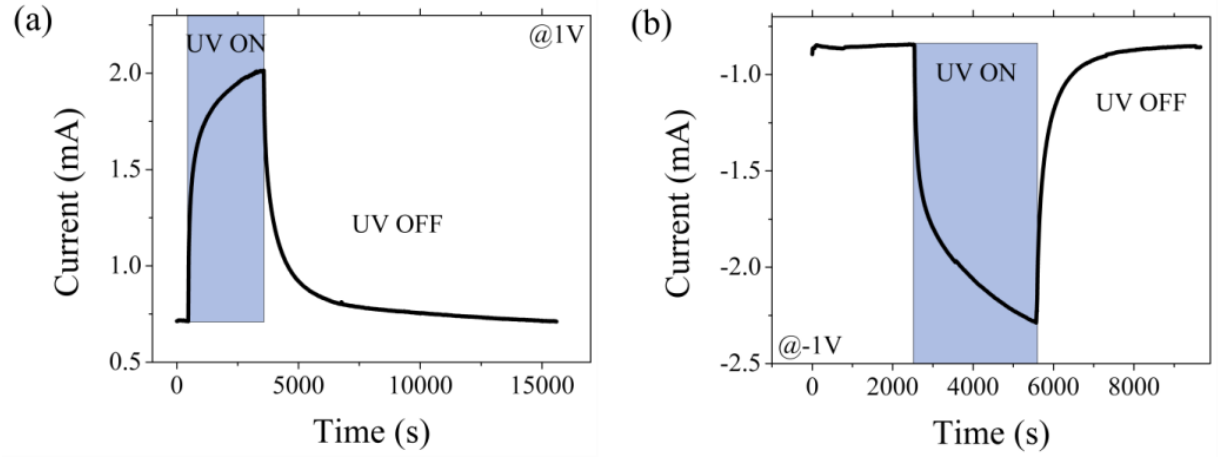

Figure 77: UV photoresponse of the Au/ZnO rods/FTO device applying a positive (a) and (b) negative voltage.

The time constants under positive voltage are τ_1= 251 s and τ_2= 1940 s, while for the negative voltage the relaxation time constants are τ_1= 95 s and τ_2= 600 s. These results are in agreement with our hypothesis, thus after switching OFF the UV lamp, the nature of the interface metal/ZnO rods affects the concentration of chemisorbed oxygen, which lead to a change in the barrier height, resulting in a slower photodecay rate.

In order to further investigate the photoresponse we carried out different electrical measurements applying a constant negative voltage of -1V to the grounded FTO while turning ON/OFF the UV lamp for different time intervals. In Figure 78(a-b) are displayed the variation of the current when the device was kept alternatively in dark and under UV irradiation for 5 minutes and 1 minute, respectively.

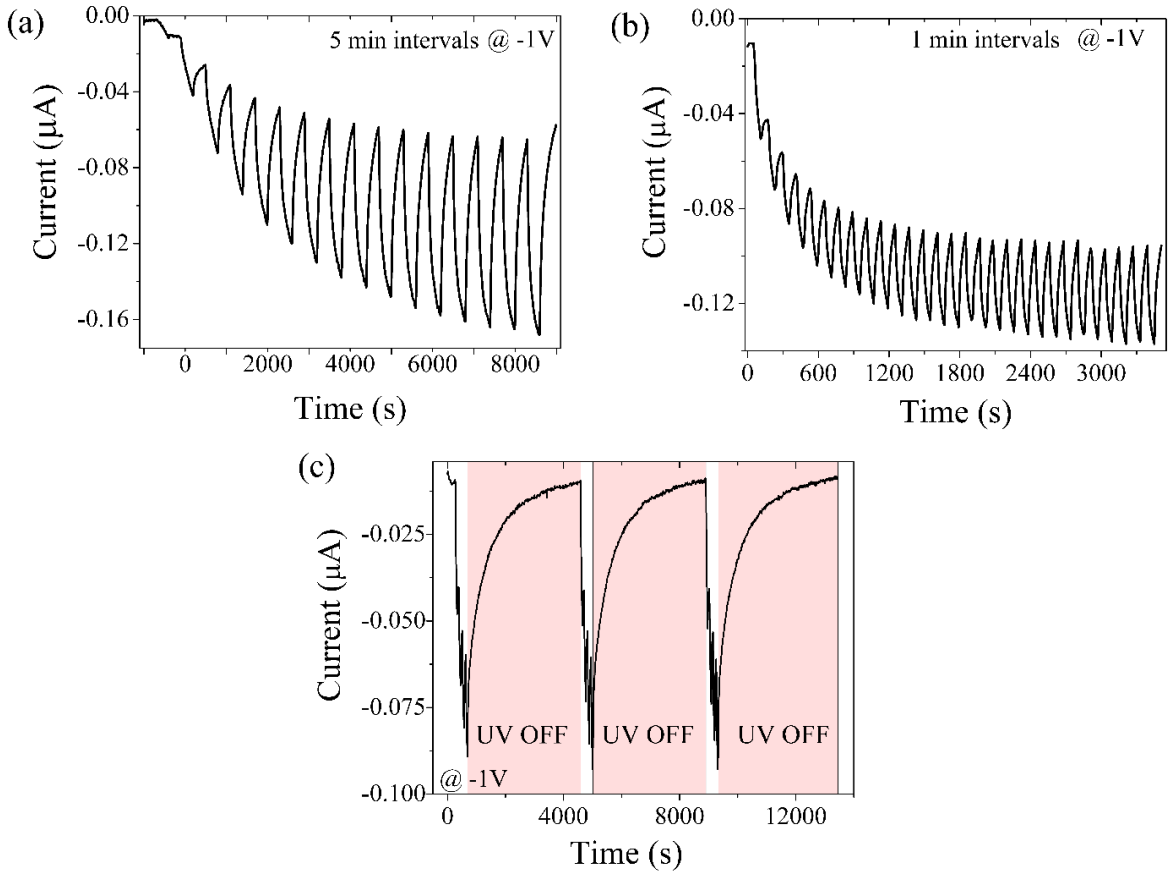

Figure 78: (a) Photocurrent response at -1V of the Ag/ZnOrods/FTO device turning ON and OFF the UV lamp with 5 minutes and (b) 1 min intervals; (c) reproducibility of the photo-induced multilevel current amplification in dark and during UV irradiation

It is possible to notice that after each ON/OFF cycle it is observed a current amplification behavior until the saturation is reached. The explanation for this current amplification is to be attributed to the long recombination rate. Indeed, as we previously describe, the relaxation time constants are much longer than the ON/OFF intervals, therefore the unpaired electrons will accumulate and when the lamp is turned back ON, more electrons-holes pair are photogenerated and this leads to the current amplification. The current response of our devices under dark and UV irradiation conditions is stable and reproducible. In Figure 78c, it shown that after 4 cycles

of ON/OFF with 1 minute intervals, the device was kept in dark condition until the initial dark current value is reached. When the ON/OFF cycles are repeated, the current values reached under UV illumination are constant and reproducible.

7.4. Summary

For the first time, the multilevel current amplification of ZnO rods induced by UV irradiation has been reported. The ZnO rods synthesized by cathodic deposition on seeded FTO substrates were used for the fabrication of an Ag/ZnOrods/FTO device and their electrical performances were tested in the dark and under UV light. The devices showed a bipolar resistive switching behavior due to the presence of intrinsic defects (oxygen vacancies) in the ZnO rods structure. The UV illumination, improved the stability of the device and the conductivity was higher than the one measured for the devices in dark. This result is in agreement with the current literature; however we observed a multilevel current amplification of the device under illumination. Investigations of the photodecay mechanisms revealed that the multilevel current amplification behavior is due to the slow photoconductivity decay of our devices.

Chapter 8. Conclusions and Outlook

Overview

In this thesis, alternative synthetic approaches of different materials have been developed. In Chapter 4 and Chapter 5, it has been demonstrated that the synthesis of GQDs and the phase transformation of TiO_2 can be performed in an ecofriendly way through laser ablation in water, respectively. Moreover, in Chapter 6 the synthesis of CNWs has been performed by the EPD of a solution of polyynes dispersed in water obtained by arc discharge of graphite electrodes in water. The advantages and the disadvantages of the explored techniques are summarized in Table 9 .

The understanding of the processes' mechanisms was used to control and modify the materials structure in order to obtain materials with improved mechanical and/or electrical properties for their use in emerging applications. In particular, laser ablation in liquids and electrochemical processes were employed as straightforward techniques for the synthesis and modification of graphene-based nanomaterials, TiO_2 nanoparticles and ZnO rods. Applications of the synthesized materials as conductive inks or for the fabrication of next generation memory devices were explored. This chapter contains the major conclusions from this work, together with some recommendations for future research areas.

Table 9: Advantages and disadvantages of the explored techniques

	Laser Ablation in Water	Electrophoretic deposition	Electrochemical Oxidation
Ecofriendly Process	✓	✓	✗
Straightforward process	✓	✓	✓
Versatile Technique	✓	✓	✓
Equipment Cost	✗	✓	✓
Scaling of the Synthetic Process	✗	✓	✓
Safety of the Process	✗	✓	✓

8.1. Conclusions

8.1.1. Single-step synthesis of graphene quantum dots by femtosecond laser ablation of graphene oxide dispersions

Graphene quantum dots (GQDs) were synthesized for the first time by femtosecond laser ablation of GO dispersion. Laser ablation time and laser power are the two key parameters for the synthesis of GQDs of different size and different type of nanostructures. Compared to other fabrication methods, the approach we used allows the synthesis of the GQDs in an eco-friendly, straightforward and time-effective way. Moreover, the obtained GQDs were mixed, without any purification, with silver nanoparticles for the fabrication of a hybrid conductive ink (GQDs@AgNP) to be used for printing electronic devices. In particular, from the resistivity measurements it was found that the GQDs@AgNP ink showed resistivity two orders of magnitude that of printed graphene sheets. The GQDs have the potential to be used as material for the fabrication of a more conductive and/or reducing costs of conductive inks by decreasing the concentration of silver nanoparticles (AgNPs) in the ink.

8.1.2. Phase Transformation of TiO_2 Nanoparticles by Femtosecond Laser Ablation in Aqueous Solutions and Deposition on Conductive Substrates

The laser ablation can be employed not only as a technique to synthesize materials with different dimensionality, but it can be used as a tool to induce modification of the material's structure. In particular, the phase transformation of TiO_2 nanoparticles dispersed in water and deposited onto FTO was explored. From the study it was found that the phase of TiO_2 nanoparticles dispersed in water can be engineered controlling the ablation time. Short ablation time resulted in the formation of larger particles, where rutile phase is the predominant phase. At longer ablation times, due to a reduction of the particle sizes, the predominant phase is anatase. The TiO2 nanoparticles deposited on FTO were transformed to rutile upon laser ablation and it was observed that the laser patterned areas possessed a higher refractive index leading to the possibility of using these patterned substrates for the fabrication of light trapping layers.

8.1.3. Carbon Materials for Next Generation Resistive Switching Memory Devices

Electrophoretic deposition (EPD) of polyynes obtained by arc discharge in water was used for the synthesis of two types of carbon-based devices. One device was made of carbon nanowalls (CNWs), obtained after 1 hour of deposition, while the second device was made of carbon structures (Cs) obtained after 2 hours of EPD and oxidized by electrochemical oxidation. The two types of devices showed bipolar resistive switching (RS) behavior, and from the investigation of the RS mechanisms it was found that it is originated by the formation of conductive filament paths built from the oxygen vacancies and structural defects. The study carried out on the relationship between material's structure and electrical properties, highlighted that the stability and the electrical performances of the carbon-based devices strongly depend on their chemical composition. In particular, the oxidized carbon structures showed improved electrical performances together with multilevel current amplification effect. The study highlights that due to the promising electrical properties of the devices, the ease and time effectiveness of the fabrication method and the possibility of controlling the materials structure and composition; denotes an engineering solution for the large-scale development of other carbon-based electronics.

8.1.4. UV-induced multilevel current amplification memory effect in zinc oxide rods resistive switching devices

The multilevel current amplification memory effect in zinc oxide (ZnO) rods resistive switching memories under ultraviolet (UV) irradiation is reported. The cathodic deposition of zinc nitrate solution on fluorine-doped tin oxide (FTO) substrates is employed as technique for the synthesis of the ZnO seed layer and for the consecutive growth of the ZnO rods. The electrical performances of the Ag/ZnO rods/FTO device are performed under dark or UV-light exposure. The device shows a forming-free bipolar resistive switching behavior under both experimental conditions attributed to the presence of conductive filaments composed of oxygen vacancies. However, when exposed to UV-light, a multilevel memory behavior is observed. To the best of our knowledge, the multilevel memory effect induced by UV-light has never been reported in ZnO resistive switching memory devices. From the investigation of the photodecay mechanisms and the electrode/metal interface it has been demonstrated that photo-induced multilevel memory

behaviour is attributed to the slow photodecay rate of the device. This study opens up the possibility of employing this material for the fabrication of resistive random memories for the storage of more than one bit per memory cell and for the realization of UV photodetectors.

8.2. Outlook

The following topics are suggested for future research:

1. Graphene quantum dots (GQDs) obtained by femtosecond laser ablation of GO dispersions were mixed with AgNPs for the fabrication of a hybrid ink, which was printed with an aerosol-jet printing system. The resistivity of the patterns printed with the hybrid GQDs@AGNPs ink was two times less than the resistivity of the AgNP patterns. (**Chapter 4**). The AgNPs solution employed has been purchased and the nanoparticles are dispersed in ethylene glycol. In order to remove the solvents from the inks and to sinter the AgNPs, the printed patterned were heat treated. The focus of this thesis is to develop straightforward, eco-friendly and time-effective method for the synthesis and modification of different materials. With this in mind, in order to develop greener approach further studies can be conducted on the combination of laser modified graphene oxides with laser synthesized and joined silver nanoparticles.

2. EPD was employed as a time-effective technique for the deposition of carbon materials (**Chapter 6**) and for the growth of ZnO rods (**Chapter 7**) on FTO substrates. From the study of the process mechanisms and from the results obtained, it has been assessed electrochemical processes can be employed to engineer the chemical composition of carbon structures (**Chapter 6**) to improve and tailor their electrical performances. Further studies can be focused on the use of EPD for the deposition of other materials such as boron nitride (BN) molybdenum disulfide (MoS_2). These materials, like carbon-based materials and ZnO rods, are good candidates for their use in electronics. A proposed research is the alternate deposition of different 2D dimensional materials of FTO and the study of their electrical properties to be employed as memory devices. The electrical properties can be tailored varying deposition parameters and chemical composition performing the electrochemical oxidation in different solvents.

3.

Chapter 9. Research Contributions

9.1. Articles Published in Refereed Journals

1. **Paola Russo**, Ming Xiao, Norman Y. Zhou, Carbon Nanowalls: A new material for resistive switching memory devices, *Carbon* 120, 54-62, 2017 **(PhD work in thesis, Chapter 6)**

2. **Paola Russo**, Robert Liang, Rui Xiu He, Y. Norman Zhou, "Phase transformation of TiO2 nanoparticles by femtosecond laser ablation in aqueous solution and deposited on conductive substrate", *Nanoscale*, 9, 6167, 2017 **(PhD work in thesis, Chapter 5)**

3. **Paola Russo**, Robert Liang, Elahe Jabari, Ehsan Marzbanrad, Ehsan Toyserkani, Y. Norman Zhou, "Single-step synthesis of graphene quantum dots by femtosecond laser ablation of graphene oxide dispersions", *Nanoscale*, 8, 8863, 2016. **(PhD work in thesis, Chapter 4)**

4. Simona Filice, Giuseppe Compagnini, Roberto Fiorenza, Salvatore Scirè, Luisa D'Urso, Maria Elena Fragalà, **Paola Russo**, Enza Fazio, Silvia Scalese, "Laser processing of TiO_2 colloids for an enhanced photocatalytic water splitting activity", *Journal of Colloid and Interface Science*, 489, 131-137, 2017.

5. Behnam Meschi Amoli, Josh Trinidad, Geoffrey Rivers, Abel Sy, **Paola Russo**, Aping Yu, Norman Y. Zhou, and Boxin Zhao, SDS-stabilized graphene nanosheets for highly electrically conductive adhesives, *Carbon*, 91, 188–199, 2015.

6. **Paola Russo**, Luisa D'Urso, Anming Hu, Norman Zhou, Giuseppe Compagnini, In liquid laser treated graphene oxide for dye removal, *Applied Surface Science*, 348, 85-91, 2015. **(PhD work not included in the thesis)**

7. Simon Federico Spanò, Giuseppe Isgrò, **Paola Russo**, Maria Elena Fragalà, Giuseppe Compagnini, "Tunable Properties of Graphene Oxide Reduced by Laser Irradiation", *Applied Physics A,* 117, 19-23, 2014 (**Work in Literature Review**)

8. **Paola Russo**, Anming Hu, Giuseppe Compagnini, Walter W. Duley, and Norman Y. Zhou, "Femtosecond laser ablation of highly oriented pyrolytic graphite: green route for

large-scale production of porous graphene and graphene quantum dots", *Nanoscale*, 6, 2381, 2014. (**Work in Literature Review**)

9. **Russo, Paola**; Hu, Anming; Compagnini, Giuseppe, "Synthesis, properties and potential applications of porous graphene: a review", *Nano-Micro Lett*. 5 (4), 260-273, (2013). (**Work in Literature Review**)

10. G.Compagnini, **P. Russo**, F.Tomarchio, O. Puglisi, L.D'Urso, S. Scalese; "Laser assisted green synthesis of free standing reduced graphene oxides at the water–air interface." *Nanotechnolog*y, 23, 505601 (6pp), (2012). (**Work in Literature Review**)

11. G. Compagnini, M. Sinatra, **P. Russo**, G. Messina, O. Puglisi, S. Scalese; "Deposition of fewlayer graphene nanowalls at the electrodes during electric field-assisted laser ablation of carbon in water". *Carbon*, 50, 6, 2362-2365, (2012). (**Work in Literature Review**)

9.2. Submitted/To be submitted

1. **Paola Russo**, Ming Xiao, Norman Y. Zhou, Engineering of carbon-based devices' electrical performances through electrochemical oxidation, Submitted to Nano Research, ID NARE-D-17-01404 **(PhD work in thesis, Chapter 6)**

2. **Paola Russo**, Ming Xiao, Robert Liang, Norman Y. Zhou. UV induced multilevel current amplification memory effect in zinc oxide nanorods restive switching memories. Submitted to Advanced Functional Materials: adfm.201706230 **(PhD work in thesis, Chapter 7)**

9.3. Conference Presentations/Attendance:

1. **Paola Russo,** Ming Xiao, Norman Zhou, "Carbon Nanowalls: a New Material for Resistive Switching Memory Devices", presented at the 2017 CAMJ International Workshop on Advanced Materials Joining and Processing, University of Waterloo, Canada, October 2017 **(PhD work in thesis, Chapter 6)**

2. **Paola Russo,** Ming Xiao, N. Zhou, "Resistive switching devices fabricated with Carbon Nanowalls" presented at the International Forum on Micro-nano Manufacturing Technology for Graduate students, Beijing, China, July 2017 **(PhD work in thesis, Chapter 6)**

3. 25-28 September 2016, International Conference on Nanojoining and Microjoining 2016 (NMJ 2016), Niagara Falls, Canada. **(PhD work in thesis, Chapter 5)**

4. **Paola Russo**, Robert Liang, Norman Y. Zhou, "Femtosecond laser synthesis of luminescent graphene quantum dots" Presented at Graphene Canada, Montreal, October 2015 (**Work in Literature Review**)

9.4. Posters

1. **P. Russo**, R. Liang, and N. Zhou, "Fabrication of a hybrid ink made of laser reduced graphene oxide and silver nanoparticles for future electronics devices". Presented at the conference: NMJ 2016 held in Niagara Falls, Canada, September 2016 **(PhD work in thesis, Chapter 4)**

2. **Paola Russo**, Giuseppe Isgrò, Simon Federico Spanò, Anming Hu, Giuseppe Compagnini. "Nanosecond and femtosecond laser irradiation for graphene related nanomaterials production" EMRS held in Lille (France) from 25 to 30 May 2014. **(PhD work in thesis, Chapter 4)**

9.5. Awards received

1. WIN Nanofellowship (Waterloo Institute of Nanotechnology), at University of Waterloo, August 2017 (Valued $10.000 CAD). This prestigious scholarship is awarded to students with outstanding academic qualifications and research potential.
2. Best Poster Presentation Award at NMJ 2016 held in Niagara Falls, Canada, September 2016 (Awarded $500.00 CAD)
3. Best Student Oral presentation Award at ANGEL 2012-2nd Conference on Laser Ablation and Nanoparticle Generation in Liquids (2012)

Copyright Permissions

The copyright permissions have been obtained for the following figures embedded within this thesis:

- Figure 2
- Figure 5
- Figure 6
- Figure 7
- Figure 8
- Figure 9
- Figure 10
- Figure 11
- Figure 12
- Figure 13
- Figure 14
- Figure 15

The copyright permission has been obtained for the following chapter of this thesis:

Chapter 6

Chapter 4 and Chapter 5 are papers published by RSC and as stated by the journal policy, the published papers can be used in thesis chapters without requesting permissions. However, acknowledgment of the publications needs to be provided. The titles of the chapters 4 and 5 and the figures embedded in those chapters are accompanied by the reference numbers, acknowledging the published papers.

Chapter 7 is a paper submitted to Advanced Functional Materials:

Copyright Clearance Center

Note: Copyright.com supplies permissions but not the copyrighted content itself.

1 PAYMENT 2 REVIEW 3 CONFIRMATION

Step 3: Order Confirmation

Thank you for your order! A confirmation for your order will be sent to your account email address. If you have questions about your order, you can call us 24 hrs/day, M-F at +1.855.239.3415 Toll Free, or write to us at info@copyright.com. This is not an invoice.

Confirmation Number: 11661736
Order Date: 08/09/2017

If you paid by credit card, your order will be finalized and your card will be charged within 24 hours. If you choose to be invoiced, you can change or cancel your order until the invoice is generated.

Payment Information

Paola Russo p3russo@uwaterloo.ca
+1 (519) 888-4567
Payment Method: n/a

Order Details

Journal of Physics : Condensed Matter

Order detail ID: 70635536
Order License Id: 4164800158180
ISSN: 0953-8984
Publication Type: Journal
Volume:
Issue:
Start page:
Publisher: IOP Publishing

Permission Status: Granted
Permission type: Republish or display content
Type of use: Thesis/Dissertation
Requestor type Academic institution
Format Print, Electronic
Portion image/photo
Number of images/photos requested 1
Title or numeric reference of the portion(s) Figure 1 (a-e)
Title of the article or chapter the portion is from Electronic and optoelectronic nano- devices based on carbon nanotubes
Editor of portion(s) Journal of Physics: Condensed Matter
Author of portion(s) M Scarselli et al.

Note: This item will be invoiced or charged separately through CCC's **RightsLink** service. More info **$ 0.00**

This is not an invoice.

Total order items: 1 **Order Total: 0.00 USD**

Confirmation Number: 11661736

Special Rightsholder Terms & Conditions

The following terms & conditions apply to the specific publication under which they are listed

---

Journal of Physics : Condensed Matter
Permission type: Republish or display content
Type of use: Thesis/Dissertation

TERMS AND CONDITIONS

The following terms are individual to this publisher:

These special terms and conditions are in addition to the standard terms and conditions for CCC's Republication Service and, together with those standard terms and conditions, govern the use of the Works.

As the "User" you will make all reasonable efforts to contact the author(s) of the article which the Work is to be reused from, to seek consent for your intended use. Contacting one author who is acting expressly as authorised agent for their co-author(s) is acceptable.

User will reproduce the following wording prominently alongside the Work:

the source of the Work, including author, article title, title of journal, volume number, issue number (if relevant), page range (or first page if this is the only information available) and date of first publication. This information can be contained in a footnote or reference note; and

a link back to the article (via DOI); and

if practicable, and IN ALL CASES for new works published under any of the Creative Commons licences, the words "© IOP Publishing. Reproduced with permission. All rights reserved"

Without the express permission of the author(s) and the Rightsholder of the article from which the Work is to be reused, User shall not use it in any way which, in the opinion of the Rightsholder, could: (i) distort or alter the author(s)' original intention(s) and meaning; (ii) be prejudicial to the honour or reputation of the author(s); and/or
(iii) imply endorsement by the author(s) and/or the Rightsholder.

This licence does not apply to any article which is credited to another source and which does not have the copyright line '© IOP Publishing Ltd'. User must check the copyright line of the article from which the Work is to be reused to check that IOP Publishing Ltd has all the necessary rights to be able to grant permission. User is solely responsible for identifying and obtaining separate licences and permissions from the copyright owner for reuse of any such third party material/figures which the Rightsholder is not the copyright owner of. The Rightsholder shall not reimburse any fees which User pays for a republication license for such third party content.

This licence does not apply to any material/figure which is credited to another source in the Rightsholder's publication or has been obtained from a third party. User must check the Version of Record of the article from which the Work is to be reused, to check whether any of the material in the Work is third party material. Third party citations and/or copyright notices and/or permissions statements may not be included in any other version of the article from which the Work is to be reused and so cannot be relied upon by the User. User is solely responsible for identifying and obtaining separate licences and permissions from the copyright owner for reuse of any such third party material/figures where the Rightsholder is not the copyright owner. The Rightsholder shall not reimburse any fees which User pays for a republication license for such third party content.

User and CCC acknowledge that the Rightsholder may, from time to time, make changes or additions to these special terms and conditions without express notification, provided that these shall not apply to permissions already secured and paid for by User prior to such change or addition.

User acknowledges that the Rightsholder (which includes companies within its group and third parties for whom it publishes its titles) may make use of personal data collected through the service in the course of their business.

If User is the author of the Work, User may automatically have the right to reuse it under the rights granted back when User transferred the copyright in the article to the Rightsholder. User should check the copyright form and the relevant author rights policy to check whether permission is required. If User is the author of the Work and does require permission for proposed reuse of the Work, User should select 'Author of requested content' as the Requestor Type. The Rightsholder shall not reimburse any fees which User pays for a republication license.

If User is the author of the article which User wishes to reuse in User's thesis or dissertation, the republication licence covers the right to include the Accepted Manuscript version (not the Version of Record) of the article. User must include citation details and, for online use, a link to the Version of Record of the article on the Rightsholder's website. User may need to obtain separate permission for any third party content included within the article. User must check this with the copyright owner of such third party content. User may not include the article in a thesis or dissertation which is published by ProQuest. Any other commercial use of User's thesis or dissertation containing the article would also need to be expressly notified in writing to the Rightsholder at the time of request and would require separate written permission from the Rightsholder.

User does not need to request permission for Work which has been published under a CC BY licence. User must check the Version of Record of the CC BY article from which the Work is to be reused, to check whether any of the material in the Work is third party material and so not published under the CC BY licence. User is solely responsible for identifying and obtaining separate licences and permissions from the copyright owner for reuse of any such third party material/figures. The Rightsholder shall not reimburse any fees which User pays for such licences and permissions.

As well as CCC, the Rightsholder shall have the right to bring any legal action that it deems necessary to enforce its rights should it consider that the Work infringes those rights in any way.

For STM Signatories ONLY (as agreed as part of the STM Guidelines)

Any licence granted for a particular edition of a Work will apply also to subsequent editions of it and for editions in other languages, provided such editions are for the Work as a whole in situ and do not involve the separate exploitation of the permitted illustrations or excerpts.

Other Terms and Conditions:

STANDARD TERMS AND CONDITIONS

1. Description of Service; Defined Terms. This Republication License enables the User to obtain licenses for republication of one or more copyrighted works as described in detail on the relevant Order Confirmation (the "Work(s)"). Copyright Clearance Center, Inc. ("CCC") grants licenses through the Service on behalf of the rightsholder identified on the Order Confirmation (the "Rightsholder"). "Republication", as used herein, generally means the inclusion of a Work, in whole or in part, in a new work or works, also as described on the Order Confirmation. "User", as used herein, means the person or entity making such republication.

2. The terms set forth in the relevant Order Confirmation, and any terms set by the Rightsholder with respect to a particular Work, govern the terms of use of Works in connection with the Service. By using the Service, the person transacting for a republication license on behalf of the User represents and warrants that he/she/it (a) has been duly authorized by the User to accept, and hereby does accept, all such terms and conditions on behalf of User, and (b) shall inform User of all such terms and conditions. In the event such person is a "freelancer" or other third party independent of User and CCC, such party shall be deemed jointly a "User" for purposes of these terms and conditions. In any event, User shall be deemed to have accepted and agreed to all such terms and conditions if User republishes the Work in any fashion.

3. Scope of License; Limitations and Obligations.

3.1 All Works and all rights therein, including copyright rights, remain the sole and exclusive property of the Rightsholder. The license created by the exchange of an Order Confirmation (and/or any invoice) and payment by User of the full amount set forth on that document includes only those rights expressly set forth in the Order Confirmation and in these terms and conditions, and conveys no other rights in the Work(s) to User. All rights not expressly granted are hereby reserved.

3.2 General Payment Terms: You may pay by credit card or through an account with us payable at the end of the month. If you and we agree that you may establish a standing account with CCC, then the following terms apply: Remit Payment to: Copyright Clearance Center, 29118 Network Place, Chicago, IL 60673-1291. Payments Due: Invoices are payable upon their delivery to you (or upon our notice to you that they are available to you for downloading). After 30 days, outstanding amounts will be subject to a service charge of 1-1/2% per month or, if less, the maximum rate allowed by applicable law. Unless otherwise specifically set forth in the Order Confirmation or in a separate written agreement signed by CCC, invoices are due and payable on "net 30" terms. While User may exercise the rights licensed immediately upon issuance of the Order Confirmation, the license is automatically revoked and is null and void, as if it had never been issued, if complete payment for the license is not received on a timely basis either from User directly or through a payment agent, such as a credit card company.

3.3 Unless otherwise provided in the Order Confirmation, any grant of rights to User (i) is "one-time" (including the editions and product family specified in the license), (ii) is non-exclusive and non-transferable and (iii) is subject to any and all limitations and restrictions (such as, but not limited to, limitations on duration of use or circulation) included in the Order Confirmation or invoice and/or in these terms and conditions. Upon completion of the licensed use, User shall either secure a new permission for further use of the Work(s) or immediately cease any new use of the Work(s) and shall render inaccessible (such as by deleting or by removing or severing links or other locators) any further copies of the Work (except for copies printed on paper in accordance with this license and still in User's stock at the end of such period).

3.4 In the event that the material for which a republication license is sought includes third party materials (such as photographs, illustrations, graphs, inserts and similar materials) which are identified in such material as having been used by permission, User is responsible for identifying, and seeking separate licenses (under this Service or otherwise) for, any of such third party materials; without a separate license, such third party materials may not be used.

3.5 Use of proper copyright notice for a Work is required as a condition of any license granted under the Service. Unless otherwise provided in the Order Confirmation, a proper copyright notice will read substantially as follows: "Republished with permission of [Rightsholder's name], from [Work's title, author, volume, edition number and year of copyright]; permission conveyed through Copyright Clearance Center, Inc. " Such notice must be provided in a reasonably legible font size and must be placed either immediately adjacent to the Work as used (for example, as part of a by-line or footnote but not as a separate electronic link) or in the place where substantially all other credits or notices for the new work containing the republished Work are located. Failure to include the required notice results

in loss to the Rightsholder and CCC, and the User shall be liable to pay liquidated damages for each such failure equal to twice the use fee specified in the Order Confirmation, in addition to the use fee itself and any other fees and charges specified.

3.6 User may only make alterations to the Work if and as expressly set forth in the Order Confirmation. No Work may be used in any way that is defamatory, violates the rights of third parties (including such third parties' rights of copyright, privacy, publicity, or other tangible or intangible property), or is otherwise illegal, sexually explicit or obscene. In addition, User may not conjoin a Work with any other material that may result in damage to the reputation of the Rightsholder. User agrees to inform CCC if it becomes aware of any infringement of any rights in a Work and to cooperate with any reasonable request of CCC or the Rightsholder in connection therewith.

4. Indemnity. User hereby indemnifies and agrees to defend the Rightsholder and CCC, and their respective employees and directors, against all claims, liability, damages, costs and expenses, including legal fees and expenses, arising out of any use of a Work beyond the scope of the rights granted herein, or any use of a Work which has been altered in any unauthorized way by User, including claims of defamation or infringement of rights of copyright, publicity, privacy or other tangible or intangible property.

5. Limitation of Liability. UNDER NO CIRCUMSTANCES WILL CCC OR THE RIGHTSHOLDER BE LIABLE FOR ANY DIRECT, INDIRECT, CONSEQUENTIAL OR INCIDENTAL DAMAGES (INCLUDING WITHOUT LIMITATION DAMAGES FOR LOSS OF BUSINESS PROFITS OR INFORMATION, OR FOR BUSINESS INTERRUPTION) ARISING OUT OF THE USE OR INABILITY TO USE A WORK, EVEN IF ONE OF THEM HAS BEEN ADVISED OF THE POSSIBILITY OF SUCH DAMAGES. In any event, the total liability of the Rightsholder and CCC (including their respective employees and directors) shall not exceed the total amount actually paid by User for this license. User assumes full liability for the actions and omissions of its principals, employees, agents, affiliates, successors and assigns.

6. Limited Warranties. THE WORK(S) AND RIGHT(S) ARE PROVIDED "AS IS". CCC HAS THE RIGHT TO GRANT TO USER THE RIGHTS GRANTED IN THE ORDER CONFIRMATION DOCUMENT. CCC AND THE RIGHTSHOLDER DISCLAIM ALL OTHER WARRANTIES RELATING TO THE WORK(S) AND RIGHT(S), EITHER EXPRESS OR IMPLIED, INCLUDING WITHOUT LIMITATION IMPLIED WARRANTIES OF MERCHANTABILITY OR FITNESS FOR A PARTICULAR PURPOSE. ADDITIONAL RIGHTS MAY BE REQUIRED TO USE ILLUSTRATIONS, GRAPHS, PHOTOGRAPHS, ABSTRACTS, INSERTS OR OTHER PORTIONS OF THE WORK (AS OPPOSED TO THE ENTIRE WORK) IN A MANNER CONTEMPLATED BY USER; USER UNDERSTANDS AND AGREES THAT NEITHER CCC NOR THE RIGHTSHOLDER MAY HAVE SUCH ADDITIONAL RIGHTS TO GRANT.

7. Effect of Breach. Any failure by User to pay any amount when due, or any use by User of a Work beyond the scope of the license set forth in the Order Confirmation and/or these terms and conditions, shall be a material breach of the license created by the Order Confirmation and these terms and conditions. Any breach not cured within 30 days of written notice thereof shall result in immediate termination of such license without further notice. Any unauthorized (but licensable) use of a Work that is terminated immediately upon notice thereof may be liquidated by payment of the Rightsholder's ordinary license price therefor; any unauthorized (and unlicensable) use that is not terminated immediately for any reason (including, for example, because materials containing the Work cannot reasonably be recalled) will be subject to all remedies available at law or in equity, but in no event to a payment of less than three times the Rightsholder's ordinary license price for the most closely analogous licensable use plus Rightsholder's and/or CCC's costs and expenses incurred in collecting such payment.

8. **Miscellaneous**

8.1 User acknowledges that CCC may, from time to time, make changes or additions to the Service or to these terms and conditions, and CCC reserves the right to send notice to the User by electronic mail or otherwise for the purposes of notifying User of such changes or additions; provided that any such changes or additions shall not apply to permissions already secured and paid for.

8.2 Use of User-related information collected through the Service is governed by CCC's privacy policy, available online here: http://www.copyright.com/content/cc3/en/tools/footer/privacypolicy.html.

8.3 The licensing transaction described in the Order Confirmation is personal to User. Therefore, User may not assign or transfer to any other person (whether a natural person or an organization of any kind) the license created by the Order Confirmation and these terms and conditions or any rights granted hereunder; provided, however, that User may assign such license in its entirety on written notice to CCC in the event of a transfer of all or substantially all of User's rights in the new material which includes the Work(s) licensed under this Service.

8.4 No amendment or waiver of any terms is binding unless set forth in writing and signed by the parties. The Rightsholder and CCC hereby object to any terms contained in any writing prepared by the User or its principals, employees, agents or affiliates and purporting to govern or otherwise relate to the licensing transaction described in the Order Confirmation, which terms are in any way inconsistent with any terms set forth in the Order Confirmation and/or in these terms and conditions or CCC's standard operating procedures, whether such writing is prepared prior to, simultaneously with or subsequent to the Order Confirmation, and whether such writing appears on a copy of the Order Confirmation or in a separate instrument.

8.5 The licensing transaction described in the Order Confirmation document shall be governed by and construed under the law of the State of New York, USA, without regard to the principles thereof of conflicts of law. Any case, controversy, suit, action, or proceeding arising out of, in connection with, or related to such licensing transaction shall be brought, at CCC's sole discretion, in any federal or state court located in the County of New York, State of New York, USA, or in any federal or state court whose geographical jurisdiction covers the location of the Rightsholder set forth in the Order Confirmation. The parties expressly submit to the personal jurisdiction and venue of each such federal or state court.If you have any comments or questions about the Service or Copyright Clearance Center, please contact us at 978-750-8400 or send an e-mail to info@copyright.com.

v 1.1

Close

Confirmation Number: 11661736

Citation Information

Order Detail ID: 70635536

Journal of Physics : Condensed Matter by IOP Publishing. Reproduced with permission of IOP Publishing in the format Thesis/Dissertation via Copyright Clearance Center.

Close

ROYAL SOCIETY OF CHEMISTRY LICENSE TERMS AND CONDITIONS

Aug 09, 2017

This Agreement between Dr. Paola Russo ("You") and Royal Society of Chemistry ("Royal Society of Chemistry") consists of your license details and the terms and conditions provided by Royal Society of Chemistry and Copyright Clearance Center.

License Number	4164811207593
License date	Aug 09, 2017
Licensed Content Publisher	Royal Society of Chemistry
Licensed Content Publication	Polymer Chemistry
Licensed Content Title	Latex routes to graphene-based nanocomposites
Licensed Content Author	Elodie Bourgeat-Lami,Jenny Faucheu,Amélie Noël
Licensed Content Date	Jun 22, 2015
Licensed Content Volume	6
Licensed Content Issue	30
Type of Use	Thesis/Dissertation
Requestor type	academic/educational
Portion	figures/tables/images
Number of figures/tables /images	1
Format	print and electronic
Distribution quantity	5000
Will you be translating?	no
Order reference number	0
Title of the thesis/dissertation	Development of green synthetic approaches for the potential application of carbon and semiconductor nanomaterials for emerging applications
Expected completion date	Feb 2018
Estimated size	250
Requestor Location	University of Waterloo 200 University Avenue Waterloo, ON N2L3G1 Canada Attn: Dr. Paola Russo
Billing Type	Invoice
Billing Address	Dr. Paola Russo 200 University Avenue Waterloo, ON N2L3G1 Canada Attn: Dr. Paola Russo
Total	0.00 CAD
Terms and Conditions	

this content into the languages you requested. A professional translator must perform all translations and reproduce the content word for word preserving the integrity of the article.
Intranet
If the licensed material is being posted on an Intranet, the Intranet is to be password-protected and made available only to bona fide students or employees only. All content posted to the Intranet must maintain the copyright information line on the bottom of each image. You must also fully reference the material and include a hypertext link as specified above.
Copies of Whole Articles
All copies of whole articles must maintain, if available, the copyright information line on the bottom of each page.
Other Conditions
v1.2
Gratis licenses (referencing $0 in the Total field) are free. Please retain this printable license for your reference. No payment is required.
If you would like to pay for this license now, please remit this license along with yourpayment made payable to "COPYRIGHT CLEARANCE CENTER" otherwise you will be invoiced within 48 hours of the license date. Payment should be in the form of a check or money order referencing your account number and this invoice number {Invoice Number}. Once you receive your invoice for this order, you may pay your invoice by credit card.
Please follow instructions provided at that time.
Make Payment To:
Copyright Clearance Center
29118 Network Place
Chicago, IL 60673-1291
For suggestions or comments regarding this order, contact Rightslink Customer Support: customercare@copyright.com or +1-855-239-3415 (toll free in the US) or +1-978-646-2777.

Questions? customercare@copyright.com or +1-855-239-3415 (toll free in the US) or +1-978-646-2777.

AMERICAN PHYSICAL SOCIETY LICENSE TERMS AND CONDITIONS

Aug 09, 2017

This Agreement between Dr. Paola Russo ("You") and American Physical Society ("American Physical Society") consists of your license details and the terms and conditions provided by American Physical Society and Copyright Clearance Center.

License Number	4164810017677
License date	Aug 09, 2017
Licensed Content Publisher	American Physical Society
Licensed Content Publication	Reviews of Modern Physics
Licensed Content Title	The electronic properties of graphene
Licensed Content Author	A. H. Castro Neto et al.
Licensed Content Date	Jan 14, 2009
Licensed Content Volume	81
Type of Use	Thesis/Dissertation
Requestor type	Student
Format	Print, Electronic
Portion	image/photo
Number of images/photos requested	1
Portion description	Figure 3
Rights for	Main product
Duration of use	Life of Current Edition
Creation of copies for the disabled	no
With minor editing privileges	no
For distribution to	Worldwide
In the following language(s)	Original language of publication
With incidental promotional use	no
The lifetime unit quantity of new product	1000 to 4999
The requesting person/organization is:	Paola Russo
Order reference number	
Title of your thesis / dissertation	Development of green synthetic approaches for the potential application of carbon and semiconductor nanomaterials for emerging applications
Expected completion date	Feb 2018
Expected size (number of pages)	250

Requestor Location
Dr. Paola Russo
200 University Avenue

Waterloo, ON N2L3G1

Canada
Attn: Dr. Paola Russo

Billing Type
Invoice

Billing Address
Dr. Paola Russo
200 University Avenue

Waterloo, ON N2L3G1 Canada
Attn: Dr. Paola Russo

Total
0.00 CAD

Terms and Conditions

Terms and Conditions

The American Physical Society (APS) is pleased to grant the Requestor of this license a non-exclusive, non-transferable permission, limited to [**print** and/or **electronic** format, depending on what they chose], provided all criteria outlined below are followed.

1. You must also obtain permission from at least one of the lead authors for each separate work, if you haven't done so already. The author's name and affiliation can be found on the first page of the published Article.
2. For electronic format permissions, Requestor agrees to provide a hyperlink from the reprinted APS material using the source material's DOI on the web page where the work appears. The hyperlink should use the standard DOI resolution URL, http://dx.doi.org /{DOI}. The hyperlink may be embedded in the copyright credit line.
3. For print format permissions, Requestor agrees to print the required copyright credit line on the first page where the material appears: "Reprinted (abstract/excerpt/figure) with permission from [(FULL REFERENCE CITATION) as follows: Author's Names, APS Journal Title, Volume Number, Page Number and Year of Publication.] Copyright (YEAR) by the American Physical Society."
4. Permission granted in this license is for a one-time use and does not include permission for any future editions, updates, databases, formats or other matters. Permission must be sought for any additional use.
5. Use of the material does not and must not imply any endorsement by APS.
6. Under no circumstance does APS purport or intend to grant permission to reuse materials to which it does not hold copyright. It is the requestors sole responsibility to ensure the licensed material is original to APS and does not contain the copyright of another entity, and that the copyright notice of the figure, photograph, cover or table does not indicate that it was reprinted by APS, with permission from another source.
7. The permission granted herein is personal to the Requestor for the use specified and is not transferable or assignable without express written permission of APS. This license may not be amended except in writing by APS.
8. You may not alter, edit or modify the material in any manner.
9. You may translate the materials only when translation rights have been granted.
10. You may not use the material for promotional, sales, advertising or marketing purposes.
11. The foregoing license shall not take effect unless and until APS or its agent, Copyright Clearance Center (CCC), receives payment in full in accordance with CCC Billing and Payment Terms and Conditions, which are incorporated herein by reference.
12. Should the terms of this license be violated at any time, APS or CCC may revoke the license with no refund to you and seek relief to the fullest extent of the laws of the USA.

Official written notice will be made using the contact information provided with the permission request. Failure to receive such notice will not nullify revocation of the permission.

13. APS reserves all rights not specifically granted herein.

14. This document, including the CCC Billing and Payment Terms and Conditions, shall be the entire agreement between the parties relating to the subject matter hereof.

Other Terms and Conditions

Version 1.1

Questions? customercare@copyright.com or +1-855-239-3415 (toll free in the US) or +1-978-646-2777.

THE AMERICAN ASSOCIATION FOR THE ADVANCEMENT OF SCIENCE LICENSE TERMS AND CONDITIONS

Aug 09, 2017

This Agreement between Dr. Paola Russo ("You") and The American Association for the Advancement of Science ("The American Association for the Advancement of Science") consists of your license details and the terms and conditions provided by The American Association for the Advancement of Science and Copyright Clearance Center.

License Number	4164820897585
License date	Aug 09, 2017
Licensed Content Publisher	The American Association for the Advancement of Science
Licensed Content Publication	Science
Licensed Content Title	Electric Field Effect in Atomically Thin Carbon Films
Licensed Content Author	K. S. Novoselov,A. K. Geim,S. V. Morozov,D. Jiang,Y. Zhang,S. V. Dubonos,I. V. Grigorieva,A. A. Firsov
Licensed Content Date	Oct 22, 2004
Licensed Content Volume	306
Licensed Content Issue	569
6 Volume number	306
Issue number	5696
Type of Use	Thesis / Dissertation
Requestor type	Scientist/individual at a research institution
Format	Print and electronic
Portion	Figure
Number of figures/tables	1
Order reference number	
Title of your thesis / dissertation	Development of green synthetic approaches for the potential application of carbon and semiconductor nanomaterials for emerging applications
Expected completion date	Feb 2018
Estimated size(pages)	250
Requestor Location	University of Waterloo 200 University Avenue Waterloo, ON N2L3G1 Canada Attn: Dr. Paola Russo
Billing Type	Invoice
Billing Address	Dr. Paola Russo 200 University Avenue Waterloo, ON N2L3G1 Canada Attn: Dr. Paola Russo
Total	0.00 CAD
Terms and Conditions	

American Association for the Advancement of Science TERMS AND CONDITIONS
Regarding your request, we are pleased to grant you non-exclusive, non-transferable permission, to republish the AAAS material identified above in your work identified above, subject to the terms and conditions herein. We must be contacted for permission for any uses other than those specifically identified in your request above.
The following credit line must be printed along with the AAAS material: "From [Full Reference Citation]. Reprinted with permission from AAAS."
All required credit lines and notices must be visible any time a user accesses any part of the AAAS material and must appear on any printed copies and authorized user might make.
This permission does not apply to figures / photos / artwork or any other content or materials included in your work that are credited to non-AAAS sources. If the requested material is sourced to or references non-AAAS sources, you must obtain authorization from that source as well before using that material. You agree to hold harmless and indemnify AAAS against any claims arising from your use of any content in your work that is credited to non-AAAS sources.
If the AAAS material covered by this permission was published in Science during the years 1974 - 1994, you must also obtain permission from the author, who may grant or withhold permission, and who may or may not charge a fee if permission is granted. See original article for author's address. This condition does not apply to news articles.
The AAAS material may not be modified or altered except that figures and tables may be modified with permission from the author. Author permission for any such changes must be secured prior to your use.
Whenever possible, we ask that electronic uses of the AAAS material permitted herein include a hyperlink to the original work on AAAS's website (hyperlink may be embedded in the reference citation).
AAAS material reproduced in your work identified herein must not account for more than 30% of the total contents of that work.
AAAS must publish the full paper prior to use of any text.
AAAS material must not imply any endorsement by the American Association for the Advancement of Science.
This permission is not valid for the use of the AAAS and/or Science logos.
AAAS makes no representations or warranties as to the accuracy of any information contained in the AAAS material covered by this permission, including any warranties of merchantability or fitness for a particular purpose.
If permission fees for this use are waived, please note that AAAS reserves the right to charge for reproduction of this material in the future.
Permission is not valid unless payment is received within sixty (60) days of the issuance of this permission. If payment is not received within this time period then all rights granted herein shall be revoked and this permission will be considered null and void.
In the event of breach of any of the terms and conditions herein or any of CCC's Billing and Payment terms and conditions, all rights granted herein shall be revoked and this permission will be considered null and void.
AAAS reserves the right to terminate this permission and all rights granted herein at its discretion, for any purpose, at any time. In the event that AAAS elects to terminate this permission, you will have no further right to publish, publicly perform, publicly display, distribute or otherwise use any matter in which the AAAS content had been included, and all fees paid hereunder shall be fully refunded to you. Notification of termination will be sent to the contact information as supplied by you during the request process and termination shall be immediate upon sending the notice. Neither AAAS nor CCC shall be liable for any costs, expenses, or damages you may incur as a result of the termination of this permission, beyond the refund noted above.
This Permission may not be amended except by written document signed by both parties.

The terms above are applicable to all permissions granted for the use of AAAS material. Below you will find additional conditions that apply to your particular type of use.

FOR A THESIS OR DISSERTATION

If you are using figure(s)/table(s), permission is granted for use in print and electronic versions of your dissertation or thesis. A full text article may be used in print versions only of a dissertation or thesis.

Permission covers the distribution of your dissertation or thesis on demand by ProQuest / UMI, provided the AAAS material covered by this permission remains in situ.

If you are an Original Author on the AAAS article being reproduced, please refer to your License to Publish for rules on reproducing your paper in a dissertation or thesis.

FOR JOURNALS:

Permission covers both print and electronic versions of your journal article, however the AAAS material may not be used in any manner other than within the context of your article.

FOR BOOKS/TEXTBOOKS:

If this license is to reuse figures/tables, then permission is granted for non-exclusive world rights in all languages in both print and electronic formats (electronic formats are defined below).

If this license is to reuse a text excerpt or a full text article, then permission is granted for non-exclusive world rights in English only. You have the option of securing either print or electronic rights or both, but electronic rights are not automatically granted and do garner additional fees. Permission for translations of text excerpts or full text articles into other languages must be obtained separately.

Licenses granted for use of AAAS material in electronic format books/textbooks are valid only in cases where the electronic version is equivalent to or substitutes for the print version of the book/textbook. The AAAS material reproduced as permitted herein must remain in situ and must not be exploited separately (for example, if permission covers the use of a full text article, the article may not be offered for access or for purchase as a stand-alone unit), except in the case of permitted textbook companions as noted below.

You must include the following notice in any electronic versions, either adjacent to the reprinted AAAS material or in the terms and conditions for use of your electronic products: "Readers may view, browse, and/or download material for temporary copying purposes only, provided these uses are for noncommercial personal purposes. Except as provided by law, this material may not be further reproduced, distributed, transmitted, modified, adapted, performed, displayed, published, or sold in whole or in part, without prior written permission from the publisher."

If your book is an academic textbook, permission covers the following companions to your textbook, provided such companions are distributed only in conjunction with your textbook at no additional cost to the user:

- Password-protected website
- Instructor's image CD/DVD and/or PowerPoint resource
- Student CD/DVD

All companions must contain instructions to users that the AAAS material may be used for non-commercial, classroom purposes only. Any other uses require the prior written permission from AAAS.

If your license is for the use of AAAS Figures/Tables, then the electronic rights granted herein permit use of the Licensed Material in any Custom Databases that you distribute the electronic versions of your textbook through, so long as the Licensed Material remains within the context of a chapter of the title identified in your request and cannot be downloaded by a user as an independent image file.

Rights also extend to copies/files of your Work (as described above) that you are required to provide for use by the visually and/or print disabled in compliance with state and federal

laws.
This permission only covers a single edition of your work as identified in your request.
FOR NEWSLETTERS:
Permission covers print and/or electronic versions, provided the AAAS material reproduced as permitted herein remains in situ and is not exploited separately (for example, if permission covers the use of a full text article, the article may not be offered for access or for purchase as a stand-alone unit)
FOR ANNUAL REPORTS:
Permission covers print and electronic versions provided the AAAS material reproduced as permitted herein remains in situ and is not exploited separately (for example, if permission covers the use of a full text article, the article may not be offered for access or for purchase as a stand-alone unit)
FOR PROMOTIONAL/MARKETING USES:
Permission covers the use of AAAS material in promotional or marketing pieces such as information packets, media kits, product slide kits, brochures, or flyers limited to a single print run. The AAAS Material may not be used in any manner which implies endorsement or promotion by the American Association for the Advancement of Science (AAAS) or Science of any product or service. AAAS does not permit the reproduction of its name, logo or text on promotional literature.
If permission to use a full text article is permitted, The Science article covered by this permission must not be altered in any way. No additional printing may be set onto an article copy other than the copyright credit line required above. Any alterations must be approved in advance and in writing by AAAS. This includes, but is not limited to, the placement of sponsorship identifiers, trademarks, logos, rubber stamping or self-adhesive stickers onto the article copies.
Additionally, article copies must be a freestanding part of any information package (i.e. media kit) into which they are inserted. They may not be physically attached to anything, such as an advertising insert, or have anything attached to them, such as a sample product. Article copies must be easily removable from any kits or informational packages in which they are used. The only exception is that article copies may be inserted into three-ring binders.
FOR CORPORATE INTERNAL USE:
The AAAS material covered by this permission may not be altered in any way. No additional printing may be set onto an article copy other than the required credit line. Any alterations must be approved in advance and in writing by AAAS. This includes, but is not limited to the placement of sponsorship identifiers, trademarks, logos, rubber stamping or self-adhesive stickers onto article copies.
If you are making article copies, copies are restricted to the number indicated in your request and must be distributed only to internal employees for internal use.
If you are using AAAS Material in Presentation Slides, the required credit line must be visible on the slide where the AAAS material will be reprinted
If you are using AAAS Material on a CD, DVD, Flash Drive, or the World Wide Web, you must include the following notice in any electronic versions, either adjacent to the reprinted AAAS material or in the terms and conditions for use of your electronic products: "Readers may view, browse, and/or download material for temporary copying purposes only, provided these uses are for noncommercial personal purposes. Except as provided by law, this material may not be further reproduced, distributed, transmitted, modified, adapted, performed, displayed, published, or sold in whole or in part, without prior written permission from the publisher." Access to any such CD, DVD, Flash Drive or Web page must be restricted to your organization's employees only.
FOR CME COURSE and SCIENTIFIC SOCIETY MEETINGS:
Permission is restricted to the particular Course, Seminar, Conference, or Meeting indicated

in your request. If this license covers a text excerpt or a Full Text Article, access to the reprinted AAAS material must be restricted to attendees of your event only (if you have been granted electronic rights for use of a full text article on your website, your website must be password protected, or access restricted so that only attendees can access the content on your site).
If you are using AAAS Material on a CD, DVD, Flash Drive, or the World Wide Web, you must include the following notice in any electronic versions, either adjacent to the reprinted AAAS material or in the terms and conditions for use of your electronic products: "Readers may view, browse, and/or download material for temporary copying purposes only, provided these uses are for noncommercial personal purposes. Except as provided by law, this material may not be further reproduced, distributed, transmitted, modified, adapted, performed, displayed, published, or sold in whole or in part, without prior written permission from the publisher."

FOR POLICY REPORTS:

These rights are granted only to non-profit organizations and/or government agencies. Permission covers print and electronic versions of a report, provided the required credit line appears in both versions and provided the AAAS material reproduced as permitted herein remains in situ and is not exploited separately.

FOR CLASSROOM PHOTOCOPIES:

Permission covers distribution in print copy format only. Article copies must be freestanding and not part of a course pack. They may not be physically attached to anything or have anything attached to them.

FOR COURSEPACKS OR COURSE WEBSITES:

These rights cover use of the AAAS material in one class at one institution. Permission is valid only for a single semester after which the AAAS material must be removed from the Electronic Course website, unless new permission is obtained for an additional semester. If the material is to be distributed online, access must be restricted to students and instructors enrolled in that particular course by some means of password or access control.

FOR WEBSITES:

You must include the following notice in any electronic versions, either adjacent to the reprinted AAAS material or in the terms and conditions for use of your electronic products: "Readers may view, browse, and/or download material for temporary copying purposes only, provided these uses are for noncommercial personal purposes. Except as provided by law, this material may not be further reproduced, distributed, transmitted, modified, adapted, performed, displayed, published, or sold in whole or in part, without prior written permission from the publisher."
Permissions for the use of Full Text articles on third party websites are granted on a case by case basis and only in cases where access to the AAAS Material is restricted by some means of password or access control. Alternately, an E-Print may be purchased through our reprints department (brocheleau@rockwaterinc.com).

REGARDING FULL TEXT ARTICLE USE ON THE WORLD WIDE WEB IF YOU ARE AN 'ORIGINAL AUTHOR' OF A SCIENCE PAPER

If you chose "Original Author" as the Requestor Type, you are warranting that you are one of authors listed on the License Agreement as a "Licensed content author" or that you are acting on that author's behalf to use the Licensed content in a new work that one of the authors listed on the License Agreement as a "Licensed content author" has written.
Original Authors may post the 'Accepted Version' of their full text article on their personal or on their University website and not on any other website. The 'Accepted Version' is the version of the paper accepted for publication by AAAS including changes resulting from peer review but prior to AAAS's copy editing and production (in other words not the AAAS published version).

FOR MOVIES / FILM / TELEVISION:

Permission is granted to use, record, film, photograph, and/or tape the AAAS material in connection with your program/film and in any medium your program/film may be shown or heard, including but not limited to broadcast and cable television, radio, print, world wide web, and videocassette.
The required credit line should run in the program/film's end credits.

FOR MUSEUM EXHIBITIONS:

Permission is granted to use the AAAS material as part of a single exhibition for the duration of that exhibit. Permission for use of the material in promotional materials for the exhibit must be cleared separately with AAAS (please contact us at permissions@aaas.org).

FOR TRANSLATIONS:

Translation rights apply only to the language identified in your request summary above. The following disclaimer must appear with your translation, on the first page of the article, after the credit line: "This translation is not an official translation by AAAS staff, nor is it endorsed by AAAS as accurate. In crucial matters, please refer to the official English- language version originally published by AAAS."

FOR USE ON A COVER:

Permission is granted to use the AAAS material on the cover of a journal issue, newsletter issue, book, textbook, or annual report in print and electronic formats provided the AAAS material reproduced as permitted herein remains in situ and is not exploited separately

By using the AAAS Material identified in your request, you agree to abide by all the terms and conditions herein.

Questions about these terms can be directed to the AAAS Permissions department permissions@aaas.org.

Other Terms and Conditions: v

2

AMERICAN PHYSICAL SOCIETY LICENSE TERMS AND CONDITIONS

Aug 09, 2017

This Agreement between Dr. Paola Russo ("You") and American Physical Society ("American Physical Society") consists of your license details and the terms and conditions provided by American Physical Society and Copyright Clearance Center.

License Number	4164840868033
License date	Aug 09, 2017
Licensed Content Publisher	American Physical Society
Licensed Content Publication	Physical Review Letters
Licensed Content Title	Theory for the Ultrafast Ablation of Graphite Films
Licensed Content Author	Harald O. Jeschke, Martin E. Garcia, and K. H. Bennemann
Licensed Content Date	Jun 19, 2001
Licensed Content Volume	87
Type of Use	Thesis/Dissertation
Requestor type	Student
Format	Print, Electronic
Portion	image/photo
Number of images/photos requested	2
Portion description	Figure 1, Figure 2
Rights for	Main product
Duration of use	Life of Current Edition
Creation of copies for the disabled	no
With minor editing privileges	no
For distribution to	Worldwide
In the following language(s)	Original language of publication
With incidental promotional use	no
The lifetime unit quantity of new product	20000 to 44999
The requesting person/organization is:	University of Waterloo
Order reference number	
Title of your thesis / dissertation	Development of green synthetic approaches for the potential application of carbon and semiconductor nanomaterials for emerging applications
Expected completion date	Feb 2018
Expected size (number of pages)	250

Requestor Location 200 University Avenue Waterloo, ON N2L3G1 Canada Attn: Dr. Paola Russo	Dr. Paola Russo
Billing Type	Invoice
Billing Address 200 University Avenue	Dr. Paola Russo Waterloo, ON N2L3G1 Canada Attn: Dr. Paola Russo
Total	0.00 CAD
Terms and Conditions	

Terms and Conditions

The American Physical Society (APS) is pleased to grant the Requestor of this license a non-exclusive, non-transferable permission, limited to [**print** and/or **electronic** format, depending on what they chose], provided all criteria outlined below are followed.

1. You must also obtain permission from at least one of the lead authors for each separate work, if you haven't done so already. The author's name and affiliation can be found on the first page of the published Article.
2. For electronic format permissions, Requestor agrees to provide a hyperlink from the reprinted APS material using the source material's DOI on the web page where the work appears. The hyperlink should use the standard DOI resolution URL, http://dx.doi.org /{DOI}. The hyperlink may be embedded in the copyright credit line.
3. For print format permissions, Requestor agrees to print the required copyright credit line on the first page where the material appears: "Reprinted (abstract/excerpt/figure) with permission from [(FULL REFERENCE CITATION) as follows: Author's Names, APS Journal Title, Volume Number, Page Number and Year of Publication.] Copyright (YEAR) by the American Physical Society."
4. Permission granted in this license is for a one-time use and does not include permission for any future editions, updates, databases, formats or other matters. Permission must be sought for any additional use.
5. Use of the material does not and must not imply any endorsement by APS.
6. Under no circumstance does APS purport or intend to grant permission to reuse materials to which it does not hold copyright. It is the requestors sole responsibility to ensure the licensed material is original to APS and does not contain the copyright of another entity, and that the copyright notice of the figure, photograph, cover or table does not indicate that it was reprinted by APS, with permission from another source.
7. The permission granted herein is personal to the Requestor for the use specified and is not transferable or assignable without express written permission of APS. This license may not be amended except in writing by APS.
8. You may not alter, edit or modify the material in any manner.
9. You may translate the materials only when translation rights have been granted.
10. You may not use the material for promotional, sales, advertising or marketing purposes.
11. The foregoing license shall not take effect unless and until APS or its agent, Copyright Clearance Center (CCC), receives payment in full in accordance with CCC Billing and Payment Terms and Conditions, which are incorporated herein by reference.
12. Should the terms of this license be violated at any time, APS or CCC may revoke the license with no refund to you and seek relief to the fullest extent of the laws of the USA. Official written notice will be made using the contact information provided with the permission request. Failure to receive such notice will not nullify revocation of the permission.
13. APS reserves all rights not specifically granted herein.
14. This document, including the CCC Billing and Payment Terms and Conditions, shall be the entire agreement between the parties relating to the subject matter hereof.

Other Terms and Conditions

Version 1.1

Questions? customercare@copyright.com or +1-855-239-3415 (toll free in the US) or +1-978-646-2777.

Copyright Clearance Center

Note: Copyright.com supplies permissions but not the copyrighted content itself.

1 PAYMENT 2 REVIEW 3 CONFIRMATION

Step 3: Order Confirmation

Thank you for your order! A confirmation for your order will be sent to your account email address. If you have questions about your order, you can call us 24 hrs/day, M-F at +1.855.239.3415 Toll Free, or write to us at info@copyright.com. This is not an invoice.

Confirmation Number: 11661844
Order Date: 08/09/2017

If you paid by credit card, your order will be finalized and your card will be charged within 24 hours. If you choose to be invoiced, you can change or cancel your order until the invoice is generated.

Payment Information

Paola Russo
p3russo@uwaterloo.ca

Nanotechnology

Permission Status: Granted

Permission type: Republish or display content

ISSN:	0957-4484
Publication Type:	
Volume:	
Issue:	IOP Publishing

Requestor type	Academic institution
Format	Print, Electronic
Portion	image/photo
Number of images/photos requested	1
Title or numeric reference of the portion(s)	Figure 2
Title of the article or chapter the portion is from	Laser assisted green synthesis of free standing reduced graphene oxides at the water–air interface
Editor of portion(s)	Nanotechnology
Author of portion(s)	Compagnini G. et al

Note: This item will be invoiced or charged separately through CCC's **RightsLink** service. More info **$ 0.00**

This is not an invoice.

Total order items: 1 **Order Total: 0.00 USD**

Confirmation Number: 11661844

Special Rightsholder Terms & Conditions

The following terms & conditions apply to the specific publication under which they are listed

Nanotechnology
Permission type: Republish or display content
Type of use: Thesis/Dissertation

TERMS AND CONDITIONS

The following terms are individual to this publisher:

These special terms and conditions are in addition to the standard terms and conditions for CCC's Republication Service and, together with those standard terms and conditions, govern the use of the Works.

As the "User" you will make all reasonable efforts to contact the author(s) of the article which the Work is to be reused from, to seek consent for your intended use. Contacting one author who is acting expressly as authorised agent for their co-author(s) is acceptable.

User will reproduce the following wording prominently alongside the Work:

the source of the Work, including author, article title, title of journal, volume number, issue number (if relevant), page range (or first page if this is the only information available) and date of first publication. This information can be contained in a footnote or reference note; and

a link back to the article (via DOI); and

if practicable, and IN ALL CASES for new works published under any of the Creative Commons licences, the words "© IOP Publishing. Reproduced with permission. All rights reserved"

Without the express permission of the author(s) and the Rightsholder of the article from which the Work is to be reused, User shall not use it in any way which, in the opinion of the Rightsholder, could: (i) distort or alter the author(s)' original intention(s) and meaning; (ii) be prejudicial to the honour or reputation of the author(s); and/or
(iii) imply endorsement by the author(s) and/or the Rightsholder.

This licence does not apply to any article which is credited to another source and which does not have the copyright line '© IOP Publishing Ltd'. User must check the copyright line of the article from which the Work is to be reused to check that IOP Publishing Ltd has all the necessary rights to be able to grant permission. User is solely responsible for identifying and obtaining separate licences and permissions from the copyright owner for reuse of any such third party material/figures which the Rightsholder is not the copyright owner of. The Rightsholder shall not reimburse any fees which User pays for a republication license for such third party content.

This licence does not apply to any material/figure which is credited to another source in the Rightsholder's publication or has been obtained from a third party. User must check the Version of Record of the article from which the Work is to be reused, to check whether any of the material in the Work is third party material. Third party citations and/or copyright notices and/or permissions statements may not be included in any other version of the article from which the Work is to be reused and so cannot be relied upon by the User. User is solely responsible for identifying and obtaining separate licences and permissions from the copyright owner for reuse of any such third party material/figures where the Rightsholder is not the copyright owner. The Rightsholder shall not reimburse any fees which User pays for a republication license for such third party content.

User and CCC acknowledge that the Rightsholder may, from time to time, make changes or additions to these special terms and conditions without express notification, provided that these shall not apply to permissions already secured and paid for by User prior to such change or addition.

User acknowledges that the Rightsholder (which includes companies within its group and third parties for whom it publishes its titles) may make use of personal data collected through the service in the course of their business.

If User is the author of the Work, User may automatically have the right to reuse it under the rights granted back when User transferred the copyright in the article to the Rightsholder. User should check the copyright form and the relevant author rights policy to check whether permission is required. If User is the author of the Work and does require permission for proposed reuse of the Work, User should select 'Author of requested content' as the Requestor Type. The Rightsholder shall not reimburse any fees which User pays for a republication license.

If User is the author of the article which User wishes to reuse in User's thesis or dissertation, the republication licence covers the right to include the Accepted Manuscript version (not the Version of Record) of the article. User must include citation details and, for online use, a link to the Version of Record of the article on the Rightsholder's website. User may need to obtain separate permission for any third party content included within the article. User must check this with the copyright owner of such third party content. User may not include the article in a thesis or dissertation which is published by ProQuest. Any other commercial use of User's thesis or dissertation containing the article would also need to be expressly notified in writing to the Rightsholder at the time of request and would require separate written permission from the Rightsholder.

User does not need to request permission for Work which has been published under a CC BY licence. User must check the Version of Record of the CC BY article from which the Work is to be reused, to check whether any of the material in the Work is third party material and so not published under the CC BY licence. User is solely responsible for identifying and obtaining separate licences and permissions from the copyright owner for reuse of any such third party material/figures. The Rightsholder shall not reimburse any fees which User pays for such licences and permissions.

As well as CCC, the Rightsholder shall have the right to bring any legal action that it deems necessary to enforce its rights should it consider that the Work infringes those rights in any way.

For STM Signatories ONLY (as agreed as part of the STM Guidelines)

Any licence granted for a particular edition of a Work will apply also to subsequent editions of it and for editions in other languages, provided such editions are for the Work as a whole in situ and do not involve the separate exploitation of the permitted illustrations or excerpts.

Other Terms and Conditions:

STANDARD TERMS AND CONDITIONS

1. Description of Service; Defined Terms. This Republication License enables the User to obtain licenses for republication of one or more copyrighted works as described in detail on the relevant Order Confirmation (the "Work(s)"). Copyright Clearance Center, Inc. ("CCC") grants licenses through the Service on behalf of the rightsholder identified on the Order Confirmation (the "Rightsholder"). "Republication", as used herein, generally means the inclusion of a Work, in whole or in part, in a new work or works, also as described on the Order Confirmation. "User", as used herein, means the person or entity making such republication.

2. The terms set forth in the relevant Order Confirmation, and any terms set by the Rightsholder with respect to a particular Work, govern the terms of use of Works in connection with the Service. By using the Service, the person transacting for a republication license on behalf of the User represents and warrants that he/she/it (a) has been duly authorized by the User to accept, and hereby does accept, all such terms and conditions on behalf of User, and (b) shall inform User of all such terms and conditions. In the event such person is a "freelancer" or other third party independent of User and CCC, such party shall be deemed jointly a "User" for purposes of these terms and conditions. In any event, User shall be deemed to have accepted and agreed to all such terms and conditions if User republishes the Work in any fashion.

3. Scope of License; Limitations and Obligations.

3.1 All Works and all rights therein, including copyright rights, remain the sole and exclusive property of the Rightsholder. The license created by the exchange of an Order Confirmation (and/or any invoice) and payment by User of the full amount set forth on that document includes only those rights expressly set forth in the Order Confirmation and in these terms and conditions, and conveys no other rights in the Work(s) to User. All rights not expressly granted are hereby reserved.

3.2 General Payment Terms: You may pay by credit card or through an account with us payable at the end of the month. If you and we agree that you may establish a standing account with CCC, then the following terms apply: Remit Payment to: Copyright Clearance Center, 29118 Network Place, Chicago, IL 60673-1291. Payments Due: Invoices are payable upon their delivery to you (or upon our notice to you that they are available to you for downloading). After 30 days, outstanding amounts will be subject to a service charge of 1-1/2% per month or, if less, the maximum rate allowed by applicable law. Unless otherwise specifically set forth in the Order Confirmation or in a separate written agreement signed by CCC, invoices are due and payable on "net 30" terms. While User may exercise the rights licensed immediately upon issuance of the Order Confirmation, the license is automatically revoked and is null and void, as if it had never been issued, if complete payment for the license is not received on a timely basis either from User directly or through a payment agent, such as a credit card company.

3.3 Unless otherwise provided in the Order Confirmation, any grant of rights to User (i) is "one-time" (including the editions and product family specified in the license), (ii) is non-exclusive and non-transferable and (iii) is subject to any and all limitations and restrictions (such as, but not limited to, limitations on duration of use or circulation) included in the Order Confirmation or invoice and/or in these terms and conditions. Upon completion of the licensed use, User shall either secure a new permission for further use of the Work(s) or immediately cease any new use of the Work(s) and shall render inaccessible (such as by deleting or by removing or severing links or other locators) any further copies of the Work (except for copies printed on paper in accordance with this license and still in User's stock at the end of such period).

3.4 In the event that the material for which a republication license is sought includes third party materials (such as photographs, illustrations, graphs, inserts and similar materials) which are identified in such material as having been used by permission, User is responsible for identifying, and seeking separate licenses (under this Service or otherwise) for, any of such third party materials; without a separate license, such third party materials may not be used.

3.5 Use of proper copyright notice for a Work is required as a condition of any license granted under the Service. Unless otherwise provided in the Order Confirmation, a proper copyright notice will read substantially as follows: "Republished with permission of [Rightsholder's name], from [Work's title, author, volume, edition number and year of copyright]; permission conveyed through Copyright Clearance Center, Inc. " Such notice must be provided in a reasonably legible font size and must be placed either immediately adjacent to the Work as used (for example, as part of a by-line or footnote but not as a separate electronic link) or in the place where substantially all other credits or notices for the new work containing the republished Work are located. Failure to include the required notice results

in loss to the Rightsholder and CCC, and the User shall be liable to pay liquidated damages for each such failure equal to twice the use fee specified in the Order Confirmation, in addition to the use fee itself and any other fees and charges specified.

3.6 User may only make alterations to the Work if and as expressly set forth in the Order Confirmation. No Work may be used in any way that is defamatory, violates the rights of third parties (including such third parties' rights of copyright, privacy, publicity, or other tangible or intangible property), or is otherwise illegal, sexually explicit or obscene. In addition, User may not conjoin a Work with any other material that may result in damage to the reputation of the Rightsholder. User agrees to inform CCC if it becomes aware of any infringement of any rights in a Work and to cooperate with any reasonable request of CCC or the Rightsholder in connection therewith.

4. Indemnity. User hereby indemnifies and agrees to defend the Rightsholder and CCC, and their respective employees and directors, against all claims, liability, damages, costs and expenses, including legal fees and expenses, arising out of any use of a Work beyond the scope of the rights granted herein, or any use of a Work which has been altered in any unauthorized way by User, including claims of defamation or infringement of rights of copyright, publicity, privacy or other tangible or intangible property.

5. Limitation of Liability. UNDER NO CIRCUMSTANCES WILL CCC OR THE RIGHTSHOLDER BE LIABLE FOR ANY DIRECT, INDIRECT, CONSEQUENTIAL OR INCIDENTAL DAMAGES (INCLUDING WITHOUT LIMITATION DAMAGES FOR LOSS OF BUSINESS PROFITS OR INFORMATION, OR FOR BUSINESS INTERRUPTION) ARISING OUT OF THE USE OR INABILITY TO USE A WORK, EVEN IF ONE OF THEM HAS BEEN ADVISED OF THE POSSIBILITY OF SUCH DAMAGES. In any event, the total liability of the Rightsholder and CCC (including their respective employees and directors) shall not exceed the total amount actually paid by User for this license. User assumes full liability for the actions and omissions of its principals, employees, agents, affiliates, successors and assigns.

6. Limited Warranties. THE WORK(S) AND RIGHT(S) ARE PROVIDED "AS IS". CCC HAS THE RIGHT TO GRANT TO USER THE RIGHTS GRANTED IN THE ORDER CONFIRMATION DOCUMENT. CCC AND THE RIGHTSHOLDER DISCLAIM ALL OTHER WARRANTIES RELATING TO THE WORK(S) AND RIGHT(S), EITHER EXPRESS OR IMPLIED, INCLUDING WITHOUT LIMITATION IMPLIED WARRANTIES OF MERCHANTABILITY OR FITNESS FOR A PARTICULAR PURPOSE. ADDITIONAL RIGHTS MAY BE REQUIRED TO USE ILLUSTRATIONS, GRAPHS, PHOTOGRAPHS, ABSTRACTS, INSERTS OR OTHER PORTIONS OF THE WORK (AS OPPOSED TO THE ENTIRE WORK) IN A MANNER CONTEMPLATED BY USER; USER UNDERSTANDS AND AGREES THAT NEITHER CCC NOR THE RIGHTSHOLDER MAY HAVE SUCH ADDITIONAL RIGHTS TO GRANT.

7. Effect of Breach. Any failure by User to pay any amount when due, or any use by User of a Work beyond the scope of the license set forth in the Order Confirmation and/or these terms and conditions, shall be a material breach of the license created by the Order Confirmation and these terms and conditions. Any breach not cured within 30 days of written notice thereof shall result in immediate termination of such license without further notice. Any unauthorized (but licensable) use of a Work that is terminated immediately upon notice thereof may be liquidated by payment of the Rightsholder's ordinary license price therefor; any unauthorized (and unlicensable) use that is not terminated immediately for any reason (including, for example, because materials containing the Work cannot reasonably be recalled) will be subject to all remedies available at law or in equity, but in no event to a payment of less than three times the Rightsholder's ordinary license price for the most closely analogous licensable use plus Rightsholder's and/or CCC's costs and expenses incurred in collecting such payment.

8. Miscellaneous.

8.1 User acknowledges that CCC may, from time to time, make changes or additions to the Service or to these terms and conditions, and CCC reserves the right to send notice to the User by electronic mail or otherwise for the purposes of notifying User of such changes or additions; provided that any such changes or additions shall not apply to permissions already secured and paid for.

8.2 Use of User-related information collected through the Service is governed by CCC's privacy policy, available online here: http://www.copyright.com/content/cc3/en/tools/footer/privacypolicy.html.

8.3 The licensing transaction described in the Order Confirmation is personal to User. Therefore, User may not assign or transfer to any other person (whether a natural person or an organization of any kind) the license created by the Order Confirmation and these terms and conditions or any rights granted hereunder; provided, however, that User may assign such license in its entirety on written notice to CCC in the event of a transfer of all or substantially all of User's rights in the new material which includes the Work(s) licensed under this Service.

8.4 No amendment or waiver of any terms is binding unless set forth in writing and signed by the parties. The Rightsholder and CCC hereby object to any terms contained in any writing prepared by the User or its principals, employees, agents or affiliates and purporting to govern or otherwise relate to the licensing transaction described in the Order Confirmation, which terms are in any way inconsistent with any terms set forth in the Order Confirmation and/or in these terms and conditions or CCC's standard operating procedures, whether such writing is prepared prior to, simultaneously with or subsequent to the Order Confirmation, and whether such writing appears on a copy of the Order Confirmation or in a separate instrument.

8.5 The licensing transaction described in the Order Confirmation document shall be governed by and construed under the law of the State of New York, USA, without regard to the principles thereof of conflicts of law. Any case, controversy, suit, action, or proceeding arising out of, in connection with, or related to such licensing transaction shall be brought, at CCC's sole discretion, in any federal or state court located in the County of New York, State of New York, USA, or in any federal or state court whose geographical jurisdiction covers the location of the Rightsholder set forth in the Order Confirmation. The parties expressly submit to the personal jurisdiction and venue of each such federal or state court.If you have any comments or questions about the Service or Copyright Clearance Center, please contact us at 978-750-8400 or send an e-mail to info@copyright.com.

v 1.1

Close

Confirmation Number: 11661844 Citation

Information

Order Detail ID: 70635838

Nanotechnology by IOP Publishing. Reproduced with permission of IOP Publishing in the format Thesis/Dissertation via Copyright Clearance Center.

AIP PUBLISHING LLC LICENSE TERMS AND CONDITIONS

Aug 09, 2017

This Agreement between Dr. Paola Russo ("You") and AIP Publishing LLC ("AIP Publishing LLC") consists of your license details and the terms and conditions provided by AIP Publishing LLC and Copyright Clearance Center.

License Number	4164850725737
License date	Aug 09, 2017
Licensed Content Publisher	AIP Publishing LLC
Licensed Content Publication	Applied Physics Letters
Licensed Content Title	Making graphene visible
Licensed Content Author	P. Blake, E. W. Hill, A. H. Castro Neto, et al
Licensed Content Date	Aug 6, 2007
Licensed Content Volume	91
Licensed Content Issue	6
Type of Use	Thesis/Dissertation
Requestor type	University or Educational Institution
Format	Print and electronic
Portion	Figure/Table
Number of figures/tables	1
Title of your thesis / dissertation	Development of green synthetic approaches for the potential application of carbon and semiconductor nanomaterials for emerging applications
Expected completion date	Feb 2018
Estimated size (number of pages)	250
Requestor Location	University of Waterloo 200 University Avenue Waterloo, ON N2L3G1 Canada Attn: Dr. Paola Russo
Billing Type	Invoice
Billing Address	Dr. Paola Russo 200 University Avenue Waterloo, ON N2L3G1 Canada Attn: Dr. Paola Russo
Total	0.00 CAD

Terms and Conditions

AIP Publishing LLC -- Terms and Conditions: Permissions Uses

AIP Publishing hereby grants to you the non-exclusive right and license to use and/or distribute the Material according to the use specified in your order, on a one-time basis, for the specified term, with a maximum distribution equal to the number that you have ordered. Any links or other content accompanying the Material are not the subject of this license.

1. You agree to include the following copyright and permission notice with the reproduction of the Material:"Reprinted from [FULL CITATION], with the permission of AIP Publishing." For an article, the credit line and permission notice must be printed on the first page of the article or book chapter. For photographs, covers, or tables, the notice may appear with the Material, in a footnote, or in the reference list.
2. If you have licensed reuse of a figure, photograph, cover, or table, it is your responsibility to ensure that the material is original to AIP Publishing and does not contain the copyright of another entity, and that the copyright notice of the figure, photograph, cover, or table does not indicate that it was reprinted by AIP Publishing, with permission, from another source. Under no circumstances does AIP Publishing purport or intend to grant permission to reuse material to which it does not hold appropriate rights.

You may not alter or modify the Material in any manner. You may translate the Material into another language only if you have licensed translation rights. You may not use the Material for promotional purposes.

3. The foregoing license shall not take effect unless and until AIP Publishing or its agent, Copyright Clearance Center, receives the Payment in accordance with Copyright Clearance Center Billing and Payment Terms and Conditions, which are incorporated herein by reference.
4. AIP Publishing or Copyright Clearance Center may, within two business days of granting this license, revoke the license for any reason whatsoever, with a full refund payable to you. Should you violate the terms of this license at any time, AIP Publishing, or Copyright Clearance Center may revoke the license with no refund to you. Notice of such revocation will be made using the contact information provided by you. Failure to receive such notice will not nullify the revocation.
5. AIP Publishing makes no representations or warranties with respect to the Material. You agree to indemnify and hold harmless AIP Publishing, and their officers, directors, employees or agents from and against any and all claims arising out of your use of the Material other than as specifically authorized herein.
6. The permission granted herein is personal to you and is not transferable or assignable without the prior written permission of AIP Publishing. This license may not be amended except in a writing signed by the party to be charged.
7. If purchase orders, acknowledgments or check endorsements are issued on any forms containing terms and conditions which are inconsistent with these provisions, such inconsistent terms and conditions shall be of no force and effect. This document, including the CCC Billing and Payment Terms and Conditions, shall be the entire agreement between the parties relating to the subject matter hereof.

This Agreement shall be governed by and construed in accordance with the laws of the State of New York. Both parties hereby submit to the jurisdiction of the courts of New York County for purposes of resolving any disputes that may arise hereunder.

V1.1

Questions? customercare@copyright.com or +1-855-239-3415 (toll free in the US) or +1-978-646-2777.

AMERICAN PHYSICAL SOCIETY LICENSE TERMS AND CONDITIONS

Aug 09, 2017

This Agreement between Dr. Paola Russo ("You") and American Physical Society ("American Physical Society") consists of your license details and the terms and conditions provided by American Physical Society and Copyright Clearance Center.

License Number	4164851422846
License date	Aug 09, 2017
Licensed Content Publisher	American Physical Society
Licensed Content Publication	Physical Review Letters
Licensed Content Title	Raman Spectrum of Graphene and Graphene Layers
Licensed Content Author	A. C. Ferrari et al.
Licensed Content Date	Oct 30, 2006
Licensed Content Volume	97
Type of Use	Thesis/Dissertation
Requestor type	Student
Format	Print, Electronic
Portion	image/photo
Number of images/photos requested	1
Portion description	Figure 2 (a) and (b)
Rights for	Main product
Duration of use	Life of Current Edition
Creation of copies for the disabled	no
With minor editing privileges	no
For distribution to	Worldwide
In the following language(s)	Original language of publication
With incidental promotional use	no
The lifetime unit quantity of new product	5000 to 9999
The requesting person/organization is:	University of Waterloo
Order reference number	
Title of your thesis / dissertation	Development of green synthetic approaches for the potential application of carbon and semiconductor nanomaterials for emerging applications
Expected completion date	Feb 2018
Expected size (number of pages)	250

Requestor Location University of Waterloo 200 University Avenue

Waterloo, ON N2L3G1

Canada
Attn: Dr. Paola Russo

Billing Type Invoice

Billing Address Dr. Paola Russo
200 University Avenue

Waterloo, ON N2L3G1 Canada
Attn: Dr. Paola Russo

Total 0.00 CAD

Terms and Conditions

Terms and Conditions

The American Physical Society (APS) is pleased to grant the Requestor of this license a non-exclusive, non-transferable permission, limited to [**print** and/or **electronic** format, depending on what they chose], provided all criteria outlined below are followed.

1. You must also obtain permission from at least one of the lead authors for each separate work, if you haven't done so already. The author's name and affiliation can be found on the first page of the published Article.
2. For electronic format permissions, Requestor agrees to provide a hyperlink from the reprinted APS material using the source material's DOI on the web page where the work appears. The hyperlink should use the standard DOI resolution URL, http://dx.doi.org /{DOI}. The hyperlink may be embedded in the copyright credit line.
3. For print format permissions, Requestor agrees to print the required copyright credit line on the first page where the material appears: "Reprinted (abstract/excerpt/figure) with permission from [(FULL REFERENCE CITATION) as follows: Author's Names, APS Journal Title, Volume Number, Page Number and Year of Publication.] Copyright (YEAR) by the American Physical Society."
4. Permission granted in this license is for a one-time use and does not include permission for any future editions, updates, databases, formats or other matters. Permission must be sought for any additional use.
5. Use of the material does not and must not imply any endorsement by APS.
6. Under no circumstance does APS purport or intend to grant permission to reuse materials to which it does not hold copyright. It is the requestors sole responsibility to ensure the licensed material is original to APS and does not contain the copyright of another entity, and that the copyright notice of the figure, photograph, cover or table does not indicate that it was reprinted by APS, with permission from another source.
7. The permission granted herein is personal to the Requestor for the use specified and is not transferable or assignable without express written permission of APS. This license may not be amended except in writing by APS.
8. You may not alter, edit or modify the material in any manner.
9. You may translate the materials only when translation rights have been granted.
10. You may not use the material for promotional, sales, advertising or marketing purposes.
11. The foregoing license shall not take effect unless and until APS or its agent, Copyright Clearance Center (CCC), receives payment in full in accordance with CCC Billing and Payment Terms and Conditions, which are incorporated herein by reference.
12. Should the terms of this license be violated at any time, APS or CCC may revoke the license with no refund to you and seek relief to the fullest extent of the laws of the USA.

Official written notice will be made using the contact information provided with the permission request. Failure to receive such notice will not nullify revocation of the permission.

13. APS reserves all rights not specifically granted herein.
14. This document, including the CCC Billing and Payment Terms and Conditions, shall be the entire agreement between the parties relating to the subject matter hereof.

Other Terms and Conditions

Version 1.1

Questions? customercare@copyright.com or +1-855-239-3415 (toll free in the US) or +1-978-646-2777.

ELSEVIER LICENSE TERMS AND CONDITIONS

Aug 03, 2017

This Agreement between Dr. Paola Russo ("You") and Elsevier ("Elsevier") consists of your license details and the terms and conditions provided by Elsevier and Copyright Clearance Center.

License Number	4161530308422
License date	Aug 03,
2017 Licensed Content Publisher	
	Elsevier
Licensed Content Publication	Carbon
Licensed Content Title	Carbon nanowalls: A new material for resistive switching memory devices
Licensed Content Author	Paola Russo,Ming Xiao,Norman Y.
Zhou Licensed Content Date	Aug 1, 2017
Licensed Content Volume	120
Licensed Content Issue	n/a
Licensed Content Pages	9
Start Page	54
End Page	62
Type of Use	reuse in a thesis/dissertation
Portion	full article
Format	both print and electronic
Are you the author of this Elsevier article?	Yes
Will you be translating?	No
Title of your thesis/dissertation	Development of green synthetic approaches for the potential application of carbon and semiconductor nanomaterials for emerging applications
Expected completion date	Feb 2018
Estimated size (number of pages)	250
Requestor Location	Dr. Paola Russo
200 University Avenue	
Waterloo, ON N2L3G1 Canada	
Attn: Dr. Paola Russo	
Total	0.00 CAD

Terms and Conditions

INTRODUCTION

1. The publisher for this copyrighted material is Elsevier. By clicking "accept" in connection with completing this licensing transaction, you agree that the following terms and conditions apply to this transaction (along with the Billing and Payment terms and conditions established by Copyright Clearance Center, Inc. ("CCC"), at the time that you opened your Rightslink account and that are available at any time at http://myaccount.copyright.com).

GENERAL TERMS

2. Elsevier hereby grants you permission to reproduce the aforementioned material subject to the terms and conditions indicated.
3. Acknowledgement: If any part of the material to be used (for example, figures) has appeared in our publication with credit or acknowledgement to another source, permission must also be sought from that source. If such permission is not obtained then that material may not be included in your publication/copies. Suitable acknowledgement to the source must be made, either as a footnote or in a reference list at the end of your publication, as follows: "Reprinted from Publication title, Vol /edition number, Author(s), Title of article / title of chapter, Pages No., Copyright (Year), with permission from Elsevier [OR APPLICABLE SOCIETY COPYRIGHT OWNER]." Also Lancet special credit - "Reprinted from The Lancet, Vol. number, Author(s), Title of article, Pages No., Copyright (Year), with permission from Elsevier."
4. Reproduction of this material is confined to the purpose and/or media for which permission is hereby given.
5. Altering/Modifying Material: Not Permitted. However figures and illustrations may be altered/adapted minimally to serve your work. Any other abbreviations, additions, deletions and/or any other alterations shall be made only with prior written authorization of Elsevier Ltd. (Please contact Elsevier at permissions@elsevier.com). No modifications can be made to any Lancet figures/tables and they must be reproduced in full.
6. If the permission fee for the requested use of our material is waived in this instance, please be advised that your future requests for Elsevier materials may attract a fee.
7. Reservation of Rights: Publisher reserves all rights not specifically granted in the combination of (i) the license details provided by you and accepted in the course of this licensing transaction, (ii) these terms and conditions and (iii) CCC's Billing and Payment terms and conditions.
8. License Contingent Upon Payment: While you may exercise the rights licensed immediately upon issuance of the license at the end of the licensing process for the transaction, provided that you have disclosed complete and accurate details of your proposed use, no license is finally effective unless and until full payment is received from you (either by publisher or by CCC) as provided in CCC's Billing and Payment terms and conditions. If full payment is not received on a timely basis, then any license preliminarily granted shall be deemed automatically revoked and shall be void as if never granted. Further, in the event that you breach any of these terms and conditions or any of CCC's Billing and Payment terms and conditions, the license is automatically revoked and shall be void as if never granted. Use of materials as described in a revoked license, as well as any use of the materials beyond the scope of an unrevoked license, may constitute copyright infringement and publisher reserves the right to take any and all action to protect its copyright in the materials.
9. Warranties: Publisher makes no representations or warranties with respect to the licensed material.
10. Indemnity: You hereby indemnify and agree to hold harmless publisher and CCC, and their respective officers, directors, employees and agents, from and against any and all claims arising out of your use of the licensed material other than as specifically authorized pursuant to this license.
11. No Transfer of License: This license is personal to you and may not be sublicensed, assigned, or transferred by you to any other person without publisher's written permission.
12. No Amendment Except in Writing: This license may not be amended except in a writing signed by both parties (or, in the case of publisher, by CCC on publisher's behalf).
13. Objection to Contrary Terms: Publisher hereby objects to any terms contained in any purchase order, acknowledgment, check endorsement or other writing prepared by you,which terms are inconsistent with these terms and conditions or CCC's Billing and Payment terms and conditions. These terms and conditions, together with CCC's Billing and

Payment terms and conditions (which are incorporated herein), comprise the entire agreement between you and publisher (and CCC) concerning this licensing transaction. In the event of any conflict between your obligations established by these terms and conditions and those established by CCC's Billing and Payment terms and conditions, these terms and conditions shall control.

14. Revocation: Elsevier or Copyright Clearance Center may deny the permissions described in this License at their sole discretion, for any reason or no reason, with a full refund payable to you. Notice of such denial will be made using the contact information provided by you. Failure to receive such notice will not alter or invalidate the denial. In no event will Elsevier or Copyright Clearance Center be responsible or liable for any costs, expenses or damage incurred by you as a result of a denial of your permission request, other than a refund of the amount(s) paid by you to Elsevier and/or Copyright Clearance Center for denied permissions.

LIMITED LICENSE

The following terms and conditions apply only to specific license types:

15. **Translation**: This permission is granted for non-exclusive world **English** rights only unless your license was granted for translation rights. If you licensed translation rights you may only translate this content into the languages you requested. A professional translator must perform all translations and reproduce the content word for word preserving the integrity of the article.

16. **Posting licensed content on any Website**: The following terms and conditions apply as follows: Licensing material from an Elsevier journal: All content posted to the web site must maintain the copyright information line on the bottom of each image; A hyper-text must be included to the Homepage of the journal from which you are licensing at http://www.sciencedirect.com/science/journal/xxxxx or the Elsevier homepage for books at http://www.elsevier.com; Central Storage: This license does not include permission for a scanned version of the material to be stored in a central repository such as that provided by Heron/XanEdu.

Licensing material from an Elsevier book: A hyper-text link must be included to the Elsevier homepage at http://www.elsevier.com . All content posted to the web site must maintain the copyright information line on the bottom of each image.

Posting licensed content on Electronic reserve: In addition to the above the following clauses are applicable: The web site must be password-protected and made available only to bona fide students registered on a relevant course. This permission is granted for 1 year only. You may obtain a new license for future website posting.

17. **For journal authors:** the following clauses are applicable in addition to the above:

Preprints:

A preprint is an author's own write-up of research results and analysis, it has not been peer- reviewed, nor has it had any other value added to it by a publisher (such as formatting, copyright, technical enhancement etc.).

Authors can share their preprints anywhere at any time. Preprints should not be added to or enhanced in any way in order to appear more like, or to substitute for, the final versions of articles however authors can update their preprints on arXiv or RePEc with their Accepted Author Manuscript (see below).

If accepted for publication, we encourage authors to link from the preprint to their formal publication via its DOI. Millions of researchers have access to the formal publications on ScienceDirect, and so links will help users to find, access, cite and use the best available version. Please note that Cell Press, The Lancet and some society-owned have different preprint policies. Information on these policies is available on the journal homepage.

Accepted Author Manuscripts: An accepted author manuscript is the manuscript of an article that has been accepted for publication and which typically includes author-incorporated changes suggested during submission, peer review and editor-author communications.
Authors can share their accepted author manuscript:

- immediately
  - via their non-commercial person homepage or blog
  - by updating a preprint in arXiv or RePEc with the accepted manuscript
  - via their research institute or institutional repository for internal institutional uses or as part of an invitation-only research collaboration work-group directly by providing copies to their students or to research collaborators for their personal use
  - for private scholarly sharing as part of an invitation-only work group on commercial sites with which Elsevier has an agreement
- After the embargo period
  - via non-commercial hosting platforms such as their institutional repository via commercial sites with which Elsevier has an agreement

In all cases accepted manuscripts should:

- link to the formal publication via its DOI
- bear a CC-BY-NC-ND license - this is easy to do
- if aggregated with other manuscripts, for example in a repository or other site, be shared in alignment with our hosting policy not be added to or enhanced in any way to appear more like, or to substitute for, the published journal article.

Published journal article (JPA): A published journal article (PJA) is the definitive final record of published research that appears or will appear in the journal and embodies all value-adding publishing activities including peer review co-ordination, copy-editing, formatting, (if relevant) pagination and online enrichment.
Policies for sharing publishing journal articles differ for subscription and gold open access articles:
Subscription Articles: If you are an author, please share a link to your article rather than the full-text. Millions of researchers have access to the formal publications on ScienceDirect, and so links will help your users to find, access, cite, and use the best available version.
Theses and dissertations which contain embedded PJAs as part of the formal submission can be posted publicly by the awarding institution with DOI links back to the formal publications on ScienceDirect.
If you are affiliated with a library that subscribes to ScienceDirect you have additional private sharing rights for others' research accessed under that agreement. This includes use for classroom teaching and internal training at the institution (including use in course packs and courseware programs), and inclusion of the article for grant funding purposes.
Gold Open Access Articles: May be shared according to the author-selected end-user license and should contain a CrossMark logo, the end user license, and a DOI link to the formal publication on ScienceDirect.
Please refer to Elsevier's posting policy for further information.
18. **For book authors** the following clauses are applicable in addition to the above: Authors are permitted to place a brief summary of their work online only. You are not allowed to download and post the published electronic version of your chapter, nor may you scan the printed edition to create an electronic version. **Posting to a repository:** Authors are permitted to post a summary of their chapter only in their institution's repository.
19. **Thesis/Dissertation**: If your license is for use in a thesis/dissertation your thesis may be

submitted to your institution in either print or electronic form. Should your thesis be published commercially, please reapply for permission. These requirements include permission for the Library and Archives of Canada to supply single copies, on demand, of the complete thesis and include permission for Proquest/UMI to supply single copies, on demand, of the complete thesis. Should your thesis be published commercially, please reapply for permission. Theses and dissertations which contain embedded PJAs as part of the formal submission can be posted publicly by the awarding institution with DOI links back to the formal publications on ScienceDirect.

Posting or linking by commercial companies for use by customers of those companies.

20. **Other**

Conditions: v1.9

References

[1] C.N.R. Rao, A.K. Sood, K.S. Subrahmanyam, A. Govindaraj, Graphene: The new two-dimensional nanomaterial, Angew. Chemie - Int. Ed. 48 (2009) 7752–7777. doi:10.1002/anie.200901678.

[2] P. V. Kamat, Graphene-based nanoassemblies for energy conversion, J. Phys. Chem. Lett. 2 (2011) 242–251. doi:10.1021/jz101639v.

[3] H. Bi, S. Sun, F. Huang, X. Xie, M. Jiang, Direct growth of few-layer graphene films on SiO2 substrates and their photovoltaic applications, J. Mater. Chem. 22 (2012) 411. doi:10.1039/c1jm14778a.

[4] C. Yan, J.H. Cho, J.-H. Ahn, Graphene-based flexible and stretchable thin film transistors, Nanoscale. 4 (2012) 4870. doi:10.1039/c2nr30994g.

[5] J.T. Robinson, F.K. Perkins, E.S. Snow, Z. Wei, P.E. Sheehan, Reduced graphene oxide molecular sensors, Nano Lett. 8 (2008) 3137–3140. doi:10.1021/nl8013007.

[6] P. Russo, A. Hu, G. Compagnini, Synthesis, Properties and Potential Applications of Porous Graphene: A Review, Nano-Micro Lett. 5 (2013) 260–273. doi:10.5101/nml.v5i4.p260-273.

[7] P. Ho, Y. Liou, C. Chuang, S. Lin, C. Tseng, D. Wang, C. Chen, W. Hung, C. Wen, C. Chen, Self-Crack-Filled Graphene Films by Metallic Nanoparticles for High-Performance Graphene Heterojunction Solar Cells, (2015) 1724–1729. doi:10.1002/adma.201404843.

[8] J. Meyer, P.R. Kidambi, B.C. Bayer, C. Weijtens, A. Kuhn, A. Centeno, A. Pesquera, A. Zurutuza, J. Robertson, S. Hofmann, Metal oxide induced charge transfer doping and band alignment of graphene electrodes for efficient organic light emitting diodes., Sci. Rep. 4 (2014) 5380. doi:10.1038/srep05380.

[9] P. Russo, L. D'Urso, A. Hu, N. Zhou, G. Compagnini, In liquid laser treated graphene oxide for dye removal, Appl. Surf. Sci. 348 (2015) 85–91. doi:10.1016/j.apsusc.2014.12.014.

[10] S.P. Surwade, S.N. Smirnov, I. V. Vlassiouk, R.R. Unocic, G.M. Veith, S. Dai, S.M. Mahurin, Water desalination using nanoporous single-layer graphene, Nat. Nanotechnol. 10 (2015) 459–464. doi:10.1038/nnano.2015.37.

[11] B. Meschi Amoli, J. Trinidad, G. Rivers, S. Sy, P. Russo, A. Yu, N.Y. Zhou, B. Zhao, SDS-stabilized graphene nanosheets for highly electrically conductive adhesives, Carbon N. Y. 91 (2015) 188–199. doi:10.1016/j.carbon.2015.04.039.

[12] Y.-A. Li, Y.-J. Chen, N.-H. Tai, Fast process to decorate silver nanoparticles on carbon nanomaterials for preparing high-performance flexible transparent conductive films., Langmuir. 29 (2013) 8433–9. doi:10.1021/la401662d.

[13] L.Y. Xu, G.Y. Yang, H.Y. Jing, J. Wei, Y.D. Han, Ag-graphene hybrid conductive ink for writing electronics., Nanotechnology. 25 (2014) 55201. doi:10.1088/0957-4484/25/5/055201.

[14] J. Chen, H. Bi, S. Sun, Y. Tang, W. Zhao, T. Lin, D. Wan, F. Huang, X. Zhou, X. Xie, M. Jiang, Highly conductive and flexible paper of 1D silver-nanowire-doped graphene, ACS Appl. Mater. Interfaces. 5 (2013) 1408–1413. doi:10.1021/am302825w.

[15] P. Russo, M. Xiao, N.Y. Zhou, Carbon nanowalls: A new material for resistive switching memory devices, Carbon N. Y. 120 (2017) 54–62. doi:10.1016/j.carbon.2017.05.004.

[16] A. Nel, T. Xia, L. Mädler, N. Li, Toxic potential of materials at the nanolevel., Science. 311 (2006) 622–627. doi:10.1126/science.1114397.

[17] J. Wu, G. Yue, Y. Xiao, J. Lin, M. Huang, Z. Lan, Q. Tang, Y. Huang, L. Fan, S. Yin, T. Sato, An ultraviolet responsive hybrid solar cell based on titania/poly(3-hexylthiophene)., Sci. Rep. 3 (2013) 1283. doi:10.1038/srep01283.

[18] M. Xiao, K.P. Musselman, W.W. Duley, N.Y. Zhou, Resistive Switching Memory of TiO2 Nanowire Networks Grown on Ti Foil by a Single Hydrothermal Method, Nano-Micro Lett. 9 (2017) 15. doi:10.1007/s40820-016-0116-2.

[19] S. Singh, S. Jit, S.-H. Park, Characterization of Ag/ZnO Nanorod Schottky Diode-Based Low-Voltage Ultraviolet Photodetector, Nano. 12 (2017) 1750063. doi:10.1142/S1793292017500631.

[20] P.Y. Lee, S.P. Chang, J.F. Chang, E.H. Hsu, S.J. Chang, Highly transparent nanostructured zinc oxide photodetector prepared by successive ionic layer adsorption and reaction, Int. J. Electrochem. Sci. 8 (2013) 6425–6432.

[21] B. Weintraub, Z. Zhou, Y. Li, Y. Deng, Solution synthesis of one-dimensional ZnO nanomaterials and their applications, Nanoscale. 2 (2010) 1573. doi:10.1039/c0nr00047g.

[22] M. Willander, O. Nur, K. Hasan, G. Amin, M. Soomro, Zinc Oxide Nanostructures: Synthesis, Characterization, and Device Applications on Nonconventional Substrates, Zinc Oxide Nanostructures. 2 (2014) 185–212. doi:10.1201/b15661-7.

[23] A. Kushwaha, M. Aslam, Defect induced high photocurrent in solution grown vertically aligned ZnO nanowire array films, J. Appl. Phys. 112 (2012). doi:10.1063/1.4749808.

[24] J. Park, S. Lee, K. Yong, Photo-stimulated resistive switching of ZnO nanorods, Nanotechnology. 23 (2012) 385707. doi:10.1088/0957-4484/23/38/385707.

[25] D.C. Hurum, a G. Agrios, K. a Gray, T. Rajh, M.C. Thurnauer, Explaining the enhanced photocatalytic activity of Degussa P25 mixed-phase TiO2 using EPR, J. Phys. Chem. B. 107 (2003) 4545–4549. doi:Doi 10.1021/Jp0273934.

[26] H. Lu, B. Zhao, R. Pan, J. Yao, J. Qiu, L. Luo, Y. Liu, Safe and facile hydrogenation of commercial Degussa P25 at room temperature with enhanced photocatalytic activity, RSC Adv. 4 (2014) 1128–1132. doi:10.1039/C3RA44493G.

[27] V.G. Bessergenev, M.C. Mateus, A.M.B. do Rego, M. Hantusch, E. Burkel, An improvement of photocatalytic activity of TiO2 Degussa P25 powder, Appl. Catal. A Gen. 500 (2015) 40–50. doi:10.1016/j.apcata.2015.05.002.

[28] Y. Zhu, L. Zhang, C. Gao, L. Cao, The synthesis of nanosized TiO2 powder using a sol-

gel method with TiCl4 as a precursor, J. Mater. Sci. 35 (2000) 4049–4054. doi:10.1023/A:1004882120249.

[29] X. Chen, S.S. Mao, Titanium Dioxide Nanomaterials: Synthesis, Properties, Modifications, and Applications, Chem. Rev. 107 (2007) 2891–2959. doi:10.1021/cr0500535.

[30] Z. Lai, F. Peng, Y. Wang, H. Wang, H. Yu, P. Liu, H. Zhao, Low temperature solvothermal synthesis of anatase TiO2 single crystals with wholly {100} and {001} faceted surfaces, J. Mater. Chem. 22 (2012) 23906. doi:10.1039/c2jm34880b.

[31] M. Scarselli, P. Castrucci, M. De Crescenzi, Electronic and optoelectronic nano-devices based on carbon nanotubes, J. Phys. Condens. Matter. 24 (2012) 313202. doi:10.1088/0953-8984/24/31/313202.

[32] H.W. Kroto, J.R. Heath, S.C. O'Brien, R.F. Curl, R.E. Smalley, C 60: buckminsterfullerene, Nature. 318 (1985) 162. doi:10.1038/318162a0.

[33] S. Iijima, Helical microtubules of graphitic carbon, Nature. 354 (1991) 56–58. doi:10.1038/354056a0.

[34] K. VI, A.M. Sladkov, K. YP, N.M. Popov, V. V Korshak, Crystalline forms of linear modification of carbon, Dokl. Akad. Nauk SSSR. 177 (1967) 358.

[35] K.S. Novoselov, A.K. Geim, S. V Morozov, D. Jiang, Y. Zhang, S. V Dubonos, I. V Grigorieva, A.A. Firsov, Electric field effect in atomically thin carbon films., Science. 306 (2004) 666–669. doi:10.1126/science.1102896.

[36] P.R. Wallace, The band theory of graphite, Phys. Rev. 71 (1947) 622–634. doi:10.1103/PhysRev.71.622.

[37] Y. Ando, X. Zhao, M. Ohkohchi, Production of petal-like graphite sheets by hydrogen arc discharge, Carbon N. Y. 35 (1997) 153–158. doi:10.1016/S0008-6223(96)00139-X.

[38] Y. Wu, P. Qiao, T. Chong, Z. Shen, Carbon Nanowalls Grown by Microwave Plasma Enhanced Chemical Vapor Deposition, Adv. Mater. 14 (2002) 64–67. doi:10.1002/1521-4095(20020104)14:1<64::AID-ADMA64>3.0.CO;2-G.

[39] C. Jin, F. Lin, K. Suenaga, S. Iijima, Fabrication of a freestanding boron nitride single layer and Its defect assignments, Phys. Rev. Lett. 102 (2009). doi:10.1103/PhysRevLett.102.195505.

[40] B. Garg, T. Bisht, Y.C. Ling, Graphene-based nanomaterials as heterogeneous acid catalysts: A comprehensive perspective, Molecules. 19 (2014) 14582–14614. doi:10.3390/molecules190914582.

[41] D.R. Dreyer, S. Park, C.W. Bielawski, R.S. Ruoff, The chemistry of graphene oxide., Chem. Soc. Rev. 39 (2010) 228–240. doi:10.1039/b920539j.

[42] K. Erickson, R. Erni, Z. Lee, N. Alem, W. Gannett, A. Zettl, Determination of the local chemical structure of graphene oxide and reduced graphene oxide, Adv. Mater. 22 (2010) 4467–4472. doi:10.1002/adma.201000732.

[43] M.J. Allen, V.C. Tung, R.B. Kaner, Honeycomb carbon: A review of graphene, Chem. Rev. 110 (2010) 132–145. doi:10.1021/cr900070d.

[44] S. Park, R.S. Ruoff, Chemical methods for the production of graphenes., Nat. Nanotechnol. 4 (2009) 217–224. doi:10.1038/nnano.2009.58.

[45] L. Shahriary, A. a. Athawale, Graphene Oxide Synthesized by using Modified Hummers Approach, Int. J. Renew. Energy Environ. Eng. 2 (2014) 58–63.

[46] S. Pei, H.M. Cheng, The reduction of graphene oxide, Carbon N. Y. 50 (2012) 3210–3228. doi:10.1016/j.carbon.2011.11.010.

[47] L. Li, G. Wu, G. Yang, J. Peng, J. Zhao, J.-J. Zhu, Focusing on luminescent graphene quantum dots: current status and future perspectives., Nanoscale. 5 (2013) 4015–39. doi:10.1039/c3nr33849e.

[48] Z. Zhang, J. Zhang, N. Chen, L. Qu, Graphene quantum dots: an emerging material for energy-related applications and beyond, Energy Environ. Sci. 5 (2012) 8869. doi:10.1039/c2ee22982j.

[49] X. Li, M. Rui, J. Song, Z. Shen, H. Zeng, Carbon and Graphene Quantum Dots for Optoelectronic and Energy Devices: A Review, Adv. Funct. Mater. (2015) n/a--n/a. doi:10.1002/adfm.201501250.

[50] C.X. Guo, H. Bin Yang, Z.M. Sheng, Z.S. Lu, Q.L. Song, C.M. Li, Layered graphene/quantum dots for photovoltaic devices, Angew. Chemie - Int. Ed. 49 (2010) 3014–3017. doi:10.1002/anie.200906291.

[51] V. Gupta, N. Chaudhary, R. Srivastava, G.D. Sharma, R. Bhardwaj, S. Chand, Luminscent graphene quantum dots for organic photovoltaic devices, J Am Chem Soc. 133 (2011) 9960–9963. doi:10.1021/ja2036749.

[52] J. Shen, Y. Zhu, X. Yang, C. Li, Graphene quantum dots: emergent nanolights for bioimaging, sensors, catalysis and photovoltaic devices, Chem. Commun. 48 (2012) 3686. doi:10.1039/c2cc00110a.

[53] M. Bacon, S.J. Bradley, T. Nann, Graphene Quantum Dots, Part. Part. Syst. Charact. 31 (2014) 415–428. doi:10.1002/ppsc.201300252.

[54] C.K. Chua, Z. Sofer, P. Šimek, O. Jankovský, K. Klímová, S. Bakardjieva, Š. Hrdličková Kučková, M. Pumera, Synthesis of Strongly Fluorescent Graphene Quantum Dots by Cage-Opening Buckminsterfullerene, ACS Nano. 9 (2015) 2548–2555. doi:10.1021/nn505639q.

[55] D. Pan, J. Zhang, Z. Li, M. Wu, Hydrothermal route for cutting graphene sheets into blue-luminescent graphene quantum dots, Adv. Mater. 22 (2010) 734–738. doi:10.1002/adma.200902825.

[56] S. Chen, J.-W. Liu, M.-L. Chen, X.-W. Chen, J.-H. Wang, Unusual emission transformation of graphene quantum dots induced by self-assembled aggregation, Chem. Commun. 48 (2012) 7637. doi:10.1039/c2cc32984k.

[57] X. Zhou, Y. Zhang, C. Wang, X. Wu, Y. Yang, B. Zheng, H. Wu, S. Guo, J. Zhang, Photo-Fenton reaction of graphene oxide: A new strategy to prepare graphene quantum dots for DNA cleavage, ACS Nano. 6 (2012) 6592–6599. doi:10.1021/nn301629v.

[58] S. Kim, S.W. Hwang, M.K. Kim, D.Y. Shin, D.H. Shin, C.O. Kim, S.B. Yang, J.H. Park, E. Hwang, S.H. Choi, G. Ko, S. Sim, C. Sone, H.J. Choi, S. Bae, B.H. Hong, Anomalous behaviors of visible luminescence from graphene quantum dots: Interplay between size and shape, ACS Nano. 6 (2012) 8203–8208. doi:10.1021/nn302878r.

[59] X. Yan, X. Cui, L.S. Li, Synthesis of large, stable colloidal graphene quantum dots with tunable size, J. Am. Chem. Soc. 132 (2010) 5944–5945. doi:10.1021/ja1009376.

[60] L. Tang, R. Ji, X. Cao, J. Lin, H. Jiang, X. Li, K.S. Teng, Deep Ultraviolet Photoluminescence Graphene Quantum Dots, (2012) 5102–5110.

[61] J. Lu, P.S.E. Yeo, C.K. Gan, P. Wu, K.P. Loh, Transforming C60 molecules into graphene quantum dots., Nat. Nanotechnol. 6 (2011) 247–252. doi:10.1038/nnano.2011.30.

[62] G. Takyo, S. Kono, T. Goto, H. Sasaoka, K. Nishimura, Origin of field emission from a nano-diamond/carbon nanowall electron emitter, Jpn. J. Appl. Phys. 47 (2008) 2241–2243. doi:10.1143/JJAP.47.2241.

[63] E. Yoo, T. Okata, T. Akita, M. Kohyama, J. Nakamura, I. Honma, Enhanced electrocatalytic activity of Pt subnanoclusters on graphene nanosheet surface, Nano Lett. 9 (2009) 2255–2259. doi:10.1021/nl900397t.

[64] T.C. Hung, C.F. Chen, W.T. Whang, Deposition of carbon nanowall flowers on two-dimensional sheet for electrochemical capacitor application, Electrochem. Solid-State Lett. 12 (2009) K41–K44. doi:10.1149/1.3099325.

[65] O. Tanaike, N. Kitada, H. Yoshimura, H. Hatori, K. Kojima, M. Tachibana, Lithium insertion behavior of carbon nanowalls by dc plasma CVD and its heat-treatment effect, Solid State Ionics. 180 (2009) 381–385. doi:10.1016/j.ssi.2009.01.012.

[66] M. Hiramatsu, M. Hori, Carbon Nanowalls, Springer Vienna, Vienna, 2010. doi:10.1007/978-3-211-99718-5.

[67] M. Hiramatsu, K. Shiji, H. Amano, M. Hori, Fabrication of vertically aligned carbon nanowalls using capacitively coupled plasma-enhanced chemical vapor deposition assisted by hydrogen radical injection, Appl. Phys. Lett. 84 (2004) 4708–4710. doi:10.1063/1.1762702.

[68] K. Shiji, M. Hiramatsu, A. Enomoto, M. Nakamura, H. Amano, M. Hori, Vertical growth of carbon nanowalls using rf plasma-enhanced chemical vapor deposition, Diam. Relat. Mater. 14 (2005) 831–834. doi:10.1016/j.diamond.2004.10.021.

[69] G. Compagnini, M. Sinatra, P. Russo, G.C. Messina, O. Puglisi, S. Scalese, Deposition of few layer graphene nanowalls at the electrodes during electric field-assisted laser ablation of carbon in water, Carbon N. Y. 50 (2012) 2362–2365. doi:10.1016/j.carbon.2012.01.038.

[70] A.E. Goresy, G. Donnay, A New Allotropic Form of Carbon from the Ries Crater, Science

(80-.). 161 (1968) 363–364. doi:10.1126/science.161.3839.363.

[71] A.G. Whittaker, P.L. Kintner, Carbon: Observations on the New Allotropic Form, Science (80-.). 165 (1969) 589 LP-591.

[72] A.G. Whittaker, G.M. Wolten, Carbon: A Suggested New Hexagonal Crystal Form, Science (80-.). 178 (1972) 54 LP-56.

[73] R.B. Heimann, S.E. Evsyukov, K. L., Carbyne and Carbynoid Structures, Springer Netherlands, Dordrecht, 1999. doi:10.1007/978-94-011-4742-2.

[74] L. Kavan, Electrochemical Carbyne-Like Materials, Carbon N. Y. 36 (1998) 801–808.

[75] G. Compagnini, V. Mita, L. D'Urso, R.S. Cataliotti, O. Puglisi, Spectroscopic study of polyynes obtained by laser ablation in liquids, J. Raman Spectrosc. 39 (2008) 177–181. doi:10.1002/jrs.1837.

[76] A. Hu, J. Sanderson, A.A. Zaidi, C. Wang, T. Zhang, Y. Zhou, W.W. Duley, Direct synthesis of polyyne molecules in acetone by dissociation using femtosecond laser irradiation, Carbon N. Y. 46 (2008) 1823–1825. doi:10.1016/j.carbon.2008.07.036.

[77] S.K. Shin, J.K. Song, S.M. Park, Preparation of polyynes by laser ablation of graphite in aqueous media, Appl. Surf. Sci. 257 (2011) 5156–5158. doi:10.1016/j.apsusc.2010.10.074.

[78] S.K. Shin, S.M. Park, Preparation of polyynes by the laser ablation of graphite in water and organic solvents, Bull. Korean Chem. Soc. 33 (2012) 597–600. doi:10.1016/j.apsusc.2010.10.074.

[79] F. Cataldo, A method for synthesizing polyynes in solution, Carbon N. Y. 43 (2005) 2792–2800. doi:10.1016/j.carbon.2005.05.024.

[80] F. Cataldo, Polyynes: A new class of carbon allotropes. About the formation of dicyanopolyynes from an electric arc between graphite electrodes in liquid nitrogen, Polyhedron. 23 (2004) 1889–1896. doi:10.1016/j.poly.2004.04.024.

[81] F. Cataldo, Synthesis of polyynes in a submerged electric arc in organic solvents, Carbon N. Y. 42 (2004) 129–142. doi:10.1016/j.carbon.2003.10.016.

[82] E. Bourgeat-Lami, J. Faucheu, A. Noël, Latex routes to graphene-based nanocomposites, Polym. Chem. 6 (2015) 5323–5357. doi:10.1039/C5PY00490J.

[83] A.H. Castro Neto, F. Guinea, N.M.R. Peres, K.S. Novoselov, A.K. Geim, The electronic properties of graphene, Rev. Mod. Phys. 81 (2009) 109–162. doi:10.1103/RevModPhys.81.109.

[84] S. Das, W. Choi, Graphene Synthesis, in: Graphene, CRC Press, 2011: pp. 27–64. doi:10.1201/b11259-3.

[85] R. Balog, B. Jørgensen, L. Nilsson, M. Andersen, E. Rienks, M. Bianchi, M. Fanetti, E. Lægsgaard, A. Baraldi, S. Lizzit, Z. Sljivancanin, F. Besenbacher, B. Hammer, T.G. Pedersen, P. Hofmann, L. Hornekær, Bandgap opening in graphene induced by patterned hydrogen adsorption, Nat. Mater. 9 (2010) 315–319. doi:10.1038/nmat2710.

[86] K.Y. Lian, Y.F. Ji, X.F. Li, M.X. Jin, D.J. Ding, Y. Luo, Big bandgap in highly reduced graphene oxides, J. Phys. Chem. C. 117 (2013) 6049–6054. doi:10.1021/jp3118067.

[87] D. Wei, Y. Liu, Y. Wang, H. Zhang, L. Huang, G. Yu, Synthesis of n-doped graphene by chemical vapor deposition and its electrical properties, Nano Lett. 9 (2009) 1752–1758. doi:10.1021/nl803279t.

[88] F. Cervantes-Sodi, G. Cs??nyi, S. Piscanec, A.C. Ferrari, Edge-functionalized and substitutionally doped graphene nanoribbons: Electronic and spin properties, Phys. Rev. B - Condens. Matter Mater. Phys. 77 (2008). doi:10.1103/PhysRevB.77.165427.

[89] C. Gómez-Navarro, R.T. Weitz, A.M. Bittner, M. Scolari, A. Mews, M. Burghard, K. Kern, Electronic transport properties of individual chemically reduced graphene oxide sheets, Nano Lett. 7 (2007) 3499–3503. doi:10.1021/nl072090c.

[90] L. Guo, R.Q. Shao, Y.L. Zhang, H.B. Jiang, X. Bin Li, S.Y. Xie, B. Bin Xu, Q.D. Chen, J.F. Song, H.B. Sun, Bandgap tailoring and synchronous microdevices patterning of graphene oxides, J. Phys. Chem. C. 116 (2012) 3594–3599. doi:10.1021/jp209843m.

[91] M. Acik, Y.J. Chabal, A Review on Reducing Graphene Oxide for Band Gap Engineering, J. Mater. Sci. Res. 2 (2012) 101–112. doi:10.5539/jmsr.v2n1p101.

[92] M.A. Velasco-Soto, S.A. Pérez-García, J. Alvarez-Quintana, Y. Cao, L. Nyborg, L. Licea-Jiménez, Selective band gap manipulation of graphene oxide by its reduction with mild reagents, Carbon N. Y. 93 (2015) 967–973. doi:10.1016/j.carbon.2015.06.013.

[93] C. Lee, X. Wei, J.W. Kysar, J. Hone, =, Measurement of the Elastic Properties and Intrinsic Strength of Monolayer Graphene, Science (80-.). 321 (2008) 385–388. doi:10.1126/science.1157996.

[94] S. Zhu, J. Zhang, X. Liu, B. Li, X. Wang, S. Tang, Q. Meng, Y. Li, C. Shi, R. Hu, B. Yang, Graphene quantum dots with controllable surface oxidation, tunable fluorescence and up-conversion emission, RSC Adv. 2 (2012) 2717. doi:10.1039/c2ra20182h.

[95] S. Zhu, J. Zhang, C. Qiao, S. Tang, Y. Li, W. Yuan, B. Li, L. Tian, F. Liu, R. Hu, H. Gao, H. Wei, H. Zhang, H. Sun, B. Yang, Strongly green-photoluminescent graphene quantum dots for bioimaging applications., Chem. Commun. (Camb). 47 (2011) 6858–6860. doi:10.1039/c1cc11122a.

[96] J.M. Yoo, J.H. Kang, B.H. Hong, Graphene-based nanomaterials for versatile imaging studies, Chem. Soc. Rev. 44 (2015) 4835–4852. doi:10.1039/C5CS00072F.

[97] Y. Zhang, H. Gao, J. Niu, B. Liu, Facile synthesis and photoluminescence of graphene oxide quantum dots and their reduction products, New J. Chem. 38 (2014) 4970–4974. doi:10.1039/C4NJ01187B.

[98] Y. Dong, J. Shao, C. Chen, H. Li, R. Wang, Y. Chi, X. Lin, G. Chen, Blue luminescent graphene quantum dots and graphene oxide prepared by tuning the carbonization degree of citric acid, Carbon N. Y. 50 (2012) 4738–4743. doi:10.1016/j.carbon.2012.06.002.

[99] D. Pan, L. Guo, J. Zhang, C. Xi, Q. Xue, H. Huang, J. Li, Z. Zhang, W. Yu, Z. Chen, Z. Li, M. Wu, Cutting sp2 clusters in graphene sheets into colloidal graphene quantum dots

with strong green fluorescence, J. Mater. Chem. 22 (2012) 3314. doi:10.1039/c2jm16005f.

[100] Z. Wang, J. Xia, C. Zhou, B. Via, Y. Xia, F. Zhang, Y. Li, L. Xia, J. Tang, Synthesis of strongly green-photoluminescent graphene quantum dots for drug carrier, Colloids Surfaces B Biointerfaces. 112 (2013) 192–196. doi:10.1016/j.colsurfb.2013.07.025.

[101] V. Gupta, N. Chaudhary, R. Srivastava, G.D. Sharma, R. Bhardwaj, S. Chand, Luminscent graphene quantum dots for organic photovoltaic devices, J. Am. Chem. Soc. 133 (2011) 9960–9963. doi:10.1021/ja2036749.

[102] Y. Zhang, J.P. Small, W. V. Pontius, P. Kim, Fabrication and electric-field-dependent transport measurements of mesoscopic graphite devices, Appl. Phys. Lett. 86 (2005) 1–3. doi:10.1063/1.1862334.

[103] K.S.K.S. Novoselov, A.K. a. K. Geim, S.V.S. V Morozov, D. Jiang, Y. Zhang, S.V. V Dubonos, I.V. V Grigorieva, a. a. a Firsov, Electric field effect in atomically thin carbon films., Science (80-.). 306 (2004) 666–669. doi:10.1126/science.1102896.

[104] M. Cai, D. Thorpe, D.H. Adamson, H.C. Schniepp, Methods of graphite exfoliation, J. Mater. Chem. (2012) 24992–25002. doi:10.1039/c2jm34517j.

[105] Y. Hernandez, V. Nicolosi, M. Lotya, F.M. Blighe, Z. Sun, S. De, I.T. McGovern, B. Holland, M. Byrne, Y.K. Gun'Ko, J.J. Boland, P. Niraj, G. Duesberg, S. Krishnamurthy, R. Goodhue, J. Hutchison, V. Scardaci, A.C. Ferrari, J.N. Coleman, High-yield production of graphene by liquid-phase exfoliation of graphite, Nat. Nanotechnol. 3 (2008) 563–568. doi:10.1038/nnano.2008.215.

[106] J. Zhang, H. Yang, G. Shen, P. Cheng, J. Zhang, S. Guo, Reduction of graphene oxide via L-ascorbic acid., Chem. Commun. (Camb). 46 (2010) 1112–1114. doi:10.1039/b917705a.

[107] K. Ai, Y. Liu, L. Lu, X. Cheng, L. Huo, A novel strategy for making soluble reduced graphene oxide sheets cheaply by adopting an endogenous reducing agent, J. Mater. Chem. 21 (2011) 3365. doi:10.1039/c0jm02865g.

[108] G. Williams, B. Seger, P. V Kamat, UV-Assisted Photocatalytic Reduction of Graphene Oxide, 2 (2008) 1487–1491.

[109] J. Shen, Y. Hu, M. Shi, X. Lu, C. Qin, C. Li, M. Ye, Fast and facile preparation of graphene oxide and reduced graphene oxide nanoplatelets, Chem. Mater. 21 (2009) 3514–3520. doi:10.1021/cm901247t.

[110] J. William S. Hummers, R.E. Offeman, Preparation of Graphitic Oxide, J. Am. Chem. Soc. 80 (1958) 1339. doi:10.1021/ja01539a017.

[111] D.C. Marcano, D. V. Kosynkin, J.M. Berlin, A. Sinitskii, Z. Sun, A. Slesarev, L.B. Alemany, W. Lu, J.M. Tour, Improved synthesis of graphene oxide, ACS Nano. 4 (2010) 4806–4814. doi:10.1021/nn1006368.

[112] V.C. Tung, M.J. Allen, Y. Yang, R.B. Kaner, High-throughput solution processing of large-scale graphene, Nat. Nanotechnol. 4 (2009) 25–29. doi:10.1038/nnano.2008.329.

[113] S. Zhu, J. Zhang, X. Liu, B. Li, X. Wang, S. Tang, Q. Meng, Y. Li, C. Shi, R. Hu, B.

Yang, Graphene quantum dots with controllable surface oxidation, tunable fluorescence and up-conversion emission, RSC Adv. 2 (2012) 2717. doi:10.1039/c2ra20182h.

[114] N.G. Shang, F.C.K. Au, X.M. Meng, C.S. Lee, I. Bello, S.T. Lee, Uniform carbon nanoflake films and their field emissions, Chem. Phys. Lett. 358 (2002) 187–191. doi:10.1016/S0009-2614(02)00430-X.

[115] T. Mori, M. Hiramatsu, K. Yamakawa, K. Takeda, M. Hori, Fabrication of carbon nanowalls using electron beam excited plasma-enhanced chemical vapor deposition, Diam. Relat. Mater. 17 (2008) 1513–1517. doi:10.1016/j.diamond.2008.01.070.

[116] H. Zeng, X.W. Du, S.C. Singh, S.A. Kulinich, S. Yang, J. He, W. Cai, Nanomaterials via laser ablation/irradiation in liquid: A review, Adv. Funct. Mater. 22 (2012) 1333–1353. doi:10.1002/adfm.201102295.

[117] M. Stafe, A. Marcu, N. Puscas, Pulsed Laser Ablation of Solids: Basics, Theory and Applications, 2013. doi:10.1007/978-3-642-40978-3.

[118] G.W. Yang, Laser ablation in liquids: Applications in the synthesis of nanocrystals, Prog. Mater. Sci. 52 (2007) 648–698. doi:10.1016/j.pmatsci.2006.10.016.

[119] M.S. Brown, C.B. Arnold, Laser Precision Microfabrication, Springer Ser. Mater. Sci. 135 (2010) 91–120. doi:10.1007/978-3-642-10523-4.

[120] J. Neddersen, G. Chumanov, T.M. Cotton, Laser Ablation of Metals, Appl. Spectrosc. 47 (1993) 1959–1964.

[121] G. Compagnini, A.A. Scalisi, O. Puglisi, C. Spinella, Synthesis of gold colloids by laser ablation in thiol-alkane solutions, J. Mater. Res. 19 (2004) 2795–2798. doi:10.1557/JMR.2004.0401.

[122] E. Messina, G. Compagnini, L. D'Urso, O. Puglisi, S. Bagiante, S. Scalese, Size distribution and particle shape in silver colloids prepared by laser ablation in water, Radiat. Eff. Defects Solids. 165 (2010) 579–583. doi:10.1080/10420151003723014.

[123] G. Compagnini, V. Mita, R.S. Cataliotti, L. D'Urso, O. Puglisi, Short polyyne chains produced by pulsed laser ablation of graphite in water, Carbon N. Y. 45 (2007) 2456–2458. doi:10.1016/j.carbon.2007.07.002.

[124] M. Tsuji, S. Kuboyama, T. Matsuzaki, T. Tsuji, Formation of hydrogen-capped polyynes by laser ablation of C60 particles suspended in solution, Carbon N. Y. 41 (2003) 2141–2148. doi:10.1016/S0008-6223(03)00241-0.

[125] H.O. Jeschke, M.E. Garcia, K.H. Bennemann, Theory for the ultrafast ablation of graphite films., Phys. Rev. Lett. 87 (2001) 15003. doi:10.1103/PhysRevLett.87.015003.

[126] F. Carbone, P. Baum, P. Rudolf, a H. Zewail, Structural Preablation Dynamics of Grahite Observed by Ultrafast Electron Crystallography, Phys. Rev. Lett. 100 (2008) 4. doi:10.1103/PhysRevLett.100.035501.

[127] Y. Miyamoto, H. Zhang, D. Tománek, Photoexfoliation of graphene from graphite: An Ab initio study, Phys. Rev. Lett. 104 (2010) 19–22. doi:10.1103/PhysRevLett.104.208302.

[128] M. Qian, Y.S. Zhou, Y. Gao, J.B. Park, T. Feng, S.M. Huang, Z. Sun, L. Jiang, Y.F. Lu, Formation of graphene sheets through laser exfoliation of highly ordered pyrolytic graphite, Appl. Phys. Lett. 98 (2011) 1–4. doi:10.1063/1.3584021.

[129] G. Compagnini, P. Russo, F. Tomarchio, O. Puglisi, L. D'Urso, S. Scalese, Laser assisted green synthesis of free standing reduced graphene oxides at the water-air interface., Nanotechnology. 23 (2012) 505601. doi:10.1088/0957-4484/23/50/505601.

[130] S.F. Spanò, G. Isgrò, P. Russo, M.E. Fragalà, G. Compagnini, Tunable properties of graphene oxide reduced by laser irradiation, Appl. Phys. A. 117 (2014) 19–23. doi:10.1007/s00339-014-8508-y.

[131] H. Wang, K. Kawaguchi, A. Pyatenko, X. Li, Z. Swiatkowska-Warkocka, Y. Katou, N. Koshizaki, General bottom-up construction of spherical particles by pulsed laser irradiation of colloidal nanoparticles: a case study on CuO., Chemistry. 18 (2012) 163–9. doi:10.1002/chem.201102079.

[132] A. Pyatenko, H. Wang, N. Koshizaki, Growth Mechanism of Monodisperse Spherical Particles under Nanosecond Pulsed Laser Irradiation, J. Phys. Chem. C. 118 (2014) 4495–4500. doi:10.1021/jp411958v.

[133] M. Grätzel, Solar energy conversion by dye-sensitized photovoltaic cells, Inorg. Chem. 44 (2005) 6841–6851. doi:10.1021/ic0508371.

[134] K. Zhao, S. Zhao, J. Qi, H. Yin, C. Gao, A.M. Khattak, Y. Wu, A. Iqbal, L. Wu, Y. Gao, R. Yu, Z. Tang, Cu2O clusters grown on TiO2nanoplates as efficient photocatalysts for hydrogen generation, Inorg. Chem. Front. 3 (2016) 488–493. doi:10.1039/c5qi00284b.

[135] V. Galstyan, E. Comini, G. Faglia, G. Sberveglieri, TiO2 nanotubes: recent advances in synthesis and gas sensing properties., Sensors (Basel). 13 (2013) 14813–38. doi:10.3390/s131114813.

[136] M. Xiao, K.P. Musselman, W.W. Duley, Y.N. Zhou, Reliable and Low-Power Multilevel Resistive Switching in TiO2 Nanorod Arrays Structured with a TiOx Seed Layer, ACS Appl. Mater. Interfaces. 9 (2017) 4808–4817. doi:10.1021/acsami.6b14206.

[137] X. Wu, Z. Xu, Z. Yu, T. Zhang, F. Zhao, T. Sun, Z. Ma, Z. Li, S. Wang, Resistive switching behavior of photochemical activation solution-processed thin films at low temperatures for flexible memristor applications, J. Phys. D. Appl. Phys. 48 (2015) 115101. doi:10.1088/0022-3727/48/11/115101.

[138] O. Carp, C.L. Huisman, A. Reller, Photoinduced reactivity of titanium dioxide, Prog. Solid State Chem. 32 (2004) 33–177. doi:10.1016/j.progsolidstchem.2004.08.001.

[139] P. Russo, R. Liang, R.X. He, Y.N. Zhou, Phase transformation of TiO2 nanoparticles by femtosecond laser ablation in aqueous solution and deposited on conductive substrate, Nanoscale. (2017) 6167–6177. doi:10.1039/C7NR00201G.

[140] A. Moezzi, A.M. McDonagh, M.B. Cortie, Zinc oxide particles: Synthesis, properties and applications, Chem. Eng. J. 185–186 (2012) 1–22. doi:10.1016/j.cej.2012.01.076.

[141] Z. Fan, J.G. Lu, Zinc Oxide Nanostructures: Synthesis and Properties, J. Nanosci.

Nanotechnol. 5 (2005) 1561–1573. doi:10.1166/jnn.2005.182.

[142] H. Cheng, J. Ma, Z. Zhao, L. Qi, Hydrothermal Preparation of Uniform Nanosize Rutile and Anatase Particles, Chem. Mater. 7 (1995) 663–671. doi:10.1021/cm00052a010.

[143] A. Hu, X. Zhang, K.D. Oakes, P. Peng, Y.N. Zhou, M.R. Servos, Hydrothermal growth of free standing TiO2 nanowire membranes for photocatalytic degradation of pharmaceuticals., J. Hazard. Mater. 189 (2011) 278–85. doi:10.1016/j.jhazmat.2011.02.033.

[144] Y.F. Zhu, L. Zhang, C. Gao, L.L. Cao, The synthesis of nanosized TiO$_2$ powder using a sol-gel method with TiCl$_4$ as a precursor, J. Mater. Sci. 35 (2000) 4049–4054.

[145] K. Farhadian Azizi, M.M. Bagheri-Mohagheghi, Transition from anatase to rutile phase in titanium dioxide (TiO 2) nanoparticles synthesized by complexing sol-gel process: Effect of kind of complexing agent and calcinating temperature, J. Sol-Gel Sci. Technol. 65 (2013) 329–335. doi:10.1007/s10971-012-2940-2.

[146] H. Choi, E. Stathatos, D.D. Dionysiou, Sol-gel preparation of mesoporous photocatalytic TiO2 films and TiO2/Al2O3 composite membranes for environmental applications, Appl. Catal. B Environ. 63 (2006) 60–67. doi:10.1016/j.apcatb.2005.09.012.

[147] C.H. Liang, Y. Shimizu, T. Sasaki, N. Koshizaki, Synthesis, characterization, and phase stability of ultrafine TiO2 nanoparticles by pulsed laser ablation in liquid media, J. Mater. Res. 19 (2004) 1551–1557. doi:10.1557/jmr.2004.0208.

[148] M. Boutinguiza, B. Rodríguez-González, J. del Val, R. Comesaña, F. Lusquiños, J. Pou, Laser-assisted production of spherical TiO2 nanoparticles in water., Nanotechnology. 22 (2011) 195606. doi:10.1088/0957-4484/22/19/195606.

[149] A. Nath, S.S. Laha, A. Khare, Synthesis of TiO 2 Nanoparticles Via Laser Ablation at Titanium-Water Interface, Integr. Ferroelectr. 121 (2010) 58–64. doi:10.1080/10584587.2010.492020.

[150] A. Kolodziejczak-Radzimska, T. Jesionowski, Zinc oxide-from synthesis to application: A review, Materials (Basel). 7 (2014) 2833–2881. doi:10.3390/ma7042833.

[151] S. Baruah, J. Dutta, Hydrothermal growth of ZnO nanostructures, Sci. Technol. Adv. Mater. 10 (2009) 13001. doi:10.1088/1468-6996/10/1/013001.

[152] B. Baruwati, D.K. Kumar, S. V. Manorama, Hydrothermal synthesis of highly crystalline ZnO nanoparticles: A competitive sensor for LPG and EtOH, Sensors Actuators B Chem. 119 (2006) 676–682. doi:10.1016/j.snb.2006.01.028.

[153] T.H. Meen, W. Water, Y.S. Chen, W.R. Chen, L.W. Ji, C.J. Huang, Growth Of ZnO Nanorods by Hydrothermal Method Under Different Temperatures, (2007) 617–620.

[154] L. Miao, S. Cai, Z. Xiao, Preparation and characterization of nanostructured ZnO thin film by electrophoretic deposition from ZnO colloidal suspensions, J. Alloys Compd. 490 (2010) 422–426. doi:10.1016/j.jallcom.2009.10.021.

[155] H.K. Park, S.P. Hong, Y.R. Do, Y. Rag, Vertical Growth of ZnO Nanorods Prepared on

an ITO-Coated Glass Substrate by Hydrothermal-Electrochemical Deposition, J. Electrochem. Soc. 159 (2012) D355. doi:10.1149/2.078206jes.

[156] Y.H. Ko, M.S. Kim, J.S. Yu, Controllable electrochemical synthesis of ZnO nanorod arrays on flexible ITO/PET substrate and their structural and optical properties, Appl. Surf. Sci. 259 (2012) 99–104. doi:10.1016/j.apsusc.2012.06.109.

[157] M. Verde, M. Peiteado, M. Villegas, B. Ferrari, A.C. Caballero, Soft solution processing of ZnO nanoarrays by combining electrophoretic deposition and hydrothermal growth, Mater. Chem. Phys. 140 (2013) 75–80. doi:10.1016/j.matchemphys.2013.02.067.

[158] S.K. Park, J.H. Park, K.Y. Ko, S. Yoon, K.S. Chu, W. Kim, Y.R. Do, Hydrothermal - Electrochemical Synthesis of ZnO Nanorods, Cryst. Growth Des. 9 (2009) 3615–3620. doi:10.1021/cg9003593.

[159] D.S.L. Abergel, A. Russell, V.I. Fal'Ko, Visibility of graphene flakes on a dielectric substrate, Appl. Phys. Lett. 91 (2007) 2–5. doi:10.1063/1.2768625.

[160] I. Jung, M. Pelton, R. Piner, D.A. Dikin, S. Stankovich, S. Watcharotone, M. Hausner, R.S. Ruoff, Simple approach for high-contrast optical imaging and characterization of graphene-based sheets, Nano Lett. 7 (2007) 3569–3575. doi:10.1021/nl0714177.

[161] P. Blake, E.W. Hill, A.H. Castro Neto, K.S. Novoselov, D. Jiang, R. Yang, T.J. Booth, A.K. Geim, Making graphene visible, Appl. Phys. Lett. 91 (2007). doi:10.1063/1.2768624.

[162] M.S. Dresselhaus, G. Dresselhaus, R. Saito, a. Jorio, Raman spectroscopy of carbon nanotubes, Phys. Rep. 409 (2005) 47–99. doi:10.1016/j.physrep.2004.10.006.

[163] L.G. Cançado, M.A. Pimenta, B.R.A. Neves, G. Medeiros-Ribeiro, T. Enoki, Y. Kobayashi, K. Takai, K.I. Fukui, M.S. Dresselhaus, R. Saito, A. Jorio, Anisotropy of the Raman spectra of nanographite ribbons, Phys. Rev. Lett. 93 (2004) 47403–1. doi:10.1103/PhysRevLett.93.047403.

[164] I. Childres, L. Jauregui, W. Park, H. Cao, Y. Chen, Raman Spectroscopy of Graphene and Related Materials, New Dev. Phot. Mater. Res. (2013) 1–20. doi:10.1016/B978-0-444-53175-9.00016-7.

[165] M.A. Pimenta, G. Dresselhaus, M.S. Dresselhaus, L.G. Cançado, A. Jorio, R. Saito, Studying disorder in graphite-based systems by Raman spectroscopy, Phys. Chem. Chem. Phys. 9 (2007) 1276–1291. doi:10.1039/b613962k.

[166] L.M. Malard, M.A. Pimenta, G. Dresselhaus, M.S. Dresselhaus, Raman spectroscopy in graphene, Phys. Rep. 473 (2009) 51–87. doi:10.1016/j.physrep.2009.02.003.

[167] A.C. Ferrari, J.C. Meyer, V. Scardaci, C. Casiraghi, M. Lazzeri, F. Mauri, S. Piscanec, D. Jiang, K.S. Novoselov, S. Roth, A.K. Geim, Raman spectrum of graphene and graphene layers, Phys. Rev. Lett. 97 (2006). doi:10.1103/PhysRevLett.97.187401.

[168] K.N. Kudin, B. Ozbas, H.C. Schniepp, R.K. Prud'Homme, I. a Aksay, R. Car, Raman spectra of graphite oxide and functionalized graphene sheets, Nano Lett. 8 (2008) 36–41. doi:10.1021/nl071822y.

[169] T. Jiao, Y. Liu, Y. Wu, Q. Zhang, X. Yan, F. Gao, A.J.P. Bauer, J. Liu, T. Zeng, B. Li, Facile and Scalable Preparation of Graphene Oxide-Based Magnetic Hybrids for Fast and Highly Efficient Removal of Organic Dyes, Nat. Publ. Gr. (2015) 1–10. doi:10.1038/srep12451.

[170] W.F. Zhang, Y.L. He, M.S. Zhang, Z. Yin, Q. Chen, Raman scattering study on anatase TiO 2 nanocrystals, J. Phys. D. Appl. Phys. 33 (2000) 912–916. doi:10.1088/0022-3727/33/8/305.

[171] J.C. Parker, R.W. Siegel, Raman microprobe study of nanophase TiO2 and oxidation-induced spectral changes, J. Mater. Res. 5 (1990) 1246–1252. doi:10.1557/JMR.1990.1246.

[172] C. a. Melendres, a. Narayanasamy, V. a. Maroni, R.W. Siegel, Raman spectroscopy of nanophase TiO2, J. Mater. Res. 4 (1989) 1246–1250. doi:10.1557/JMR.1989.1246.

[173] C.S. Campos, E.R. Spada, F.R. De Paula, F.T. Reis, R.M. Faria, M.L. Sartorelli, Raman and XRD study on brookite-anatase coexistence in cathodic electrosynthesized titania, J. Raman Spectrosc. 43 (2012) 433–438. doi:10.1002/jrs.3048.

[174] J.C. Parker, R.W. Siegel, Calibration of the Raman spectrum to the oxygen stoichiometry of nanophase TiO2, Appl. Phys. Lett. 57 (1990) 943–945. doi:10.1063/1.104274.

[175] J. Medina-Valtierra, C. Frausto-Reyes, M. Ortiz-Morales, Phase transformation in semi-transparent TiO2 films irradiated with CO2 laser, Mater. Lett. 66 (2012) 172–175. doi:10.1016/j.matlet.2011.08.076.

[176] K.A. Alim, V.A. Fonoberov, M. Shamsa, A.A. Balandin, Micro-Raman investigation of optical phonons in ZnO nanocrystals, J. Appl. Phys. 97 (2005) 1–5. doi:10.1063/1.1944222.

[177] A.G. Milekhin, N. a. Yeryukov, L.L. Sveshnikova, T.A. Duda, E.I. Zenkevich, S.S. Kosolobov, a. V. Latyshev, C. Himcinski, N. V. Surovtsev, S. V. Adichtchev, Z.C. Feng, C.C. Wu, D.S. Wuu, D.R.T. Zahn, Surface enhanced Raman scattering of light by ZnO nanostructures, J. Exp. Theor. Phys. 113 (2011) 983–991. doi:10.1134/S1063776111140184.

[178] A. Khan, Raman Spectroscopic Study of the ZnO Nanostructures, J. Pakistan Mater. Soc. 4 (2010) 5–9.

[179] H. Hiura, H. Miyazaki, K. Tsukagoshi, Determination of the number of graphene layers: Discrete distribution of the secondary electron intensity stemming from individual graphene layers, Appl. Phys. Express. 3 (2010). doi:10.1143/APEX.3.095101.

[180] A. Reina, X. Jia, J. Ho, D. Nezich, H. Son, V. Bulovic, M.S. Dresselhaus, K. Jing, Large area, few-layer graphene films on arbitrary substrates by chemical vapor deposition, Nano Lett. 9 (2009) 30–35. doi:10.1021/nl801827v.

[181] J.H. Warner, M.H. Rümmeli, A. Bachmatiuk, B. Büchner, Examining the stability of folded graphene edges against electron beam induced sputtering with atomic resolution., Nanotechnology. 21 (2010) 325702. doi:10.1088/0957-4484/21/32/325702.

[182] T. Takamura, K. Endo, L. Fu, Y. Wu, K.J. Lee, T. Matsumoto, Identification of nano-sized holes by TEM in the graphene layer of graphite and the high rate discharge capability of Li-ion battery anodes, Electrochim. Acta. 53 (2007) 1055–1061. doi:10.1016/j.electacta.2007.03.052.

[183] J.C. Meyer, C. Kisielowski, R. Erni, M.D. Rossell, M.F. Crommie, A. Zettl, Direct imaging of lattice atoms and topological defects in graphene membranes, Nano Lett. 8 (2008) 3582–3586. doi:10.1021/nl801386m.

[184] Y.T. Huang, S.Y. Yu, C.L. Hsin, C.W. Huang, C.F. Kang, F.H. Chu, J.Y. Chen, J.C. Hu, L.T. Chen, J.H. He, W.W. Wu, In situ TEM and energy dispersion spectrometer analysis of chemical composition change in ZnO nanowire resistive memories, Anal. Chem. 85 (2013) 3955–3960. doi:10.1021/ac303528m.

[185] R. Divakar, J. Basu, C.B. Carter, TEM Characterization of ZnO Nanorods, Microsc. Semicond. Mater. 2007. (2007) 237–240. doi:10.1007/978-1-4020-8615-1_52.

[186] A. Arora, S. Devi, V. Jaswal, J. Singh, M. Kinger, V. Gupta, Synthesis and characterization of ZnO nanoparticles, Orient. J. Chem. 30 (2014) 1671–1679. doi:10.13005/ojc/300427.

[187] H. Yan, R. He, J. Johnson, M. Law, R.J. Saykally, P. Yang, Dendritic nanowire ultraviolet laser array, J. Am. Chem. Soc. 125 (2003) 4728–4729. doi:10.1021/ja034327m.

[188] S. Niyogi, E. Bekyarova, M.E. Itkis, J.L. McWilliams, M.A. Hamon, R.C. Haddon, Solution properties of graphite and graphene, J. Am. Chem. Soc. 128 (2006) 7720–7721. doi:10.1021/ja060680r.

[189] F. Liu, M.H. Jang, H.D. Ha, J.H. Kim, Y.H. Cho, T.S. Seo, Facile synthetic method for pristine graphene quantum dots and graphene oxide quantum dots: Origin of blue and green luminescence, Adv. Mater. 25 (2013) 3657–3662. doi:10.1002/adma.201300233.

[190] J. Luo, L.J. Cote, V.C. Tung, A.T.L. Tan, P.E. Goins, J. Wu, J. Huang, Graphene oxide nanocolloids, J. Am. Chem. Soc. 132 (2010) 17667–17669. doi:10.1021/ja1078943.

[191] E. Messina, G. Compagnini, L. D'Urso, O. Puglisi, S. Bagiante, S. Scalese, Size distribution and particle shape in silver colloids prepared by laser ablation in water, Radiat. Eff. Defects Solids. 165 (2010) 579–583. doi:10.1080/10420151003723014.

[192] X. Li, H. Wang, Y. Shimizu, A. Pyatenko, K. Kawaguchi, N. Koshizaki, Preparation of carbon quantum dots with tunable photoluminescence by rapid laser passivation in ordinary organic solvents., Chem. Commun. (Camb). 47 (2011) 932–934. doi:10.1039/c0cc03552a.

[193] V. Nguyen, L. Yan, J. Si, X. Hou, Femtosecond laser-induced size reduction of carbon nanodots in solution: Effect of laser fluence, spot size, and irradiation time, J. Appl. Phys. 117 (2015). doi:10.1063/1.4909506.

[194] S. Hu, J. Liu, J. Yang, Y. Wang, S. Cao, Laser synthesis and size tailor of carbon quantum dots, J. Nanoparticle Res. 13 (2011) 7247–7252. doi:10.1007/s11051-011-0638-y.

[195] D. Tan, S. Zhou, J. Qiu, N. Khusro, Preparation of functional nanomaterials with

femtosecond laser ablation in solution, J. Photochem. Photobiol. C Photochem. Rev. 17 (2013) 50–68. doi:10.1016/j.jphotochemrev.2013.08.002.

[196] H. Yu, X. Li, X. Zeng, Y. Lu, Preparation of carbon dots by non-focusing pulsed laser irradiation in toluene, Chem. Commun. 52 (2016) 819–822. doi:10.1039/C5CC08384B.

[197] H.P.S. Castro, V.S. Souza, J.D. Scholten, J.H. Dias, J.A. Fernandes, F.S. Rodembusch, R. dos Reis, J. Dupont, S.R. Teixeira, R.R.B. Correia, Synthesis and Characterisation of Fluorescent Carbon Nanodots Produced in Ionic Liquids by Laser Ablation, Chem. - A Eur. J. 22 (2016) 138–143. doi:10.1002/chem.201503286.

[198] P. Russo, A. Hu, G. Compagnini, W.W. Duley, N.Y. Zhou, Femtosecond laser ablation of highly oriented pyrolytic graphite: a green route for large-scale production of porous graphene and graphene quantum dots., Nanoscale. 6 (2014) 2381–2389. doi:10.1039/c3nr05572h.

[199] T.N. Lin, K.H. Chih, C.T. Yuan, J.L. Shen, C. a. J. Lin, W.R. Liu, Laser-ablation production of graphene oxide nanostructures: from ribbons to quantum dots, Nanoscale. 7 (2015) 2708–2715. doi:10.1039/C4NR05737F.

[200] B.N. Chichkov, C. Momma, S. Nolte, F. von Alvensleben, a. Tünnermann, Femtosecond, picosecond and nanosecond laser ablation of solids, Appl. Phys. A Mater. Sci. Process. 63 (1996) 109–115. doi:10.1007/s003390050359.

[201] R. Pasricha, S. Gupta, A.K. Srivastava, A facile and novel synthesis of Ag-graphene-based nanocomposites., Small. 5 (2009) 2253–2259. doi:10.1002/smll.200900726.

[202] P. Russo, R. Liang, E. Jabari, E. Marzbanrad, E. Toyserkani, Y.N.N. Zhou, Single-step synthesis of graphene quantum dots by femtosecond laser ablation of graphene oxide dispersions, Nanoscale. 8 (2016) 8863–8877. doi:10.1039/C6NR01148A.

[203] J.H. Lienhard, A Heat Transfer Textbook, J. Heat Transfer. 82 (2010) 198. doi:10.1115/1.3246887.

[204] D. Ivanov, L. Zhigilei, Combined atomistic-continuum modeling of short-pulse laser melting and disintegration of metal films, Phys. Rev. B. 68 (2003) 1–22. doi:10.1103/PhysRevB.68.064114.

[205] L. Lin, S. Zhang, Creating high yield water soluble luminescent graphene quantum dots via exfoliating and disintegrating carbon nanotubes and graphite flakes, Chem. Commun. 48 (2012) 10177. doi:10.1039/c2cc35559k.

[206] X. Wu, H. Zhao, M. Zhong, H. Murakawa, M. Tsukamoto, The Formation of Molecular Junctions between Graphene Sheets, Mater. Trans. 54 (2013) 940–946. doi:10.2320/matertrans.MD201213.

[207] X. Ye, T. Huang, Z. Lin, M. Zhong, L. Li, Y. Yan, H. Zhu, Lap joining of graphene flakes by current-assisted CO2 laser irradiation, Carbon N. Y. 61 (2013) 329–335. doi:10.1016/j.carbon.2013.05.012.

[208] A. Kruusing, Underwater and water-assisted laser processing: Part 1 - General features, steam cleaning and shock processing, Opt. Lasers Eng. 41 (2004) 307–327.

doi:10.1016/S0143-8166(02)00142-2.

[209] C. Schaffer, N. Nishimura, E. Glezer, A. Kim, E. Mazur, Dynamics of femtosecond laser-induced breakdown in water from femtoseconds to microseconds., Opt. Express. 10 (2002) 196–203. doi:10.1364/OE.10.000196.

[210] J.G. Fujimoto, J.M. Liu, E.P. Ippen, N. Bloembergen, Femtosecond laser interaction with metallic tungsten and nonequilibrium electron and lattice temperatures, Phys. Rev. Lett. 53 (1984) 1837–1840. doi:10.1103/PhysRevLett.53.1837.

[211] C. Rullière, Femtosecond laser pulses, 2005. doi:10.1007/b137908.

[212] R. Fang, D. Zhang, H. Wei, Z. Li, F. Yang, Y. Gao, Improved two-temperature model and its application in femtosecond laser ablation of metal target, Laser Part. Beams. 28 (2010) 157. doi:10.1017/S0263034610000030.

[213] M.E. Povarnitsyn, T.E. Itina, K. V. Khishchenko, P.R. Levashov, Multi-material two-temperature model for simulation of ultra-short laser ablation, Appl. Surf. Sci. 253 (2007) 6343–6346. doi:10.1016/j.apsusc.2007.01.103.

[214] A.R. Holkundkar, G. Mishra, N.K. Gupta, Molecular dynamic simulation for laser-cluster interaction, Phys. Plasmas. 18 (2011) 53102. doi:10.1063/1.3581061.

[215] Holman J.P., Heat Transfer, (2010).

[216] S.L. Chin, S. Lagacé, Generation of H(2), O(2), and H(2)O(2) from water by the use of intense femtosecond laser pulses and the possibility of laser sterilization., Appl. Opt. 35 (1996) 907–911. doi:10.1364/AO.35.000907.

[217] J. Shen, Y. Zhu, X. Yang, J. Zong, J. Zhang, C. Li, One-pot hydrothermal synthesis of graphene quantum dots surface-passivated by polyethylene glycol and their photoelectric conversion under near-infrared light, New J. Chem. 36 (2012) 97. doi:10.1039/c1nj20658c.

[218] M. Baraket, S.G. Walton, Z. Wei, E.H. Lock, J.T. Robinson, P. Sheehan, Reduction of graphene oxide by electron beam generated plasmas produced in methane/argon mixtures, Carbon N. Y. 48 (2010) 3382–3390. doi:10.1016/j.carbon.2010.05.031.

[219] J.I. Paredes, S. Villar-Rodil, P. Solís-Fernández, a. Martínez-Alonso, J.M.D. Tascón, Atomic force and scanning tunneling microscopy imaging of graphene nanosheets derived from graphite oxide, Langmuir. 25 (2009) 5957–5968. doi:10.1021/la804216z.

[220] S. Stankovich, D. a. Dikin, R.D. Piner, K. a. Kohlhaas, A. Kleinhammes, Y. Jia, Y. Wu, S.T. Nguyen, R.S. Ruoff, Synthesis of graphene-based nanosheets via chemical reduction of exfoliated graphite oxide, Carbon N. Y. 45 (2007) 1558–1565. doi:10.1016/j.carbon.2007.02.034.

[221] M.M. Lucchese, F. Stavale, E.H.M. Ferreira, C. Vilani, M.V.O. Moutinho, R.B. Capaz, C. a. Achete, a. Jorio, Quantifying ion-induced defects and Raman relaxation length in graphene, Carbon N. Y. 48 (2010) 1592–1597. doi:10.1016/j.carbon.2009.12.057.

[222] L.G. Cançado, a. Jorio, E.H.M. Ferreira, F. Stavale, C. a. Achete, R.B. Capaz, M.V.O.

Moutinho, a. Lombardo, T.S. Kulmala, a. C. Ferrari, Quantifying defects in graphene via Raman spectroscopy at different excitation energies, Nano Lett. 11 (2011) 3190–3196. doi:10.1021/nl201432g.

[223] S. Kim, D. Hee Shin, C. Oh Kim, S. Seok Kang, S. Sin Joo, S.-H. Choi, S. Won Hwang, C. Sone, Size-dependence of Raman scattering from graphene quantum dots: Interplay between shape and thickness, Appl. Phys. Lett. 102 (2013) 53108. doi:10.1063/1.4790641.

[224] S. Kim, D. Hee Shin, C. Oh Kim, S. Seok Kang, S. Sin Joo, S.H. Choi, S. Won Hwang, C. Sone, Size-dependence of Raman scattering from graphene quantum dots: Interplay between shape and thickness, Appl. Phys. Lett. 102 (2013). doi:10.1063/1.4790641.

[225] S. Zhu, Y. Song, X. Zhao, J. Shao, J. Zhang, B. Yang, The photoluminescence mechanism in carbon dots (graphene quantum dots, carbon nanodots, and polymer dots): current state and future perspective, Nano Res. 8 (2015) 355–381. doi:10.1007/s12274-014-0644-3.

[226] S.H. Jin, D.H. Kim, G.H. Jun, S.H. Hong, S. Jeon, Tuning the Photoluminescence of Graphene Quantum Dots through the Charge Transfer Effect of Functional Groups, ACS Nano. 7 (2013) 1239–1245. doi:Doi 10.1021/Nn3046759.

[227] S. Zhu, J. Zhang, S. Tang, C. Qiao, L. Wang, H. Wang, X. Liu, B. Li, Y. Li, W. Yu, X. Wang, H. Sun, B. Yang, Surface chemistry routes to modulate the photoluminescence of graphene quantum dots: From fluorescence mechanism to up-conversion bioimaging applications, Adv. Funct. Mater. 22 (2012) 4732–4740. doi:10.1002/adfm.201201499.

[228] N. Fuyuno, D. Kozawa, Y. Miyauchi, S. Mouri, R. Kitaura, H. Shinohara, T. Yasuda, N. Komatsu, K. Matsuda, Size-Dependent Luminescence Properties of Chromatographically-Separated Graphene Quantum Dots, arXiv. (2013).

[229] K. Habiba, V.I. Makarov, J. Avalos, M.J.F. Guinel, B.R. Weiner, G. Morell, Luminescent graphene quantum dots fabricated by pulsed laser synthesis, Carbon N. Y. 64 (2013) 341–350. doi:10.1016/j.carbon.2013.07.084.

[230] C.T. Chien, S.S. Li, W.J. Lai, Y.C. Yeh, H.A. Chen, I.S. Chen, L.C. Chen, K.H. Chen, T. Nemoto, S. Isoda, M. Chen, T. Fujita, G. Eda, H. Yamaguchi, M. Chhowalla, C.W. Chen, Tunable photoluminescence from graphene oxide, Angew. Chemie - Int. Ed. 51 (2012) 6662–6666. doi:10.1002/anie.201200474.

[231] H. Sun, L. Wu, W. Wei, X. Qu, Recent advances in graphene quantum dots for sensing, Mater. Today. 16 (2013) 433–442. doi:10.1016/j.mattod.2013.10.020.

[232] J. Gu, M.J. Hu, Q.Q. Guo, Z.F. Ding, X.L. Sun, J. Yang, High-yield synthesis of graphene quantum dots with strong green photoluminescence, RSC Adv. 4 (2014) 50141–50144. doi:10.1039/C4RA10011E.

[233] J. Sun, S. Yang, Z. Wang, H. Shen, T. Xu, L. Sun, H. Li, W. Chen, X. Jiang, G. Ding, Z. Kang, X. Xie, M. Jiang, Ultra-High Quantum Yield of Graphene Quantum Dots: Aromatic-Nitrogen Doping and Photoluminescence Mechanism, Part. Part. Syst. Charact. 32 (2015) 434–440. doi:10.1002/ppsc.201400189.

[234] M.L. Mueller, X. Yan, J. a. McGuire, L.S. Li, Triplet states and electronic relaxation in photoexcited graphene quantum dots, Nano Lett. 10 (2010) 2679–2682.

doi:10.1021/nl101474d.

[235] E. Jabari, S. Tong, A. Azhari, E. Toyserkani, Non-planar interconnects in double-sided flexible Cu-PET substrates using a laser-assisted maskless microdeposition process: 3D finite element modeling and experimental analysis, Opt. Lasers Eng. 54 (2014) 117–127. doi:10.1016/j.optlaseng.2013.10.002.

[236] E. Jabari, E. Toyserkani, Micro-scale Aerosol-jet Printing of Graphene Interconnects, Carbon N. Y. 91 (2015) 321–329. doi:10.1016/j.carbon.2015.04.094.

[237] Elahe Jabari; Ehsan Toyserkani, Aerosol-Jet Printing of Highly Flexible and Conductive Graphene/Silver Patterns, Mater. Lett. (n.d.).

[238] E. Jabari, Additive Manufacturing of Graphene-based Patterns, Ph.D. Diss. Dept. Mech. Mechatronics Eng., Univ. Waterloo, Waterloo, Canada, 2016. (2016).

[239] C.N. Huang, J.S. Bow, Y. Zheng, S.Y. Chen, N.J. Ho, P. Shen, Nonstoichiometric titanium oxides via pulsed laser ablation in water, Nanoscale Res. Lett. 5 (2010) 972–985. doi:10.1007/s11671-010-9591-4.

[240] P. Liu, W. Cai, M. Fang, Z. Li, H. Zeng, J. Hu, X. Luo, W. Jing, Room temperature synthesized rutile TiO2 nanoparticles induced by laser ablation in liquid and their photocatalytic activity., Nanotechnology. 20 (2009) 285707. doi:10.1088/0957-4484/20/28/285707.

[241] H.L. Ma, J.Y. Yang, Y. Dai, Y.B. Zhang, B. Lu, G.H. Ma, Raman study of phase transformation of TiO2 rutile single crystal irradiated by infrared femtosecond laser, Appl. Surf. Sci. 253 (2007) 7497–7500. doi:10.1016/j.apsusc.2007.03.047.

[242] F. Barreca, N. Acacia, E. Barletta, D. Spadaro, G. Currò, F. Neri, Small size TiO2 nanoparticles prepared by laser ablation in water, Appl. Surf. Sci. 256 (2010) 6408–6412. doi:10.1016/j.apsusc.2010.04.026.

[243] Y. Cui, J. Sun, Z. Hu, W. Yu, N. Xu, N. Xu, Z. Ying, J. Wu, Synthesis, phase transition and optical properties of nanocrystalline titanium dioxide films deposited by plasma assisted reactive pulsed laser deposition, Surf. Coatings Technol. 231 (2013) 180–184. doi:10.1016/j.surfcoat.2012.05.062.

[244] A. Białous, M. Gazda, K. Grochowska, P. Atanasov, A. Dikovska, N. Nedyalkov, J. Reszczyńska, A. Zaleska-Medynska, G.Ƚiwiński, Nanoporous TiO2 electrode grown by laser ablation of titanium in air at atmospheric pressure and room temperature, Thin Solid Films. 601 (2016) 41–44. doi:10.1016/j.tsf.2015.10.069.

[245] H. Ma, G. Guo, J. Yang, Y. Guo, N. Ma, Femtosecond laser irradiation-induced phase transformation on titanium dioxide crystal surface, Nucl. Instruments Methods Phys. Res. Sect. B Beam Interact. with Mater. Atoms. 264 (2007) 61–65. doi:10.1016/j.nimb.2007.08.006.

[246] M. Boutinguiza, M. Meixus, J. del Val, A. Riveiro, R. Comesaña, F. Lusquiños, J. Pou, Synthesis and Characterization of Pd Nanoparticles by Laser Ablation in Water Using Nanosecond Laser, Phys. Procedia. 83 (2016) 36–45. doi:10.1016/j.phpro.2016.08.005.

[247] A. Hahn, Influences on Nanoparticle Production during Pulsed Laser Ablation, J. Laser Micro/Nanoengineering. 3 (2008) 73–77. doi:10.2961/jlmn.2008.02.0003.

[248] M.H. Tsai, S.Y. Chen, P. Shen, Laser ablation condensation of TiO 2 particles: Effects of laser energy, oxygen flow rate and phase transformation, J. Aerosol Sci. 36 (2005) 13–25. doi:10.1016/j.jaerosci.2004.08.007.

[249] M. Boutinguiza, B. Rodriguez-Gonzalez, J. Del Val, R. Comesaña, F. Lusquiños, J. Pou, Production of TiO 2 crystalline nanoparticles by laser ablation in ethanol, Appl. Surf. Sci. 258 (2012) 9484–9486. doi:10.1016/j.apsusc.2012.05.148.

[250] A. Fujishima, T.N. Rao, D. a. Tryk, Titanium dioxide photocatalysis, J. Photochem. Photobiol. C Photochem. Rev. 1 (2000) 1–21. doi:10.1016/S1389-5567(00)00002-2.

[251] B. Sha, W. Gao, X. Cui, L. Wang, F. Xu, The potential health challenges of TiO 2 nanomaterials, J. Appl. Toxicol. 35 (2015) 1086–1101. doi:10.1002/jat.3193.

[252] C. Gao, Q. Meng, K. Zhao, H. Yin, D. Wang, J. Guo, S. Zhao, L. Chang, M. He, Q. Li, H. Zhao, X. Huang, Y. Gao, Z. Tang, Co3O4 Hexagonal Platelets with Controllable Facets Enabling Highly Efficient Visible-Light Photocatalytic Reduction of CO2, Adv. Mater. (2016) 6485–6490. doi:10.1002/adma.201601387.

[253] J. Qi, K. Zhao, G. Li, Y. Gao, H. Zhao, R. Yu, Z. Tang, Multi-shelled CeO_2 hollow microspheres as superior photocatalysts for water oxidation., Nanoscale. 6 (2014) 4072–7. doi:10.1039/c3nr06822f.

[254] K. Zhao, J. Qi, H. Yin, Z. Wang, S. Zhao, X. Ma, J. Wan, L. Chang, Y. Gao, R. Yu, Z. Tang, Efficient water oxidation under visible light by tuning surface defects on ceria nanorods, J. Mater. Chem. A. 3 (2015) 20465–20470. doi:10.1039/C5TA05817A.

[255] S. Filice, G. Compagnini, R. Fiorenza, S. Scirè, L. D'Urso, M.E. Fragalà, P. Russo, E. Fazio, S. Scalese, Laser processing of TiO<inf>2</inf> colloids for an enhanced photocatalytic water splitting activity, J. Colloid Interface Sci. 489 (2017) 131–137. doi:10.1016/j.jcis.2016.08.013.

[256] M. Grätzel, Photoelectrochemical cells, Nature. 414 (2001) 338–344. doi:10.1038/35104607.

[257] Y. Alivov, H. Funke, P. Nagpal, Air-gating and chemical-gating in transistors and sensing devices made from hollow TiO $_2$ semiconductor nanotubes, Nanotechnology. 26 (2015) 295203. doi:10.1088/0957-4484/26/29/295203.

[258] J. van de Lagemaat, N.-G. Park, a J. Frank, Influence of Electrical Potential Distribution, Charge Transport, and Recombination on the Photopotential and Photocurrent Conversion Efficiency of Dye-Sensitized Nanocrystalline TiO 2 Solar Cells: A Study by Electrical Impedance and Optical Modulation Te, J. Phys. Chem. B. 104 (2000) 2044–2052. doi:10.1021/jp993172v.

[259] V.N. Koparde, P.T. Cummings, Molecular dynamics simulation of titanium dioxide nanoparticle sintering, J. Phys. Chem. B. 109 (2005) 24280–24287. doi:10.1021/jp054667p.

[260] V.N. Koparde, P.T. Cummings, Phase transformations during sintering of titania nanoparticles, ACS Nano. 2 (2008) 1620–1624. doi:10.1021/nn800092m.

[261] D. a H. Hanaor, C.C. Sorrell, Review of the anatase to rutile phase transformation, J. Mater. Sci. 46 (2011) 855–874. doi:10.1007/s10853-010-5113-0.

[262] S.M. Gupta, M. Tripathi, A review of TiO2 nanoparticles, Chinese Sci. Bull. 56 (2011) 1639–1657. doi:10.1007/s11434-011-4476-1.

[263] N.H. Vu, H. V Le, T.M. Cao, V. V Pham, H.M. Le, D. Nguyen-Manh, Anatase–rutile phase transformation of titanium dioxide bulk material: a DFT + U approach, J. Phys. Condens. Matter. 24 (2012) 405501. doi:10.1088/0953-8984/24/40/405501.

[264] G.C. Vásquez, M.A. Peche-Herrero, D. Maestre, A. Gianoncelli, J. Ramírez-Castellanos, A. Cremades, J.M. González-Calbet, J. Piqueras, Laser-Induced Anatase-to-Rutile Transition in TiO_2 Nanoparticles: Promotion and Inhibition Effects by Fe and Al Doping and Achievement of Micropatterning, J. Phys. Chem. C. 119 (2015) 11965–11974. doi:10.1021/acs.jpcc.5b01736.

[265] S.-C. Zhu, S.-H. Xie, Z.-P. Liu, Nature of Rutile Nuclei in Anatase-to-Rutile Phase Transition, J. Am. Chem. Soc. 137 (2015) 11532–11539. doi:10.1021/jacs.5b07734.

[266] R.D. Shannon, Phase transformation studies in TiO2 supporting different defect mechanisms in vacuum-reduced and hydrogen-reduced rutile, J. Appl. Phys. 35 (1964) 3414–3416. doi:10.1063/1.1713231.

[267] M.S.P. Francisco, V.R. Mastelaro, Inhibition of the Anatase−Rutile Phase Transformation with Addition of CeO 2 to CuO−TiO 2 System: Raman Spectroscopy, X-ray Diffraction, and Textural Studies, Chem. Mater. 14 (2002) 2514–2518. doi:10.1021/cm011520b.

[268] V. Körstgens, S. Pröller, T. Buchmann, D. Moseguí González, L. Song, Y. Yao, W. Wang, J. Werhahn, G. Santoro, S. V. Roth, H. Iglev, R. Kienberger, P. Müller-Buschbaum, Laser-ablated titania nanoparticles for aqueous processed hybrid solar cells, Nanoscale. 7 (2015) 2900–2904. doi:10.1039/C4NR06782G.

[269] M. a. Pugachevskii, Ultraviolet absorption spectrum of laser-ablated titanium dioxide nanoparticles, Tech. Phys. Lett. 39 (2013) 36–38. doi:10.1134/S1063785013010239.

[270] J. Qian, P. Liu, Y. Xiao, Y. Jiang, Y. Cao, X. Ai, H. Yang, TiO2-coated multilayered SnO2 hollow microspheres for dye-sensitized solar cells, Adv. Mater. 21 (2009) 3663–3667. doi:10.1002/adma.200900525.

[271] J. Du, J. Qi, D. Wang, Z. Tang, Facile synthesis of Au@TiO2 core–shell hollow spheres for dye-sensitized solar cells with remarkably improved efficiency, Energy Environ. Sci. 5 (2012) 6914. doi:10.1039/c2ee21264a.

[272] R. Liang, M. Hatat-Fraile, M. Arlos, M. Servos, Y.N. Zhou, TiO<inf>2</inf> nanowires membranes for the use in photocatalytic filtration processes, in: 14th IEEE Int. Conf. Nanotechnol., IEEE, 2014: pp. 975–980. doi:10.1109/NANO.2014.6968144.

[273] S.I. Alnassar, E. Akman, B.G. Oztoprak, E. Kacar, O. Gundogdu, a. Khaleel, a. Demir, Study of the fragmentation phenomena of TiO2 nanoparticles produced by femtosecond

laser ablation in aqueous media, Opt. Laser Technol. 51 (2013) 17–23. doi:10.1016/j.optlastec.2013.02.013.

[274] A. Nath, S.S. Laha, A. Khare, Synthesis of TiO 2 Nanoparticles Via Laser Ablation at Titanium-Water Interface, Integr. Ferroelectr. 121 (2010) 58–64. doi:10.1080/10584587.2010.492020.

[275] F. Tian, J. Sun, J. Yang, P. Wu, H.L. Wang, X.W. Du, Preparation and photocatalytic properties of mixed-phase titania nanospheres by laser ablation, Mater. Lett. 63 (2009) 2384–2386. doi:10.1016/j.matlet.2009.08.018.

[276] J. Zhang, M. Li, Z. Feng, J. Chen, C. Li, UV Raman spectroscopic study on TiO2. I. Phase transformation at the surface and in the bulk., J. Phys. Chem. B. 110 (2006) 927–935. doi:10.1021/jp0552473.

[277] F. Hardcastle, Raman Spectroscopy of Titania (TiO2) Nanotubular Water-Splitting Catalysts, J. Ark. Acad. Sci. 65 (2011) 43–48.

[278] F.D. Hardcastle, Raman Spectroscopy of Titania (TiO 2) Nanotubular Water-Splitting Catalysts, 65 (2011) 43–48.

[279] P. V Kamat, M. Flumiani, G. V Hartland, Picosecond Dynamics of Silver Nanoclusters. Photoejection of Electrons and Fragmentation, J. Phys. Chem. B. 102 (1998) 3123–3128. doi:10.1021/jp980009b.

[280] A. Takami, H. Kurita, S. Koda, Laser-Induced Size Reduction of Noble Metal Particles, J. Phys. Chem. B. 103 (1999) 1226–1232. doi:10.1021/jp983503o.

[281] A. Pyatenko, M. Yamaguchi, M. Suzuki, Synthesis of spherical silver nanoparticles with controllable sizes in aqueous solutions, J. Phys. Chem. C. 111 (2007) 7910–7917. doi:10.1021/jp071080x.

[282] R. a. Spurr, H. Myers, Quantitative Analysis of Anatase-Rutile Mixtures with an X-Ray Diffractometer, Anal. Chem. 29 (1957) 760–762. doi:10.1021/ac60125a006.

[283] N. Serpone, D. Lawless, R. Khairutdinov, Size Effects on the Photophysical Properties of Colloidal Anatase TiO2 Particles: Size Quantization versus Direct Transitions in This Indirect Semiconductor?, J. Phys. Chem. 99 (1995) 16646–16654. doi:10.1021/j100045a026.

[284] G. Lassaletta, A. Fernandez, J.P. Espinos, A.R. Gonzalez-Elipe, Spectroscopic characterization of quantum-sized TiO2 supported on silica: influence of size and TiO2-SiO2 interface composition, J. Phys. Chem. 99 (1995) 1484–1490. doi:10.1021/j100005a019.

[285] J. Robertson, Band offsets of wide-band-gap oxides and implications for future electronic devices, J. Vac. Sci. Technol. B Microelectron. Nanom. Struct. 18 (2000) 1785. doi:10.1116/1.591472.

[286] V. Bessergenev, H.L. Gomes, Electrical properties of thin-films wide-band gap semiconductor TiO 2 prepared by CVD, Phys. Status Solidi Curr. Top. Solid State Phys. 7 (2010) 949–952. doi:10.1002/pssc.200982713.

[287] D. Eder, I. a Kinloch, A.H. Windle, Pure rutile nanotubes., Chem. Commun. (Camb). 30 (2006) 1448–1450. doi:10.1039/b517260h.

[288] X. Zhang, L. Chen, H. Pan, Z. Bao, X. Zhou, Light-trapping photoanode using high refractive index rutile TiO2 microspheres as sandwiched layer, Thin Solid Films. 573 (2014) 107–111. doi:10.1016/j.tsf.2014.10.099.

[289] H. Zhang, X. Liu, Y. Li, Q. Sun, Y. Wang, B.J. Wood, P. Liu, D. Yang, H. Zhao, Vertically aligned nanorod-like rutileTiO2 single crystal nanowire bundles with superior electron transport and photoelectrocatalytic properties, J. Mater. Chem. 22 (2012) 2465–2472. doi:10.1039/C2JM15546J.

[290] P. Mazumder, S.M. Kang, R. Waser, Memristors: Devices, models, and applications [scanning the issue], Proc. IEEE. 100 (2012) 1911–1919. doi:10.1109/JPROC.2012.2190812.

[291] L.O. Chua, Memristor—The Missing Circuit Element, IEEE Trans. Circuit Theory. 18 (1971) 507–519. doi:10.1109/TCT.1971.1083337.

[292] I. Valov, R. Waser, J.R. Jameson, M.N. Kozicki, Electrochemical metallization memories--fundamentals, applications, prospects., Nanotechnology. 22 (2011) 254003. doi:10.1088/0957-4484/22/28/289502.

[293] F. Pan, C. Chen, Z. Wang, Y. Yang, J. Yang, F. Zeng, Nonvolatile resistive switching memories-characteristics, mechanisms and challenges, Prog. Nat. Sci. Mater. Int. 20 (2010) 1–15. doi:10.1016/S1002-0071(12)60001-X.

[294] B.P. Mazumder, F. Ieee, Memristors : Devices , Models , and Applications, 100 (2012) 1911–1919.

[295] Y. Li, S. Long, Q. Liu, H. Lü, S. Liu, M. Liu, An overview of resistive random access memory devices, Chinese Sci. Bull. 56 (2011) 3072–3078. doi:10.1007/s11434-011-4671-0.

[296] E. Gale, TiO2-based memristors and ReRAM: materials, mechanisms and models (a review), Semicond. Sci. Technol. 29 (2014) 104004. doi:10.1088/0268-1242/29/10/104004.

[297] C.-H.H. Huang, J.-S.S. Huang, S.-M.M. Lin, W.-Y.Y. Chang, J.-H.H. He, Y.-L.L. Chueh, ZnO 1- x nanorod arrays/ZnO thin film bilayer structure: From homojunction diode and high-performance memristor to complementary 1D1R application, ACS Nano. 6 (2012) 8407–8414. doi:10.1021/nn303233r.

[298] D.S. Jeong, R. Thomas, R.S. Katiyar, J.F. Scott, H. Kohlstedt, a Petraru, C.S. Hwang, Emerging memories: resistive switching mechanisms and current status, Reports Prog. Phys. 75 (2012) 76502. doi:10.1088/0034-4885/75/7/076502.

[299] L. Lin, L. Liu, K. Musselman, G. Zou, W.W. Duley, Y.N. Zhou, Plasmonic-Radiation-Enhanced Metal Oxide Nanowire Heterojunctions for Controllable Multilevel Memory, Adv. Funct. Mater. 26 (2016) 5979–5986. doi:10.1002/adfm.201601143.

[300] Z.J. Liu, J.Y. Gan, T.R. Yew, ZnO-based one diode-one resistor device structure for

crossbar memory applications, Appl. Phys. Lett. 100 (2012) 153503. doi:10.1063/1.3701722.

[301] R. Mundle, C. Carvajal, A.K. Pradhan, ZnO/Al:ZnO Transparent Resistive Switching Devices Grown by Atomic Layer Deposition for Memristor Applications, Langmuir. 32 (2016) 4983–4995. doi:10.1021/acs.langmuir.6b01014.

[302] S. Nau, C. Wolf, K. Popovic, A. Blümel, F. Santoni, A. Gagliardi, A. di Carlo, S. Sax, E.J.W. List-Kratochvil, Inkjet-Printed Resistive Switching Memory Based on Organic Dielectric Materials: From Single Elements to Array Technology, Adv. Electron. Mater. 1 (2015) 1400003. doi:10.1002/aelm.201400003.

[303] K. Oka, T. Yanagida, K. Nagashima, M. Kanai, T. Kawai, J.S. Kim, B.H. Park, Spatial nonuniformity in resistive-switching memory effects of nio, J. Am. Chem. Soc. 133 (2011) 12482–12485. doi:10.1021/ja206063m.

[304] K. Oka, T. Yanagida, K. Nagashima, T. Kawai, J.S. Kim, B.H. Park, Resistive-switching memory effects of NiO nanowire/metal junctions, J. Am. Chem. Soc. 132 (2010) 6634–6635. doi:10.1021/ja101742f.

[305] S. Porro, A. Jasmin, K. Bejtka, D. Conti, D. Perrone, S. Guastella, C.F. Pirri, A. Chiolerio, C. Ricciardi, Low-temperature atomic layer deposition of TiO 2 thin layers for the processing of memristive devices, J. Vac. Sci. Technol. A Vacuum, Surfaces, Film. 34 (2016) 01A147. doi:10.1116/1.4938465.

[306] J.P. Strachan, J.J. Yang, L.A. Montoro, C.A. Ospina, A.J. Ramirez, A.L.D. Kilcoyne, G. Medeiros-Ribeiro, R.S. Williams, Characterization of electroforming-free titanium dioxide memristors, Beilstein J. Nanotechnol. 4 (2013) 467–473. doi:10.3762/bjnano.4.55.

[307] H. Wang, B. Zhu, X. Ma, Y. Hao, X. Chen, Physically Transient Resistive Switching Memory Based on Silk Protein, Small. 12 (2016) 2715–2719. doi:10.1002/smll.201502906.

[308] E.J. Yoo, M. Lyu, J. Yun, C.J. Kang, Y.J. Choi, L. Wang, Resistive Switching Behavior in Organic–Inorganic Hybrid CH3NH3PbI3−xClx Perovskite for Resistive Random Access Memory Devices, Adv. Mater. 27 (2015) 6170–6175. doi:10.1002/adma.201502889.

[309] H.Y. Jeong, J.Y. Kim, J.W. Kim, J.O. Hwang, J.-E. Kim, J.Y. Lee, T.H. Yoon, B.J. Cho, S.O. Kim, R.S. Ruoff, S.-Y. Choi, Graphene Oxide Thin Films for Flexible Nonvolatile Memory Applications, Nano Lett. 10 (2010) 4381–4386. doi:10.1021/nl101902k.

[310] G. Khurana, P. Misra, R.S. Katiyar, Forming free resistive switching in graphene oxide thin film for thermally stable nonvolatile memory applications, J. Appl. Phys. 114 (2013) 124508. doi:10.1063/1.4823734.

[311] H. Seo, S. Ahn, J. Kim, Y.-A. Lee, K.-H. Chung, K.-J. Jeon, Multi-resistive Reduced Graphene Oxide Diode with Reversible Surface Electrochemical Reaction induced Carrier Control, Sci. Rep. 4 (2015) 5642. doi:10.1038/srep05642.

[312] S.K. Pradhan, B. Xiao, S. Mishra, A. Killam, A.K. Pradhan, Resistive switching behavior of reduced graphene oxide memory cells for low power nonvolatile device application, Sci. Rep. 6 (2016) 26763. doi:10.1038/srep26763.

[313] O.A. Ageev, Y.F. Blinov, O.I. Il'in, A.S. Kolomiitsev, B.G. Konoplev, M. V. Rubashkina, V.A. Smirnov, A.A. Fedotov, Memristor effect on bundles of vertically aligned carbon nanotubes tested by scanning tunnel microscopy, Tech. Phys. 58 (2013) 1831–1836. doi:10.1134/S1063784213120025.

[314] O.A. Ageev, Y.F. Blinov, O.I. Il'in, B.G. Konoplev, M. V. Rubashkina, V.A. Smirnov, A.A. Fedotov, Study of the resistive switching of vertically aligned carbon nanotubes by scanning tunneling microscopy, Phys. Solid State. 57 (2015) 825–831. doi:10.1134/S1063783415040034.

[315] P. Avouris, Z. Chen, V. Perebeinos, Carbon-based electronics, Nat. Nanotechnol. 2 (2007) 605–615. doi:10.1038/nnano.2007.300.

[316] Y. Chen, B. Zhang, G. Liu, X. Zhuang, E.T. Kang, Graphene and its derivatives: switching ON and OFF, Chem Soc Rev. 41 (2012) 4688–4707. doi:10.1039/c2cs35043b.

[317] C.A. Santini, A. Sebastian, C. Marchiori, V.P. Jonnalagadda, L. Dellmann, W.W. Koelmans, M.D. Rossell, C.P. Rossel, E. Eleftheriou, Oxygenated amorphous carbon for resistive memory applications, Nat. Commun. 6 (2015) 8600. doi:10.1038/ncomms9600.

[318] M.-D. Yi, J.-L. Guo, B. Hu, X.-H. Xia, Q.-L. Fan, L.-H. Xie, W. Huang, Memory Behaviors Based on ITO/Graphene Oxide/Al Structure, Chinese Phys. Lett. 32 (2015) 77201. doi:10.1088/0256-307X/32/7/077201.

[319] E.G. Gerstner, D.R. McKenzie, Cycling effects in nitrogen doped tetrahedral amorphous carbon non-volatile memory cells, Solid. State. Electron. 44 (2000) 1641–1645. doi:10.1016/S0038-1101(00)00092-7.

[320] F. Zhuge, R.-W. Li, C. He, Z. Liu, X. Zhou, Non-volatile resistive switching in graphene oxide thin films, Phys. Appl. Graphene - Exp. 2 (2011) 421–438. doi:10.5772/15201.

[321] C. Tsai, F. Xiong, E. Pop, M. Shim, M. Science, F. Seitz, C. Engineering, U. States, Resistive Random Access Memory Enabled by Carbon Nanotube, ACS Nano. 7 (2013) 5360–5366.

[322] L. Li, D. Wen, Memory behavior of multi-bit resistive switching based on multiwalled carbon nanotubes, Org. Electron. 34 (2016) 12–17. doi:10.1016/j.orgel.2016.03.041.

[323] C.E. Cava, C. Persson, A.J.G. Zarbin, L.S. Roman, Resistive Switching in Iron-oxide-filled Carbon Nanotubes, Nanoscale. 6 (2014) 378–384. doi:10.1039/c3nr04320g.

[324] Y. Chai, Y. Wu, K. Takei, H.Y. Chen, S. Yu, P.C.H. Chan, A. Javey, H.S.P. Wong, Resistive switching of carbon-based RRAM with CNT electrodes for ultra-dense memory, Tech. Dig. - Int. Electron Devices Meet. IEDM. (2010) 2–5. doi:10.1109/IEDM.2010.5703328.

[325] S.K. Kim, J.Y. Kim, B.C. Jang, M.S. Cho, S.Y. Choi, J.Y. Lee, H.Y. Jeong, Conductive Graphitic Channel in Graphene Oxide-Based Memristive Devices, Adv. Funct. Mater. 26 (2016) 7406–7414. doi:10.1002/adfm.201602748.

[326] S.K. Kim, J.Y. Kim, S.Y. Choi, J.Y. Lee, H.Y. Jeong, Direct Observation of Conducting Nanofilaments in Graphene-Oxide-Resistive Switching Memory, Adv. Funct. Mater. 25

(2015) 6710–6715. doi:10.1002/adfm.201502734.

[327] G. Khurana, P. Misra, N. Kumar, S. Kooriyattil, J.F. Scott, R.S. Katiyar, Enhanced resistive switching in forming-free graphene oxide films embedded with gold nanoparticles deposited by electrophoresis, Nanotechnology. 27 (2016) 15702. doi:10.1088/0957-4484/27/1/015702.

[328] R. Waser, M. Aono, Nanoionics-based resistive switching memories., Nat. Mater. 6 (2007) 833–40. doi:10.1038/nmat2023.

[329] R. Waser, R. Dittmann, C. Staikov, K. Szot, Redox-based resistive switching memories nanoionic mechanisms, prospects, and challenges, Adv. Mater. 21 (2009) 2632–2663. doi:10.1002/adma.200900375.

[330] Z. Wang, V. Tjoa, L. Wu, W.J. Liu, Z. Fang, X. a. Tran, J. Wei, W.G. Zhu, H.Y. Yu, Mechanism of Different Switching Directions in Graphene Oxide Based RRAM, J. Electrochem. Soc. 159 (2012) K177. doi:10.1149/2.068206jes.

[331] F. Zhuge, B. Hu, C. He, X. Zhou, Z. Liu, R.W. Li, Mechanism of nonvolatile resistive switching in graphene oxide thin films, Carbon N. Y. 49 (2011) 3796–3802. doi:10.1016/j.carbon.2011.04.071.

[332] S. Ki Hong, J. Eun Kim, S.O. Kim, B. Jin Cho, Analysis on switching mechanism of graphene oxide resistive memory device, J. Appl. Phys. 110 (2011). doi:10.1063/1.3624947.

[333] L.H. Wang, W. Yang, Q.Q. Sun, P. Zhou, H.L. Lu, S.J. Ding, D. Wei Zhang, The mechanism of the asymmetric SET and RESET speed of graphene oxide based flexible resistive switching memories, Appl. Phys. Lett. 100 (2012) 1–5. doi:10.1063/1.3681366.

[334] E. Lim, R. Ismail, Conduction Mechanism of Valence Change Resistive Switching Memory: A Survey, Electronics. 4 (2015) 586–613. doi:10.3390/electronics4030586.

[335] F.C. Chiu, A review on conduction mechanisms in dielectric films, Adv. Mater. Sci. Eng. 2014 (2014) 1–18. doi:10.1155/2014/578168.

[336] Y. Wu, B. Yang, B. Zong, H. Sun, Z. Shen, Y. Feng, Carbon nanowalls and related materials, J. Mater. Chem. 14 (2004) 469. doi:10.1039/b311682d.

[337] B. Yang, Y. Wu, B. Zong, Z. Shen, Electrochemical synthesis and characterization of magnetic nanoparticles on carbon nanowall templates, Nano Lett. 2 (2002) 751–754. doi:10.1021/nl025572r.

[338] H.F. Yen, Y.Y. Horng, M.S. Hu, W.H. Yang, J.R. Wen, A. Ganguly, Y. Tai, K.H. Chen, L.C. Chen, Vertically aligned epitaxial graphene nanowalls with dominated nitrogen doping for superior supercapacitors, Carbon N. Y. 82 (2015) 124–134. doi:10.1016/j.carbon.2014.10.042.

[339] V.A. Krivchenko, D.M. Itkis, S.A. Evlashin, D.A. Semenenko, E.A. Goodilin, A.T. Rakhimov, A.S. Stepanov, N. V. Suetin, A.A. Pilevsky, P. V. Voronin, Carbon nanowalls decorated with silicon for lithium-ion batteries, Carbon N. Y. 50 (2012) 1438–1442. doi:10.1016/j.carbon.2011.10.042.

[340] Z. Bo, S. Mao, Z. Jun Han, K. Cen, J. Chen, K. (Ken) Ostrikov, Emerging energy and environmental applications of vertically-oriented graphenes, Chem. Soc. Rev. 2015 (2015) 97–108. doi:10.1039/C4CS00352G.

[341] F. Yuan, Y.-R. Ye, J.-C. Wang, Z. Zhang, L. Pan, J. Xu, C.-S. Lai, Retention behavior of graphene oxide resistive switching memory on flexible substrate, in: 2013 IEEE 5th Int. Nanoelectron. Conf., IEEE, 2013: pp. 288–290. doi:10.1109/INEC.2013.6466025.

[342] A. Younis, D. Chu, A.H. Shah, H. Du, S. Li, Interfacial Redox Reactions Associated Ionic Transport in Oxide-Based Memories, ACS Appl. Mater. Interfaces. 9 (2017) 1585–1592. doi:10.1021/acsami.6b13416.

[343] I. Valov, W.D. Lu, Nanoscale electrochemistry using dielectric thin films as solid electrolytes, Nanoscale. 8 (2016) 13828–13837. doi:10.1039/C6NR01383J.

[344] M. Lübben, P. Karakolis, V. Ioannou-Sougleridis, P. Normand, P. Dimitrakis, I. Valov, Graphene-Modified Interface Controls Transition from VCM to ECM Switching Modes in Ta/TaO x Based Memristive Devices, Adv. Mater. 27 (2015) 6202–6207. doi:10.1002/adma.201502574.

[345] N.S. Komarova, A.G. Krivenko, E. V. Stenina, L.N. Sviridova, K. V. Mironovich, Y.M. Shulga, V.A. Krivchenko, Enhancement of the Carbon Nanowall Film Capacitance. Electron Transfer Kinetics on Functionalized Surfaces, Langmuir. 31 (2015) 7129–7137. doi:10.1021/acs.langmuir.5b00391.

[346] A. Achour, S. Vizireanu, G. Dinescu, L. Le Brizoual, M.A. Djouadi, M. Boujtita, Electrochemical anodic oxidation of nitrogen doped carbon nanowall films: X-ray photoelectron and Micro-Raman spectroscopy study, Appl. Surf. Sci. 273 (2013) 49–57. doi:10.1016/j.apsusc.2013.01.112.

[347] F. Cataldo, Simple generation and detection of polyynes in an arc discharge between graphite electrodes submerged in various solvents, Carbon N. Y. 41 (2003) 2671–2674. doi:10.1016/S0008-6223(03)00345-2.

[348] K. Vasu, K. Pramoda, K. Moses, A. Govindaraj, C.N.R. Rao, Single-walled nanohorns and other nanocarbons generated by submerged arc discharge between carbon electrodes in liquid argon and other media, Mater. Res. Express. 1 (2013) 15001. doi:10.1088/2053-1591/1/1/015001.

[349] S.K. Shin, S.M. Park, Preparation of polyynes by the laser ablation of graphite in water and organic solvents, Bull. Korean Chem. Soc. 33 (2012) 597–600. doi:10.1016/j.apsusc.2010.10.074.

[350] R.B. Heimann, S.E. Evsyukov, K. L., Carbyne and Carbynoid Stuctures, Chem. Phys. Lett. 207 (1999) 480–486. doi:10.1016/0009-2614(93)89033-E.

[351] D. Yang, A. Velamakanni, G. Bozoklu, S. Park, M. Stoller, R.D. Piner, S. Stankovich, I. Jung, D.A. Field, C.A. Ventrice, R.S. Ruoff, Chemical analysis of graphene oxide films after heat and chemical treatments by X-ray photoelectron and Micro-Raman spectroscopy, Carbon N. Y. 47 (2009) 145–152. doi:10.1016/j.carbon.2008.09.045.

[352] V. a Krivchenko, S. a Evlashin, K. V Mironovich, N.I. Verbitskiy, A. Nefedov, C. Wöll,

a Y. Kozmenkova, N. V Suetin, S.E. Svyakhovskiy, D. V Vyalikh, a T. Rakhimov, a V Egorov, L. V Yashina, Carbon nanowalls: the next step for physical manifestation of the black body coating, Sci. Rep. 3 (2013) 3328. doi:10.1038/srep03328.

[353] S. Kurita, A. Yoshimura, H. Kawamoto, T. Uchida, K. Kojima, M. Tachibana, P. Molina-Morales, H. Nakai, Raman spectra of carbon nanowalls grown by plasma-enhanced chemical vapor deposition, J. Appl. Phys. 97 (2005). doi:10.1063/1.1900297.

[354] Haomin Wang, Yihong Wu, C.K.S. Choong, Jun Zhang, Kie Leong Teo, Zhenhua Ni, Zexiang Shen, Disorder induced bands in first order Raman spectra of carbon nanowalls, in: 2006 Sixth IEEE Conf. Nanotechnol., IEEE, 2006: pp. 219–222. doi:10.1109/NANO.2006.247613.

[355] I. Musa, D. Munindrasdasa, G. Amaratunga, W. Eccleston, Ultra-low-threshold field emission from conjugated polymers, Nature. 395 (1998) 362–365. doi:10.1038/26444.

[356] Y.J. Fu, F.J. Xia, Y.L. Jia, C.J. Jia, J.Y. Li, X.H. Dai, G.S. Fu, B.Y. Zhu, B.T. Liu, Bipolar resistive switching behavior of La 0.5 Sr 0.5 CoO 3−σ films for nonvolatile memory applications, Appl. Phys. Lett. 104 (2014) 223505. doi:10.1063/1.4881720.

[357] K. Yu, Z. Bo, G. Lu, S. Mao, S. Cui, Y. Zhu, X. Chen, R.S. Ruoff, J. Chen, Growth of carbon nanowalls at atmospheric pressure for one-step gas sensor fabrication., Nanoscale Res. Lett. 6 (2011) 202. doi:10.1186/1556-276X-6-202.

[358] K. Kinoshita, Carbon: electrochemical and physicochemical properties, Wiley-Interscience. (1988) 560. doi:978-0-471-84802-8.

[359] A. Pandy, Z. Yang, M. Gummalla, V. V. Atrazhev, N.Y. Kuzminyh, V.I. Sultanov, S. Burlatsky, A Carbon Corrosion Model to Evaluate the Effect of Steady State and Transient Operation of a Polymer Electrolyte Membrane Fuel Cell, J. Electrochem. Soc. 160 (2013) F972–F979. doi:10.1149/2.036309jes.

[360] W. Zhang, J. Chen, G.F. Swiegers, Z.-F. Ma, G.G. Wallace, Microwave-assisted synthesis of Pt/CNT nanocomposite electrocatalysts for PEM fuel cells., Nanoscale. 2 (2010) 282–286. doi:10.1039/b9nr00140a.

[361] B. Avasarala, R. Moore, P. Haldar, Surface oxidation of carbon supports due to potential cycling under PEM fuel cell conditions, Electrochim. Acta. 55 (2010) 4765–4771. doi:10.1016/j.electacta.2010.03.056.

[362] O.C. Compton, S.T. Nguyen, Graphene oxide, highly reduced graphene oxide, and graphene: Versatile building blocks for carbon-based materials, Small. 6 (2010) 711–723. doi:10.1002/smll.200901934.

[363] N. Bandara, Y. Esparza, J. Wu, Exfoliating nanomaterials in canola protein derived adhesive improves strength and water resistance, RSC Adv. 7 (2017) 6743–6752. doi:10.1039/C6RA27470F.

[364] G. Sobon, J. Sotor, J. Jagiello, R. Kozinski, M. Zdrojek, M. Holdynski, P. Paletko, J. Boguslawski, L. Lipinska, K.M. Abramski, Graphene Oxide vs Reduced Graphene Oxide as saturable absorbers for Er-doped passively mode-locked fiber laser, Opt. Express. 20 (2012) 19463. doi:10.1364/OE.20.019463.

[365] A.C. Ferrari, J. Robertson, Resonant Raman spectroscopy of disordered, amorphous, and diamondlike carbon, Phys. Rev. B. 64 (2001) 75414. doi:10.1103/PhysRevB.64.075414.

[366] L. Bokobza, J.-L. Bruneel, M. Couzi, Raman Spectra of Carbon-Based Materials (from Graphite to Carbon Black) and of Some Silicone Composites, C—Journal Carbon Res. 1 (2015) 77–94. doi:10.3390/c1010077.

[367] C. Xu, X. Shi, A. Ji, L. Shi, C. Zhou, Y. Cui, Fabrication and characteristics of reduced graphene oxide produced with different green reductants, PLoS One. 10 (2015). doi:10.1371/journal.pone.0144842.

[368] X. Cartoixà, R. Rurali, J. Suñé, Transport properties of oxygen vacancy filaments in metal/crystalline or amorphous HfO 2/metal structures, Phys. Rev. B - Condens. Matter Mater. Phys. 86 (2012) 1–5. doi:10.1103/PhysRevB.86.165445.

[369] S.Z. Rahaman, S. Maikap, W.S. Chen, H.Y. Lee, F.T. Chen, M.J. Kao, M.J. Tsai, Repeatable unipolar/bipolar resistive memory characteristics and switching mechanism using a Cu nanofilament in a GeOx film, Appl. Phys. Lett. 101 (2012) 73106. doi:10.1063/1.4745783.

[370] Z. Zhang, H. Li, L. Shi, The role of single oxygen or metal induced defect and correlated multiple defects in the formation of conducting filaments, (n.d.) 1–15.

[371] F. Pan, Experimental and Simulation Study of Resistive Switches for Memory Applications, (2013).

[372] C.L. He, F. Zhuge, X.F. Zhou, M. Li, G.C. Zhou, Y.W. Liu, J.Z. Wang, B. Chen, W.J. Su, Z.P. Liu, Y.H. Wu, P. Cui, R.W. Li, Nonvolatile resistive switching in graphene oxide thin films, Appl. Phys. Lett. 95 (2009). doi:10.1063/1.3271177.

[373] P. Stoliar, P. Levy, M.J. Sanchez, A.G. Leyva, C.A. Albornoz, F. Gomez-Marlasca, A. Zanini, C. Toro Salazar, N. Ghenzi, M.J. Rozenberg, Nonvolatile multilevel resistive switching memory cell: A transition metal oxide-based circuit, IEEE Trans. Circuits Syst. II Express Briefs. 61 (2014) 21–25. doi:10.1109/TCSII.2013.2290921.

[374] Q.H. Qin, L. Äkäslompolo, N. Tuomisto, L. Yao, S. Majumdar, J. Vijayakumar, A. Casiraghi, S. Inkinen, B. Chen, A. Zugarramurdi, M. Puska, S. van Dijken, Resistive Switching in All-Oxide Ferroelectric Tunnel Junctions with Ionic Interfaces, Adv. Mater. (2016) 6852–6859. doi:10.1002/adma.201504519.

[375] N. Raeis Hosseini, J. Lee, Resistive Switching Memory Based on Bioinspired Natural Solid Polymer Electrolytes, ACS Nano. 9 (2015) 419–426. doi:10.1021/nn5055909.

[376] A. Kim, K. Song, Y. Kim, J. Moon, All solution-processed, fully transparent resistive memory devices, ACS Appl. Mater. Interfaces. 3 (2011) 4525–4530. doi:10.1021/am201215e.

[377] C. Hu, M.D. McDaniel, A. Posadas, A.A. Demkov, J.G. Ekerdt, E.T. Yu, Highly controllable and stable quantized conductance and resistive switching mechanism in single-crystal TiO2 resistive memory on silicon, Nano Lett. 14 (2014) 4360–4367. doi:10.1021/nl501249q.

[378] E. Yoo, M. Lyu, J.-H. Yun, C. Kang, Y. Choi, L. Wang, Bifunctional resistive switching behavior in an organolead halide perovskite based Ag/$CH_3NH_3PbI_{3-x}Cl_x$/FTO structure, J. Mater. Chem. C. 4 (2016) 7824–7830. doi:10.1039/C6TC02503J.

[379] S. Murali, J.S. Rajachidambaram, S.Y. Han, C.H. Chang, G.S. Herman, J.F. Conley, Resistive switching in zinc-tin-oxide, Solid. State. Electron. 79 (2013) 248–252. doi:10.1016/j.sse.2012.06.016.

[380] N.M. Muhammad, N. Duraisamy, K. Rahman, H.W. Dang, J. Jo, K.H. Choi, Fabrication of printed memory device having zinc-oxide active nano-layer and investigation of resistive switching, Curr. Appl. Phys. 13 (2013) 90–96. doi:10.1016/j.cap.2012.06.017.

[381] S. Deshpande, V.V. Nair, Resistive Switching of Al/Sol-Gel ZnO/Al Devices for Resistive Random Access Memory Applications, in: 2009 Int. Conf. Adv. Comput. Control. Telecommun. Technol., IEEE, 2009: pp. 471–473. doi:10.1109/ACT.2009.122.

[382] G. Anoop, V. Panwar, T.Y. Kim, J.Y. Jo, Resistive Switching in ZnO Nanorods / Graphene Oxide Hybrid Multilayer Structures, 1600418 (2017) 1–9. doi:10.1002/aelm.201600418.

[383] F.M. Simanjuntak, D. Panda, K. Wei, T. Tseng, Status and Prospects of ZnO-Based Resistive Switching Memory Devices, Nanoscale Res. Lett. 11 (2016) 368. doi:10.1186/s11671-016-1570-y.

[384] G. Khurana, P. Misra, N. Kumar, R.S. Katiyar, Tunable power switching in nonvolatile flexible memory devices based on graphene oxide embedded with zno nanorods, J. Phys. Chem. C. 118 (2014) 21357–21364. doi:10.1021/jp506856f.

[385] W.H. Xue, W. Xiao, J. Shang, X.X. Chen, X.J. Zhu, L. Pan, H.W. Tan, W.B. Zhang, Z.H. Ji, G. Liu, X.-H. Xu, J. Ding, R.-W. Li, Intrinsic and interfacial effect of electrode metals on the resistive switching behaviors of zinc oxide films, Nanotechnology. 25 (2014) 425204. doi:10.1088/0957-4484/25/42/425204.

[386] H.-L. Ma, Z.-Q. Wang, H.-Y. Xu, L. Zhang, X.-N. Zhao, M.-S. Han, J.-G. Ma, Y.-C. Liu, Coexistence of unipolar and bipolar modes in Ag/ZnO/Pt resistive switching memory with oxygen-vacancy and metal-Ag filaments, Chinese Phys. B. 25 (2016) 127303. doi:10.1088/1674-1056/25/12/127303.

[387] V.S. Yalishev, Y.S. Kim, B.H. Park, S.U. Yuldashev, Resistance states dependence of photoluminescence in Ag/ZnO/Pt structures, Appl. Phys. Lett. 99 (2011). doi:10.1063/1.3607290.

[388] Z. Ibupoto, K. Khun, M. Eriksson, M. AlSalhi, M. Atif, A. Ansari, M. Willander, Hydrothermal Growth of Vertically Aligned ZnO Nanorods Using a Biocomposite Seed Layer of ZnO Nanoparticles, Materials (Basel). 6 (2013) 3584–3597. doi:10.3390/ma6083584.

[389] B. Liu, H.C. Zeng, Hydrothermal Synthesis of ZnO Nanorods in the Diameter Regime of 50 nm, J. Am. Chem. Soc. 125 (2003) 4430–4431. doi:10.1021/ja0299452.

[390] Y. Sun, D.J. Riley, M.N.R. Ashfbld, Mechanism of ZnO nanotube growth by hydrothermal methods on ZnO film-coated Si substrates, J. Phys. Chem. B. 110 (2006)

15186–15192. doi:10.1021/jp062299z.

[391] a Wei, X.W. Sun, C.X. Xu, Z.L. Dong, Y. Yang, S.T. Tan, W. Huang, Growth mechanism of tubular ZnO formed in aqueous solution, Nanotechnology. 17 (2006) 1740–1744. doi:10.1088/0957-4484/17/6/033.

[392] S. Park, J.H. Lee, H.-D. Kim, S.M. Hong, H.-M. An, T.G. Kim, Resistive switching characteristics of sol-gel based ZnO nanorods fabricated on flexible substrates, Phys. Status Solidi - Rapid Res. Lett. 7 (2013) 493–496. doi:10.1002/pssr.201307187.

[393] H.W. Chen, C.Y. Lin, Y.H. Lai, J.G. Chen, C.C. Wang, C.W. Hu, C.Y. Hsu, R. Vittal, K.C. Ho, Electrophoretic deposition of ZnO film and its compression for a plastic based flexible dye-sensitized solar cell, J. Power Sources. 196 (2011) 4859–4864. doi:10.1016/j.jpowsour.2011.01.057.

[394] Z.H. Gu, T.Z. Fahidy, Electrochemical Deposition of ZnO Thin Films on Tin-Coated Glasses, J. Electrochem. Soc. 146 (1999) 156–159.

[395] B. Jun, Preparation of ZnO thin film by electrophoretic deposition(EPD), J. Korean Ceram. Soc. 49 (2012) 78–83. doi:10.4191/kcers.2012.49.1.078.

[396] M. Verde, M. Peiteado, A.C. Caballero, M. Villegas, B. Ferrari, Electrophoretic Deposition of Transparent ZnO Thin Films from Highly Stabilized Colloidal Suspensions, J. Colloid Interface Sci. 373 (2012) 27–33. doi:10.1016/j.jcis.2011.09.039.

[397] T.G. Kim, J.-T. Jang, H. Ryu, W.-J. Lee, Vertical growth of ZnO nanorods on ITO substrate by using a two-step-potential electrochemical deposition method, J. Korean Phys. Soc. 63 (2013) 78–82. doi:10.3938/jkps.63.78.

[398] T.G. Kim, J.-T. Jang, H. Ryu, W.-J. Lee, Vertical growth of ZnO nanorods on ITO substrate by using a two-step-potential electrochemical deposition method, J. Korean Phys. Soc. 63 (2013) 78–82. doi:10.3938/jkps.63.78.

[399] B. Prijamboedi, E. Maryanti, T. Haryati, Preparation of vertically aligned ZnO crystal rods in aqueous solution at external electric field, Mater. Sci. 32 (2014) 157–163. doi:10.2478/s13536-013-0191-8.

[400] A.S. Zoolfakar, R. Ab Kadir, R.A. Rani, S. Balendhran, X. Liu, E. Kats, S.K. Bhargava, M. Bhaskaran, S. Sriram, S. Zhuiykov, A.P. O'Mullane, K. Kalantar-zadeh, Engineering electrodeposited ZnO films and their memristive switching performance, Phys. Chem. Chem. Phys. 15 (2013) 10376. doi:10.1039/c3cp44451a.

[401] B. Postels, A. Bakin, H.H. Wehmann, M. Suleiman, T. Weimann, P. Hinze, A. Waag, Electrodeposition of ZnO nanorods for device application, Appl. Phys. A Mater. Sci. Process. 91 (2008) 595–599. doi:10.1007/s00339-008-4487-1.

[402] X.H. Sun, S. Lam, T.K. Sham, F. Heigl, A. Jürgensen, N.B. Wong, Synthesis and synchrotron light-induced luminescence of ZnO nanostructures: Nanowires, nanoneedles, nanoflowers, and tubular whiskers, J. Phys. Chem. B. 109 (2005) 3120–3125. doi:10.1021/jp044926v.

[403] H. Fukushima, T. Kozu, H. Shima, H. Funakubo, H. Uchida, T. Katoda, K. Nishida,

Evaluation of oxygen vacancy in ZnO using Raman spectroscopy, 2015 Jt. IEEE Int. Symp. Appl. Ferroelectr. Int. Symp. Integr. Funct. Piezoelectric Force Microsc. Work. ISAF/ISIF/PFM 2015. (2015) 28–31. doi:10.1109/ISAF.2015.7172660.

[404] R. Al-Gaashani, S. Radiman, A.R. Daud, N. Tabet, Y. Al-Douri, XPS and optical studies of different morphologies of ZnO nanostructures prepared by microwave methods, Ceram. Int. 39 (2013) 2283–2292. doi:10.1016/j.ceramint.2012.08.075.

[405] V. Gaddam, R.R. Kumar, M. Parmar, M.M. Nayak, K. Rajanna, Synthesis of ZnO nanorods on a flexible Phynox alloy substrate: influence of growth temperature on their properties, RSC Adv. 5 (2015) 89985–89992. doi:10.1039/C5RA12773D.

[406] F. Hai-Bo, Y. Shao-Yan, Z. Pan-Feng, W. Hong-Yuan, L. Xiang-Lin, J. Chun-Mei, Z. Qin-Sheng, C. Yong-Hai, W. Zhan-Guo, Investigation of Oxygen Vacancy and Interstitial Oxygen Defects in ZnO Films by Photoluminescence and X-Ray Photoelectron Spectroscopy, Chinese Phys. Lett. 24 (2007) 2108–2111. doi:10.1088/0256-307X/24/7/089.

[407] C. Soci, A. Zhang, B. Xiang, S.A. Dayeh, D.P.R. Aplin, J. Park, X.Y. Bao, Y.H. Lo, D. Wang, ZnO nanowire UV photodetectors with high internal gain, Nano Lett. 7 (2007) 1003–1009. doi:10.1021/nl070111x.

[408] B.A. Albiss, M.-A. AL-Akhras, I. Obaidat, Ultraviolet photodetector based on ZnO nanorods grown on a flexible PDMS substrate, Int. J. Environ. Anal. Chem. 95 (2015) 339–348. doi:10.1080/03067319.2015.1016010.

[409] J.R.D. Retamal, C.-F. Kang, C.-H. Ho, J.-J. Ke, W.-Y. Chang, J.-H. He, Effect of ultraviolet illumination on metal oxide resistive memory, Appl. Phys. Lett. 105 (2014) 253111. doi:10.1063/1.4904396.

[410] L.M. Kukreja, P. Misra, J. Fallert, D.M. Phase, H. Kalt, Correlation of spectral features of photoluminescence with residual native defects of ZnO thin films annealed at different temperatures, J. Appl. Phys. 112 (2012). doi:10.1063/1.4730774.

[411] R. Laiho, D.S. Poloskin, Y.P. Stepanov, M.P. Vlasenko, L.S. Vlasenko, V.S. Zakhvalinskii, Persistent photoconductivity and electron paramagnetic resonance in zinc oxide ceramics, J. Appl. Phys. 106 (2009). doi:10.1063/1.3159646.

[412] P. Wu, J. Zhang, J. Lu, X. Li, C. Wu, R. Sun, L. Feng, Q. Jiang, B. Lu, X. Pan, Z. Ye, Instability induced by ultraviolet light in ZnO thin-film transistors, IEEE Trans. Electron Devices. 61 (2014) 1431–1435. doi:10.1109/TED.2014.2312947.

[413] P. Liu, G. She, Z. Liao, Y. Wang, Z. Wang, W. Shi, X. Zhang, S.T. Lee, D. Chen, Observation of persistent photoconductance in single ZnO nanotube, Appl. Phys. Lett. 94 (2009). doi:10.1063/1.3082173.

[414] S.A. Studenikin, M. Cocivera, Time-resolved luminescence and photoconductivity of polycrystalline ZnO films, J. Appl. Phys. 91 (2002) 5060–5065. doi:10.1063/1.1461890.

[415] J. Park, S. Lee, K. Yong, Photo-stimulated resistive switching of ZnO nanorods, Nanotechnology. 23 (2012) 385707. doi:10.1088/0957-4484/23/38/385707.

[416] J.R.D. Retamal, C.-F. Kang, C.-H. Ho, J.-J. Ke, W.-Y. Chang, J.-H. He, Effect of ultraviolet illumination on metal oxide resistive memory, Appl. Phys. Lett. 105 (2014) 253111. doi:10.1063/1.4904396.

[417] K. Vanheusden, W.L. Warren, C.H. Seager, D.R. Tallant, J.A. Voigt, B.E. Gnade, Mechanisms behind green photoluminescence in ZnO phosphor powders, J. Appl. Phys. 79 (1996) 7983–7990. doi:10.1063/1.362349.

[418] J. Qi, M. Olmedo, J. Ren, N. Zhan, J. Zhao, J.G. Zheng, J. Liu, Resistive switching in single epitaxial ZnO nanoislands, ACS Nano. 6 (2012) 1051–1058. doi:10.1021/nn204809a.

[419] S. Bayan, D. Mohanta, Defect mediated optical emission of randomly oriented ZnO nanorods and unusual rectifying behavior of Schottky nanojunctions, J. Appl. Phys. 110 (2011). doi:10.1063/1.3631792.

[420] Z.M. Liao, H.Z. Zhang, Y.B. Zhou, J. Xu, J.M. Zhang, D.P. Yu, Surface effects on photoluminescence of single ZnO nanowires, Phys. Lett. Sect. A Gen. At. Solid State Phys. 372 (2008) 4505–4509. doi:10.1016/j.physleta.2008.04.013.

[421] N. Liu, G. Fang, W. Zeng, H. Zhou, F. Cheng, Q. Zheng, L. Yuan, X. Zou, X. Zhao, Direct growth of lateral ZnO nanorod UV photodetectors with schottky contact by a single-step hydrothermal reaction, ACS Appl. Mater. Interfaces. 2 (2010) 1973–1979. doi:10.1021/am100277q.

[422] L.J. Mandalapu, F.X. Xiu, Z. Yang, J.L. Liu, Ultraviolet photoconductive detectors based on Ga-doped ZnO films grown by molecular-beam epitaxy, Solid. State. Electron. 51 (2007) 1014–1017. doi:10.1016/j.sse.2007.05.009.

[423] J.D. Prades, F. Hernandez-Ramirez, R. Jimenez-Diaz, M. Manzanares, T. Andreu, A. Cirera, A. Romano-Rodriguez, J.R. Morante, The effects of electron–hole separation on the photoconductivity of individual metal oxide nanowires, Nanotechnology. 19 (2008) 465501. doi:10.1088/0957-4484/19/46/465501.

[424] I. Mora-Sero, L. Bertoluzzi, V. Gonzalez-Pedro, S. Gimenez, F. Fabregat-Santiago, K.W. Kemp, E.H. Sargent, J. Bisquert, Selective contacts drive charge extraction in quantum dot solids via asymmetry in carrier transfer kinetics., Nat. Commun. 4 (2013) 2272. doi:10.1038/ncomms3272.